



HAL
open science

Localization processes within active faults

Mai Linh Doan

► **To cite this version:**

Mai Linh Doan. Localization processes within active faults: Insights from high strain rate experiments and in-situ characterization. Geophysics [physics.geo-ph]. Université Joseph Fourier (Grenoble 1), 2013. tel-04357398

HAL Id: tel-04357398

<https://hal.science/tel-04357398>

Submitted on 21 Dec 2023

HAL is a multi-disciplinary open access archive for the deposit and dissemination of scientific research documents, whether they are published or not. The documents may come from teaching and research institutions in France or abroad, or from public or private research centers.

L'archive ouverte pluridisciplinaire **HAL**, est destinée au dépôt et à la diffusion de documents scientifiques de niveau recherche, publiés ou non, émanant des établissements d'enseignement et de recherche français ou étrangers, des laboratoires publics ou privés.

HABILITATION À DIRIGER DES RECHERCHES

Spécialité : **Sciences de la Terre**

Présentée par

Mai-Linh DOAN

préparée au sein d' **ISTerre**
et de l'**Ecole Doctorale Terre, Univers, Environnement**

Localization processes within active faults

Insights from high strain rate experiments and in-situ characterization

Thèse soutenue publiquement le **20 novembre 2013**,
devant le jury composé de :

M., Georg DRESEN

GFZ Postdam, Germany, Rapporteur

M., Daniel FAULKNER

Liverpool University, United Kingdom, Rapporteur

M., Yves GUGLIELMI

Université Aix-Marseille / CEREGE, France, Rapporteur

M., Fabrice COTTON

Université Grenoble Alpes, France, Examineur

M., Jean CHERY

Université de Montpellier II, France, Examineur



Contents

0	Résumé étendu en français	4
1	Introduction	8
2	Localization process at the onset of coseismic slip	11
2.1	Water dependence of talc friction at high strain rate	11
2.2	Effect of small amount of talc on the onset of friction of gouges of serpentine and talc	12
2.3	Conclusions	14
3	Damage localization during an earthquake	16
3.1	Pulverization: an extreme case of dynamic damage	17
3.1.1	Can we reproduce pulverization ?	17
3.1.2	What are the conditions for pulverizing rocks ?	19
3.2	Microscopic characterization of dynamic damage	21
3.2.1	Reproduction of microscopic pulverization	21
3.2.2	What are the transport properties of rocks damaged dynamically?	23
3.3	Conclusions	24
4	In-situ measurements of hydraulic properties across active faults	25
4.1	Direct pumping tests	28
4.1.1	Cross-hole testing along Chelungpu Fault, Taiwan	28
4.1.2	Exploiting the MDT tool data provided by the NanTroSEIZE project	28
4.2	Assessing hydraulic profiles from logs	29
4.3	Long term monitoring of pore pressure	30
4.3.1	Extracting hydromechanical properties from tidal analysis	30
4.3.2	Triggering of sliding episode of landslide within a clay-rich slope	34
4.4	Conclusions	34
5	Conclusions and Perspectives	36
5.1	Conclusions	36
5.2	Future work	36
5.2.1	Experimental dynamic damage	37
5.2.2	Drilling to more seismogenic conditions	39
	Bibliography	41
A	Curriculum Vitae	46
A.1	Education / Professional cursus	46
A.2	Committee memberships and awards	46
A.3	Collaborations	46
A.4	Supervision of students	47
B	Publications	48
B.1	Publication list	48
B.2	Papers in preparation	49
C	A selection of papers	50

C.1	High velocity experiments with talc	51
	C.1.1 Boutareaud et al, J. Geophys. Res., 2012	52
	C.1.2 Doan et al, to be submitted to J. Struct. Geol.	73
C.2	High strain rate damage	97
	C.2.1 Doan and Gary, Nature Geoscience, 2009	98
	C.2.2 Doan and Billi, Geophys. Res. Lett., 2011	102
	C.2.3 Doan and d’Hour, ,J. Struct. Geol. 2012	108
	C.2.4 Gratier et al., Geology, 2011	120
	C.2.5 Richard et al., to be submitted to J. Geophys. Res.	124
C.3	Borehole geophysics	164
	C.3.1 Doan et al, Geophys. Res. Lett., 2006	165
	C.3.2 Doan et al, Earth Planet. Sci. Lett., 2007	170
	C.3.3 Lin et al. , Geophys. Res. Lett., 2010	182
	C.3.4 Doan et al, Geochem. Geophys. Geosyst., 2011	188
	C.3.5 Doan et al., to be submitted to Geophys. Res. Lett.	200

Chapter 0

Résumé étendu en français

La mécanique des failles actives est une science jeune. Une question en apparence aussi simple que la structure des failles actives est encore une question ouverte. La structure fine d'une faille active est en effet difficile à prédire *a priori*. Or cette structuration est un pré-requis pour comprendre la mécanique d'une faille active, des processus de nucléation présismiques, des processus de propagation du glissement cosismiques, ou encore des processus de recimentation postsismiques.

Sur le terrain, les failles présentent différentes structures. Certaines peuvent se présenter comme une faille simple, où la déformation est localisée dans un cœur de faille entouré d'une zone endommagée. D'autres sont plus complexes, avec plusieurs zones localisant le glissement. Cette structuration est le reflet d'interactions entre les processus d'initiation du glissement, d'endommagement et de recimentation.

Mes travaux traitent des processus de localisation dans des failles actives, par une approche multi-échelle. De l'échelle métrique à décamétrique, les données en forage permettent d'avoir un profil continu des propriétés physiques à travers une faille. Les forages permettent aussi l'installation d'observatoires long terme. A l'échelle centimétrique, les expériences de laboratoire permettent d'identifier et de caractériser les processus contrôlant l'évolution de l'endommagement et de la localisation de la déformation.

0.1 Résumé des travaux

0.1.1 Caractérisation in-situ des failles actives

Durant la dernière décennie, plusieurs forages ont été entrepris pour caractériser les failles actives en profondeur. Forer apporte plusieurs informations inaccessibles autrement: il est possible (1) d'obtenir des échantillons frais, sans altération, (2) de caractériser la structure et les propriétés des failles dans des conditions de température et de contraintes in-situ, de l'échelle décimétrique à décamétrique (3) d'installer des observatoires permanents pour suivre au plus près l'évolution des failles au cours du cycle sismique. Au cours de mon activité de recherche, j'ai pu couvrir tous ces aspects.

Processus de fluage au sein de la faille de San Andreas

Lors de la thèse de Julie Richard, co-encadrée avec Jean-Pierre Gratier, j'ai pu observer des échantillons récoltés dans le forage SAFOD (San Andreas Fault Observatory at Depth).

Dans la zone endommagée entourant le cœur de de faille, on peut observer des traces importantes de dissolution-cristallisation [Gratier *et al.*, 2011]. Ce processus est activé par la microfracturation intense des grains, dont on ne peut écarter une origine dynamique [Doan and Gary, 2009].

Dans la zone de faille, la déformation est accommodée par des phyllosilicates de friction très faible, qui présente de multiples zone de localisation le long de nombreuses structures S-C. La dissolution-cristallisation reste toutefois importante [Richard *et al.*, 2014a].

Caractérisation in situ des propriétés hydrauliques des failles

Les forages permettent d'accéder aux roches de failles en condition in-situ. Les mesures réalisées ne sont donc pas biaisées par d'éventuelles décompressions ou de changement de géochimie des fluides interstitiels. C'est donc une méthode de choix pour caractériser les propriétés hydromécaniques du milieu.

Quasi systématiquement, des diagraphies en forage sont réalisées. Elles permettent d'obtenir des profils continus des propriétés physiques des roches en place, comme la résistivité électrique des roches, les vitesses des ondes sismiques ou l'émission radioactive naturelle. Indirectement, elles permettent d'accéder à la porosité des roches (par exemple *Doan et al.* [2011]). Elles permettent aussi d'inférer un profil continu de perméabilité, au moins qualitatif [*Saffer et al.*, 2013; *Doan et al.*, a], ce qui permettrait de caractériser l'extension de la zone endommagée d'une faille.

Ces données sont couplées à des mesures hydrauliques directes par essai de pompage. Ces méthodes sont assez couteuses et ponctuelles, mais donnent des mesures fiables. Une première méthode consiste à immerger une pompe et tester un large intervalle du puits: cette méthode est peu précise spatialement mais elle permet d'étudier un large volume si le pompage est suffisamment long. Par exemple, *Doan et al.* [2006a] ont pu mesurer la perméabilité de la zone endommagée de la faille de Chelungpu, à l'origine du séisme de Chichi en 1999. Cet essai par choc hydraulique été mesuré sur 2 semaines. La faible diffusivité hydraulique mesurée ($\sim 7 \times 10^{-5} \text{ m}^2/\text{s}$) rendrait plus efficace l'adoucissement de la faille par pressurisation thermique.

Une autre méthode consiste à utiliser une sonde spécifique, comme le MDT (Modular formation Dynamics Tester) de Schlumberger. Cet outil issu de l'industrie pétrolière permet d'effectuer des essais hydrauliques sur des sections de forage isolées par des obturateurs. Les essais peuvent être réalisés à l'échelle centimétrique ou métrique. Le coût est très élevé, et l'outil demande un puits de bonne qualité et de grand diamètre. Son premier déploiement dans le cadre d'IODP (International Oceanic Drilling Program) n'a donc pu se faire que lors de la mission IODP 319 [*Moe et al.*, 2012], qui a été la première à utiliser la technologie riser dans le cadre du programme NanTroSEIZE (Nankai Trough SEImic Zone Experiment). Grâce à cet outil, on a pu obtenir une perméabilité in-situ à l'échelle métrique et centimétrique [*Boutt et al.*, 2012], et estimer des profils de pression de pore [*Saffer et al.*, 2013] et de contraintes [*Ito et al.*, 2013].

Suivi long terme de l'évolution de la pression interstitielle

L'installation d'un observatoire permet de suivre l'évolution de la faille au cours du temps. Même en dehors du cycle sismique, les failles peuvent subir des variations importantes de pression. Par exemple, lors de ma thèse [*Doan*, 2005], j'avais pu observer que la pression de pore mesurée près de la faille d'Aigion chutait au passage des ondes téléseismiques générées par un séisme d'épicentre éloigné de plus 10 000 km [*Doan and Cornet*, 2007].

Le dépouillement des données demande un filtrage des marées terrestres et des fluctuations barométriques. La réponse à ces forçages renseignent indirectement sur les propriétés hydromécaniques du milieu [*Doan et al.*, 2006b].

L'accès à ces données est difficile, car peu d'observatoires ont été installés dans des failles actives. Cette activité se fait en collaboration. J'ai pu ainsi accéder aux données de pression acquises par l'instrumentation installée dans phase 1 du projet Deep Fault Drilling Project, qui étudie la faille de San Andreas.

0.1.2 Étude en laboratoire de la localisation dynamique de l'endommagement

En marge de mes activités de forage, au potentiel scientifique important, mais de nature épisodique, je me suis consacrée à des expériences de mécanique des roches en laboratoire. Ces études concernent aussi la problématique de la localisation de la déformation lors d'un séisme, que ce soit dans la zone endommagée cernant la zone de faille, ou dans le cœur de faille.

Inhibition de la localisation lors de l'endommagement dynamique des roches

Les vitesses de glissement cosismiques atteignent le mètre par seconde, voire la dizaine de mètre par seconde. De plus, les vitesses de propagation du glissement sont proches des vitesses des ondes dans le milieu. On entre dans le domaine de la mécanique de la fracture dynamique.

Les effets inertiels deviennent alors non négligeables [Grady and Kipp, 1987]: la vitesse de propagation des fractures au sein du milieu devient limitée par la vitesse des ondes sismiques [Bhat et al., 2012]. Les temps caractéristiques d'interaction entre fractures deviennent similaires à ceux de la propagation des fractures les plus favorables [Denoual and Hild, 2000]. On s'attend donc à la propagation simultanées de plusieurs fractures et à la multifragmentation du milieu, comme ce qui est observé près des zones d'impact de météorite [Melosh, 1989].

Curieusement, l'étude de l'endommagement dynamique a été délaissée jusque vers le milieu des années 2000. Mes études ont été motivées par la découverte de roches pulvérisées [Wilson et al., 2005; Dor et al., 2006] près des zones de failles. Ces roches sont finement fragmentées mais restent peu déformées. Elles s'étendent de manière continue plusieurs centaines de mètres autour du cœur de faille. Tout se passe comme si la déformation restait diffuse au lieu de se localiser le long de grandes fractures, comme observé à cette distance du cœur de faille. Cet endommagement rappelle l'endommagement dynamique des roches.

Pour tester l'origine dynamique des roches pulvérisées, j'ai testé des échantillons de roches prélevées près du segment Mojave de la faille de San Andreas sur un banc de barres de Hopkinson. Avec un tel dispositif, on peut obtenir des courbes contraintes-déformation jusque des vitesses de déformation de plusieurs milliers par seconde. Les expériences ont permis de reproduire un endommagement proche de la pulvérisation [Doan and Gary, 2009]. On observe en effet macroscopiquement trois états finaux pour les échantillons: soit les échantillons restent intacts, soit les échantillons sont fendus en 2 ou 3 fragments, soit les échantillons sont finement multifragmentés. La transition semble contrôlée par la vitesse de déformation, plutôt que par la déformation ou par le confinement dynamique. Cette observation a été renouvelée sur d'autres roches cristallines [Yuan et al., 2011; Doan and D'Hour, 2012]. Par contre, des expériences sur des marbres ne permettent pas de retrouver une pulvérisation à haute vitesse de déformation et faible déformation [Doan and Billi, 2011]. Ceci est cohérent avec l'absence de roches pulvérisées trouvées dans les roches carbonatées [Dor et al., 2006]. Le seuil en vitesse de déformation est contrôlée par la distribution statistique de défauts dans le milieu. Notamment, le seuil est abaissé pour une roche très endommagée. Des chargements multiples au cours de plusieurs cycles sismiques contribuent à une fracturation plus fine des roches pulvérisées près du cœur de failles.

Dans une deuxième étape, j'ai collaboré avec des géologues structuraux pour caractériser l'endommagement dynamique. Les échantillons ont été chargés en deçà du seuil de rupture de façon à obtenir des échantillons préservés, dont les propriétés physiques peuvent être étudiées. Ces études ont révélé que les échantillons sont finement microfracturés, ce qui induit une diminution de la vitesse sismique des ces ondes [Doan et al., 2009], et surtout une augmentation substantielle de la perméabilité de ces roches. Les microstructures observées et les perméabilités mesurées sont proches de celle mesurées sur des échantillons prélevés près de la faille de San Jacinto [Mitchell et al., 2013].

Influence des impuretés de talc sur l'initiation du glissement dynamique de la serpentine

Avec des collègues grenoblois et lyonnais, nous avons lancé une étude sur la friction à vitesse cosismique du talc et de la serpentine. Cette étude a été lancée en 2008, au moment où du talc a été découvert dans des fragments extraits du forage SAFOD [Moore and Rymer, 2007]. Le talc est connu son faible coefficient de friction, et il a été soupçonné de lubrifier la faille de San Andreas. Comme le talc est issu de la décomposition de pyroxène en milieu saturé de silice, son association avec la serpentine est attendue dans des failles sismiques, comme les failles de subduction.

L'étude a d'abord consisté en l'étude du talc seul, dont les propriétés de friction à haute vitesse de cisaillement n'avaient pas été étudiées jusque là [Boutareaud et al., 2012]. Nous avons montré que

le talc sec avait une forte friction initiale, beaucoup plus importante que le talc à faible vitesse de déformation. Au contraire, le talc humide ne présente pas de pic initial de friction, comme ce qui a été observé pour d'autres phyllosilicates [Faulkner et al., 2011]. L'humidité altère aussi la localisation de la déformation dans l'échantillon.

La suite de l'étude a consisté en l'étude de la friction de mélanges de talc et de serpentine [Doan et al., b]. En conditions humides, où le talc est un matériau faible, le talc altère la friction initiale dès des concentrations de 5% de talc. Les microstructures observées sont beaucoup plus diffuses que dans le cas de la serpentine pure, avec une déformation répartie sur l'ensemble de la gouge, initiée sur les grains de talc en cours de délamination, qui servent à microlocaliser le glissement.

Dans ces deux études, la localisation du glissement est fortement dépendante de la proportion de microdéfauts susceptibles de localiser la déformation. Dans les deux cas, en cas de chargement rapide, la localisation de la déformation peut être inhibée.

0.2 Perspectives

0.2.1 S'approcher des conditions sismogéniques

Les forages traversant les failles actives tendent à viser des profondeurs de plus en plus importantes (table 4.1). On aborde alors des contraintes et des températures plus élevées. Ces conditions activent des processus de fluage, soit par pression-solution, soit par activation de la plasticité des minéraux. Les processus que j'ai étudiés jusqu'à présent relevaient surtout du domaine fragile. A moyen terme, je compte m'approcher de conditions plus ductiles, et ce pour les deux approches expérimentales et in-situ.

L'activité en forage est une activité fortement épisodique, du fait du faible nombre de forages internationaux en cours. J'ai cependant été amenée à participer à plusieurs workshops d'avant projet concernant des forages traversant des failles actives:

- La faille Alpine en Nouvelle-Zélande a une composante inverse qui fait remonter des matériaux ductile. Elle induit aussi une anomalie thermique. On peut donc étudier par des forages de profondeur modérée des processus ductiles. Je suis partie prenante de la phase 2 du projet qui vise à forer et instrumenter la faille à près de 1500 m de profondeur.
- Le projet NantroSEIZE vise à percer le décollement de la zone de subduction de Nankai. Il est prévu de prolonger le puits C002 jusqu'à intercepter ce décollement à 7000 m de profondeur
- Le projet Japan Beyond Brittle Project est un projet de géothermie profonde, visant à faire circuler des fluides à haute enthalpie dans des matériaux ductiles. Bien que le projet ne vise pas des failles actives préexistantes en particulier, il approche des thématiques liées, comme le suivi microsismique et la vitesse de recimentation des fractures. J'ai été invité à participer au workshop ICDP préliminaire en mars 2013.

0.2.2 Réunir les approches expérimentales et in-situ

Les travaux réalisés jusqu'à présent concernaient surtout l'endommagement des matériaux fragiles. Le lien entre expériences en laboratoire et les travaux en forage restent encore ténu. Le verrou principal est l'absence de fort confinement des expériences en laboratoire. A cela s'ajoute la faible saturation en eau des roches. L'arrivée à Grenoble de Pascal Forquin va permettre de développer ces aspects par des essais œdométriques d'échantillons saturés.

Pour les travaux de pulvérisation, il est important de mieux caractériser l'endommagement. Pour cela, nous envisageons d'utiliser un surfacemètre BET, en voie d'acquisition à ISTerre.

La création d'un réseau microfracturé va altérer la circulation de fluide. La faible distance interfracture est notamment suspecté d'activer les processus de recimentation et fluage des failles par pression-solution. Nous comptons donc effectuer des expériences de percolation sous contrainte pour étudier ces processus. Ces travaux initiés lors de la thèse de Julie Richard seront poursuivis lors de la thèse de Frans Aben.

Chapter 1

Introduction

Predicting earthquakes is the Graal of seismologists, a dream so far not realized. Major faults can experience precursory activity [*Bouchon et al., 2011*], as monitored from seismic network. However, surface observations failed to provide systematic precursors prior to an earthquake, even when an extensive network of instruments has been deployed, like at Parkfield, California [*Johnston et al., 2006*]. A major obstacle to predictability of the behavior of active faults is their structural complexity.

Let illustrate this complexity with the San Andreas Fault Observatory at Depth (SAFOD) project, that was drilled through the San Andreas Fault, deeper than 3 km (figure 1.1). The project is one of the greatest recent achievements in fault drilling and provided many outcomes: it showed that the creep behavior could be better explained by the weak friction coefficient of the saponite, a subproduct of alteration [*Lockner et al., 2011*] or by pressure-solution process [*Gratier et al., 2011*], but certainly not by high fluid pressure [*Rice, 1992*].

It provided also many surprises. The fault was not separating the crystalline Salinian formation from the Franciscan mélange: instead, unexpected arkosic sandstone laid on the western side of the fault. The fault itself is much thicker than the simple planar structures envisioned by seismologist and geodesist, with a damage zone more than 200 m wide. Within this fault core, two major deformation zones were able to twist the metallic casing of the hole. Several observations don't match the standard pictures described by structural geologists [*Chester and Logan, 1986*]: cores did not show principal shear zone localizing deformation within few centimeters, as seen for instance within the Chelungpu fault [*Ma et al., 2006*], whereas the damage zone stops abruptly on one of the deformation zone.

Note also how the authors of figure 1.1 try to connect the two major deformation zone seen in the SAFOD borehole to the microseismic swarm found about 100 m away from the borehole. Given the errors in event locations, it is a bit audacious. This illustrates the major challenge towards predictive fault mechanics: it is difficult to extrapolate the structures observed outside the range of observation.

This difficulty in structure predictability is annoying, since the structure of a fault affects several properties:

- Their propensity to fail. The gouge of last slipping strand can be substantially weak, but it is also consolidated by healing, sometimes becoming stronger than prior to slip. Healing of this zone depends on the fluid geochemistry, that can be changed by enhanced permeability along fault (fault valve effect, [*Sibson, 1992*]). Pressure solution is also enhanced by smaller grain size, that can be due to co-seismic fragmentation [*Doan and Gary, 2009*], and the presence in moderate amount of clays [*Bos et al., 2000*].
- Their transport properties, as permeability varies as the cube of the fracture aperture. It is often seen that fractures are found along not in the core itself (because gouges are often plastic, full of clay), but in the nearby damage zone (large fractures take a longer time to heal [*Gratier and Gueydan, 2007; Gratier et al., 2011*]).

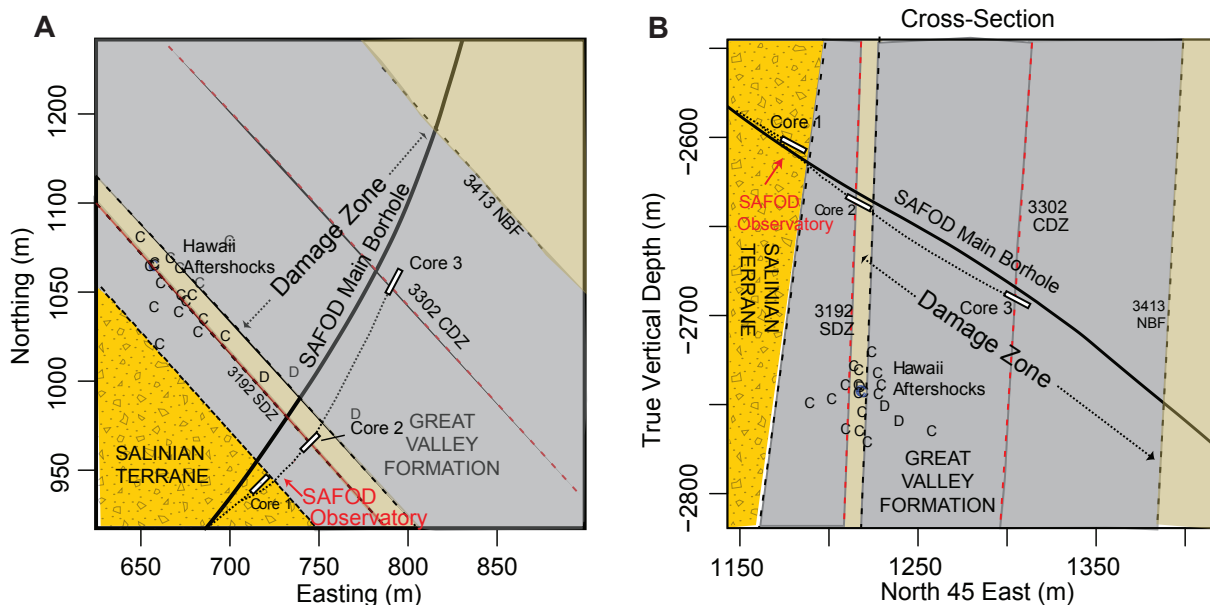
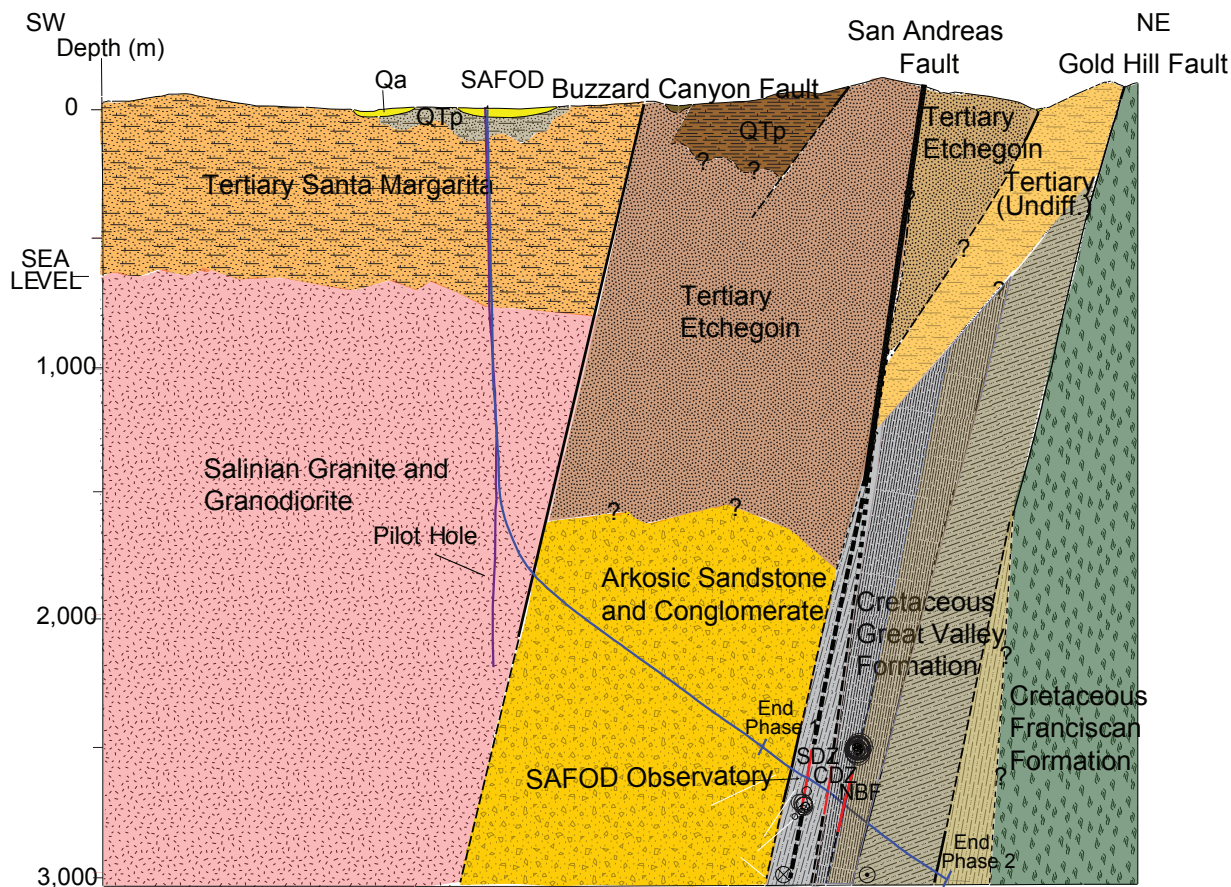


Figure 1.1: Cross section of the SAFOD boreholes. The 2 close-up at the bottom zooms on the borehole trajectory within the San Andreas Fault (lower left: map view, lower right: cross section, zoom from the above figure). From [Zoback et al. \[2011\]](#).

- Their mechanical compliance, not only because of the presence of weak components like clay, but because the large amount of fractures within the damage zone. Mechanical compliance may control the sensitivity of fault to static triggering by nearby earthquakes or dynamic triggering by teleseismic waves.

How to improve our knowledge on fault structure ?

A first approach is by observing more natural faults, and trying to identify several typical structures. Natural active faults have a variety of structures [*Faulkner et al., 2010*; *Caine et al., 1996*]. They can be composed of a single very localized strand [*Chester and Logan, 1986*] or be formed of a series of anastomosing fault surfaces [*Faulkner et al., 2003*] that isolate strong lenses within a fault [*Candela and Renard, 2012*]. These structures can be described by the variation of the physical parameters, which can be quantified and characterized at several scales.

I performed such a quantification using geophysical data from boreholes drilled through active faults. Boreholes provide exceptional opportunities to understand fault structures in in-situ conditions and monitor fault evolution at depth. Using such data, I could provide and help refining models describing profiles of permeability across several major active faults (Chelungpu Fault, San Andreas Fault, Nankai Trough). From long term monitoring, I could show how these parameters can vary through time.

A second approach is by performing laboratory experiments to reproduce these structures, and identifying and explaining how a fault gets structured. Scale there is centimetric, much smaller than the field scale observation. Hence I redesigned the experiments to understand the more general question of strain localization, and how it is controlled by strain rate. I especially discuss the high strain rate processes, that are expected to occur during slip, or even at the arrival of the seismic waves of the approaching rupture patch, and how they prepare the fault prior to its slip. In particular, I focus on high strain rate damage. I also worked on the dynamic structuration of a fault gouge during high velocity shearing, using a technique that revolutionized friction studies [*Di Toro et al., 2011*].

The report is structured from small-scale process to large scale processes, from the sub-centimetric fault core which localized slip to the decametric structure of the damage zone.

- We start from the center of the fault, with high velocity friction experiments on mixture of talc and serpentine, at the millimetric scale. At high velocity, structure and friction interplay. Especially, small amount of talc help localizing deformation along many small shear planes, thus limiting strain concentration on the principal shear zone at the edge of the sample. Minor changes in gouge composition can change the width of the shear zone, or alter the easiness a creation of new shear zone. This is bad omen for predicting fault structure.
- We then discuss high strain rate fragmentation in the damage zone, at the centrimetric scale. I pioneered the application of high strain damage experiments to fault mechanics, to understand pulverized rocks, a damage feature recently discovered [*Dor et al., 2006*]. I showed that high strain rate inhibit strain localization. Therefore, pulverized rocks might be related to coseismic damage, and that they could be marker of previous large earthquakes [*Doan and Gary, 2009*]. Pulverization can also change permeability drastically [*Mitchell et al., 2013*], showing that fault structure is time-dependent.
- We finish with borehole studies in active faults. I show how it is possible to get continuous profiles of permeability and porosity to characterize damage extent around faults [*Doan et al., 2011, a*] at the decametric scale. I also discuss how long term pore pressure monitoring could monitor fault destabilisation either from teleseismic waves, or even prior a major fault disturbance.

Chapter 2

Localization process at the onset of coseismic slip

In this section, we will discuss the behavior of fault gouge at the millimetric scale to understand how a mixture of weak and strong material behaves at high sliding velocities. Such high velocity friction experiments revolutionized our knowledge of fault friction, by showing dramatic reduction in friction properties [*Di Toro et al., 2011*], through many processes, often thermally activated (thermal pressurization [*Wibberley and Shimamoto, 2005*], phase transitions like decarbonation [*Han et al., 2010*], melting [*Hirose, 2005*],...).

For usual friction experiments, inserting material of weak friction randomly in a mixture is not very effective, as large concentrations are needed to reduce the effective friction of the mixture (eg, see the 50%-50% results for mixture of talc and quartz by *Carpenter et al. [2009]*). The mixture needs to be structured to change the friction, with the constitution of a continuous layer of weak material [*Niemeijer et al., 2010; Moore and Lockner, 2011*]. Are weak heterogeneities more efficient at high sliding velocity ?

Together with Takehiro Hirose, Sébastien Boutareaud, Muriel Andréani and Anne-Marie Boullier, I conducted high velocity friction experiments on mixtures of gouge and talc. This mixture is pertinent geologically, since talc is a product of alteration of pyroxene in silica-rich environment and is often associated with serpentine in ultramafic rocks. The layers of this phyllosilicate slide easily also their basal direction, so that its friction is very small (about 0.15 [*Moore and Rymer, 2007*], much less than the 0.6-0.8 range found for most material [*Byerlee, 1978*]). Such combination are expected to occur in along faults bordering core-complexes at mid-ocean ridges [*Ildefonse et al., 2007*], subduction zones [*Manning, 1995*]. We launched the project at the time when talc fragments were identified within the SAFOD borehole [*Moore and Rymer, 2007*]. Given its very low friction coefficient, it was suspected to lubricate the San Andreas Fault.

2.1 Water dependence of talc friction at high strain rate

We first investigated the high velocity friction behavior of talc, in both saturated and unsaturated conditions, since at that time its properties at high velocity friction experiments were not characterized.

Figure 2.1 shows that unsaturated talc exhibits very large friction compared to slow slip rate conditions. Figure 2.2 shows the associated microstructures seen with Scanning Electron Microscopy (SEM). A S-C structure pervades the center of the gouge, so that most of the grains are not favorably oriented to accommodate the formation. At the boundary with the rotating cylinder driving the sample rotation, a principal slip zone (PSZ) seems to accommodate the deformation: it is finely comminuted, with some remnants of layers of talc parallel to the shear direction. Transmission Electron Microscopy (TEM) on the PSZ shows that talc has been finely delaminated and advected by the rotational movement to form nanometric aggregates (figure 2.3). It is probable that the peak

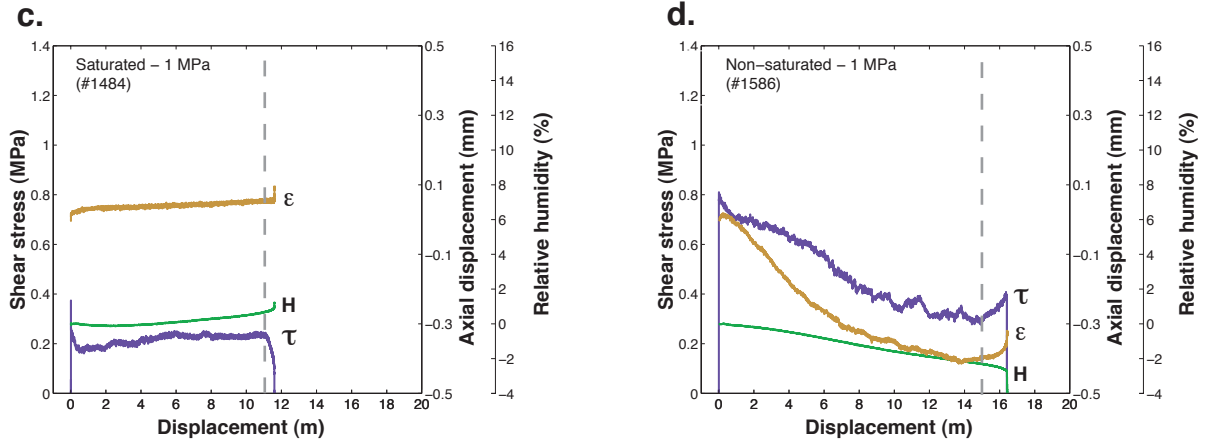


Figure 2.1: Evolution of friction coefficient with displacement for water saturated talc (left graph) and dry talc (right graph). From [Boutareaud et al. \[2012\]](#).

in friction is caused by jamming of the talc particles, that was resolved within the PSZ by intense delamination.

The experimental curves obtained for wet talc give lower friction, closer to the slow strain rate results, once friction induced by friction on the teflon ring holding the artificial gouge has been removed. Almost from the onset of slip, talc friction is small. The effect of water can be multiple: it can be related either to thermal pressurization, as for other wet phyllosilicate gouges [[Faulkner et al., 2011](#)], or to hydrodynamic lubrication at the boundary of the hydrophobic talc layers, that facilitates the rotation of talc grains to the most favorable angle, parallel to the shear direction.

2.2 Effect of small amount of talc on the onset of friction of gouges of serpentine and talc

To tackle the friction properties of serpentine and talc, we kept saturated conditions, where talc has low friction coefficient, and can be considered as the weak component of the gouge mixture. Several mixtures of various proportions were tested. For these experiments, we used a loose Teflon ring of standardized dimension to limit its effect on friction. To assess the effect of the Teflon sleeve on the recorded friction experiments, we performed dummy tests, with only the Teflon ring and water inside the ring. The Teflon effect is reproducible and negligible: the shear stress due to friction on Teflon ring is 0.03 MPa.

The experiments in wet conditions show a spectacular weakening effect of talc on the mixture (figure 2.4). Pure serpentine experiences strong slip weakening, with a peak friction coefficient of 0.5 that falls exponentially to a steady-state value of 0.2 with a characteristic slip-weakening distance D_c of 7 m. Talc has a very different behavior: it begins to slide without a sharp friction peak and keeps nearly constant friction coefficient of 0.2-0.25. Adding more than 5%wt talc levels off the initial peak in friction and initial friction is reduced to 0.37. Friction levels to this value before rejoining the decay curve of pure serpentine after 3 m of slip.

The two gouge components have very different behaviors (figure 2.3, left). Serpentine tends to break into angular fragments. Hence, pure serpentine gouge tends to form PSZ finely comminuted (figure 2.5, A). On the contrary, talc tends to kink and delaminate easily. The insertion of talc seems to reduce the extent of the principal shear zone. Meanwhile within the center of the gouge, several shear zones appear, creating a flowing structures. The small shear fractures follow alignment of talc grains that delaminated (figure 2.5, F).

A possible scenario is that peak in friction is related to jamming of serpentine grains that was resolved by the abrasion of serpentine grains and possibly thermal pressurization. Introducing talc,

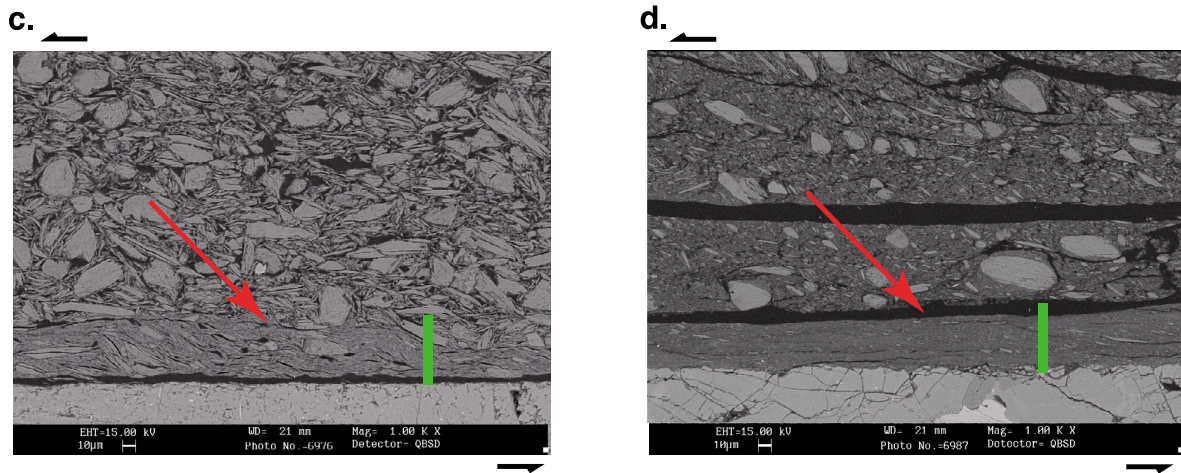


Figure 2.2: Microstructures of the principal slip zones (PSZ) generated during the experiments shown on figure 2.1. (Left) SEM backscattered images in wet conditions, the PSZ contains talc lamellae of large dimensions; entangled in a tight S-C structure. The top of the image shows that in the less disturbed center of the gouge, talc grains get oriented parallel to the slip direction, in a direction favorable for a basal slip. (Right) SEM backscattered image in dry conditions. The center of the gouge shows the tip of the S-C structure pervading the center of the gouge, where most of the grains are not orientated favorably for S-C sliding. From [Boutareaud et al. \[2012\]](#).

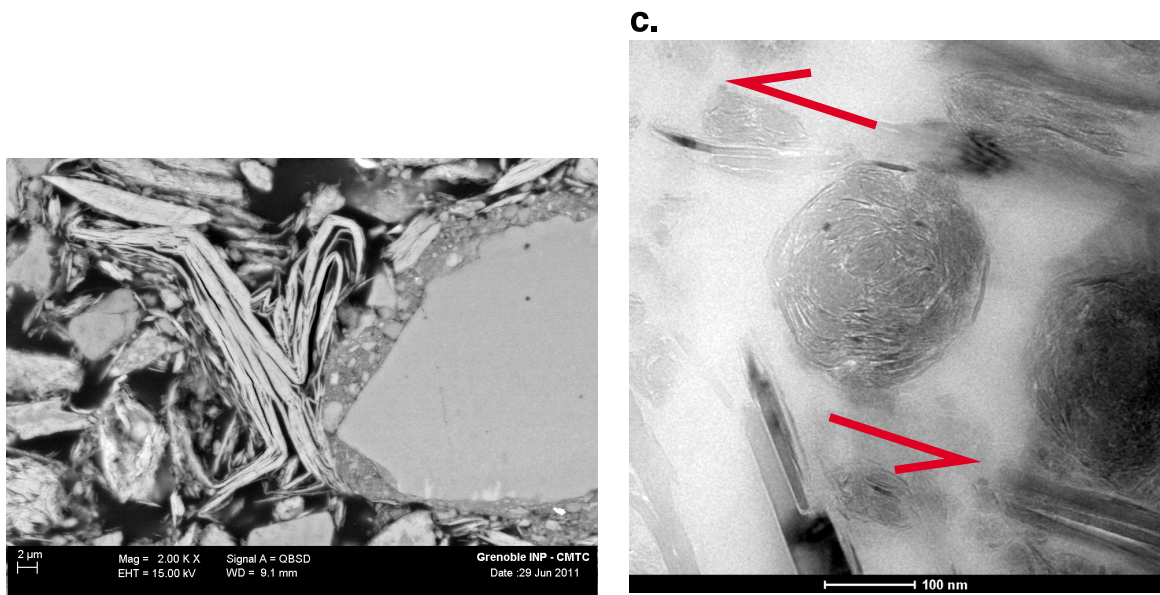


Figure 2.3: Microstructural image showing easy talc delamination. (Left) SEM photograph showing the easy delamination of talc compared, whereas serpentine grains tend to break into angular fragments. (Right) TEM photograph, where extremely delaminated talc was rolled to nanometric aggregate (from [Boutareaud et al. \[2012\]](#)).

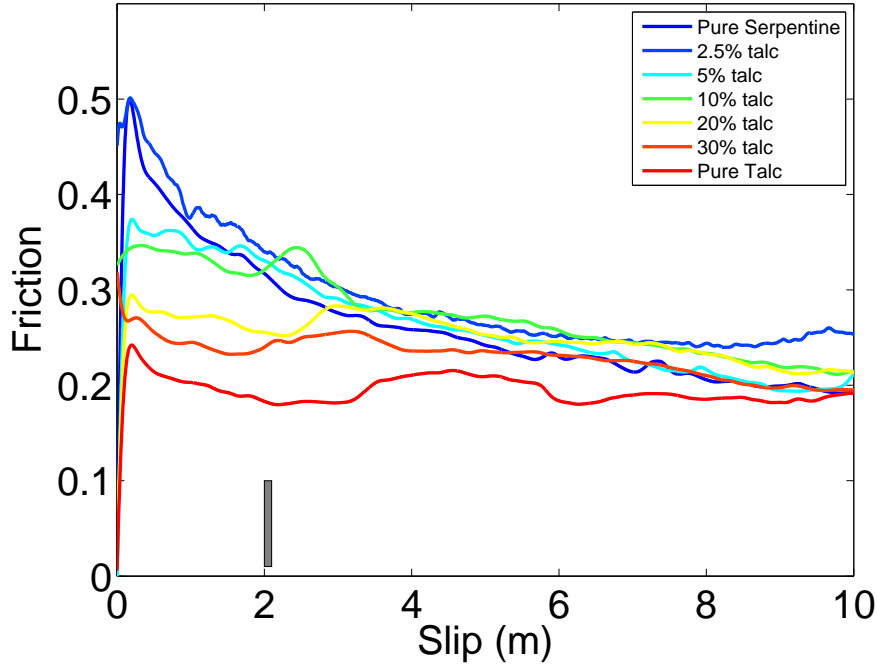


Figure 2.4: Evolution of friction coefficient with displacement for wet mixtures of serpentine and talc. Talc concentration as small as 5%wt is enough to reduce the initial peak in friction. From *Doan et al.* [b]

eased the formation of local shear zone, that helped overcome the grain-to-grain interlocking of serpentine.

2.3 Conclusions

In this section, we showed that the dynamic properties of friction were quite different from the low strain rate properties. For instance, jamming of dry talc prevented the reorientation of talc grains into a favorable angle and gave large friction coefficients. Similar happens for serpentine gouge alone.

The softening process seems to be eased by "strain catalysts". For wet talc, water seems to favor the reorientation of talc into a favorable sliding direction. For mixtures of talc and serpentine, delamination of talc grains initiate small shear zone, creating a more diffuse pattern of strain than for serpentine. This effect occurs from the onset of friction. The reduction of the initial peak in friction has several important implication for rupture propagation [*Faulkner et al., 2011*]: it reduces the frictional strength of the fault zone and the neutral frictional behavior would make talc-rich zones, neither seismogenic, since there no slip weakening, neither barrier to further earthquake rupture since there is not slip strengthening.

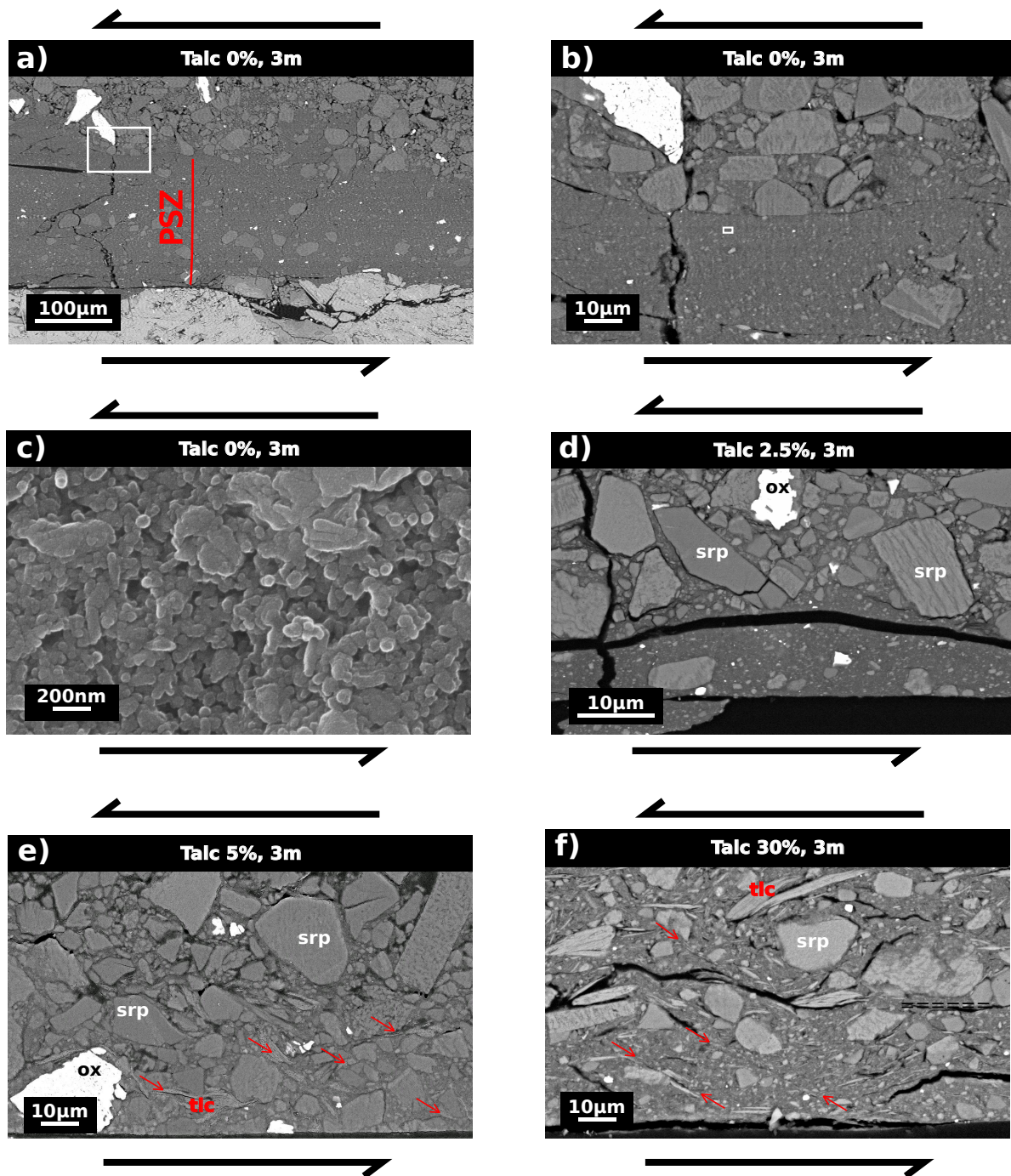


Figure 2.5: Microstructure of the sliding zone after 3 m of slip observed with a FE SEM. (A) Pure serpentinite with a 100 μm -wide Principal Shear Zone (PSZ). White grains are magnetite (iron oxyde). (B) Focus on the sharp boundary between the PSZ and the main gouge. (C) Zoom on the submicron grain constituting the PSZ matrix. (D) Mixture with 2.5%wt talc. The PSZ is thinner but the texture is still similar to the pure serpentinite case. On this photograph, the heterogeneous color contrast of the serpentinite grains is due to the fact that serpentinite grains are aggregates of small crystals. (E) Mixture with 5% talc. Comminution of serpentine grains within the PSZ is reduced. Grains of talc coat the serpentinite grains (red arrows). (F) Mixture with 30%wt talc. There is no developed PSZ, but there are many shear planes characterized by alignment of talc grains (red arrows). From *Doan et al.* [b].

Chapter 3

Damage localization during an earthquake

Fault localizes slip within a narrow core filled by fine-grained material named gouge. Around this core, lies a damage zone of variable extension, with decreasing fracture density with distance from the core. Damage near fault can be generated by several processes [Mitchell and Faulkner, 2009], either statically from the slow extension of the fault, or dynamically during the rupture process.

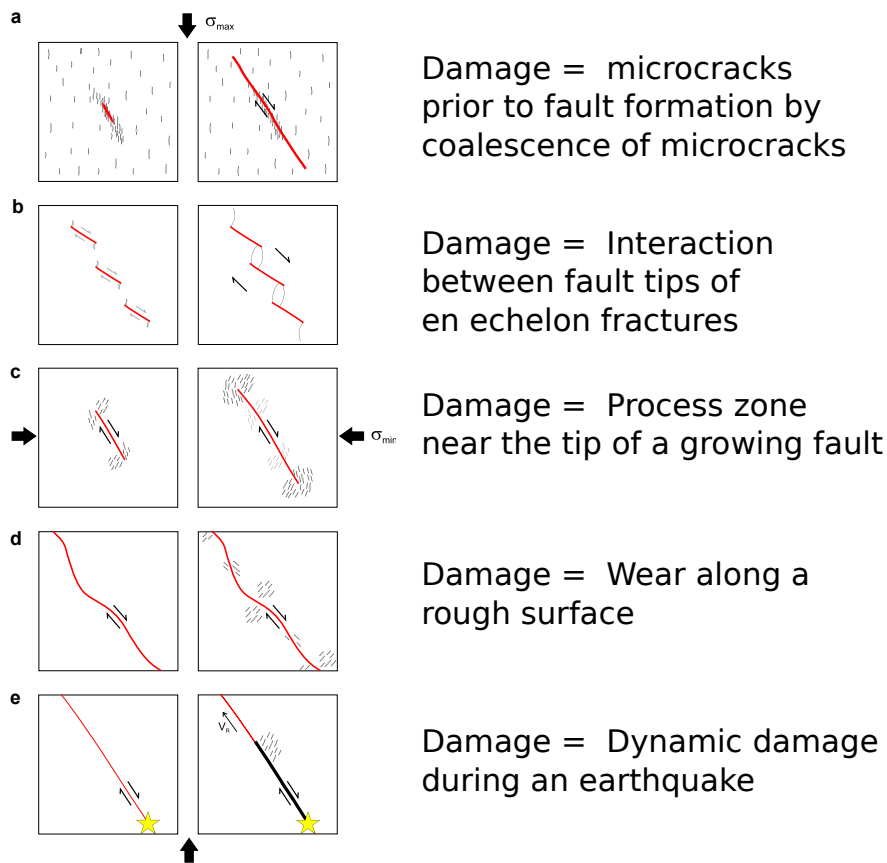


Figure 3.1: Review of 5 models explaining the damage observed around faults. Dynamic damage (model e) would be overprinted with other mechanisms of damage and subsequent fault healing. From [Mitchell and Faulkner \[2009\]](#).

Deciphering dynamic damage is difficult because of the overprinting of static damage, inherited during the maturation of the fault, and the subsequent healing. The best location to assess the extent of dynamic damage is a shallow environment – where healing is slow [[Gratier, 2011](#)] –, near

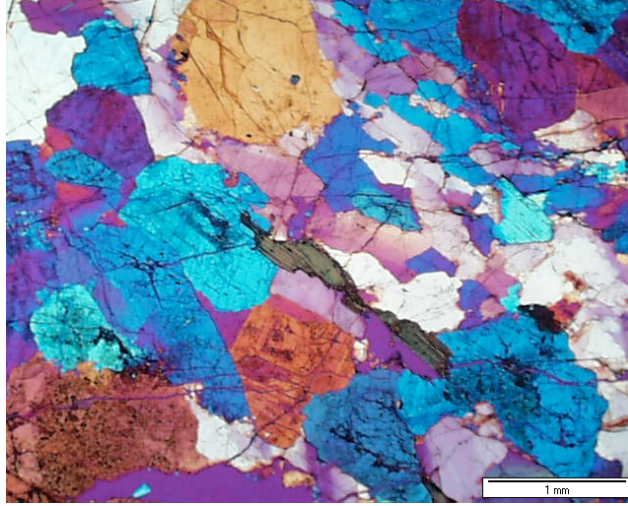


Figure 3.2: Thin section of a pulverized rock sampled near Lake Hughes, along the Mojave segment of the San Andreas Fault. The sample is microfractures, with fractures cutting through grains. The initial grain structure is preserved. Feldspar alteration is present but cannot explain the weakness of the rock. From [Doan and D'Hour \[2012\]](#)

major active faults where large earthquakes are also expected. This is where pulverized rocks have been so far detected.

3.1 Pulverization: an extreme case of dynamic damage

Pulverized rocks is a peculiar form of damage, only recently identified, first near major Californian faults [[Wilson et al., 2005](#); [Dor et al., 2006](#)], and observed thereafter on several active faults (Northern Anatolian Fault [[Dor et al., 2008](#)], Arima-Akatsuki fault [[Mitchell et al., 2011](#)]). It is characterized by an intense microfracturing, with many intragranular fractures, but with little strain recorded, as the initial microstructures are not disturbed. In the field, the rock may look fresh but is easily crumbled by hand. This microfracturing is extensive: zones of pulverized rock extending over several hundred of meters have been reported [[Dor et al., 2006](#); [Mitchell et al., 2011](#)].

Pulverized rocks are surprising because strain has not been localized, as is commonly seen in nature and in laboratory experiments [[Hild et al., 2003](#)]. During our research, we hypothesized that high strain rate loading would have inhibited strain localization. Pulverized rocks could therefore be records of previous large earthquakes occurring near the fault.

To test this hypothesis, we conducted experiments at high strain rate. Several questions were to be answered:

1. Can we reproduce pulverization ?
2. What are the conditions to get pulverization ?

3.1.1 Can we reproduce pulverization ?

We recognize experimentally pulverization as the lack of localization of damage and the fragmentation of the tested sample into multiple small fragments. The first experiments we conducted with rocks sampled near the Lake Hughes area, a road outcrop near the San Andreas Fault where intense pulverization was reported [[Dor et al., 2006](#)]. The experiments were performed in the Ecole Polytechnique at the Laboratoire de Mécanique des Solides in collaboration with Gérard Gary.

We used Split Hopkinson Pressure Bars (SHPB) to load the sample uniaxially at strain rates between 50 /s and 500 /s. At such rate, elastic wave propagation has to be taken into account. For

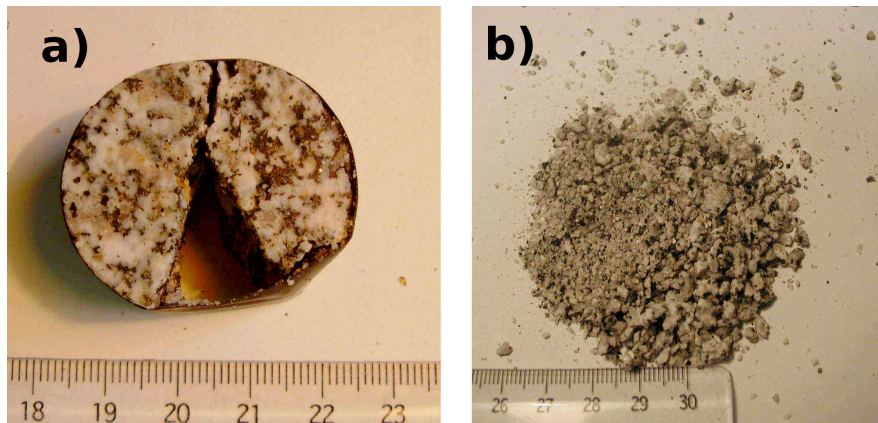


Figure 3.3: (a-left) At a low strain rate (here, 140/s), a granodiorite sample split into a few fragments when deformed in the Split Hopkinson Pressure Bar apparatus. (b-right) At a higher strain rate (here, 400/s), the sample was pulverized into numerous fragments with diameter smaller than the rock initial grain size. The ruler has centimetric marks. From [Doan and Gary \[2009\]](#)

instant, 1% strain at 500 /s is reached after $20 \mu\text{s}$. During that time, stress waves propagate over 10 cm in a metal cylinder with P wave velocity of 5000 m/s. In usual rock mechanics rigs – and in the SHPB system –, stress gauges do not record the actual stress experienced by the sample. With the simple geometry of the SHPB apparatus, it is possible to retropropagate waves to the ends of the bars, hence to the edges of the sample. That is why SHPB apparatus are commonly used to perform high strain rate experiments [[Chen and Song, 2010](#)].

Yes, for crystalline rocks

The first set of experiments we performed was on natural granodioritic samples from the San Andreas Fault, near the Lake Hughes outcrop of pulverized rocks. We took non pulverized rocks sampled at about 100 m from the fault core, and used them as a proxy of the rocks before pulverization: damaged, but only slightly. The uniaxial high strain rate experiments provided only 3 outcomes [[Doan and Gary, 2009](#)]:

1. the sample was not damaged
2. the sample was split axially in a few fragments, no more than 5. This is the typical damage observed when a rock sample is uniaxially loaded at low strain rate [[Paterson and Wong, 2005](#)].
3. the sample was shattered in multiple small fragments, smaller than the initial grain size of about 1 mm. This diffuse damage is reminiscent of pulverized rocks.

We made other experiments on the Tarn granite, which we used as a proxy for undamaged rocks, and found again only these 3 states [[Doan and D'Hour, 2012, Fig8](#)]. Other authors working independently on Westerly granite found similar results [[Yuan et al., 2011](#)].

No, for limestone

We also tried to reproduce pulverization on carbonate rocks [[Doan and Billi, 2011](#)], motivated by the observation of both pulverized granitic rocks and intact limestone on the same outcrop near Lake Hughes.

Contrary to the crystalline rocks, we think we did not achieve pulverization. First, in conditions where we collected multiple fragments, the final grains do not have a round shape, but a elongated needle-like shape not seen for crystalline rocks. Second, post-mortem samples that were jacketed and whose fracture pattern could be examined display a hierarchy of fractures (figure 3.4), suggesting

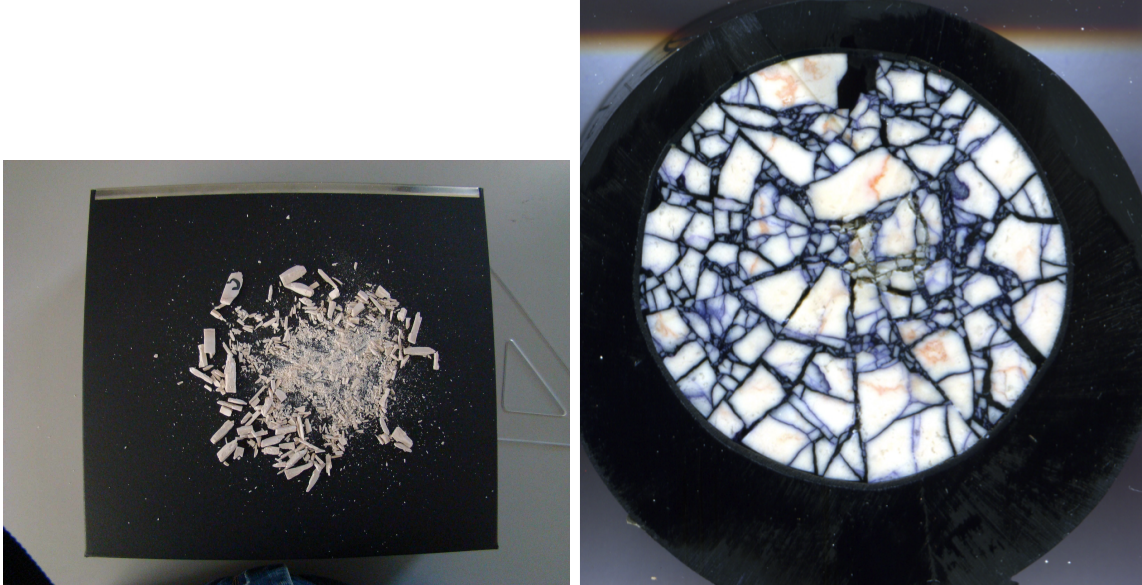


Figure 3.4: Cross-section from a "pulverized" marble sample (Sample B). Diameter is about 2.5 cm. There is a hierarchical fracture pattern, suggesting that deformation localized and the dense microfractured structure results from cumulated faults. On theunjacketed samples, the fragments have a needle shape pattern, suggesting that deformation occurs by accumulating tensile fractures perpendicular to the loading direction.

that tensile transverse deformation localized on a few fractures and create new blocks, and afterwards other fractures appear within each block. With increasing strain, intense microfracturing is observed, but with a different process from pulverized rocks: the multiple fractures appeared successively, but not simultaneously.

3.1.2 What are the conditions for pulverizing rocks ?

Strain rate effects on macroscopic damage

The intense fragmentation tends to happen at high strain rate loading. Figure 3.5 summarizes all the tests made on the San Andreas Fault samples [Doan and Gary, 2009]. Pulverization is achieved when strain rate exceeds a given threshold, here about 150 /s. This result is confirmed by other studies. For instance, we conducted a similar series of experiments on Tarn granite [Doan and D'Hour, 2012, Fig8], a non pre-damaged rock, for which the scatter of data due to variability is reduced. Similarly, Yuan *et al.* [2011] found also a threshold in pulverization on Westerly granite samples. In these two studies done on intact granitic rocks, the threshold in strain rate is also about 250 /s.

Such strain rate is not expected for a standard sub-sonic rupture propagating at a speed below the S wave velocity of the medium. Several hypotheses can be proposed to explain such high strain rate: supershear rupture [Doan and Gary, 2009], bimaterial interface [Shi and Ben-Zion, 2006] or local heterogeneities that accumulated energy and suddenly fail [Dunham *et al.*, 2003]. In all cases, pulverized rocks may be records of high frequency shaking, and it may be useful for paleoseismology.

Why does high strain rate favor pulverization ?

Several processes occur during damage of a rock: (1) crack nucleation where the local intensity factor exceeds a threshold, (2) crack coalescence and (3) crack propagation.

The classical model to describe rock failure at low strain rate is the Weibull model [Weibull, 1939]. It assumes that once a crack nucleates, it will propagate instantaneously and localize deformation. This model is valid if loading rate is so small that fracture propagation can be neglected. Given a statistics of fracture length, a statistics of failure probability with applied stress can be determined.

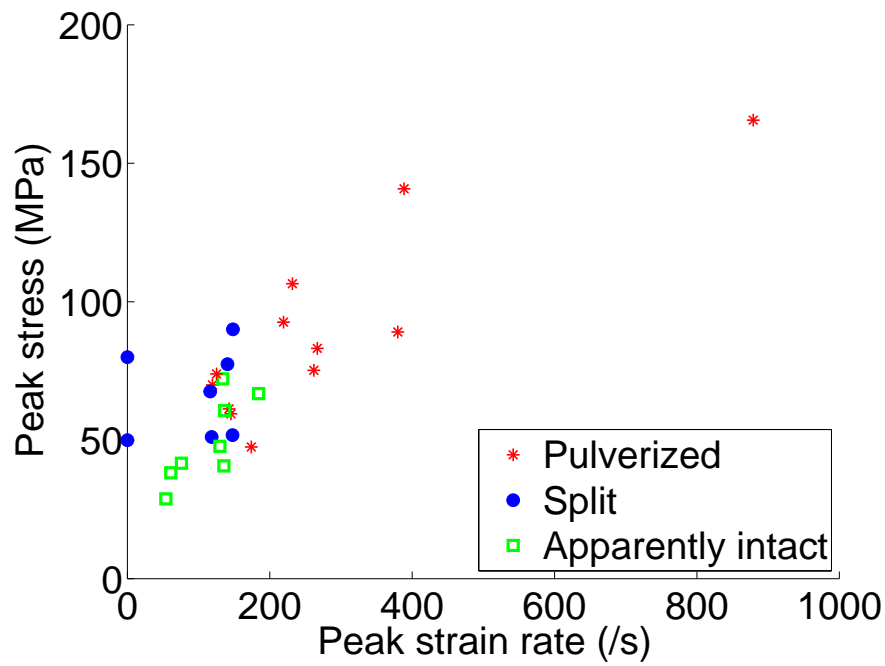


Figure 3.5: Summary of the high strain rate experiments conducted on the samples from the San Andreas Fault. We report the final state of the sample, as a function of the maximum stress reach and the maximum strain rate experienced during the loading.

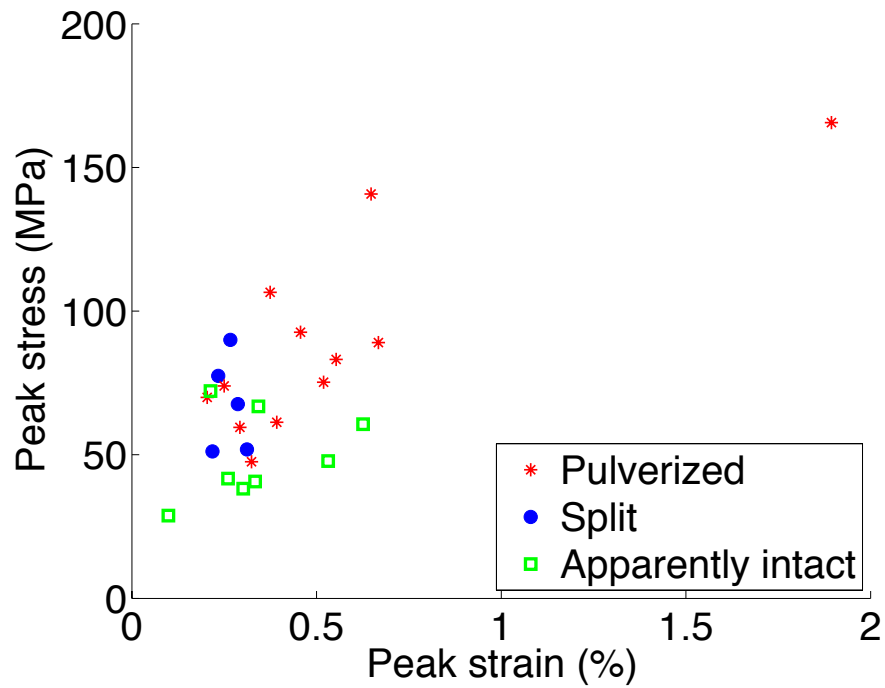


Figure 3.6: Summary of the strain reached for the same experiments as in figure 3.5.

The model of *Denoual and Hild* [2000] explains how multifracturing occurs at high strain rate. The favorable fractures prevent the nucleation of other fractures. This changes the density of fracture that can be activated. They couple the density of fractures with a mean-field theory, where local stress is screened by a damage parameter directly dependent of the density of fracture. They find that strength increases beyond a threshold stress rate, similar to the threshold we detected.

We use this model to interpret the threshold of strain rate and the influence of initial damage on our results [*Doan and D'Hour*, 2012]. The threshold diminishes with the increasing initial density of flaws. A rock next to a fault experiences many earthquakes, and are loaded repeatedly. One can expect that once a rock became pulverized, its flaw density increases sharply, so that it pulverizes more easily during the next loading, leading to the occurrence of extremely comminuted rocks. On the other hand, rocks with high pulverization threshold would not enter this feedback process. Competent rocks and pulverized rocks could therefore next to each other on the same size of the fault, as observed on the Lake Hughes outcrop on the San Andreas Fault [*Dor et al.*, 2006].

Discussion: what are the influence of parameters other than strain rate on our results

We discussed so far the trend to get pulverization at high strain rate. However, several parameters affect the macroscopic failure state.

The first one is the strain experienced by the sample. We expect a correlation between high fracture density and strain: even if microfracture propagation is not localized, damage accumulates with strain as seen in section 3.1.1. Moreover, Split Hopkinson Bars cannot be servocontrolled: if the damaged sample fails, it may accumulate large damage as the loading is not stopped at the onset of failure. To limit strain, we use a shorter striker to limit the loading duration. In the data set of *Doan and Gary* [2009] (figure 3.6) pulverization is not always systematically associated high strain, at it occurs sometimes with the same strain as for axially split sample.

There are also artifacts related to the structure of the sample. The major one is the effect of dynamic confinement, that results to the slow lateral expansion of the sample (controlled by stress wave propagation) compared to its loading rate. With lateral confinement above ~ 15 MPa, failure mode of Westerly Granite switched from axial splitting to shear fracture [*Waversik and Brace*, 1971]. When estimating lateral confinement with the formulation of *Forrestal et al.* [2007] for our test, a maximum value of ~ 10 MPa was reached, with most values around 2 MPa.

In conclusion: strain rate is a key parameter to pulverizing rocks. However, other parameters may not negligible and should be systematically checked in later studies.

3.2 Microscopic characterization of dynamic damage

Macroscopic description of damage is a convenient way to assess damage patterns, but its lacks quantitative description. To get describable states of damage, the samples were jacketed by a shrinkable jacket. In the study of *Doan and Billi* [2011, Fig3], this jacket did not alter the mechanical data. We made with Andrea Billi a preliminary observation of microstructure on limestone. With Tom Mitchell we improve further the microstructural and petrophysical studies of the samples.

Note that in this section, we do not focus on pulverized rocks only, but on any structures that could be associated with dynamic damage.

3.2.1 Reproduction of microscopic pulverization

One of the initial projects we conducted with Tom Mitchell was to investigate the effect of multiple high strain rate loadings on the microstructure. We took care to apply small strains to better preserve microstructure. To our surprise, the apparently intact samples display intense microscopic damage (figure 3.7, [*Mitchell et al.*, 2013]). No macroscopic fractures appeared, as the microfractures did not coalesce. Although we were below the strain rate threshold characterized macroscopically, damage was diffuse within the sample, as for pulverized rocks.

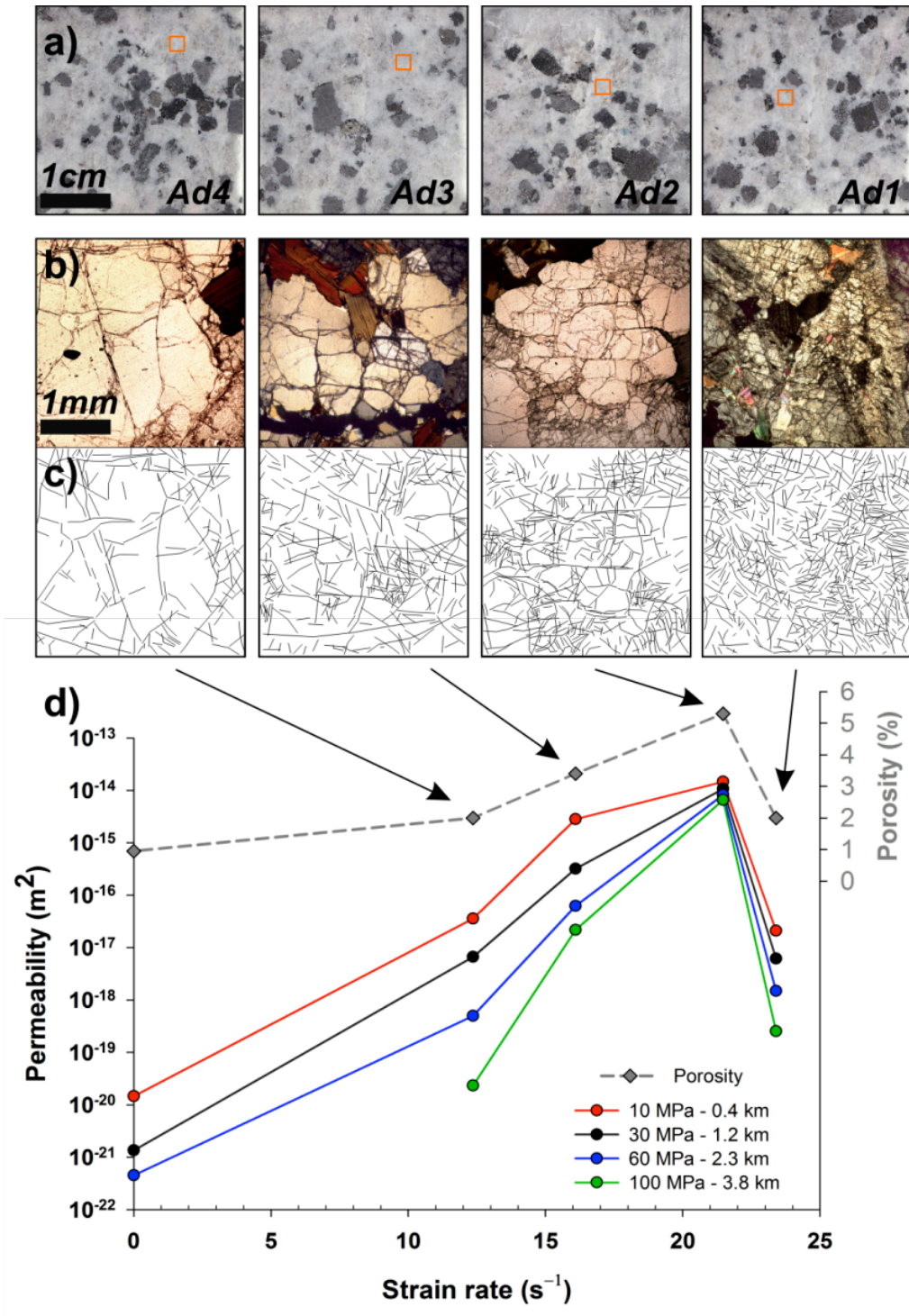


Figure 3.7: Microstructures obtained from high strain rate experiments. (Top) No fractures are visible at the macroscopic scale. (Middle) Thin section observation of the same samples as in top figure shows intense microfracturing. (Bottom) Permeability measurements shows permeability enhancement by more than 5 orders of magnitude, in a pattern similar to natural observations on the San Jacinto Fault. After *Mitchell et al.* [2013]

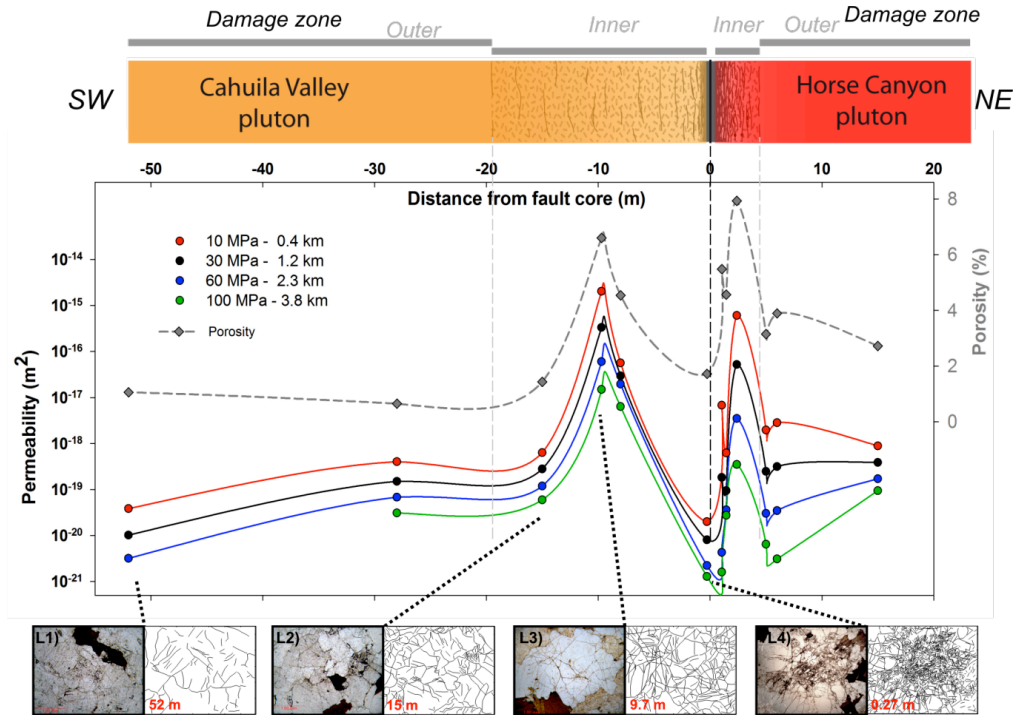


Figure 3.8: Permeability profiles measured on cores collected across the San Jacinto Fault. Permeability values and microstructures are similar to the experimental ones (figure 3.7). After Mitchell *et al.* [2013].

3.2.2 What are the transport properties of rocks damaged dynamically?

As my field work mainly focuses on the hydrological properties of faults, I will discuss here the major results retrieved on permeability and healing properties of rocks damaged at high strain rate.

Permeability

With Tom Mitchell, we were interested to the permeability of the samples damaged at high strain rate. We damaged together tonalite samples at low strain and moderate strain rate (figure 3.7). The samples were thereafter inserted it in a permeability measurement cell and confined with effective pressure up to 90 MPa. Some samples exhibit a permeability enhancement by 5 orders of magnitude, associated with the intense microfracture pattern, similarly to natural samples (figure 3.8). Note that in both natural and experimental results, the maximum permeability is not reached for the most fractured rocks. A possible explanation is that fracture lengths are smaller in pulverized rocks. As fracture width increases with fracture length, and permeability scales as the cube of fracture width, permeability is reduced despite the higher fracture density.

This dynamic enhancement of permeability has potential application on the mechanics of the seismic rupture. The early shaking due to seismic waves propagated ahead of a dynamic rupture can increase permeability and decrease the potential for thermal pressurization. It alters fluid transport, that could be of importance for subsequent healing processes.

Change in healing processes

Fault heal through many processes. One of the major process is pressure-solution, which is more efficient with smaller transport distance [Gratier and Gueydan, 2007]. For pulverized rocks, this distance is controlled by inter-fracture distance and is hence very small, which fosters intense pressure-solution. During the PhD of Julie Richard (co-supervised with Jean-Pierre Gratier), we conducted healing experiments on porous limestone (Estailade Limestone) by percolating reactive fluids through the samples during several months. We encountered many experimental issues and the results are currently being analyzed. Yet preliminary study show promising results, with a very different behavior

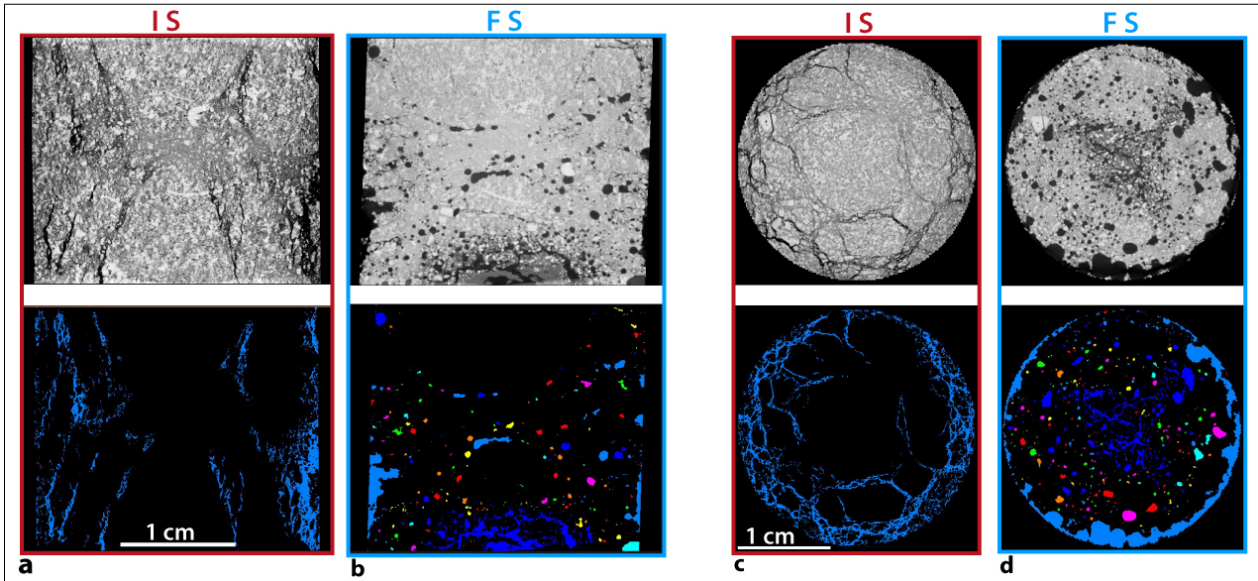


Figure 3.9: Postmortem structure after percolation of reactive fluids from X-ray CT Scan imaging. Left part gives vertical section of the initial state (IS) and final state (FS) of the sample. Right part shows cross sections of the bottom of the same sample. From [Richard et al. \[2014b\]](#)

for an intact sample and microfractured sample, as seen from X-ray CT scan images. For the microfractured sample, large dissolution features like round cavities coexist with zone apparently sealed. The occurrence of such features are very limited for the intact sample. In the case of active faults, damage associated to earthquakes is expected to greatly activate the geochemical processes: transport of fluids from depth, healing and creeping by pressure solution [[Gratier, 2011](#)].

This study is to be extended during the PhD of Frans Aben (in co-supervision with François Renard), we plan to foster with study, especially to monitor permeability evolution with time.

3.3 Conclusions

High strain rate damage seems to have a specific signature, with the extension of several fractures simultaneously. This creates a dense network of smaller fractures that changes dramatically the properties of the faults during the various phases of the coseismic cycle. The large increase in permeability can inhibit thermal pressurization during the coseismic cycle. The denser network of faults is associated with permeability changes, which may be economically interesting. It also enhance creeping processes like pressure solution, that is also involved in fault healing. As pulverized rocks are substantially weaker [[Rempe et al., 2013](#)], it can reduce the apparent friction properties at regional scale [[Faulkner et al., 2006](#)].

For instance, on the Northern Anatolian Fault, a fault segment entered a long-term creeping phase after a supershear earthquake [[Çakir et al., 2012](#)]. Dynamic damage is a possible cause of this switch in frictional behavior. One can infer that the supershear rupture created diffuse damage near the fault. The weakening of rocks decreases the strength of the core and its surrounding damage zone. Meanwhile, pressure solution activates creep. To check such a hypothesis, in situ observation are needed. Within the framework of the Flow Trans Project, a Marie Curie Initial Training Network focus on Flow in Transforming media, a team from Grenoble plans to combine outcrop studies, InSAR monitoring and laboratory experiments to understand the dynamics of the Northern Anatolian Fault. This project funds the PhD of Frans Aben (starting October 2013), that I co-supervise.

Chapter 4

In-situ measurements of hydraulic properties across active faults

Estimating permeability along faults is key to understand several stages of the seismic process. For instance, large permeability following earthquakes explains the occurrence of ore deposits of economic significance along faults [Sibson, 1992]. Permeable fault about to rupture may experience anomalous precursory activity before an earthquake, like radon emission [Ioannides, 2003] or methane emission accompanied by bubbling [Tary *et al.*, 2012]. Clay-rich gouge of low permeability are amenable to pressure solution [Wibberley and Shimamoto, 2005].

However, determining permeability is difficult. Outcrops of former active faults were exposed through erosion and therefore experienced decompression and erosion. Permeability was not preserved. Boreholes give direct access to fresh outcrops, but cores were also decompressed. In situ measurement gives the best insight of hydraulic properties within faults. It enables to explore the scale dependence of permeability [Boutt *et al.*, 2012].

Two kinds of measurements are possible:

- Direct permeability measurement, through pumping tests. The scale of the rock mass investigated depends on the duration and the flow rate of the pumping test. I performed such tests were performed with the Modular formation Dynamics Tester (MDT) tool, as part of IODP expedition 319.
- Indirect permeability measurement through geophysical logs. We use datasets of IODP 319 to derive continuous permeability profiles and compare them with direct permeability measurements made with the MDT. The technique can also be used a posteriori on datasets from SAFOD.

During the last 15 years, several drilling projects gave new insight on fault mechanics at depth. Table 4.1 summarizes the major projects. Many projects (Nojima, TCDP, WCDP, J-Fast,...) were motivated by a devastating earthquake, and enable to study the distribution of fault slip across the fault zone, get insight of the rupture mechanism and monitor the postseismic healing of the fault. Others, like SAFOD, CRL, DFDP or GONAF aim at characterizing a major fault expected to break soon .

I had the opportunity to be involved in many of these drilling projects.

Project	Year	Fault depth (m)	Objectives	Hydraulic properties
Nojima Kobe earthquake, Japan	1995	300, 700, 1100	Post-earthquake characterization	Cross-hole testing
Corinth Rift Laboratory Greece	2004	750	Fault characterization and monitoring	Long term pore pressure monitoring
TCDP Chichi earthquake, Taiwan	2004	1111, 1138	Post-earthquake characterization	Cross-hole testing
SAFOD San Andreas Fault, CA	2004-2007	~ 2700	Fault characterization and monitoring	
NantrosEIZE Offshore Japan	2004 2009	~ 2700	Fault characterization Fault monitoring	MDT Pumping test Long term pore pressure monitoring
J-FAST Tohoku Earthquake, Japan	2011	750	Post-earthquake characterization	Long term monitoring
WCDP Wenchuan Earthquake, China	2009	~ 2700	Post-earthquake characterization	Long term monitoring
DFDP Alpine Fault, New Zealand	2011 2014	100, 150 ~ 1400	Fault characterization Pre-earthquake characterization and monitoring	Pumping test Long term monitoring
GONAF Northern Anatolian Fault	??	??	Pre-earthquake characterization and monitoring	Long term monitoring

Table 4.1: Table of the major projects drilling an active fault.

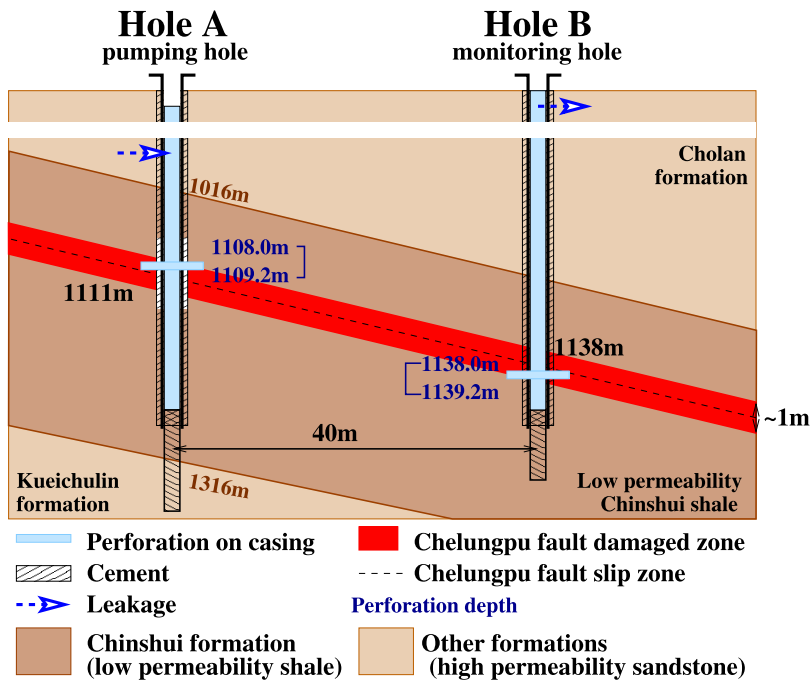


Figure 4.1: Cross-hole experiments at TCDP borehole enabling to determine the permeability of the damage zone of the Chelungpu Fault. From *Doan et al.* [2006a].

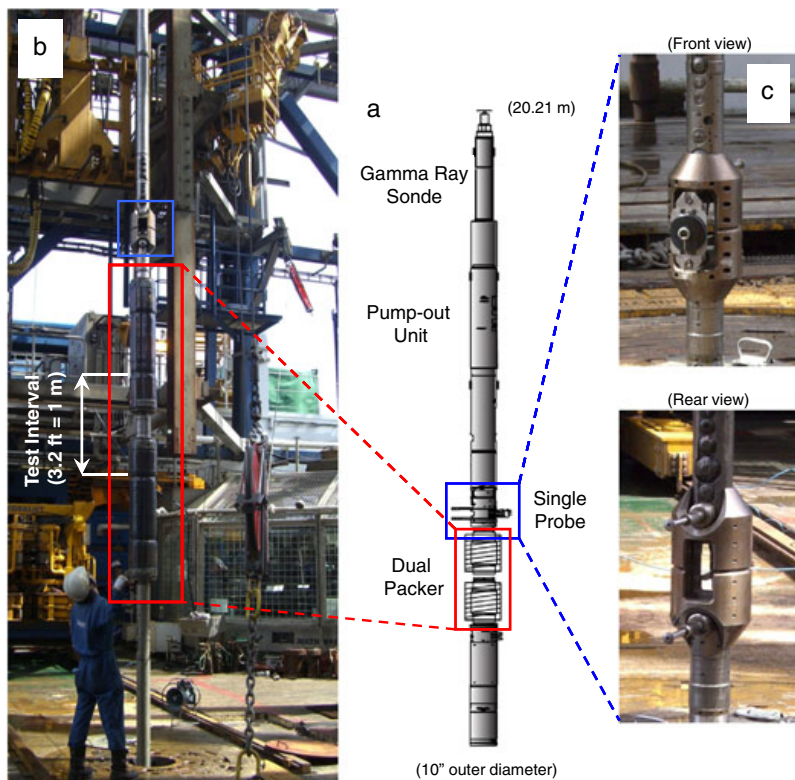


Figure 4.2: Modular formation Dynamics Tester (MDT) enabling to perform hydraulic tests and hydrofracturing at depth. From *Ito et al.* [2013].

4.1 Direct pumping tests

Pumping tests provide information on all hydrological parameters: current pore pressure, permeability and hydraulic diffusivity (and hence storativity). The volume scales as a power 3/2 of the duration of pumping, enabling to investigate the hydrological properties at large scale.

4.1.1 Cross-hole testing along Chelungpu Fault, Taiwan

As part of my postdoctoral studies, I could perform a slug test through the damage zone of the Chelungpu Fault, at the origin of the Chichi earthquake in 1999 [Doan *et al.*, 2006a]. On its northern strand, the fault experienced little acceleration but large displacement during the earthquake, and thermal pressurization was suspected to have weakened the fault. This mechanism needs low hydraulic diffusivity to maintain the high pore pressure generated by the seismic slip. We had the opportunity to use two holes drilling by the Taiwan Chelungpu-fault Drilling Project (TCDP). They were cased and perforated at the location the damage zones above and below the fault core (figure 4.1). We performed cross-hole pumping test, avoiding the influence of drilling-induced perturbation around the drillholes. As what happened during the pumping tests performed on Nojima Fault, the tests were disturbed by leaks induced by poor well completion. In our cases, we could correct our data by measuring and characterizing the leaks prior to the test. We could retrieve reliable values of hydraulic diffusivity of $(7 \pm 1) \times 10^{-5} \text{ m}^2/\text{s}$. This value is low enough to suggest that thermal pressurization is a viable weakening mechanism [Doan *et al.*, 2006a].

4.1.2 Exploiting the MDT tool data provided by the NanTroSEIZE project

I had another opportunity to perform hydraulic tests in situ within the framework of the project NanTroSEIZE (Nankai Trough SEIsmic Zone Experiment). This project aims at understanding the Nankai Trough, performing a transect with boreholes along various location of the subduction zone [Tobin and Kinoshita, 2006]. I was part of IODP expedition 319, a technological mission, where the first riser drilling in IODP history were performed in hole C0009 [Moe *et al.*, 2012]. The Kumano Basin was of little interest for the knowledge of the seismic conditions of the Nankai Trough, but it provides a simple and safe environment for scientists with experience in continental drilling to test the new methods made possible by the better drillhole and the larger pipe diameter. Among the available tool was the Modular formation Dynamics Tester (MDT) by Schlumberger. This tool embeds two pumping tests apparatuses (figure 4.2):

1. A single probe pushing a packer against the borehole wall and pump water out of a small chamber of 5 cc. This small volume enables a rapid recovery from the pumping. It provides a rough estimate of permeability (but very dependent on borehole conditions) and very importantly provides information on the local pore pressure conditions. From this tool, we could interpolate a pore pressure profile with depth, here very close to the expected hydrostatic value [Saffer *et al.*, 2013].
2. A dual packer probe, that enable to test a borehole section about one meter long. On this section, either pumping test to determine permeability or hydrofracturing is possible. In the former case, we retrieve a reliable value for permeability that is significantly higher than the permeabilities retrieved from core [Boutt *et al.*, 2012]. In the latter case, we retrieve information on the local stress field (at least, the minimum principal stress value perpendicular to the borehole direction) [Ito *et al.*, 2013].

Direct tests made in borehole provide reliable measurements, at the relevant scale and in quasi-pristine in-situ conditions. However, they provide very local information and questions arise on their spatial relevance. For instance, is there a lot of heterogeneity along the borehole?

4.2 Assessing hydraulic profiles from logs

Geophysical logs are quasi-systematically done after drilling, as they document the borehole conditions. They provide a continuous set of physical data: resistivity, seismic velocity, natural radioactivity, attenuation of gamma-rays and neutron, . . . These logs may be of lower profile than the MDT tool and they tended to be left aside by most of the scientific party of IODP expedition 319, yet with them I could extract several information of interest:

1. Using the caliper data associated with the FMI, an electrical imaging tool, I could show that the borehole section below the Kumano Basin was deformed in a N135° direction. This direction is consistent with the almost invisible breakouts and the poorly clear drilling-induced tensile fractures. It shows that the maximum horizontal principal stress direction is parallel to the convergence vector between Japan and the Philippine Plate [Lin *et al.*, 2010].
2. The sonic data are sensitive to porosity. By calibrating semi-empirical laws with core data, I was able to retrieve a full profile of macroscopic porosity along the borehole [Doan *et al.*, 2011]. Comparing with the total porosity profile, this method quantifies the water absorbed in swelling clays, like smectite. It could be used in a latter stage of the NanTroSEIZE project to track the smectite-illite transition.
3. The electrical data are disturbed by the invasion of the vicinity of the borehole by drilling fluids. The separation between the shallow resistivity curve and the deep resistivity curve hints how permeable is the drilled medium. In case of hole C0009, invasion is extensive, suggesting a

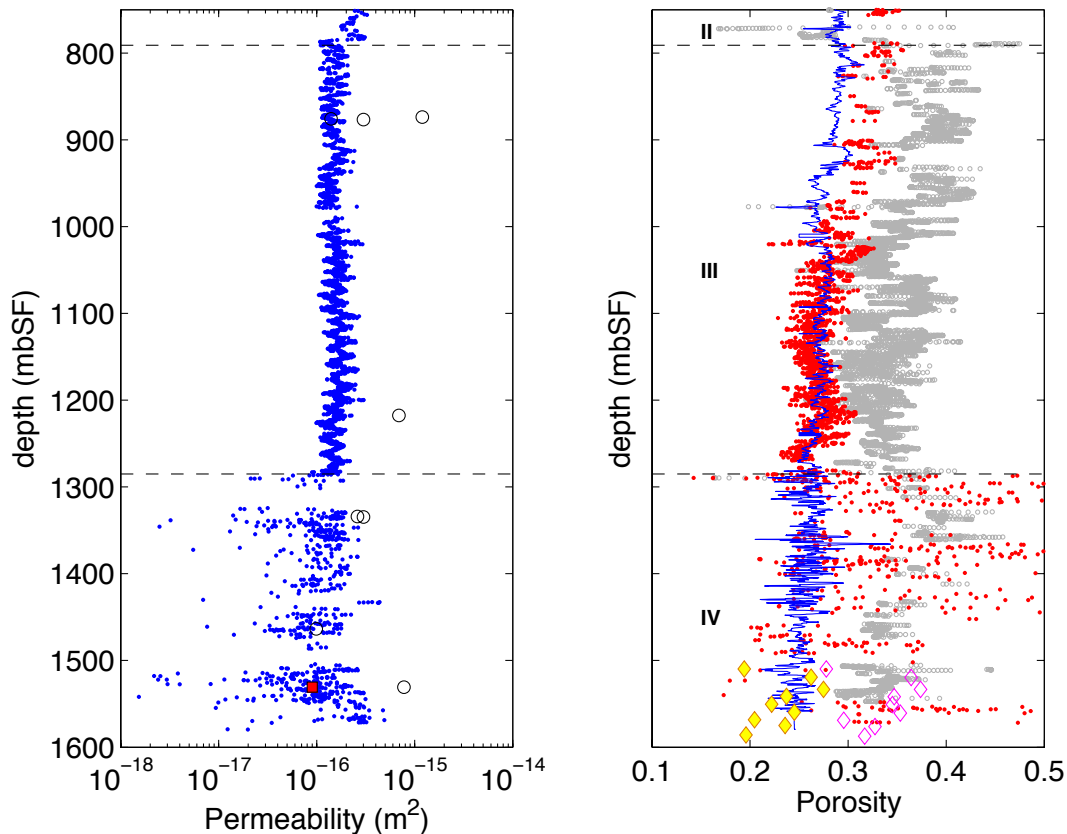


Figure 4.3: Geophysical logs enable to extrapolate the pointwise data acquired from cores and MDT data. (Left) We could retrieve a full profile of permeability from mud invasion recorded from laterolog resistivity data that compare well with MDT data, either single probe (open circles) or dual-packer (red square). (Right) We could get a continuous estimate of full profile of both macroporosity (red: resistivity data, blue: sonic data) and total porosity (grey: lithodensity).

mud cake of poor quality. We quantified the invasion process to retrieve a quantitative profile of permeability. We obtained a quantitative change in permeability when lithology changes: we could retrieve at least a good qualitative profile of permeability.

The quantification of invasion process with the electrical data is a promising tool to estimate the extent of the damage zone near an active fault. It is expected to be larger in the more permeable formation. We tested this hypothesis on two boreholes intersecting an active fault.

The J-Fast drilling is an offshore drilling project at the toe of the subduction fault that ruptured during the Tohoku earthquake in March 2011. Two boreholes were drilled, one with Logging While Drilling (LWD), the other without any logging. The LWD data were acquired a few minute after the drilling, and invasion is too limited to be perceptible.

We has better success, with the SAFOD project. Thanks to its free data policy. I could download the logging data. The shallow and deep resistivity of the laterolog data recorded a few days after drilling documents a zone with higher invasion (and no caliper anomaly) in the arkosic sandstone west to the fault. The damage is asymmetric and far from the fault. This zone is also consistent with a zone of large H₂ emission, that has been attributed as mechano-chemical hydrogen by [Wiersberg and Erzinger \[2008\]](#). It would not be surprising that this zone has larger permeability, so that it canalizes radon emission [[Wiersberg and Erzinger, 2008](#)]. This zone may be the location of intense micro-mechanical damage, similar to the pulverized rocks, but at depth.

On the other hand, the so-called 200m thick "damage zone" in figure 1.1 is impermeable with little separation between the deep and shallow resistivity. Geochemistry also suggests that little radon or hydrogen is emitted from the fault core. San Andreas Fault may be an hydraulic channel, but mainly within a "permeable" zone in arkosic sandstone, decoupled from the mechanically weak San Andreas Fault, that is impermeable.

4.3 Long term monitoring of pore pressure

Pore pressure is a key factor on fault mechanics. High fluid pressure reduces the effective Coulomb stress and weakens the fault [[Rice, 1992](#)]. Many attempts were done to record continuously fluid pressure within faults, but they are rarely successful due to the difficult drilling conditions next to the fault. For instance, the observatory installed within the SAFOD main hole lasted only a few weeks due to intense corrosion. Successful monitoring examples in continental drilling are the Corinth Rift Laboratory (but data documents the aquifers next to the fault), WCDP (but data record rather the damage fault next to the footwall) and the New Zealand DFDP (but at that stage, holes are shallow).

Long term monitoring provide many invaluable information. It provides reliable fluid pressure values, when borehole disturbances are dissipated. The recovery stage, of long duration, also documents hydraulic properties at large spatial scale. It also provides a dynamic view of the fault evolution. Rather than long term evolution associated with the seismic cycle, pore pressure monitoring also showed how faults are sensitive to triggering like teleseismic triggering [[Manga and Brodsky, 2006](#)] or permeability change following distant earthquakes [[Manga et al., 2012](#)].

Access to these data is difficult, but I could get access to the dataset collected by the permanent observatory installed during the stage 1 of the DFDP project.

4.3.1 Extracting hydromechanical properties from tidal analysis

Boreholes tapping confined reservoirs commonly exhibit periodic variations in pressure with two dominant periods: diurnal (~ 24 h) and semi-diurnal (~ 12 h)[[Agnew, 2007](#)]. These oscillations reach 10 kPa and are easily recordable. Onshore, Earth tides induce these pressure changes, whereas oceanic boreholes are dominated by oceanic loading [[Wang and Davis, 1996](#); [Davis et al., 2000](#)].

Earth tides have the immense advantage of being predictable. By comparing the actual observations and the predicted deformations, one can retrieve information about the formation surrounding

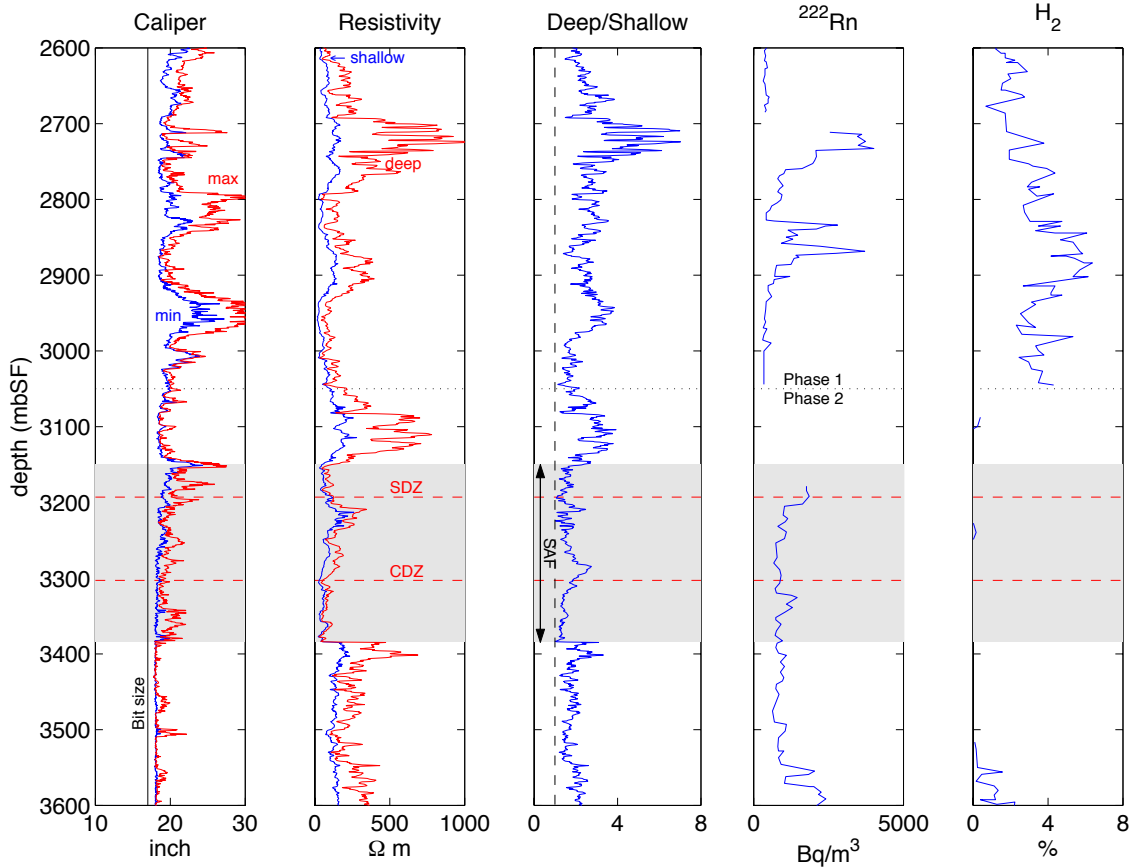


Figure 4.4: Resistivity logs showing differences in fluid invasion within the main hole of the SAFOD Project. The separation between the deep and shallow resistivities is not due only to change in borehole diameter, but rather to the permeability of the formation. The recognized creeping strands (Central Deforming Zone and Southern Deforming Zone) are impermeable, whereas the host rock at the boundary to the fault core are the most permeable. Real time gas monitoring data also show that fluid migration stands outside the fault core.

the well. This process occurs in two phases: (1) the poroelastic phase, in which the tidal strain induces change a pressure in the equilibrium and (2) the hydraulic phase in which the change in pressure in the medium induces a change in pressure in the well. This is expressed in figure 4.5.

We applied this method to the hydrological data acquired by the permanent observatory installed within the Deep Drilling Fault Project (DFDP) on the Alpine Fault, New Zealand (figure 4.6). This fault has several interesting features that motivate the drilling project: (1) according to paleoseismologic studies [Berryman et al., 2012], the fault is about to rupture with a large magnitude earthquake (2) the fault has a reverse component of about 1 cm/yr, advecting heat and rocks exhibiting ductile deformation. The DFDP project aims at better characterizing the fault properties by coring and logging and to monitor its long-term activity.

In 2010, the first part of project (DFDP-1) was conducted: two shallows holes were drilled to better characterize the fault geometry and properties (figure 4.6). DFDP-1 proved to be a great success with cores of excellent quality, especially within the fault core [Sutherland et al., 2012].

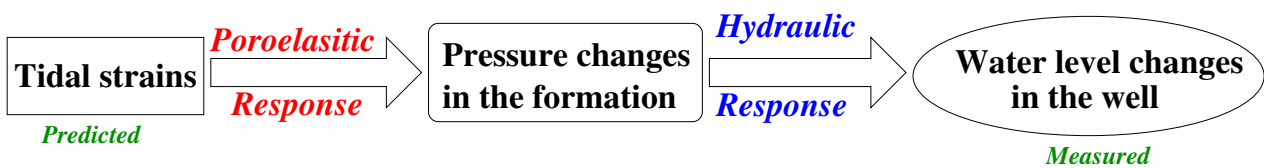


Figure 4.5: How the tidal strains are expressed as pressure changes. From Doan et al. [2006b]

Four piezometers were installed at four locations representative of zones of the fault structure: two were installed in the damaged hanging wall, one in the altered and cemented core and one in the footwall. In situ hydraulic tests performed just after drilling helped characterizing the permeability of the hanging wall with a high permeability larger than 10^{-14} m^2 . Permeability measurement on cores gave a permeability of $10^{-18} - 10^{-16} \text{ m}^2$ in the cataclasite, and $10^{-20} - 10^{-19} \text{ m}^2$ for the gouge.

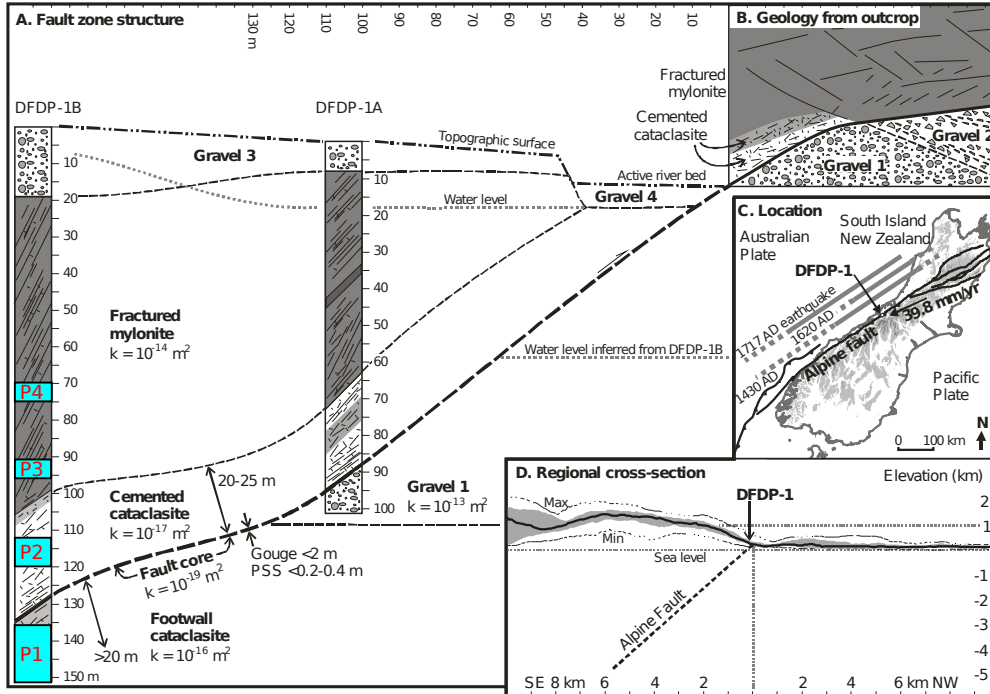


Figure 4.6: Summary of the results obtained by the first phase of the Deep Fault Drilling Project on the Alpine Fault, New Zealand, after [Sutherland et al. \[2012\]](#). The DFDP1 project included the installation of an observatory within well DFDP1-B. We highlight with blue rectangles the intervals whose pore pressure was monitored.

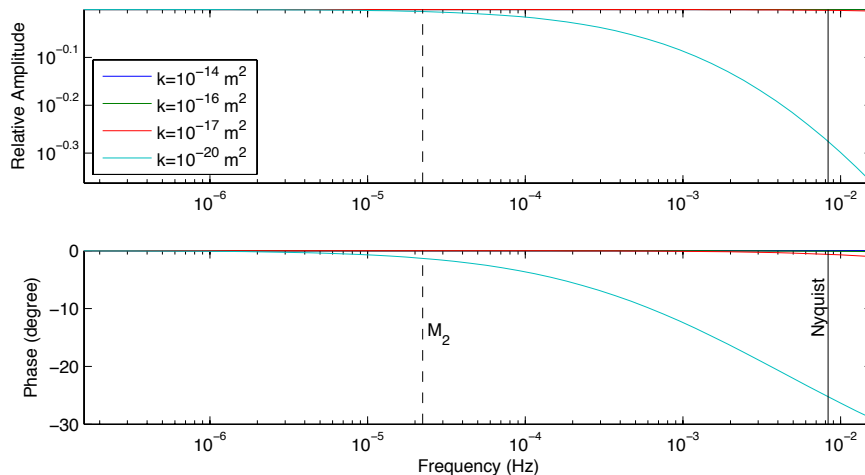


Figure 4.7: Theoretical gain response related to the hydraulic connection between the borehole and the formation. We used an adapted model [[Doan et al., 2006b](#)] of the model of [Hsieh et al. \[1987\]](#) for closed wells.

With such values, it is expected that the pore pressure recorded in the borehole reflects the pore pressure evolution within the formation, without any phase lag (figure 4.7). Indeed, tidal fluctuations were recorded with high resolution. The amplitude of the signal is of high value, suggesting very tight formation (4.2). It confirms that damage zones around the fault are currently well cement. The

Data	Apparent BKu (GPa) (Mar11-Apr12)	Phase (Deg) (Mar11-Apr12)	Apparent BKu (GPa) (Jun12-Oct12)	Phase (Deg) (Jun12-Oct12)
P1	27.73	11.4	27.56	10.2
P2	28.4	13.9	28.7	13.3
P3	24.1	8.4	24.2	8.7
P4	16.4	10.3	16.7	10.4

Table 4.2: Tidal coefficient derived for M_2 tidal component derived from tidal analysis.

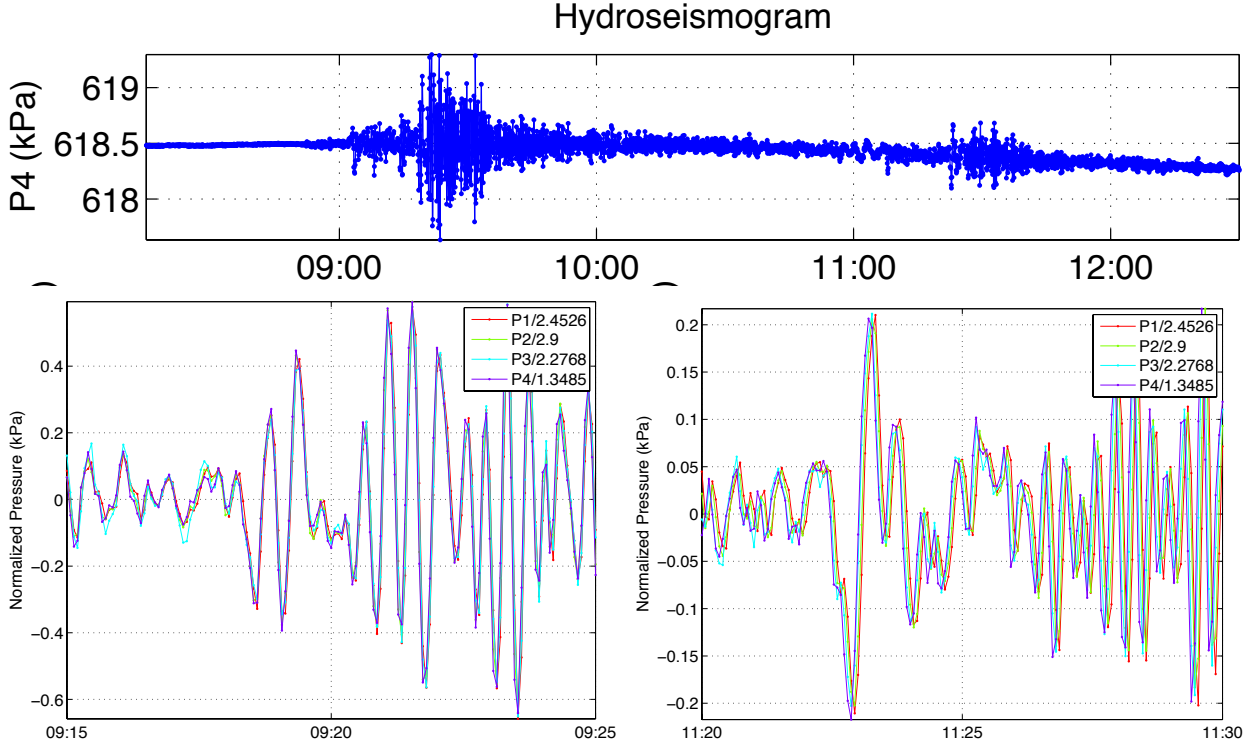


Figure 4.8: "Hydroseismograms" recorded by the DFDP1 sensors (figure /refDFDP1) during the arrival of the teleseismic waves emitted by the 2012 Sumatra earthquakes. During the passage of the first Rayleigh waves (R1), all pressure data are in phase. During the passage of the second Rayleigh waves (R2, after seismic waves travel around the Earth once), the signals exhibit different lags. Note that the x-axis are shown with the same scale. Y-data have been renormalized to highlight the similarity between each dataset.

phase lag may be explained by anisotropy effect not taken into account the by Hsieh model [Hsieh et al. \[1987\]](#) In these conditions, we can record "hydroseismograms", where pore pressure reflects the strain induced by teleseismic waves. We had one example during in the DFDP monitoring, associated with the doublet earthquakes of Sumatra, April 2012. Figure 4.8 shows two time series of seismograms. During the first arrival of Rayleigh waves, all pressure data are in phase, consistently with theoretical predictions (figure 4.7). But during the second arrival of Rayleigh waves, both pressure sensors sampling the fractured zone of the hanging walls, get some phase shift. Both seismic signals have similar frequencies, and similar direction of arrival, so that anisotropic effects cannot explain the difference. The most probable reason for this delay is a change in permeability. The Alpine Fault is therefore sensitive to seismic waves. As it is suspected to be close of its critical state, it is important to continue to monitor how this sensitivity evolves with time.

4.3.2 Triggering of sliding episode of landslide within a clay-rich slope

Another example of long term monitoring of "fault" is the long term monitoring of the Avignonet landslide, a clay landslide near Grenoble. Previous geophysical investigation, including borehole drilling and surface geophysics proved that the landslide deformation is accomodated by several localized shear zones [*Bièvre et al., 2011*] (see insert of figure 4.9). I proposed to monitor one of the shallowest shear zone with a high resolution sensor. The primary objective was to continuously monitor the hydromechanical evolution of the landslide from the tidal response. A first sensor was installed in 2010, recorded Earth Tides, but died out rapidly. A second sensor installed at the end of 2011 happened to be place in a more permeable formation and did not record tides. However, it enabled to record pore pressure evolution during more than one year, together with a lower resolution pressure sensor also located along the shear zone.

During winter, the clayish medium is saturated. However, during summer season, water level drawdowns, clays dry out and water level is not sensitive anymore to rainfall. The monitoring shows how the landslide becomes again sensitive to rainfall, and gets closer to critical state. First, the system becomes sensitive again to rainfall after a massive rain episode in October 2012 (step 1 in figure 4.9), but water level continues to decrease. Second, after another large rainfall episode, the water level stabilizes for all hydraulic sensors (step 2 in figure 4.9). The system gets closer to criticality: small amount of rain triggers a general disturbance of the landslide. Both hydraulic sensors experience a change in pressure (a decrease for the low resolution sensor, an increase for our high resolution sensor), as well as many other sensors installed along the landslide (Spontaneous Potential sensors, Time Domain Reflectometers).

4.4 Conclusions

Scientific drilling within active faults greatly improved our knowledge of the fault properties at depth, especially showing how slip get localized along thin principal shear zones of very low permeability for all drilling made in active faults. The in-situ characterization of hydraulic properties of faults was less successful. Few drillings completed the determination of a complete permeability log at the same scale and a successful installation of a monitoring system. A key issue is the poor well completion at the end of the drilling project, that impedes the pumping tests (TCDP) or prevent the installation of an observatory (SAFOD). Not surprisingly, one of the most successful project so far is the DFDP project, which has put hydraulic characterization of the fault to high priority. To get better results, fault hydrogeologists need to get involved earlier into the drilling projects.

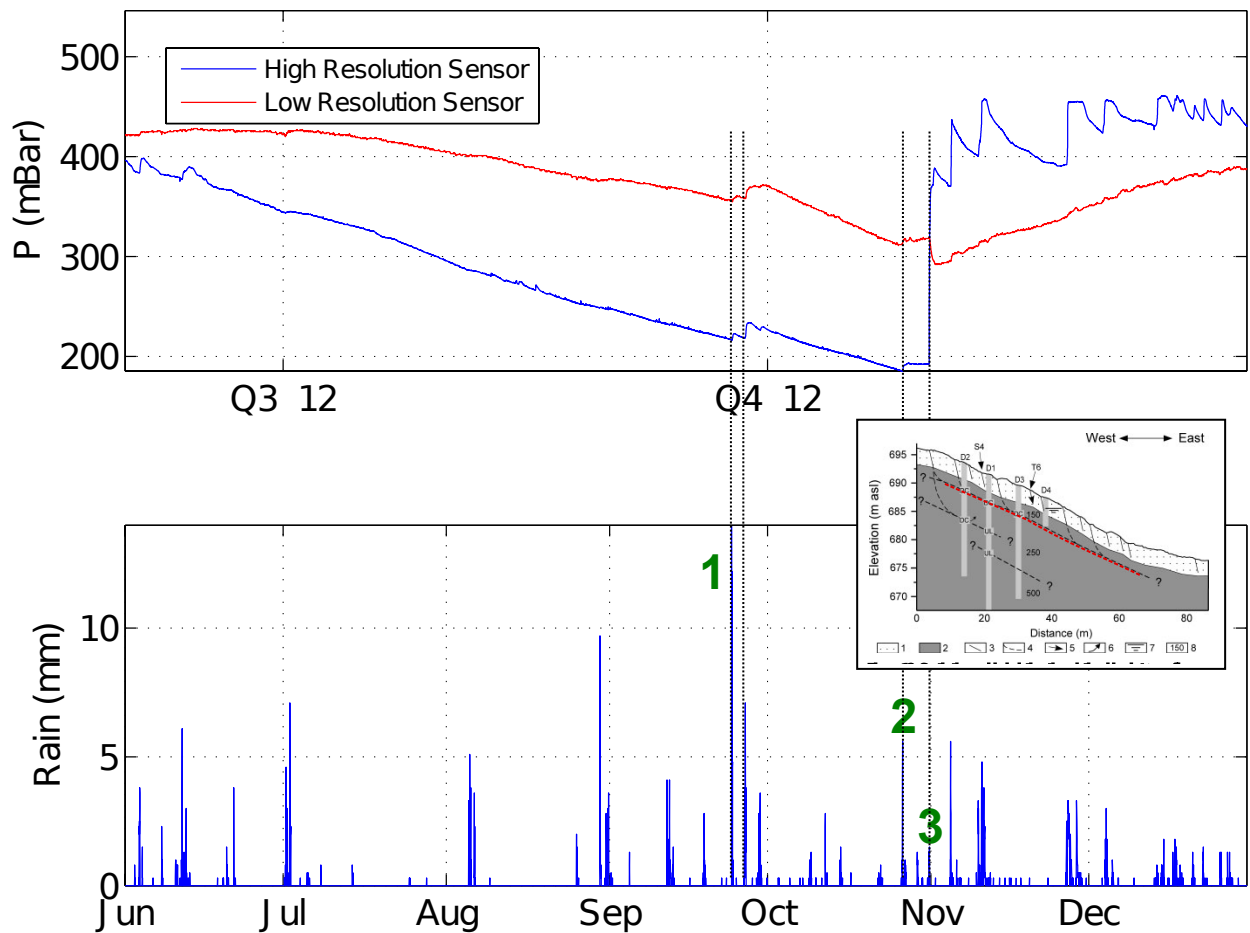


Figure 4.9: Hydraulic pressure recording within one of the main shear zone of the Avignonet landslide (red dashed line within the insert). The sensors record progressively greater sensitivity of water level fluctuations to rainfall. (1) After major rainfall, water level in the boreholes are once again sensitive to rainfall. (2) after another major rain episode, water level does not decrease any more (3) massive disturbance, with piezometric redistribution, occurs within the shear zone.

Chapter 5

Conclusions and Perspectives

5.1 Conclusions

In the previous chapters, I introduced the research I conducted on fault mechanics. Using borehole geophysics, I tried to characterize at from the metric to decametric scales a complete profile of hydromechanical properties of active faults. This data is important since such scales are cumbersome to reach in laboratory experiment and tedious to quantify in outcrop studies. On the San Andreas Fault (section 4.2), the small separation between shallow and deep resistivities curves suggests that this mature large fault has developed more than 200 m of impermeable fault core, in which sub-strands localized still more deformation. The shallow DFDP holes drilled on the Alpine Fault, New Zealand, show more incipient alteration, which only began to make the fault core and its surrounding damage zone impermeable [Sutherland *et al.*, 2012]. These results differ from the Chelungpu fault, in which several fault zones were identified. The actual strand at stake for the 1999 Chichi earthquake was difficult to identify. Our hydrological study within its damage zone confirmed it was of high permeability for shale [Doan *et al.*, 2006a]. Alteration process is not as important for this fault.

The ability for a fault to reuse the same strand throughout its seismic cycle is therefore crucial for the evolution of the fault zone, of its healing and alteration processes. This issue is tackled indirectly by my experiments, either on the Split Hopkinson Pressure Bars or High Velocity Friction experiments: at high strain rate, finite wave propagation limits correlation lengths between heterogeneities and strain can get localized elsewhere than the favored heterogeneities (the largest fractures for pulverization, the gouge boundaries for friction experiments). Hence, jamming can occur in pure talc gouge leading to unexpected high friction [Boutareaud *et al.*, 2012]. Hence, multiple fractures can propagate simultaneously at high strain rate [Doan and Gary, 2009; Doan and Billi, 2011].

I think long term monitoring is the future of the understanding of active faults. On the example of Avignonet (section 4.3.2), in which the "fault" is a subsurface shear zone. We recorded what seismologists would have dreamed to record prior to large earthquakes: the progressive destabilization of the fault under an external factor (here, rainfall), progressively getting closer to criticality and finally being triggered by a small disturbance. At another scale, the observation of Bouchon *et al.* [2011] prior to the 1999 Izmit earthquake on the Northern Anatolian Fault suggests that slow slip may occur on active faults prior to major earthquakes. Such slow slip would be monitored by the observatories of the second stage of the DFDP project, of the NantroSEIZE project or of the "Geophysical Observatory at the North Anatolian Fault" (GONAF) project [Dresen *et al.*, 2008].

5.2 Future work

I developed two technical specialties that are relatively uncommon within the Earth Science community: (1) borehole hydrogeophysical studies of active faults (2) high strain rate damage mechanics. During the following years, I plan to continue to exert this dual approach to fault mechanics, by performing experiments in conditions closer to that of the nucleation zones of earthquakes.

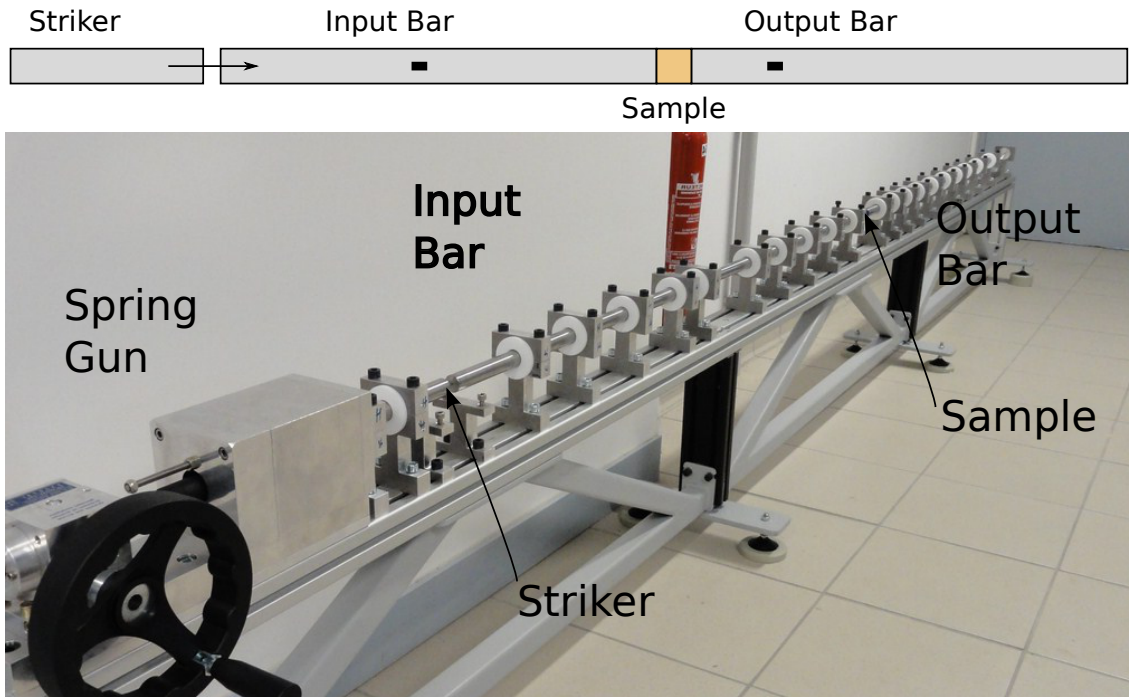


Figure 5.1: Mini-SHPB setup installed in Grenoble. This device enables to test small size samples (diameter less than 2 cm) at low strain but high strain rate. Its modular design make it easy to build up new instrumentation around the sample.

5.2.1 Experimental dynamic damage

My more immediate task on dynamic damage is to build my own experimental device. Indeed, it appeared that the remote location of the SHPB apparatus of École Polytechnique, next to Paris, combined with the retirement of Gérard Gary impeded to perform as many tests as needed. That is why we built our own system at ISTERre (figure 5.1). It is now ready, with a home-made interpretation program, and a reverse-engineered the amplification system. The mini-SHPB system has a modular design, to enable progressive enhancement with incremental funding. Another particularity of the design is its small size, with a maximum sample diameter of 2 cm. This size has several practical advantages: (1) the samples can be inserted in petrophysical apparatuses, such a permeameters, Brunauer–Emmett–Teller (BET) surfacemeters or the percolation cells of ISTERre, to get beyond simple macroscopic damage observation (2) the apparatus dimensions scale so that they just fit the experimental space available.

When we began to work on microscopic structures, we realized that diffuse damage can be generated by lower strain rate and lower strain than in our previous studies (section 3.2). We plan to couple more systematically the dynamic damage experiments with better characterization of damage patterns. In addition of thin sections, several petrophysical methods are planned to be implemented:

- P wave measurements are planned to be performed more systematically, with some plans to mount piezometers directly on the bars.
- Quantification of damage through BET measurement of surface area, that is expected to increase substantially for pulverized rocks. A study is performed in cooperation with Mike Heap to investigate the properties of volcanic rocks producing ashes.
- During the PhD of Frans Aben, starting October 2013, we plan to add permeability measurement capabilities to the percolation cells of ISTERre. They can be used to measure permeability of the damaged samples, before and during healing experiments.
- *Spencer et al.* [2012] have shown a reset of thermoluminescence data of SAFOD sample that may be remnant of the 1857 Fort Tejon earthquake. We plan to conduct dynamic experiments to control this hypothesis.

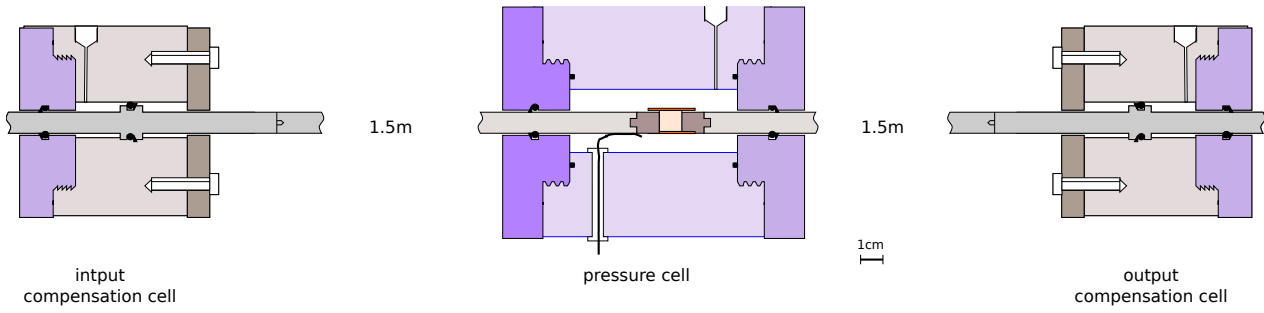


Figure 5.2: Dynamic confinement system that could be built of the mini-SHPB device (figure 5.1). The building of the experimental setup is ready but no funding was found yet.

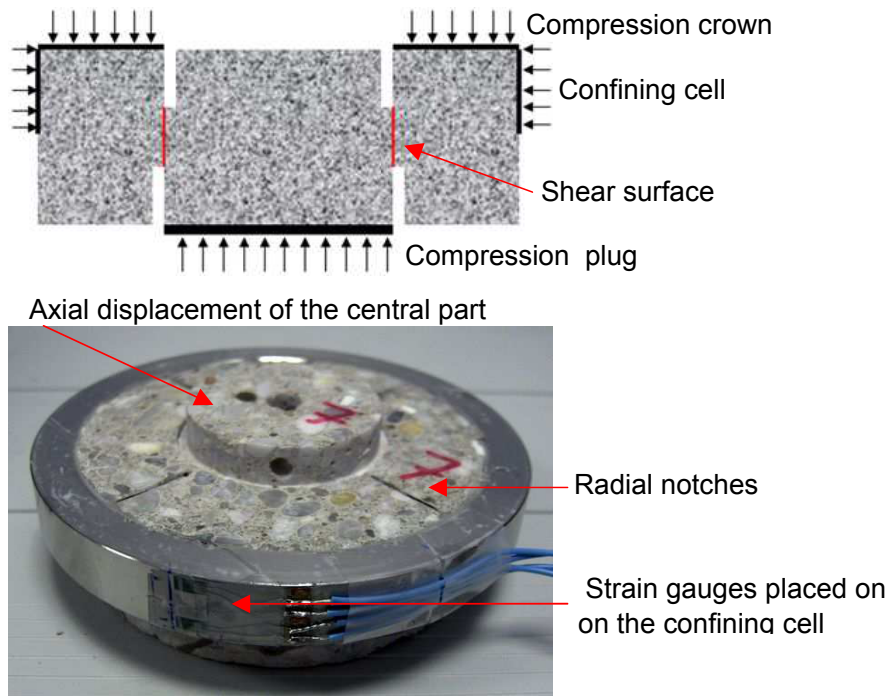


Figure 5.3: Punch-Through Shear test system used in a SHPB device by *Forquin* [2011]. We plan to test such a technique on the crystalline rocks tested in *Doan and D'Hour* [2012] to check the dependance of our results to the loading conditions.

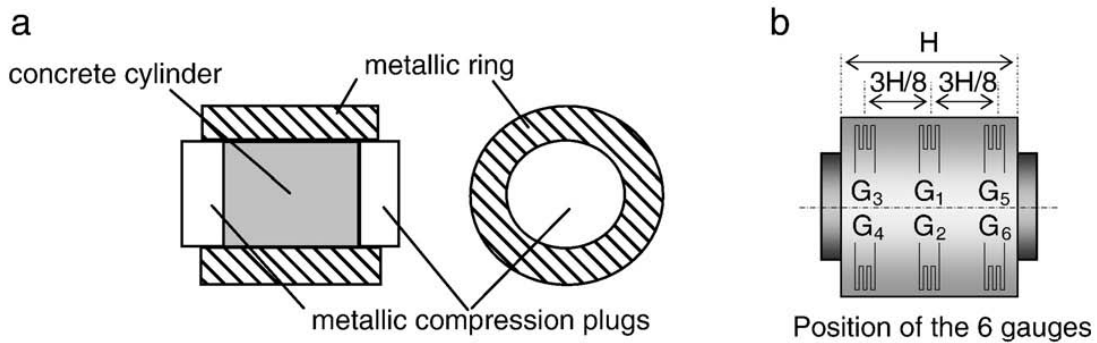


Figure 5.4: Oedometric tests performed by *Forquin et al.* [2010]. Assumptions regarding the confining behavior of the oedometric jacket can be checked with strain gages glued on the jacket. We plan to test such a technique on the crystalline rocks tested in *Doan and D'Hour* [2012] to check the dependance of our results to the loading conditions.

We plan to use the new device to characterize high strain rate behavior of lithologies relevant to fault zones:

- Clays often occur in fault gouges. Mechanically, their behavior is interesting, given their plastic behavior. If they were as sensitive to dynamic loading as crystalline rocks [Mitchell *et al.*, 2013], thermal pressurization could be inhibited. To study such weak rocks, we need to adapt the mini-SHPB to match the low acoustic impedance of clay, by switching to nylon bars.
- Water saturated rocks. We expect fluids to be undrained, inducing local tensile damage near the pores. Previous experiments on saturated concrete showed that water saturation substantially reduces the strength of the rock [Forquin *et al.*, 2010]. We plan to investigate in more detail the case of low porosity crystalline rocks tested by Doan and D'Hour [2012], focusing on tensile microstructures expected to be found near pores and fractures.

With the arrival of Pascal Forquin in Grenoble this year, we plan to perform high strain experiments in different loading conditions, rather than uniaxial unconfined loading:

- True confining experiments, with air confinement (figure 5.2). As SHPB are not servocontrolled, confinement with oil of low compressibility would induce transient large confining pressure. For security reasons, we plan to limit the air confinement to 20 MPa, which is small, but enough to go beyond the threshold in confining pressure identified by Waversik and Brace [1971] for the disappearing of axial tensile fracturing in low strain rate experiments.
- Dynamic simple shear experiments at the centimetric scale, using a Punch-Through Shear test system mounted on a SHPB device [Forquin, 2011] (figure 5.3).
- Controlled oedometric experiments (figure 5.4). The setup designed by Pascal Forquin enables to check a posteriori the assumption on the confining conditions imposed by the jacket (contrary to the experiments of Yuan *et al.* [2011]).

These devices would allow to work on rock deformation at higher confining stress. To go to realistic seismicity conditions, it would be interesting to get higher temperature. However, it is technically difficult to ensure a uniform temperature field within a sample without getting a cumbersome heating device that would complexify the stress field near the sample during dynamic loading. Given these experimental limitations, in-situ observations are the key knowledge to acquire to understand fault mechanics at depth.

5.2.2 Drilling to more seismogenic conditions

Drilling through active fault zones provided a better characterization of the properties of faults down to 2-3 km below surface. This is not deep enough to reach seismogenic conditions, but it enables to understand anomalous behaviors during earthquakes, like the small acceleration recorded during the 1999 Chichi earthquake (TCDP), or the unexpected large slip at the toe of the Tohoku décollement (J-Fast).

Several projects aim at drilling deeper or in hotter environment. In-situ conditions would then favor ductile behavior [Bürgmann and Dresen, 2008], either by activation of geochemical processes, like pressure-solution, or by activation of intracrystalline plasticity. Stable creeping becomes more common and at the transition between stable-unstable slip, slow slip events and tremor have been identified [Rubinstein *et al.*, 2010].

I am involved in several projects that could provide information of faults in more ductile environment:

- The second stage of DFDP project aims at drilling at 1500 m. Together with Philippe Pezard, we plan to conduct geophysical logs (especially laterologs), to better characterize the fault properties at depth. With the large heat advected with the uplift of the hanging wall, ductile features, creep are expected to occur.

- The NanTroSEIZE project plans to use riser technology to drill the megasplay fault at ~ 3700 mbsf, and maybe the décollement below 7000 mbsf, by extending the C002 hole. It is currently being drilled down to 3600 mbsf by expedition 348.
- The Japan Beyond Brittle Project aims at testing geothermal energy under ductile conditions, by drilling above a volcanic chamber. It is expected that seismicity generated fluid injections would be dampened by the ductile conditions. I was invited to the preliminary workshop in March 2013. Although the project does not target active faults especially, it discusses important features at hydrofracturing, sliding regimes, and speed of healing.

In all the projects cited above, hydrology is a key parameter. I hope that my expertise exerted in the examples of chapter 4 would be helpful. It would be of special interest to design tools able to stand the long temperature, especially for the long term monitoring. The examples of pore pressure monitoring of chapter 4 reveal that fault environment is quite dynamic, being disturbed by teleseismic waves or preparing a slipping episode. Slow slip events could be preliminary to large earthquakes [*Bouchon et al.*, 2011; *Kato*, 2012]; as they are difficult to monitor from the surface, in-situ monitoring would better understand how faults build before rupture and heal after rupture.

Bibliography

- Agnew, D. C. (2007), Earth Tides, in *Treatise on Geophysics: Geodesy*, edited by T. A. Herring, pp. 163–195, Elsevier B.V.
- Berryman, K. R., U. a. Cochran, K. J. Clark, G. P. Biasi, R. M. Langridge, and P. Villamor (2012), Major earthquakes occur regularly on an isolated plate boundary fault., *Science (New York, N.Y.)*, *336*(6089), 1690–3, doi:10.1126/science.1218959.
- Bhat, H. S., A. J. Rosakis, and C. G. Sammis (2012), A Micromechanics Based Constitutive Model for Brittle Failure at High Strain Rates, *Journal of Applied Mechanics*, *79*(3), 031,016, doi:10.1115/1.4005897.
- Bièvre, G., D. Jongmans, T. Winiarski, and V. Zumbo (2011), Application of geophysical measurements for assessing the role of fissures in water infiltration within a clay landslide (Trièves area , French Alps), *Hydrological Processes*, doi:10.1002/hyp.7986.
- Bos, B., C. J. Peach, and C. J. Spiers (2000), Frictional-viscous flow of simulated fault gouge caused by the combined effects of phyllosilicates and pressure solution, *Tectonophysics*, *327*(3–4), 173–194.
- Bouchon, M., H. Karabulut, M. Aktar, S. Özalaybey, J. Schmittbuhl, and M.-p. Bouin (2011), Extended Nucleation of the 1999, *Science*, *877*, doi:10.1126/science.1197341.
- Boutareaud, S., T. Hirose, M. Andréani, M. Pec, D.-G. Calugaru, A.-M. Boullier, and M.-L. Doan (2012), On the role of phyllosilicates on fault lubrication: Insight from micro- and nanostructural investigations on talc friction experiments, *Journal of Geophysical Research*, *117*(B8), B08,408, doi: 10.1029/2011JB009006.
- Boutt, D. F., D. Saffer, M.-L. Doan, W. Lin, T. Ito, Y. Kano, P. Flemings, L. C. McNeill, T. Byrne, N. W. Hayman, and K. T. Moe (2012), Scale dependence of in-situ permeability measurements in the Nankai accretionary prism: The role of fractures, *Geophysical Research Letters*, *39*(7), 2–7, doi: 10.1029/2012GL051216.
- Bürgmann, R., and G. Dresen (2008), Rheology of the lower crust and upper mantle: Evidence from rock mechanics, geodesy, and field observations, *Annu. Rev. Earth Planet. Sci.*, doi:10.1146/annurev.earth.36.031207.124326.
- Byerlee, J. (1978), Friction of rocks, *Pure and applied Geophysics*, *116*, 615–626.
- Caine, J. S., J. P. Evans, and C. B. Forster (1996), Fault zone architecture and permeability structure, *Geology*, *24*(11), 1025–1028.
- Candela, T., and F. Renard (2012), Segment linkage process at the origin of slip surface roughness: Evidence from the Dixie Valley fault, *Journal of Structural Geology*, *45*, 87–100, doi:10.1016/j.jsg.2012.06.003.
- Carpenter, B. M., C. Marone, and D. M. Saffer (2009), Frictional behavior of materials in the 3D SAFOD volume, *Geophysical Research Letters*, *36*(5), L05,302, doi:10.1029/2008GL036660.
- Çakir, Z., S. Ergintav, H. Özener, U. Dogan, A. M. Akoglu, M. Meghraoui, and R. Reilinger (2012), Onset of aseismic creep on major strike-slip faults, *Geology of the Earthquake Source: A Volume in Honour of Rick Sibson*, p. G33522, doi:10.1130/G33522.1.
- Chen, W. W., and B. Song (2010), *Split Hopkinson (Kolsky) Bar Design, testing and applications*, Springer Verlag.
- Chester, F. M., and J. M. Logan (1986), Implications for mechanical properties of brittle faults from observation of the Punchbowl Fault Zone, California, *Pure and Applied Geophysics*, *124*(1/2), 79–106.

- Davis, E. E., K. Wang, K. Becker, and R. E. Thomson (2000), Formation-scale hydraulic and mechanical properties of oceanic crust inferred from pore pressure response to periodic seafloor loading, *Journal of Geophysical Research*, 105(B6), 13,423–13,435.
- Denoual, C., and F. Hild (2000), A damage model for the dynamic fragmentation of brittle solids, *Computer Methods in Applied Mechanics and Engineering*, 183, 247–258.
- Di Toro, G., R. Han, T. Hirose, N. De Paola, S. Nielsen, K. Mizoguchi, F. Ferri, M. Cocco, and T. Shimamoto (2011), Fault lubrication during earthquakes., *Nature*, 471(7339), 494–8, doi:10.1038/nature09838.
- Doan, M.-L. (2005), Etude in-situ des interactions hydromécaniques entre fluides et failles actives: Application au Laboratoire du Rift de Corinthe, Phd, Institut de Physique du Globe de Paris.
- Doan, M.-L., and A. Billi (2011), High strain rate damage of Carrara marble, *Geophysical Research Letters*, 38(L19302), 1–6, doi:10.1029/2011GL049169.
- Doan, M.-L., and F. H. Cornet (2007), Small pressure drop triggered near a fault by small teleseismic waves, *Earth and Planetary Science Letters*, 258(1-2), 207–218, doi:10.1016/j.epsl.2007.03.036.
- Doan, M.-L., and V. D’Hour (2012), Effect of initial damage on rock pulverization along faults, *Journal of Structural Geology*, 45, 113–124, doi:10.1016/j.jsg.2012.05.006.
- Doan, M.-L., and G. Gary (2009), Rock pulverization at high strain rate near the San Andreas fault, *Nature Geoscience*, 2(10), 709–712, doi:10.1038/ngeo640.
- Doan, M.-l., D. Saffer, D. Boutt, and L. McNeill (a), A full permeability profile of Kumano Forearc Basin, Nankai Trough from modeling of electrical data, *To be submitted to GRL*.
- Doan, M.-L., T. Hirose, M. Andréani, A.-m. Boullier, D.-G. Calugaru, and S. Boutareaud (b), Talc Lubrication at High Strain Rate, *to be submitted to J. Struc. Geol.*
- Doan, M.-L., E. E. Brodsky, Y. Kano, and K.-F. Ma (2006a), In situ measurement of the hydraulic diffusivity of the active Chelungpu Fault, Taiwan, *Geophysical Research Letters*, 33(16), 1–5, doi:10.1029/2006GL026889.
- Doan, M.-l., E. E. Brodsky, R. Prioul, and C. Signer (2006b), Tidal analysis of borehole pressure : a tutorial, *Tech. rep.*, Schlumberger-Doll Research.
- Doan, M.-L., T. M. Mitchell, and G. Gary (2009), Experimental investigation of asymmetric pulverization along the Arima-Takatsuki fault, *Eos Trans. AGU 90(52), Fall Meet. Suppl.*, 90(52), Abstract T41A–1990, doi:10.1038/ngeo640.
- Doan, M.-L., M. Conin, P. Henry, T. Wiersberg, D. F. Boutt, D. Buchs, D. Saffer, L. C. McNeill, D. Cukur, and W. Lin (2011), Quantification of free gas in the Kumano fore-arc basin detected from borehole physical properties: IODP NanTroSEIZE drilling Site C0009, *Geochemistry Geophysics Geosystems*, 12(Q0AD06), doi:10.1029/2010GC003284.
- Dor, O., T. K. Rockwell, and Y. Ben-Zion (2006), Geological Observations of Damage Asymmetry in the Structure of the San Jacinto, San Andreas and Punchbowl Faults in Southern California: A Possible Indicator for Preferred Rupture Propagation Direction, *Pure and Applied Geophysics*, 163(2-3), 301–349, doi:10.1007/s00024-005-0023-9.
- Dor, O., C. Yildirim, T. K. Rockwell, Y. Ben-Zion, O. Emre, M. Sisk, and T. Y. Duman (2008), Geological and geomorphologic asymmetry across the rupture zones of the 1943 and 1944 earthquakes on the North Anatolian Fault: possible signals for preferred earthquake propagation direction, *Geophysical Journal International*, 173(2), 483–504, doi:10.1111/j.1365-246X.2008.03709.x.
- Dresen, G., M. Bohnhoff, M. Aktar, and H. Eyidogan (2008), Drilling the North Anatolian Fault, *Scientific Drilling*, 6, 58–59, doi:10.1029/1999.
- Dunham, E. M., P. Favreau, and J. M. Carlson (2003), A Supershear Transition mechanism for cracks, *Science*, 299, 1557–1559.
- Faulkner, D. R., A. Lewis, and E. H. Rutter (2003), On the internal structure and mechanics of large strike-slip fault zones: field observations of the Carboneras fault in southeastern Spain, *Tectonophysics*, 367(3-4), 235–251, doi:10.1016/S0040-1951(03)00134-3.
- Faulkner, D. R., T. M. Mitchell, D. Healy, and M. J. Heap (2006), Slip on ‘weak’ faults by the rotation of regional stress in the fracture damage zone., *Nature*, 444(7121), 922–5, doi:10.1038/nature05353.

- Faulkner, D. R., C. A. L. Jackson, R. J. Lunn, R. W. Schlische, Z. K. Shipton, C. A. J. Wibberley, and M. Withjack (2010), A review of recent developments concerning the structure, mechanics and fluid flow properties of fault zones, *Journal of Structural Geology*, *32*(11), 1557–1575, doi:10.1016/j.jsg.2010.06.009.
- Faulkner, D. R., T. M. Mitchell, J. Behnsen, T. Hirose, and T. Shimamoto (2011), Stuck in the mud? Earthquake nucleation and propagation through accretionary forearcs, *Geophysical Research Letters*, *38*(L1830), 1–5, doi:10.1029/2011GL048552.
- Forquin, P. (2011), Influence of free water and strain-rate on the shear behaviour of concrete, *Applied Mechanics and Materials*, *82*, 148–153, doi:10.4028/www.scientific.net/AMM.82.148.
- Forquin, P., K. Safa, and G. Gary (2010), Influence of free water on the quasi-static and dynamic strength of concrete in confined compression tests, *Cement and Concrete Research*, *40*(2), 321–333, doi:10.1016/j.cemconres.2009.09.024.
- Forrestal, M. J., T. W. Wright, and W. W. Chen (2007), The effect of radial inertia on brittle samples during the split Hopkinson pressure bar test, *International Journal of Impact Engineering*, *34*(3), 405–411, doi:10.1016/j.ijimpeng.2005.12.001.
- Grady, D. E., and M. E. Kipp (1987), Dynamic rock fragmentation, in *Fracture Mechanics of Rock*, edited by B. K. Atkinson, chap. 10, pp. 429–475, Academic Press Geologic Series.
- Gratier, J.-P. (2011), Fault Permeability and Strength Evolution Related to Fracturing and Healing Episodic Processes (Years to Millennia): the Role of Pressure Solution, *Oil Gas Sci. Technol. – Rev. IFP Energies nouvelles*, *66*(3), 491–506, doi:10.2516/ogst/2010014.
- Gratier, J.-P., and F. Gueydan (2007), Deformation in the Presence of Fluids and Mineral Reactions Effect of Fracturing and Fluid – Rock Interaction on Seismic Cycles, in *Tectonic Faults: agent of change on a dynamic earth*, edited by M. R. Handy and G. N. Hovius, chap. 12, pp. 319–356, The MIT Press, Cambridge, Mass.
- Gratier, J.-P., J. Richard, F. Renard, S. Mittempergher, M.-L. Doan, G. Di Toro, J. Hadizadeh, and A.-M. Boullier (2011), Aseismic sliding of active faults by pressure solution creep: Evidence from the San Andreas Fault Observatory at Depth, *Geology*, *39*(12), 1131–1134, doi:10.1130/G32073.1.
- Gratier, J.-P., F. Thouvenot, L. Jenatton, A. Tourette, M.-L. Doan, and F. Renard (2013), Geological control of the partitioning between seismic and aseismic sliding behaviours in active faults: Evidence from the Western Alps, France, *Tectonophysics*, *600*, 226–242, doi:10.1016/j.tecto.2013.02.013.
- Han, R., T. Shimamoto, T. Hirose, J.-H. Ree, and J.-I. Ando (2010), Ultralow Friction of Carbonate Faults, *Science*, *878*, 878–881, doi:10.1126/science.1139763.
- Hild, F., P. Forquin, and A. R. Cordeiro da Silva (2003), Single and multiple fragmentation of brittle geomaterials, *Revue française de génie civil*, *7*(7-8), 973–1002.
- Hirose, T. (2005), Growth of molten zone as a mechanism of slip weakening of simulated faults in gabbro during frictional melting, *Journal of Geophysical Research*, *110*(B5), 1–18, doi:10.1029/2004JB003207.
- Hsieh, P. A., J. D. Bredehoeft, and J. M. Farr (1987), Determination of aquifer transmissivity from earth tide analysis, *Water Resources Research*, *23*(10), 1824–1832.
- Ildelfonse, B., D. Blackman, B. John, Y. Ohara, D. Miller, and C. MacLeod (2007), Oceanic core complexes and crustal accretion at slow-spreading ridges, *Geology*, *35*(7), 623, doi:10.1130/G23531A.1.
- Ioannides, K. (2003), Soil gas radon: a tool for exploring active fault zones, *Applied Radiation and Isotopes*, *59*(2-3), 205–213, doi:10.1016/S0969-8043(03)00164-7.
- Ito, T., A. Funato, W. Lin, M.-l. Doan, D. F. Boutt, Y. Kano, H. Ito, D. Saffer, L. C. McNeill, T. Byrne, and K. T. Moe (2013), Determination of stress state in deep subsea formation by combination of hydraulic fracturing in situ test and core analysis : A case study in the IODP Expedition 319, *Journal of Geophysical Research*, *118*, 1–13, doi:10.1002/jgrb.50086.
- Johnston, M. J. S., R. D. Borchardt, A. T. Linde, and M. T. Gladwin (2006), Continuous Borehole Strain and Pore Pressure in the Near Field of the 28 September 2004 M 6.0 Parkfield, California, Earthquake: Implications for Nucleation, Fault Response, Earthquake Prediction, and Tremor, *Bulletin of the Seismological Society of America*, *96*(4B), S56–S72, doi:10.1785/0120050822.
- Kato, A. (2012), Propagation of Slow Slip Leading Up to the 2011 Mw 9.0 Tohoku-Oki Earthquake, *Science*, *705*, doi:10.1126/science.1215141.

- Lin, W., M. L. Doan, J. C. Moore, L. McNeill, T. B. Byrne, T. Ito, D. Saffer, M. Conin, M. Kinoshita, Y. Sanada, K. T. Moe, E. Araki, H. Tobin, D. Boutt, Y. Kano, N. W. Hayman, P. Flemings, and G. J. Huftile (2010), Present-day principal horizontal stress orientations in the Kumano forearc basin of the southwest Japan subduction zone determined from IODP NanTroSEIZE drilling Site C0009, *Geophysical Research Letters*, *37*(L13303), doi:10.1029/2010GL043158.
- Lockner, D. A., C. A. Morrow, D. E. Moore, and S. H. Hickman (2011), Low strength of deep San Andreas fault gouge from SAFOD core., *Nature*, *472*(7341), 82–85, doi:10.1038/nature09927.
- Ma, K.-F., H. Tanaka, S.-R. Song, C.-Y. Wang, J.-H. Hung, Y.-B. Tsai, J. Mori, Y.-F. Song, E.-C. Yeh, W. Soh, H. Sone, L.-W. Kuo, and H.-Y. Wu (2006), Slip zone and energetics of a large earthquake from the Taiwan Chelungpu-fault Drilling Project., *Nature*, *444*(7118), 473–6, doi:10.1038/nature05253.
- Manga, M., and E. E. Brodsky (2006), SEISMIC TRIGGERING OF ERUPTIONS IN THE FAR FIELD: Volcanoes and Geysers, *Annual Review of Earth and Planetary Sciences*, *34*(1), 263–291, doi:10.1146/annurev.earth.34.031405.125125.
- Manga, M., I. Beresnev, E. E. Brodsky, J. E. Elkhoury, D. Elsworth, S. E. Ingebritsen, D. C. Mays, and C.-y. Wang (2012), Changes in permeability caused by transient stresses : field observations, experiments and mechanisms, *Reviews of Geophysics*, *50*, doi:10.1029/2011RG000382.
- Manning, C. E. (1995), Phase-equilibrium controls on SiO₂ metasomatism by aqueous fluid in subduction zones: Reaction at constant pressure and temperature, *International Geology Review*, *37*(12), 1074–1093.
- Melosh, H. J. (1989), Cratering mechanics: contact and compression stage, in *Impact Cratering: A Geologic Process*, chap. 4, pp. 46–59, Oxford University Press.
- Mitchell, T. M., and D. R. Faulkner (2009), The nature and origin of off-fault damage surrounding strike-slip fault zones with a wide range of displacements: A field study from the Atacama fault system, northern Chile, *Journal of Structural Geology*, *31*(8), 802–816, doi:10.1016/j.jsg.2009.05.002.
- Mitchell, T. M., Y. Ben-Zion, and T. Shimamoto (2011), Pulverized fault rocks and damage asymmetry along the Arima-Takatsuki Tectonic Line , Japan, *Earth and Planetary Science Letters*, *308*(3-4), 284–297, doi:10.1016/j.epsl.2011.04.023.
- Mitchell, T. M., M.-l. Doan, H. S. Bhat, J. Renner, and G. Girty (2013), High permeabilities in the damage zone of the San Jacinto Fault induced by earthquake rupture.
- Moe, K. T., T. Ito, W. Lin, M.-l. Doan, D. Boutt, Y. Kawamura, C. K. Khong, L. McNeill, T. Byrne, D. Saffer, E. Araki, N. Eguchi, I. Sawada, P. Flemings, Y. Kano, C. Moore, M. Kinoshita, and H. J. Tobin (2012), Operational Review of the First Wireline In Situ Stress Test in Scientific Ocean Drilling, *Scientific Drilling*, *13*, 35–39, doi:10.2204/iodp.sd.13.06.2011.
- Moore, D. E., and D. A. Lockner (2011), Frictional strengths of talc-serpentine and talc-quartz mixtures, *Journal of Geophysical Research*, *116*(B1), doi:10.1029/2010JB007881.
- Moore, D. E., and M. J. Rymer (2007), Talc-bearing serpentinite and the creeping section of the San Andreas fault, *Nature*, *448*, 795–797, doi:10.1038/nature06064.
- Niemeijer, A., C. Marone, and D. Elsworth (2010), Fabric induced weakness of tectonic faults, *Geophysical Research Letters*, *37*(L03304), doi:10.1029/2009GL041689.
- Paterson, M. S., and T.-F. Wong (2005), *Experimental rock deformation—the brittle field*, Springer Verlag.
- Rempe, M., T. Mitchell, J. Renner, S. Nippres, Y. Ben-Zion, and T. Rockwell (2013), Damage and seismic velocity structure of pulverized rocks near the San Andreas Fault, *Journal of Geophysical Research: Solid Earth*, *118*(6), 2813–2831, doi:10.1002/jgrb.50184.
- Rice, J. R. (1992), Fault stress states, pore pressure distributions, and the weakness of the San Andreas fault, in *Fault mechanics and transport properties of rocks*, edited by B. Evans and T.-f. Wong, internatio ed., chap. 20, pp. 475–503, Academic Press Ltd.
- Richard, J., J.-P. Gratier, M.-L. Doan, A.-M. Boullier, and F. Renard (2014a), Time and space evolution of an active creeping fault zone: insights from the brittle and ductile microstructures in the San Andreas Fault Observatory at Depth, *To be submitted to JGR*.
- Richard, J., M.-L. Doan, J.-P. Gratier, F. Renard, and A.-M. Boullier (2014b), Microstructures of dynamic damaging and healing by fluid circulations into a porous limestone 3, *In preparation*.

- Rubinstein, J. L., D. R. Shelly, and W. L. Ellsworth (2010), Non-volcanic tremor: A window into the Roots of Fault Zones, in *New frontiers in Integrated Solid Earth Sciences*, edited by S. Cloetingh and J. Nengendank, pp. 287–314, Springer Netherlands, Dordrecht, doi:10.1007/978-90-481-2737-5.
- Saffer, D. M., P. B. Flemings, D. F. Boutt, M.-L. Doan, T. Ito, L. C. McNeill, T. B. Byrne, M. Conin, W. Lin, E. Araki, N. Eguchi, S. Toczko, and Y. Kano (2013), In situ stress and pore pressure in the Kumano Forearc Basin, offshore SW Honshu from downhole measurements during riser drilling, *Geochemistry, Geophysics, Geosystems*, *14*(5), doi:10.1002/ggge.20051.
- Shi, Z., and Y. Ben-Zion (2006), Dynamic rupture on a bimaterial interface governed by slip-weakening friction, *Geophysical Journal International*, *165*(2), 469–484, doi:10.1111/j.1365-246X.2006.02853.x.
- Sibson, R. H. (1992), Implication of fault-valve behaviour for rupture nucleation and recurrence, *Tectonophysics*, *211*, 283–293.
- Spencer, J. Q., J. Hadizadeh, J.-P. Gratier, and M.-L. Doan (2012), Dating deep? Luminescence studies of fault gouge from the San Andreas Fault zone 2.6 km beneath Earth’s surface, *Quaternary Geochronology*, *10*, 280–284, doi:10.1016/j.quageo.2012.04.023.
- Sutherland, R., V. G. Toy, J. Townend, S. C. Cox, J. D. Eccles, D. R. Faulkner, D. J. Prior, R. J. Norris, E. Mariani, C. Boulton, B. M. Carpenter, C. D. Menzies, T. A. Little, M. Hasting, G. P. De Pascale, R. M. Langridge, H. R. Scott, Z. Reid Lindroos, B. Fleming, and A. J. Kopf (2012), Drilling reveals fluid control on architecture and rupture of the Alpine fault, New Zealand, *Geology*, pp. 1–4, doi:10.1130/G33614.1.
- Tary, J.-B., L. Géli, C. Guennou, P. Henry, N. Sultan, N. Çağatay, and V. Vidal (2012), Microevents produced by gas migration and expulsion at the seabed : a study based on sea bottom recordings from the Sea of Marmara, *Geophysical Journal International*, *190*, 993–1007, doi:10.1111/j.1365-246X.2012.05533.x.
- Tobin, H. J., and M. Kinoshita (2006), NanTroSEIZE: The IODP Nankai Trough Seismogenic Zone Experiment, *Scientific Drilling*, *2*, 23–27, doi:10.2204/iodp.sd.2.06.2006.
- Wang, K., and E. E. Davis (1996), Theory for the propagation of tidally induced pore pressure variations in layered subseafloor formations, *J. Geophys. Res.*, *101*(B5), 11,483–11,495.
- Waversik, W. R., and W. F. Brace (1971), Post-Failure Behavior of a Granite and Diabase, *Rock Mechanics*, *3*(2), 61–85.
- Weibull, W. (1939), A statistical theory of the strength of materials, *Ingeniörsvetenskapsakademiens handlingar*, *151*, 1–4.
- Wibberley, C. a. J., and T. Shimamoto (2005), Earthquake slip weakening and asperities explained by thermal pressurization., *Nature*, *436*(7051), 689–92, doi:10.1038/nature03901.
- Wiersberg, T., and J. Erzinger (2008), Origin and spatial distribution of gas at seismogenic depths of the San Andreas Fault from drill-mud gas analysis, *Applied Geochemistry*, *23*(6), 1675–1690, doi:10.1016/j.apgeochem.2008.01.012.
- Wilson, B., T. A. Dewers, Z. Reches, and J. N. Brune (2005), Particle size and energetics of gouge from earthquake rupture zones Brent, *Nature*, *434*, 749—752, doi:10.1029/2003GL019277.
- Yuan, F., V. Prakash, and T. E. Tullis (2011), Origin of pulverized rocks during earthquake fault rupture, *Journal of Geophysical Research*, *116*(B6), 1–18, doi:10.1029/2010JB007721.
- Zoback, M., S. Hickman, and W. Ellsworth (2011), Scientific drilling into the San Andreas Fault Zone - An overview of SAFOD’s first five years, *Scientific Drilling*, doi:10.2204/iodp.sd.11.02.2011.

Appendix A

Curriculum Vitae

A.1 Education / Professional cursus

2007-... Assistant Professor at University Joseph Fourier, Grenoble, France

2006-2007 Postdoctoral researcher at the University of California, Santa Cruz (UCSC) with Emily BRODSKY.

End 2005 Postdoctoral researcher at the University of California, Los Angeles (UCLA) with Emily BRODSKY.

2000-2005 PhD, Institut de Physique du Globe de Paris.

Titre:

in-situ study of the hydromechanical interactions between fluids and active faults

5 juillet 2005

PhD committee :

Claude	JAUPART	Institut de Physique du Globe de Paris	President
Philippe	DAVY	Université de Rennes I	Rapporteur
Pierre	HENRY	Collège de France, Aix-en-Provence	Rapporteur
Ghislain	DE MARSILY	Université de Paris VI	Examineur
Ian	MAIN	Edinburgh University	Examineur
François	CORNET	Institut de Physique du Globe de Paris	PhD Advisor

2001 "Agrégation" of Physics

2000 Magistère Interuniversitaire de Physique, Ecole normale supérieure-Paris

A.2 Committee memberships and awards

- 2010-2011: Member of the Engineering Development Panel (EDP) of the Integrated Oceanic Drilling Program (IODP)
- 2010-2011: Member of the Conseil National des Universités (CNU / French committee)
- 2009 Best reviewer award, Geophysical Journal International
- Invited speaker at several conferences (EGU, ICDP/IODP meetings)

A.3 Collaborations

A.3.1 Pulverization

Experimental development Gérard Gary (Ecole polytechnique), Pascal Forquin (LEM3, Metz, now in Grenoble University), Jean-Pierre Gratier (Grenoble University), Frans Aben (Grenoble University)

Microstructures Tom Mitchell (now in University College London), Julie Richard (ISTerre), Andrea Billi (Consiglio Nazionale delle Ricerche, Italy), Michele Fondriest (Padova University), Joel Spencer (Kansas State University), Mike Heap (Strasbourg University), Ulrich Kueppers (Ludwig-Maximilians-Universität, Munich).

A.3.2 High velocity friction experiments

Experimental development Takehiro Hirose (JAMSTEC, Japan) that was an invited researcher in Grenoble

Microstructures Muriel Andréani (Lyon University), Anne-Marie Boullier (ISTerre), Sébastien Boutareaud (ETH Zürich, now at EuroEngineering, Pau) and Dan-Gabriel Calugaru (Institut Néel, Grenoble)

A.3.3 Drilling projects

TCDP Kuo-Fong Ma (NCU, Taiwan), Emily Brodsky (UC Santa Cruz), Yasuyuki Kano (Kyoto University)

NanTroSEIZE Pierre Henry (CEREGE), Marianne Conin (CEREGE, now Guadelupe University), Demian Saffer (PennState), David Boutt (Massachusetts University), Weiren Lin (JAMSTEC, Japan), Thomas Wiersberg (GFZ Postdam)

DFDP Rupert Sutherland (GNS), John Townend (Victoria University of Wellington), Philippe Pezard (Montpellier University)

Avignonet Grégory Bièvre (ISTerre), Denis Jongmans (ISTerre)

A.4 Supervision of students

A.4.1 PhD Students

Julie Richard (2010-2013) This PhD thesis is co-supervised together with Jean-Pierre Gratier on "Creeping mechanisms in active faults: lessons from international drilling projects". During this PhD, Julie combined microstructural studies of cores samples in SAFOD borehole together with experiments on healing of samples damages experimentally at high strain rate. During this PhD, Julie was invited to take initiatives, to meet and interact with researchers as often as possible (eg, by chairing sessions during international meetings). She will finish her PhD with 3 publications [[Gratier et al., 2011](#); [Richard et al., 2014a,b](#)]

Frans Aben (2013-2016) This PhD thesis is co-supervised together with François Renard on "Creating and clogging dynamic permeability in fault zones and geological reservoirs", funded through the FlowTrans Initial Training Network, funded by the EU. This PhD is the continuation of the PhD of Julie Richard, with more stress put on the experiments. With Frans, we plan to work on dynamic damage and by improving the instrumentation of percolation cells by adding a cell for measuring permeability.

A.4.2 Supervision of research internships

I supervised several interns from the Master of Grenoble University

Camille Litty (2012) We investigated X-ray CT scans of samples almost "pulverized" from a Himalayan Fault sampled by Anne Replumaz (ISTerre).

Virginie d'Hour (2009) We performed together high strain rate experiments on analog of intact granite, compared to damaged samples of the San Andreas Fault [[Doan and D'Hour, 2012](#)]

Alexandre Tourette (2008) We conducted field work on the structure of the Clery Fault, comparing strain localization in shales and limestone [[Gratier et al., 2013](#)].

Appendix B

Publications

B.1 Publication list

1. Gratier, J-P., Thouvenot, F., Jenatton, L., Tourette, A., **Doan, M.L.** and Renard, F. Geological control of the partitioning between seismic and aseismic sliding behaviour in active faults : evidence from the Western Alps, France., *Tectonophysics*, 600:226-242, doi:10.1016/j.tecto.2013.02.013, 2013
2. Ito, T., Funato, A., Lin, W., **Doan, M.L.**, Boutt, D., Kano, Y. Ito, H., Saffer, D. McNeill, L., Byrne, T., Moe, K. Determination of Stress State in Deep Subsea Formation by Combination of Hydraulic Fracturing In-situ Test and Core Analysis - A Case Study in the IODP Expedition 319, *J. Geophys. Res.*, 118, 1–13, doi:10.1002/jgrb.50086, 2013
3. Saffer, D., Flemings, P., Boutt, D., **Doan, M.L.**, Ito, T., McNeill, L., Byrne, T., Conin, M., Lin, W., Kano, Y., Araki, E., Eguchi, N., Toczko, S.. In Situ Stress and Pore Pressure in the Kumano Forearc Basin, offshore SW Honshu from Down-hole Measurements During Riser Drilling, *Geophys. Geochem. Geosystems*, 14(5), doi:10.1002/ggge.20051, 2013
4. Moe, K.T., Ito, T., Lin, W., **Doan, M.L.**, Boutt, D., Kawamura, Y., Khong, C.K. McNeill, L., Byrne, T., Saffer, D., Araki, E., Eguchi, N., Sawada, I., Flemings, P., Kano, Y. Moore, C., Kinoshita, M., Tobin, H. Operational Review of the First Wireline in Situ Stress Test in Scientific Ocean Drilling, *Scientific Drilling*, 13:35-39, 2012
5. Boutareaud, S., Hirose, T. Andréani, M., Pec, M., Kunze, K., Calugaru, D.-G., Boullier, A.-M., **M.-L. Doan**. On the role of phyllosilicates on fault lubrication: Insight from micro- and nanostructural investigations on talc friction experiments, *J. Geophys. Res.*, 117 (B8), B08408, doi: 10.1029/2011JB009006, 2012
6. **Doan, M.L.** and V. d'Hour, Effect of initial damage on rock pulverization along faults, *J. Struct. Geol.*, 45:113-124, 2012
7. Spencer, J.Q.G., Hadizadeh, J., Gratier, J.-P. and **M-L Doan**, Dating deep? Luminescence studies of fault gouge from the San Andreas Fault Zone 2.6 km beneath Earth's surface, *Quat. Geochronol.*, 10: 280-284, 2012
8. Boutt, D., Saffer, **M.-L. Doan**, W. Lin, T. Ito, Y. Kano, P. Flemings, L. McNeil, T. Byrne, K. Moe. Scale Dependence of In-situ Permeability Measurements in the Nankai Accretionary Prism: The Role of Fractures, *Geol. Res. Lett.*, 39, L07302, doi:10.1029/2012GL051216, 2012
9. **Doan, M.L.**, and A. Billi, [High strain rate damage of Carrara marble, *Geophys. Res. Lett.*, 38, L19302, doi:10.1029/2011GL049169, 2011
10. Gratier, J-P., J. Richard, Renard, F., S. Mittempergher, **Doan, M.L.**, G. Di Toro, J. Hadizadeh and A-M. Boullier. Aseismic sliding of active faults by pressure solution creep: Evidence from the San Andreas Fault Observatory at Depth (SAFOD). *Geology*, 39, 1131-1134, 2011
11. **Doan, M.L.**, Conin, M., Henry, P., Wiersberg, T., Boutt, D., Buchs, D., Saffer, D., McNeill, L., Cukur. Free gas in Kumano basin detected from borehole sonic data in IODP NanTroSEIZE drilling Site C0009, *Geophys. Geosystems Geochem*, 12: doi:10.1029/2010GC003284, 2011

12. Lin, W., **Doan, M.L.**, Moore, J.C., McNeill, L., Byrne, T.B., Ito, T., Saffer, D., Conin, M., Kinoshita, M., Sanada, Y., Moe, K.T., Araki, E., Tobin, H., Boutt, D., Kano, Y., Hayman, N.W., Flemings, P., Huftile, G. J., Cukur, D., Buret, C., Schleicher, A.M., Efimenko, N., Kawabata, K., Buchs, D.M., Jiang, S., Kameo, K., Horiguchi, K., Wiersberg, T., Kopf, A., Kitada, K., Eguchi, N., Toczko, S., Takahashi, K. and Kido, Y., Present-day principal horizontal stress orientations in the Kumano forearc basin of the southwest Japan subduction zone determined from IODP NanTroSEIZE drilling Site C0009, *Geophys. Res. Lett.*, 37, L13303, doi:10.1029/2010GL043158, 2010.
13. Noiriél C., Renard, F., **Doan, M.L.**, and J.-P. Gratier. Intense fracturing and fracture sealing induced by mineral growth in porous rocks. *Chem. Geol.*, 269(3-4):197-209, 2010
14. **Doan, M.L.** and G. Gary., Rock pulverization at high strain rate near the San Andreas Fault, *Nature Geoscience*, 2: 709-712, 2009
15. **Doan, M.L.** and F.H. Cornet. Small pressure drop triggered near a fault by small teleseismic waves. *Earth Planet. Sci. Lett.*, 258 (1-2): 207-218, 2007
16. **Doan, M.L.** and F.H. Cornet. Thermal Convection below the Aigio Fault, Gulf of Corinth, Greece. *Geophys. Res. Lett.*, 34 (6) doi:10.1016/j.epsl.2007.03.036, 2007
17. **Doan, M.L.**, E.E. Brodsky, Y. Kano, and K.-F. Ma, In situ measurement of the hydraulic diffusivity of the active Chelungpu Fault, Taiwan. *Geophys. Res. Lett.*, 33 (16) doi:10.1029/2006GL026889, 2006.
18. F.H. Cornet, **M.L. Doan**, I. Moretti and G. Borm. Drilling through the active Aigion fault : the AIG10 well observatory. *C.R. Géoscience*, 2004.
19. F.H. Cornet, **M.L. Doan**, and F. Fontbonne. Electrical imaging and hydraulic testing for a complete stress determination. *Int. J. Rock Mech. Min. Sci.*, 40 :1225-1241, 2003.
20. **Doan, M.L.** and F.H. Cornet. A coupled hydraulic and electrical stress determination technique. In Hammah R. et al, editor, *Mining and Tunneling Innovation and Opportunity*, volume 2, page 1413. NARMS-TAC, University of Toronto Press, 2002.

B.2 Papers in preparation

1. **Doan, M.L.** , Hirose, T., Andréani, M. Boullier, A.-M., Calugaru, D.-G., Boutareaud, S. Talc lubrication at high strain rate. To be submitted to *J. Struct. Geol.*
2. **Doan, M.L.** , Saffer, D., Boutt, D., and McNeill, L. A full permeability profile of Kumano Forearc Basin, Nankai Trough from modeling of electrical data. To be submitted to *Geophys. Res. Lett.*
3. Mitchell, T.M., **Doan, M.L.** , Bhat, H.S., Renner, J., and Girty, G. High permeabilities in the damage zone of the San Jacinto Fault induced by earthquake rupture: To be submitted to *Science*
4. Richard, J., Gratier, J.-P., **Doan, M.L.** , Boullier, A.-M., and Renard, F., Time and space evolution of an active creeping fault zone: insights from the brittle and ductile microstructures in the San Andreas Fault Observatory at Depth. To be submitted to *J. Geophys. Res.*
5. Richard, J., **Doan, M.L.** , Gratier, J.-P., Renard, F., and Boullier, A.-M., Microstructures of dynamic damaging and healing by fluid circulations into a porous limestone. In prep.

Appendix C

A selection of papers

I introduce some selected papers that are collected afterwards, by summarizing them in 2 sentences or less.

C.1 High velocity experiments with talc

Boutareaud et al, J. Geophys. Res., 2012 High velocity friction experiments on talc, with unexpected high friction coefficient for dry talc. Microstructures show nanoagregates of delaminated talc.

Doan et al, to be submitted to J. Struct. Geol. Little amount of talc (5%) is enough to level off the initial peak in friction of a serpentine gouge. It alters also microstructure by creating myriads of small shear planes along the delaminating talc platelets

C.2 High strain rate damage

Doan and Gary, Nature Geoscience, 2009 Samples of the San Andreas Fault are multifragmented when loaded with strain rate larger than 150/s, suggesting that pulverized rocks are product of supershear earthquakes.

Doan and Billi, Geophys. Res. Lett., 2009 High strain rate damage experiments on marble. Damage is controlled by strain rather than by strain rate

Doan and d'Hour, J. Struct. Geol., 2012 High strain rate damage experiments on sound granite, where pulverization could be reproduced but with a larger strain rate threshold.

Gratier et al, Geology, 2011 Extensive pressure solution is found within the SAFOD sample. This process intensity is compatible with the current creep rate of the San Andreas Fault, thanks to intense microfracturing of gouge grains.

Richard et al, to be submitted to J. Geophys. Res. Microstructural studies of the SAFOD sample with data from the saponite gouge and the surrounding material. We discuss the competition between weak friction and pressure solution.

C.3 Borehole geophysics

Doan et al, Geophys. Res. Lett., 2006 Cross-hole experiments across the Chelungpu Fault, through the damage zone bording the strand at the origin of the 1999 Chichi earthquake.

Doan et al, Earth. Planet. Sci. Lett., 2007 Long term monitoring within the Aigio Faut (Greece), with hydraulic anomaly triggered by teleseismic waves.

Lin et al., Geophys. Res. Lett., 2009 Use of data of the Formation Microseismic Imager data to get the orientation of the principal stress directions, in the C009 borehole drilled in the Nankai subduction zone during IODP expedition 319.

Doan et al., Geochem. Geophys. Geosyst., 2011 Use of sonic data to derive a full profile of porosity and gas content in the C009 borehole

Doan et al., to be submitted to Geophys. Res. Lett. Use of electrical data affected by the invasion of the formation by borehole fluids, to derive continuous profile of permeability within the C009 borehole.

C.1 High velocity experiments with talc

On the role of phyllosilicates on fault lubrication: Insight from micro- and nanostructural investigations on talc friction experiments

Sébastien Boutareaud,¹ Takehiro Hirose,² Muriel Andréani,³ Matej Pec,⁴ Dan-Gabriel Calugaru,⁵ Anne-Marie Boullier,^{6,7} and Mai-Linh Doan⁶

Received 8 November 2011; revised 18 May 2012; accepted 13 June 2012; published 11 August 2012.

[1] Exposures of mature faults at the Earth's surface show that in the shallow crust some of co-seismic slip occurs within a narrow phyllosilicate-rich gouge material. Mechanical behavior of phyllosilicates sheared at seismic slip-velocities remains a complex issue as suggested by the experimental and theoretical studies reported so far. Talc represents a simple case for common phyllosilicates in natural faults and therefore we chose talc as an analogue to better understand the mechanical behavior of clay-rich mature crustal faults. We present a series of high-velocity friction experiments conducted on talc at 1.31 m s^{-1} and normal stresses of 0.3–1.8 MPa for wet and dry conditions. At 1 MPa normal stress, both wet and dry experiments show a slip-weakening behavior, however, with a higher decreasing rate in wet conditions. Dynamic shear stress evolves from a peak value of 0.24–0.52 MPa down to a residual state value of 0.08–0.18 MPa in wet conditions, and from a peak value of 0.46–1.17 MPa down to a residual state value of 0.12–0.62 MPa in dry conditions. Based on a detailed microstructural analysis down to the nanoscale, we propose thermal-pressurization as a possible slip-weakening mechanism for wet conditions. On the contrary, in dry conditions the long-lasting weakening is interpreted to be due to a combination of *i*) progressive disappearance of geometrical incompatibilities, *ii*) solid lubrication of talc lamellae, and *iii*) powder lubrication by nanometric aggregates. We conclude that initial gouge humid conditions and inherited fabric from past sliding may have large influence on the slip-weakening for subsequent slip.

Citation: Boutareaud, S., T. Hirose, M. Andréani, M. Pec, D.-G. Calugaru, A.-M. Boullier, and M.-L. Doan (2012), On the role of phyllosilicates on fault lubrication: Insight from micro- and nanostructural investigations on talc friction experiments, *J. Geophys. Res.*, 117, B08408, doi:10.1029/2011JB009006.

1. Introduction

[2] During an earthquake, complex thermo-poro-mechanical and physico-chemical processes control fault friction [Sibson, 1989; Wintsch *et al.*, 1995; Rice, 2006; Di Toro *et al.*, 2011]. Seismology paved the way for earthquake mechanics studies by interpreting seismic waves from active faults [Lee *et al.*, 2002]. However, seismology remains an

indirect technique of study by which it is impossible to fully address issues such as variations of dynamic shear stress during earthquake [Bouchon, 1997], energy budget of an earthquake, or the physical processes that occur during earthquake rupture propagation (Kanamori and Brodsky [2004]; Lapusta [2009]; see Di Toro *et al.* [2012] for a complete review). Laboratory rotary shear experiments have been conducted for more than 15 years to gain direct information on the physico-chemical mechanisms that occur during earthquake faulting. The mechanical behavior of simulated faults seems to be coherent with seismological studies of major studied earthquakes [e.g., Mizoguchi *et al.*, 2007a; Sone and Shimamoto, 2009; De Paola *et al.*, 2011], and experimental and natural gouge microstructures show similar characteristics [e.g., Mizoguchi *et al.*, 2009b; Boutareaud *et al.*, 2010].

[3] Recent low to high slip-velocity experiments [Sone and Shimamoto, 2009] allowed reproduction of the kinematic slip history of a major earthquake rupture (1999 Chi-Chi, Taiwan, Earthquake) [Ji *et al.*, 2003]. The frictional behavior of the simulated fault has shown that faults undergo a sequence of strengthening, weakening and healing during acceleration and deceleration of slip. These results suggest that fault ruptures propagate in a pulse-like mode [Heaton,

¹Geologisches Institut, ETH Zürich, Zürich, Switzerland.

²Kochi Institute for Core Sample Research, JAMSTEC, Kochi, Japan.

³Laboratoire de Géologie de Lyon: Terre, Planètes, Environnement, UMR 5276, Ecole Normale Supérieure de Lyon et Université Lyon I, Lyon, France.

⁴Geological Institute, University of Basel, Basel, Switzerland.

⁵Institut NEEL, UPR 2940 CNRS, Grenoble, France.

⁶Institut des Sciences de la Terre, CNRS, University Joseph Fourier, Grenoble, France.

⁷International Laboratory (LIA) ADEPT, France-Taiwan, CNRS, NSC, Taipei, Taiwan.

Corresponding author: S. Boutareaud, Geologisches Institut, ETH Zürich, Sonneggstr. 5, Zürich CH-8092, Switzerland. (sebastien.boutareaud@erdw.ethz.ch)

©2012. American Geophysical Union. All Rights Reserved. 0148-0227/12/2011JB009006

1990], in which the risetime of fault slip is much shorter than the total duration of the event. The strong initial strengthening associated with increasing slip-velocity has already been observed in metallurgy in the $0.01\text{--}0.1\text{ m s}^{-1}$ range [Lim *et al.*, 1989] and should impose a barrier for rupture growth into large earthquakes. This strengthening may prevent easy generation of large earthquakes and may have a major role in determining the final rupture dimension. Thus, the first meters of slip during acceleration appear to be critical to overpass the strength barrier and to develop an appropriate slip-weakening mechanism. The cause of the initial strengthening at the microscopic scale that influences the nucleation of earthquakes has received large interest from experimentalists for low displacement rates [Paterson and Wong, 2004; Mair and Abe, 2008; Niemeijer *et al.*, 2010]. However, little attention has been paid to seismic slip-velocities so far [e.g., Mizoguchi *et al.*, 2009a, 2009b; Sone and Shimamoto, 2009].

[4] This paper aims to investigate the weakening mechanisms activated during co-seismic slip along a phyllosilicate-rich fault gouge, since multiple mechanisms can potentially occur within the slip zone [e.g., Gratier and Gueydan, 2007; Bizzarri, 2009; Niemeijer *et al.*, 2010; De Paola *et al.*, 2011]. Further, we aim at investigating the effect of pre-existing gouge fabric from an initial slip on the amplitude of the subsequent co-seismic peak shear stress and so the occurrence of consecutive thermally activated slip-weakening mechanism(s). Talc has been chosen because it represents a chemically simple case (low water adsorption, high thermal decomposition temperature, no chemical processes, no oxidation) among the phyllosilicates that compose some mature faults [Vrolijk and van der Pluijm, 1999]. We report a series of rotary shear experiments conducted on a pure talc powder at 1.31 m s^{-1} over a range of normal stresses ($0.3\text{--}1.8\text{ MPa}$). We have characterized microstructure evolution with increasing displacement by scanning electron microscopy (SEM) and transmission electron microscopy (TEM) in order to investigate how they correlate with the mechanical behavior. Microstructure development correlates with the mechanical behavior. Weakening is accompanied by re-orientation of talc grain (001) cleavage planes parallel to the (C-) shear plane direction, and the development of nanometric aggregates. We then discuss possible implications of gouge fabric development during the seismic cycle for mature crustal faults.

2. Sample Assembly and Experimental Conditions

2.1. Characterization of Initial Material

[5] Talc ($\text{Mg}_3\text{Si}_4\text{O}_{10}(\text{OH})_2$) is a trioctahedral phyllosilicate with a structure composed of stacking sequences of tetrahedral-octahedral-tetrahedral (TOT) layers in the monoclinic system. This sheeted structure is hydrophobic, completely compensated and stable. Weak Van der Waals force bonds the TOT sequences. They lead to a strong mechanical anisotropy responsible for an excellent plane of cleavage parallel to the stacking plane (001), and a high tendency for interlayer delamination and slip.

[6] The talc gouge used in our experiments is made from a natural talc schist powder acquired from VWR Corporation (<http://www.vwrsp.com>). X-ray Diffraction (XRD) and

X-ray Fluorescence (XRF) analyses show that the talc powder is a high-purity monomineralic aggregate with about 0.01 wt.% of solid impurities (orthopyroxene), and 5.9 wt.% of constitutive water (i.e., from the crystal structure). It is composed of platy-angular to subangular grains with a long axis ranging from 1 to $100\text{ }\mu\text{m}$ ($25\text{ }\mu\text{m}$ as a mean), with an axial ratio of about 0.33 for the $25\text{ }\mu\text{m}$ -thick particles, and 0.14 for the $5\text{ }\mu\text{m}$ -thick particles.

[7] Thermogravimetric-differential thermal analyses (TG-DTA) have been conducted on the talc schist powder in a helium environment for dynamic heating conditions of 10 and $50^\circ\text{C min}^{-1}$. This type of analysis provides data on the thermally activated mineralogical transformations that can possibly occur during high-velocity friction experiments. From 20 to 120°C , adsorbed water is released. Then up to 500°C interlayer water is driven off. From 500°C to 900°C , dehydroxylation of talc schist (i.e., breakage of the Mg-OH bonds) starts with a weight reduction of about 1%. Then, from 900°C to 1300°C , about 4.8 wt.% of water is released. The total amount of water loss from 500°C to 1300°C is similar to the loss on ignition calculated from XRF analyses. At around 1300°C , crystallization of enstatite with formation of amorphous silica is observed. These results are consistent with Evans and Guggenheim [1988] and Piga *et al.* [1992], but do not match reported data from Ward [1975] and Wesolowski [1984], for which crystallization of enstatite starts earlier (i.e., at about 720°C). Enstatite crystallization from talc dehydroxylation localized in the shearing zone at 860°C has also been reported by Escartin *et al.* [2008] during triaxial experiments suggesting a role of deformation on reaction kinetics. But in static experiments, we attribute this apparent discrepancy of reaction kinetics between authors to differences in the rate of temperature increase and in the size distribution of grains: the smaller the grain size, the larger the specific surface and the faster reactions take place.

2.2. Experimental Setup and Method

[8] The experimental fault consists of a 25 mm -diameter gabbro cylinder cut perpendicular to the revolution axis. Cylinder surfaces are ground with a 220# grid to obtain rough wall surfaces in order to promote shear throughout the gouge layer (Figure 1). Cylinders are assembled with an intervening layer of ca. $1\text{--}1.5\text{ mm}$ -thick talc gouge. We put 0.4 wt.% of distilled water into the gouge for wet tests. The assembly is then placed in the high-velocity rotary-shear apparatus [Shimamoto and Tsutsumi, 1994], where one cylinder remains stationary while the other rotates. See Hirose and Shimamoto [2005] and Mizoguchi *et al.* [2007a] for complete experimental setup and procedure. A Teflon sleeve surrounds the fault to avoid gouge material or liquid water expulsion during rotation. No loss of gouge is observed during our experiments down to the residual shear stress as long as the measured gouge thickness does not decrease. Note that water vapor can escape from the simulated fault system in-between the Teflon sleeve and rock cylinders during experiments [Hirose and Bystricky, 2007; Boutareaud *et al.*, 2008]. An initial pre-run load includes manual clockwise and counterclockwise $\pi/4$ rotations of the rotating cylinder to consolidate the gouge under the same normal stress as during the experiment. This increases the packing density for a larger strength of the gouge. Experiments consist of less than 60 s rotary-shear tests, leading to general

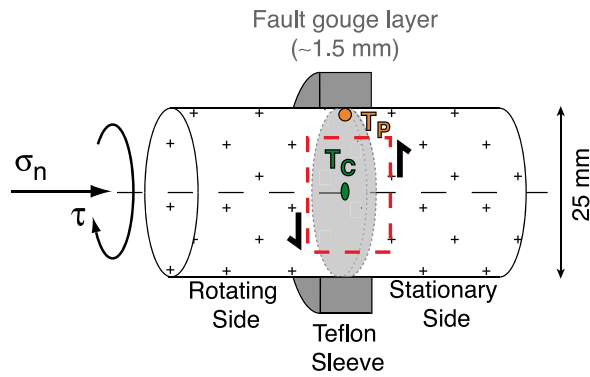


Figure 1. Schematic view of the experimental assembly. The dashed rectangle shows position of post-run thin sections. T_p stands for calculated peripheral temperature (orange circle), and T_c stands for calculated axis-center temperature (green ellipse). T_p and T_c are located at the interface of the talc gouge and the rotating cylinder.

non-coaxial shear deformation of the thin simulated fault gouge.

[9] The sample geometry implies an angular velocity increase from the center of the rotation axis to the periphery. Assuming that the shear stress τ is constant over all of the sliding surface area S , an equivalent slip velocity V_{eq} is defined such that $\tau V_{eq} S$ gives the rate of total frictional work [Shimamoto and Tsutsumi, 1994; Hirose and Shimamoto, 2005]:

$$V_{eq} = \frac{4}{3} \pi \omega R \quad (1)$$

where R is the radius of the sample and ω the angular velocity (in rad s^{-1}). The Teflon effect on shear stress is not corrected. The equivalent slip reported as “displacement” hereafter corresponds therefore to the slip at two thirds of the total radius. Twenty-three experiments have been carried out at room temperature (25°C) at a fixed rotation rate of 1500 rotations per minute, which corresponds to equivalent slip-velocities of 1.31 m s^{-1} (Table 1). The applied normal stress is fixed at 0.3 to 1.8 MPa.

[10] To monitor water vapor release by the fault during sliding in the sealed specimen chamber, a moisture sensor has been placed 20 mm away from the sliding surfaces [e.g., Hirose and Bystricky, 2007]. Thermal expansion of the two cylinders along the revolution axis by rapid frictional heating has already been calculated to be negligible compared to the measured fault gouge thickness [Boutareaud et al., 2008]. Therefore, positive or negative value of the measured fault thickness reflects either gouge dilatancy or compaction, respectively (Figure 2).

[11] Gouge porosity measurements are made from SEM images for a wide range of magnification, and named *estimated* porosity hereafter (for procedure, see section 3.2.1). *Estimated* porosity is then compared to the *dynamic porosity* calculated from the dynamic bulk volume change of the simulated fault, which is calculated from the fault gouge thickness.

[12] Two types of SEM apparatuses have been used: a FEI Quanta 200FEG, equipped with Ametek-EDAX Pegasus

analytical system including Sapphire Si(Li) detector and a Zeiss Ultra, using QBSD detector for high-kV backscattered electron contrast at 15 kV accelerating voltage for SEM images. TEM cross-sections have been obtained from a focus ion beam (FIB-SEM) apparatus: a Zeiss NVision40, using EsB detector for low-kV backscattered electron contrast at 3 kV accelerating voltage for SEM images. TEM observations have been conducted on a FEI Tecnai G2 under an acceleration voltage of 200 kV.

2.3. Temperature Calculation

[13] In order to evaluate temperature rise during the experiments, we numerically solved the heat equation taking into account the heat production and heat diffusion in the domain formed by the two cylinders and the gouge (Figure 3). Since the geometry is axisymmetric, we can restrict the computation of the temperature T only to a 2-D framework, by considering the following heat equation in a cut containing the symmetry axis:

$$\rho c_p \frac{\partial T}{\partial t} - k \Delta T = Q \quad (2)$$

where k (2) in $\text{W m}^{-1} \text{K}^{-1}$ is the thermal conductivity, c_p (1000 for gabbro and 850 for talc) in $\text{J kg}^{-1} \text{K}^{-1}$ is the specific heat capacity and ρ (2650 for gabbro and 2750 for talc) in kg m^{-3} is the mass density.

[14] All frictional work is assumed to be converted to heat. Heat generation rate Q (i.e., the quantity of produced heat per unit volume in unit time) is then expressed [Noda and Shimamoto, 2005] by

$$Q = \dot{\gamma} \tau \quad (3)$$

where $\dot{\gamma}$ is the shear-strain rate in s^{-1} and τ is the shear stress in Pa. Shear-strain rate is defined as

$$\dot{\gamma} = \frac{V}{w} \quad (4)$$

where V is the slip-rate (proportional to the radial position) in m s^{-1} and w ($30 \times 10^{-6} \text{ m}$ for #1472 and $40 \times 10^{-6} \text{ m}$ for #1475) is the width of deformation zone in m. Considering that all the deformation is localized in a narrow portion of the fault zone volume (named Principal Slip Zone or PSZ hereafter), the heat source (Q) is proportional to the shear stress and to the radial position.

[15] To solve the heat equation (2), a numerical code based on the finite element method (SETMP software) has been used [Calugaru et al., 2003; Boutareaud et al., 2008]. It uses a finite element of the second order for a good accuracy and the iterative gradient conjugate method with Symmetric Successive Over Relaxation (SSOR) preconditioner [Saad, 2003] to solve algebraic systems with a fast convergence.

[16] In order to minimize the calculation duration, talc friction at coseismic velocities is assumed to approximately follow the empirical slip-weakening equation [Mizoguchi et al., 2006]:

$$\tau_d = \tau_{ss} + (\tau_p - \tau_{ss}) \times \exp\left(\frac{\ln(0.05) \times d}{D_c}\right) \quad (5)$$

Table 1. Summary of the Principal Parameters for All Conducted High-Velocity Experiments^a

Run	Humid Conditions	Initial Peak				Steady State				Slip-Weakening Distance (m)	Total Displacement (m)	Amount of Stress Drop (MPa)	Maximum Dilatancy (mm)	Equivalent Slip-Velocity (m s ⁻¹)	Total Fracture Energy (MJ m ⁻²) at Dc	Frictional Heat (MJ m ⁻²) at Dc	Dissipated Energy (MJ m ⁻²) at Dc
		Shear Stress (MPa)	Normal Stress (MPa)	Power Density (MPa ² m s ⁻¹)	Shear Stress (MPa)	Normal Stress (MPa)	Power Density (MPa ² m s ⁻¹)										
#1472	Dry	0.77	0.95	0.85	0.21	1.02	0.73	19.49	42.49	0.57	0.34	1.31	5.52	4.06	9.58		
#1473	Dry	0.97	1.36	0.41	0.27	1.48	0.35	15.72	36.54	0.70	0.56	1.31	5.52	4.19	9.70		
#1474	Dry	0.54	0.55	2.53	0.16	0.62	1.97	24.33	42.84	0.38	0.14	1.31	4.58	3.99	8.57		
#1587	Dry	0.46	0.27	10.47	0.12	0.37	5.58	37.69	49.19	0.34	0.07	1.31	4.52	4.52	9.05		
#1588	Dry	1.17	1.80	0.24	0.32	1.86	0.22	10.70	23.67	0.85	0.62	1.31	3.42	3.42	6.85		
#1478	Dry	0.75	0.96	0.83	0.62	1.06	0.68	-	2.00	-	-	1.31	0.10	0.96	1.07		
#1479	Dry	0.73	0.95	0.84	0.58	1.06	0.67	-	2.99	-	-	1.31	0.19	1.43	1.63		
#1480	Dry	0.73	0.96	0.83	0.53	1.06	0.67	-	4.71	-	-	1.31	0.28	1.52	1.80		
#1481	Dry	0.74	0.97	0.81	0.40	1.04	0.71	-	7.36	-	-	-	-	-	-		
#1482	Dry	0.73	0.95	0.84	0.24	1.05	0.70	-	15.25	0.49	0.22	1.31	-	-	-		
#1585	Dry	0.84	0.96	0.83	0.48	1.06	0.68	-	7.44	-	-	4.26	-	-	-		
#1586	Dry	0.80	0.97	0.81	0.31	1.05	0.69	-	16.44	0.49	0.42	1.31	-	9.57	-		
#1714	Dry	0.71	0.97	0.82	0.22	1.11	0.62	23.67	40.68	0.49	0.44	1.31	5.85	5.14	10.99		
#2290	Dry	0.67	1.00	-	-	-	-	-	31.40	-	-	1.31	-	-	-		
#1475	Wet	0.50	0.97	0.81	0.15	1.03	0.72	3.72	33.67	0.35	-	1.31	0.65	0.55	1.20		
#1476	Wet	0.29	0.55	2.50	0.13	0.59	2.20	0.37	33.18	0.16	-	1.31	0.03	0.05	0.08		
#1477	Wet	0.52	1.37	0.41	0.14	1.44	0.37	6.06	24.07	0.38	-	1.31	1.16	0.83	1.99		
#1589	Wet	0.24	0.60	2.12	0.08	0.70	1.56	-	38.01	0.16	-	1.31	-	-	-		
#1590	Wet	0.24	0.25	12.21	0.12	0.33	7.01	60.87	49.47	0.12	-	1.31	3.65	7.30	10.96		
#1592	Wet	0.44	1.78	0.24	0.14	1.73	0.26	0.38	27.89	0.30	-	1.31	-	-	-		
#1483	Wet	0.35	0.97	0.82	0.17	1.01	0.75	1.59	5.68	0.17	-	1.31	0.14	0.27	0.41		
#1484	Wet	0.37	0.98	0.79	0.18	1.00	0.76	0.36	11.61	0.19	-	1.31	0.03	0.07	0.10		
#1715	Wet	0.32	0.97	0.81	0.08	0.98	0.80	0.05	26.42	0.24	-	1.31	0.01	0.004	0.01		

^aThe total fracture energy is the area under the slip-weakening curve, between the peak shear stress and the residual shear stress. The frictional heat is the work of the residual shear stress. The dissipated energy is the total mechanical energy (i.e. the sum of the total fracture energy and the frictional heat).

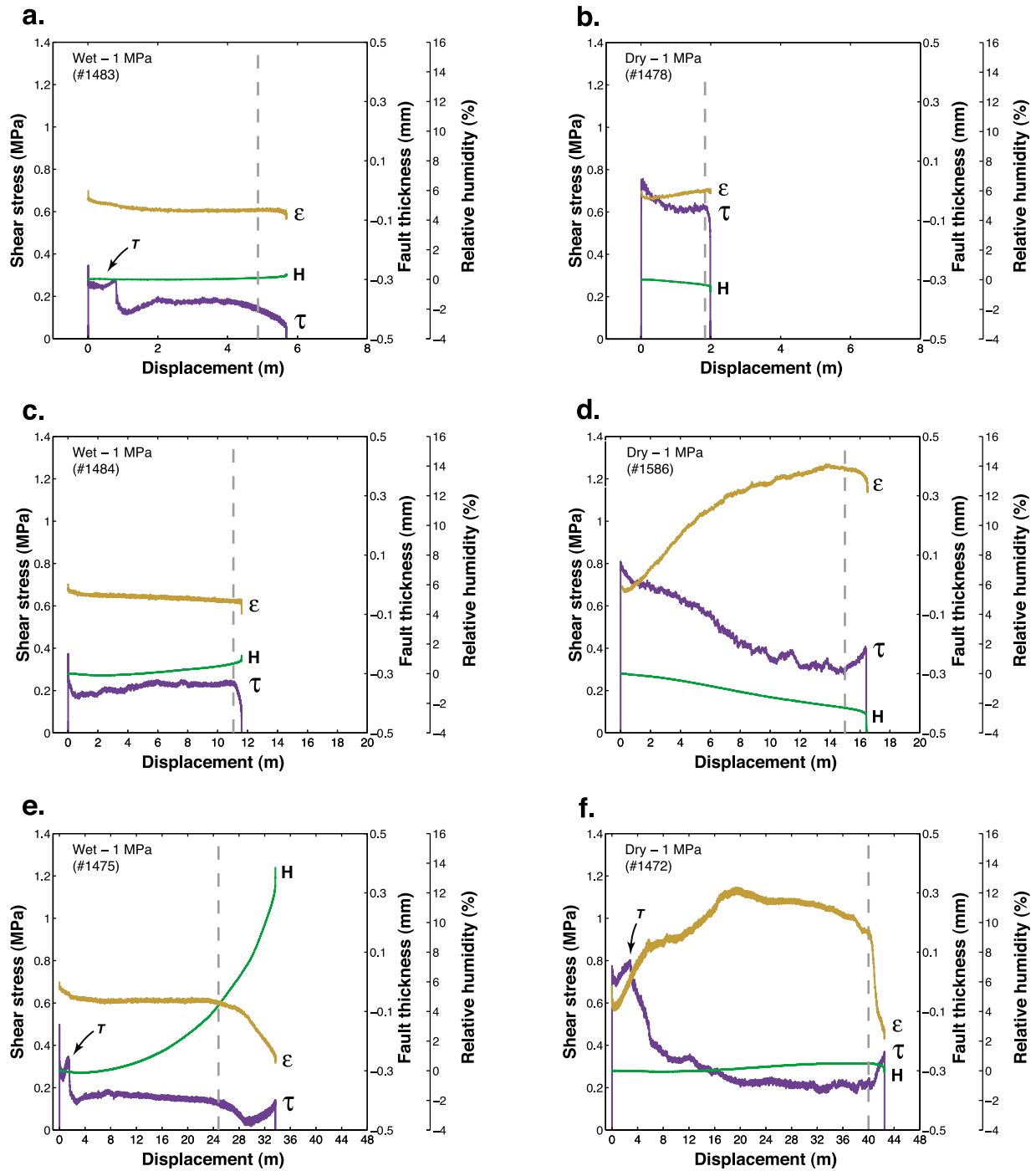


Figure 2. Representative fault shear stress (τ), the fault thickness (ϵ), and the relative humidity (H) in the sealed chamber containing the fault, versus displacement at velocity of 1.31 m s^{-1} , for wet and dry conditions. (T) stands for Teflon effect. The vertical gray dashed line indicates the arrest of the high-speed rotary-shear motor. (left) Wet conditions, (right) dry conditions. Experiments have been stopped at several different displacements: (a) 6 m, (b) 2 m, (c) 12 m, (d) 16 m, (e) 34 m and (f) 42 m.

where τ_d is the instantaneous dynamic shear stress in Pa, τ_{ss} is the residual (steady state) shear stress in Pa, τ_p is the peak shear stress in Pa, d is the displacement and D_c is the slip-weakening distance in m necessary for the fault to reach the residual shear stress. D_c is determined by fitting

equation (5) to the experimental data by the least squares method.

[17] The numerical model has been validated for wet and dry experiments, by comparing the calculated temperature from four thermocouples located in the stationary cylinder

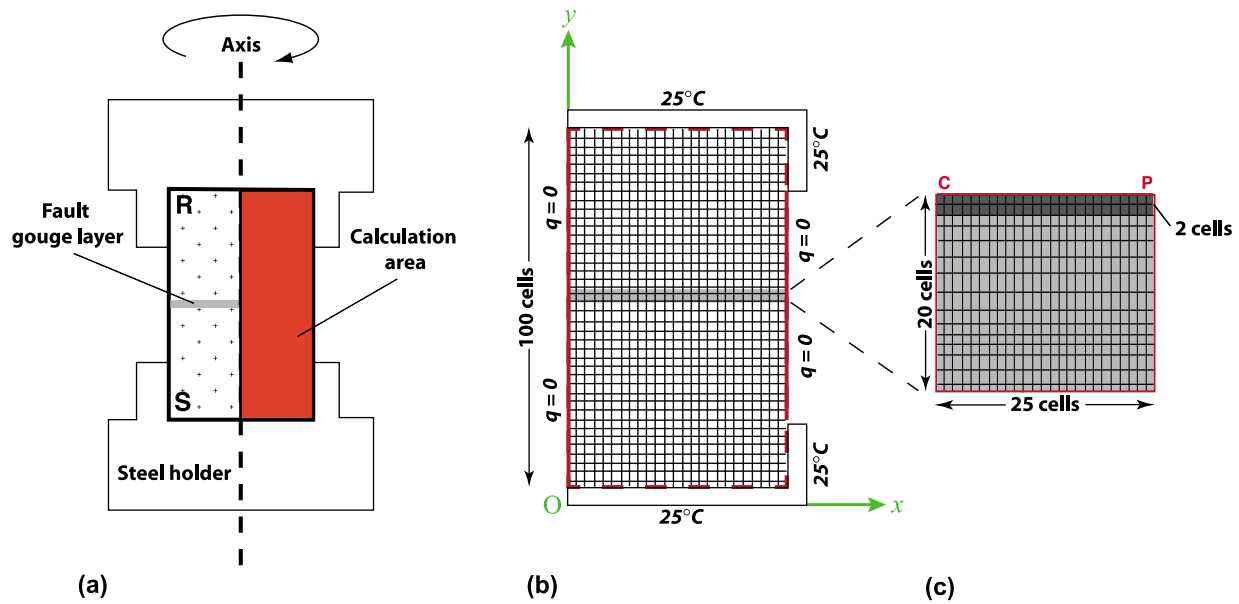


Figure 3. Sketch of the gouge-gabbro system used for numerical simulation. (a) Geometry of the specimen sample. *R* means rotary side and *S* means stationary side. (b) Enlarged sketch of the total calculation domain showing assumed boundary conditions. The light gray central part represents the gouge zone. (c) Enlarged sketch of the heat production gouge zone. The dark gray zone represents the PSZ. Only 20 by 50 cells are used to calculate the heat generation rate. *C* means central part of the heat production zone (axis-center of the cylinder where T_c is calculated), and *P* means peripheral part of the heat production zone (periphery of the cylinder where T_p is calculated).

set at different distances (1, 5, 10 and 15 mm) from the fault surface (#1714 and #1715) [Boutareaud *et al.*, 2009]. For the thermocouple closer to the fault surface, a maximum difference from calculated temperature of $\pm 5^\circ\text{C}$ for the first 11 m of displacement, and $+30^\circ\text{C}$ subsequently has been observed in wet conditions. The deviation between calculation and measurement could be probably related to the limits of the considered physical model that assumes that cylinders and gouge are solid media (not porous media) and therefore it is not able to take into account some phenomena (as the phase change of water), which could be significant.

[18] To account for the radial distribution of temperature that results from the variation in slip-velocity, the reported calculated temperatures (Figure 4) consider only two points located closely at the interface of the talc gouge and the rotating cylinder: one at the axis-center of the cylinder (T_c) and the other at the periphery of the cylinder (T_p).

3. Results

3.1. Evolution of Physical Parameters During Experiments

[19] The first-order trend of our friction experiments appears to be reproducible. It exhibits an exponential decay in fault strength from a peak value (τ_p) to a steady state (i.e., residuals shear stress) value (τ_{ss}) over a slip-weakening distance (D_c). Empirical laws can fit this slip-weakening behavior. The version in best agreement with experimental data is expressed in equation (5). In this equation (see Figure 5 for definitions), D_c represents the post-peak distance necessary to achieve 95% of the total weakening [Mizoguchi

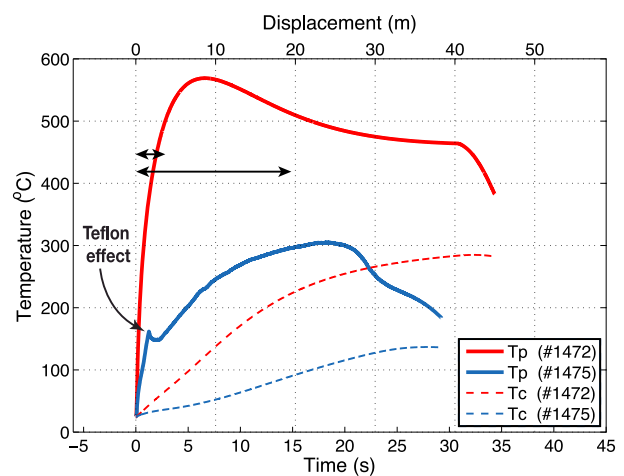


Figure 4. Calculated temperature evolution versus time for two representative experiments conducted at 1.31 m s^{-1} and 1 MPa normal stress. Red color corresponds to the dry experiment (#1472), and blue corresponds to the wet experiment (#1475). Plain lines stand for peripheral assembly temperatures (T_p), and dashed lines stand for central assembly temperatures (T_c). Long-length and short-length arrows indicate the slip-weakening duration for #1472 and #1475, respectively. The right ends of the arrows point out the slip-weakening distance necessary for the simulated faults to reach the residual shear stress.

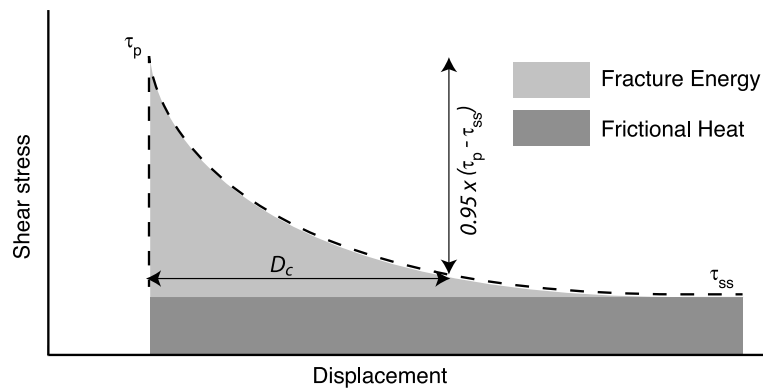


Figure 5. Schematic diagram showing the significance of the various parameters used in the empirical equation (5) to fit the weakening behavior of simulated faults at high slip-velocity.

et al., 2007a]. Two additional parameters have been calculated: the dissipative energy and the power density. The dissipative energy represents the total work per unit fault area. It refers to the summation of the total fracture energy per unit area (i.e., the area under the slip-weakening curve) equals to as $0.5 * (\tau_p - \tau_{ss}) * D_c$, and the frictional heat per unit area (i.e., the work of the residual shear stress) calculated as $\tau_{ss} * D_c$. The power density represents the energy exchanged on the sliding surface per unit time and unit area. It is equal to $1/(\tau \cdot V)^2$.

[20] A summary of experimental conditions and slip-weakening physical parameters is given for each test in Table 1. Our talc friction experiments have been conducted from 0.3 to 1.8 MPa of normal stress (see Table 1). Peak shear stress values range from 0.46 to 1.17 MPa for dry conditions, and from 0.24 to 0.52 MPa for wet conditions. Residual shear stress values range from 0.12 to 0.62 MPa for dry conditions, and from 0.08 to 0.18 MPa for wet conditions. Stress drop values range from 0.12 to 0.38 MPa for wet conditions, and from 0.34 to 0.85 MPa for dry conditions. Slip-weakening distance values D_c range from 0.05 to 60.87 m for wet conditions, and from 10.70 to 37.69 m for dry conditions. During these experiments, the torsion motor is suddenly stopped (the deceleration occurs over about few millimeters of displacement). The random increase in shears stress at the end of the experiments is due to a slight leak of gouge.

[21] Second-order trends of our friction experiments occasionally show a second peak of friction that can be preceded by a plateau and followed by a second weakening (i.e., Figure 2). Video monitoring of the sample assembly show the Teflon sleeve moving away from its initial position, which tends to impede revolution of the rotating cylinder. This problem originates from a self-adjustment of a slight misalignment of the Teflon sleeve relatively to the rotating rock cylinder (see *Sawai et al.* [2012] for a complete review on Teflon artifacts for this experimental setting). Accordingly, the second peak of friction is interpreted as an experimental artifact. It is important to note that the first-order of the mechanical behavior of the simulated faults remains independent of this experimental artifact (Figure 2).

[22] Only wet tests show a release of water (for a displacement higher than 8 m) with a relative increase of humidity in the range of $8 \pm 2\%$ once motor is stopped. This

indicates that enough heat is produced by friction to allow water phase transition from liquid to vapor. However, because our simulated fault is sealed by a Teflon sleeve, the amount of released water is directly attributed to the degree of fault sealing or sleeve movement. The negative values of humidity percentage observed in the first few meters on Figure 2 can be reasonably explained by the increase of fault temperature, leading to a small change of vapor water pressure in the vicinity of the moisture sensor. For these two reasons, the absolute measured value of humidity cannot be accurately established.

[23] The slip-weakening distance D_c represents the amount of displacement necessary for the dynamic fault shear stress to achieve 95% of the weakening from the peak shear stress to the residual shear stress. In the following, for convenience, D_c is assimilated to the distance value of the slip-weakening.

[24] The observed compaction at the beginning of all runs is usual for this type of experiments, leading to a porosity reduction and gouge consolidation [see *Boutareaud*, 2007], with contact-junction strengthening by increasing the quality of contacts between sliding surfaces [*Rice et al.*, 2001]. From the measured fault thickness changes, we have calculated the relative gouge porosity variations for dry tests, for an estimated standard deviation of $\pm 2.4\%$. Dry tests show a compaction of the gouge of 4% at about 0.5 m of displacement, which progressively decreases up to ~ 1.5 m where compaction changes to dilation (e.g., Figure 2f). From there, gouge dilatancy exponentially increases up by $\sim 23\%$ until the fault reaches the residual shear stress at D_c . Then, the fault returns to the initial porosity by compaction.

[25] For the sake of clarity, we report only data from 1 MPa normal stress experiments in this paragraph, thus the reported shear stresses equal the friction coefficient, μ . The calculated temperature evolution of experiments #1472 and #1475 (Figure 4) shows an exponential increase of T_p for dry and wet conditions. A peak value of 569°C and 304°C is reached after around 6 s (equivalent to 8 m of displacement) and 17 s (equivalent to 22 m of displacement), respectively. At D_c (see Table 1), the T_p temperature is around 512°C for dry conditions, and around 160°C for wet conditions. On the contrary, T_c increase remains logarithmic during the duration of the experiments. It reaches a maximum value of 113°C and 101°C at 6 s and 17 s for dry and wet experiments,

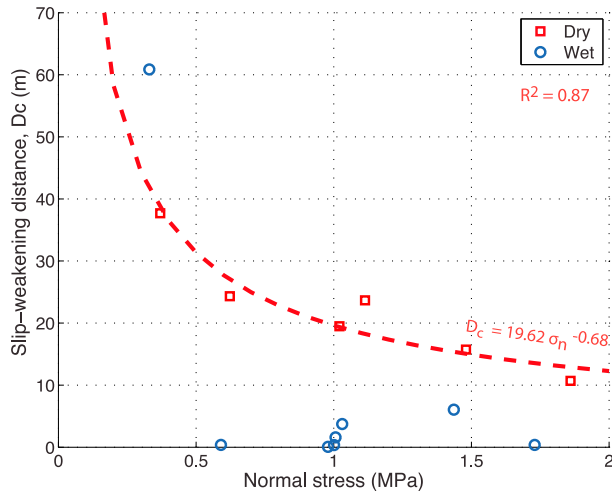


Figure 6. Slip-weakening distance (D_c) versus normal stress. Dry experiments show a decrease in power law of D_c with increasing normal stress. No reasonable fit can be obtained for wet conditions. Wet values are lower than dry values.

respectively. At D_c (see Table 1), the maximum reached T_c temperature is 228°C and 36°C for dry and wet experiments, respectively.

[26] From the measured primary fault physical parameters, we were able to investigate the fault mechanical behavior of talc at seismic slip-velocities for a limited number of relationships:

[27] 1. D_c exhibits a negative dependence in power law on applied normal stress, for dry conditions (Figure 6). No evident relation could be found for wet conditions.

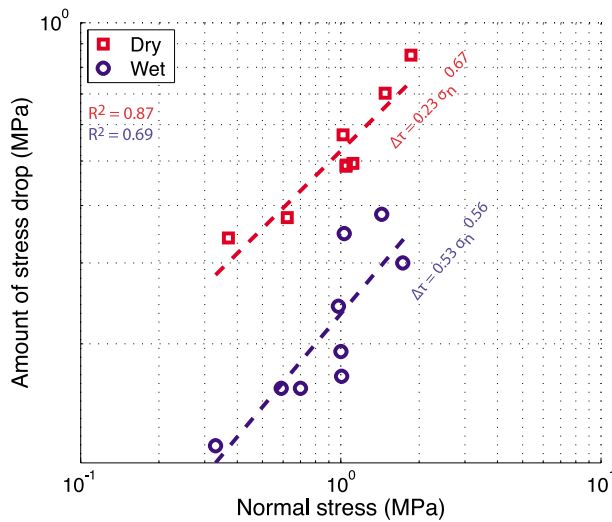


Figure 7. Amount of stress drop versus applied normal stress. The amount of stress drop is always higher in dry conditions compared to wet conditions. In best fit equations, $\Delta\tau$ stands for amount of stress drop.

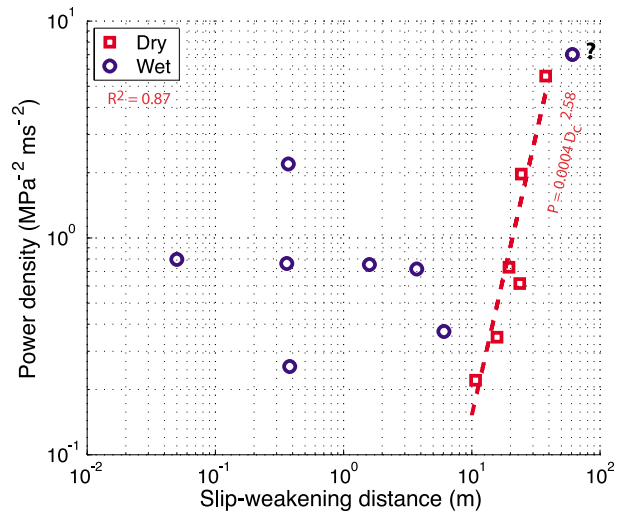


Figure 8. Fault power density at the residual state versus slip-weakening distance (D_c). In best fit equation, P stands for power density. Question mark indicates that the relevance of the point needs to be investigated. There is no apparent correlation for dry conditions.

[28] 2. Dynamic stress drop shows a positive power law dependence on applied normal stress for dry and wet conditions (Figure 7).

[29] 3. The experimental data set shows that fault power density strongly increases with D_c for dry conditions only (Figure 8). In wet conditions, the general trend does not show any dependence of fault power density on D_c .

[30] 4. The measured maximum gouge layer dilation is directly proportional to the applied normal stress, in dry conditions only (Figure 9).

[31] The relevance of these experimental data is discussed in section 4.4.

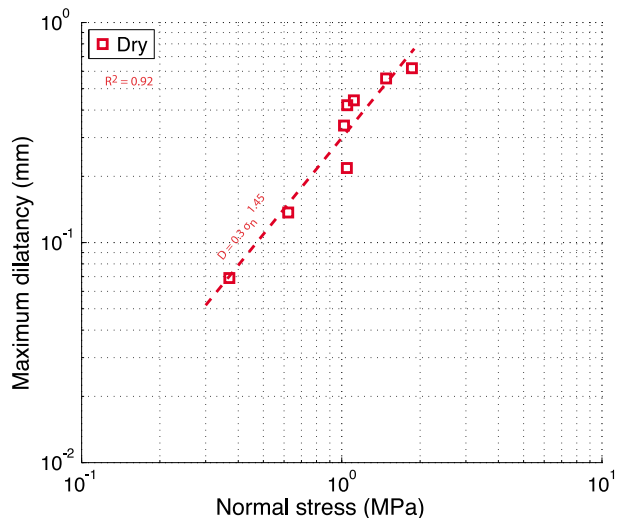


Figure 9. Fault maximum dilatancy versus applied normal stress. In best fit equation, D stands for maximum dilatancy.

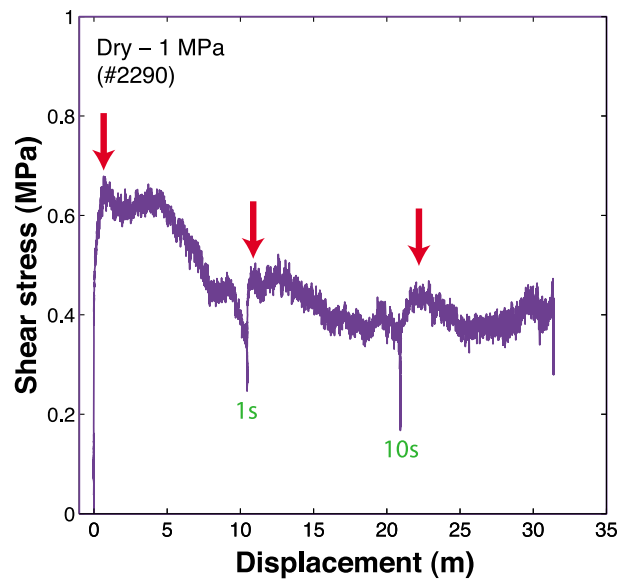


Figure 10. Evolution of shear stress as a function of displacement for two hold times from slide-hold-slide tests. Experiment has been conducted at 1.31 m s^{-1} for dry conditions. Red arrows indicate peak shear stress for each slip cycle. Green numbers indicate holding time.

[32] A representative slide-hold-slide experiment is also reported for dry conditions (Figure 10). Slip-velocity and normal stress were maintained constant at 1.31 m s^{-1} and 1 MPa, respectively. During this experiment, the torsion motor was gradually stopped (the deceleration occurs over about one meter of displacement) once an apparent steady state level of shear stress was reached. This corresponds to a hold. Hold times stand for few seconds and then, the motor was started again. Three strain-cycles are then defined. The simulated fault exhibits a slip-weakening behavior, with a higher slope for the first cycle. The shear stress evolves from a peak value of 0.67 to a steady state value of 0.44 MPa for the first strain-cycle, from 0.50 to 0.39 MPa for the second strain-cycle, and then from 0.47 to 0.37 MPa for the third strain-cycle.

3.2. Microstructures

3.2.1. Procedures and Methods for Image Analysis

[33] Experiments were stopped at different stages of slip-weakening behavior. Microstructures therefore correspond to finite strain. In order to observe intelligible microstructures, thin sections have been made at about 4 mm from the external cylindrical surface, perpendicular to the gouge layer and nearly parallel to the slip direction. A set of extra thin sections has been made through the axis-center of the assembly to complete observations.

[34] We analyzed shape-preferred orientations (SPO) of talc clasts ($\geq 20 \mu\text{m}$) using the PAROR method [Panozzo, 1983]. Remaining part of the images (talc clasts $\leq 20 \mu\text{m}$ for which a shape is hardly definable at the used magnification) is considered to be the matrix and cracks are avoided. Image analysis has been carried out with public domain MATLAB toolbox PolyLX [Lexa, 2003] (<http://petrol.natur.cuni.cz/~ondro/polylx:home>) and ImageSXM [Barrett, 2002]

(<http://www.liv.ac.uk/~sdb/ImageSXM>). We have divided the analyzed fault shear zones into three domains in order to observe spatial SPO variations. Boundary domains 1 and 3 were chosen arbitrarily at 18% of the gouge thickness and domain 2 comprises the remaining central 64%. The purpose of such distinctive analysis is to obtain SPO variations in the central part of the gouge, further away from any possible influence of the boundary domains. For comparison a bulk SPO is also calculated for every analyzed picture using clasts from all three domains (Figure 11). Clast-to-matrix ratio quantifies the amount of comminution and is calculated as the area fraction of talc clasts ($\geq 20 \mu\text{m}$) divided by the area fraction of clasts and matrix. It spans from 1 (analyzed area is formed entirely of talc clasts) to 0 (analyzed area is formed entirely of matrix; see Pec et al. [2012]).

3.2.2. Optical Microscope and SEM Observations

[35] Hereinafter, for the sake of clarity, we only report the results of 6 representative experiments conducted at 1 MPa normal stress. The progressive development of microstructures (i.e., fabrics, clast-to-matrix ratio, SPO and porosity) is then reported at 6, 12 and 34 m of displacement for wet conditions, and at 2, 16 and 42 m of displacement for dry conditions (i.e., at the early/late stage of the slip-weakening, and at the frictional steady state). At 34 and 42 m of displacement, the residual shear stress is achieved in both cases.

[36] Pre-run fault gouge exhibits a weak SPO synthetic with the induced sense of shear (Figures 11a and 11b). The clast-to-matrix ratio is ~ 0.25 and is constant through the whole gouge layer. *Estimated* gouge porosity (error of $\pm 2.5\%$) is about 20% for both wet and dry conditions.

[37] Irrespective of humidity conditions and displacement, a continuous and pervasive layer of platy grains with a strong SPO synthetic with the induced sense of shear can be observed lying immediately next to the gouge/cylinder interface. In wet conditions, this fabric consists of a complex array of variably anastomosing shear planes with a S-C or S-C-C' structure (scaly fabric; Figure 12c). In dry conditions, this fabric consists exclusively of planes parallel to the C- direction (Figure 12d). The pervasive layer is named Principal Slip Zone (or PSZ). Whatever humidity conditions, these grains show a pervasive interlayer delamination. The PSZ *estimated* porosity is 9% for wet conditions, and around 3% for dry conditions. Increasing displacement to about 15 m can lead locally to a small increase of the PSZ thickness up to $50 \mu\text{m}$ as an average, and exceptionally $150 \mu\text{m}$ as a maximum.

[38] In wet experiments, talc clasts develop a strong SPO parallel ($\pm 3.5^\circ$) to the C-shear direction already after 6 m of slip and retain this orientation with increasing displacement up to 34 m (Figures 11c, 11e and 11g). The strength of the SPO is independent on the amount of displacement. Some grains have a (001) preferred orientation parallel to an incipient S-foliation at 30° with respect to shear direction. The fine-grained matrix is mainly composed of thin platy grains. This matrix surrounds larger platy grains (Figure 12a). Some of these grains show significant interlayer delamination. Few platy subrounded grains can also be observed for all three steps (6, 12 and 34 m). The clast-to-matrix ratio remains unchanged (within the error of image analysis) compared to the starting material and is independent on the amount of displacement as well. *Estimated* gouge porosity in the central part at $\sim 2\text{--}15$ m of displacement remains around 10%, but

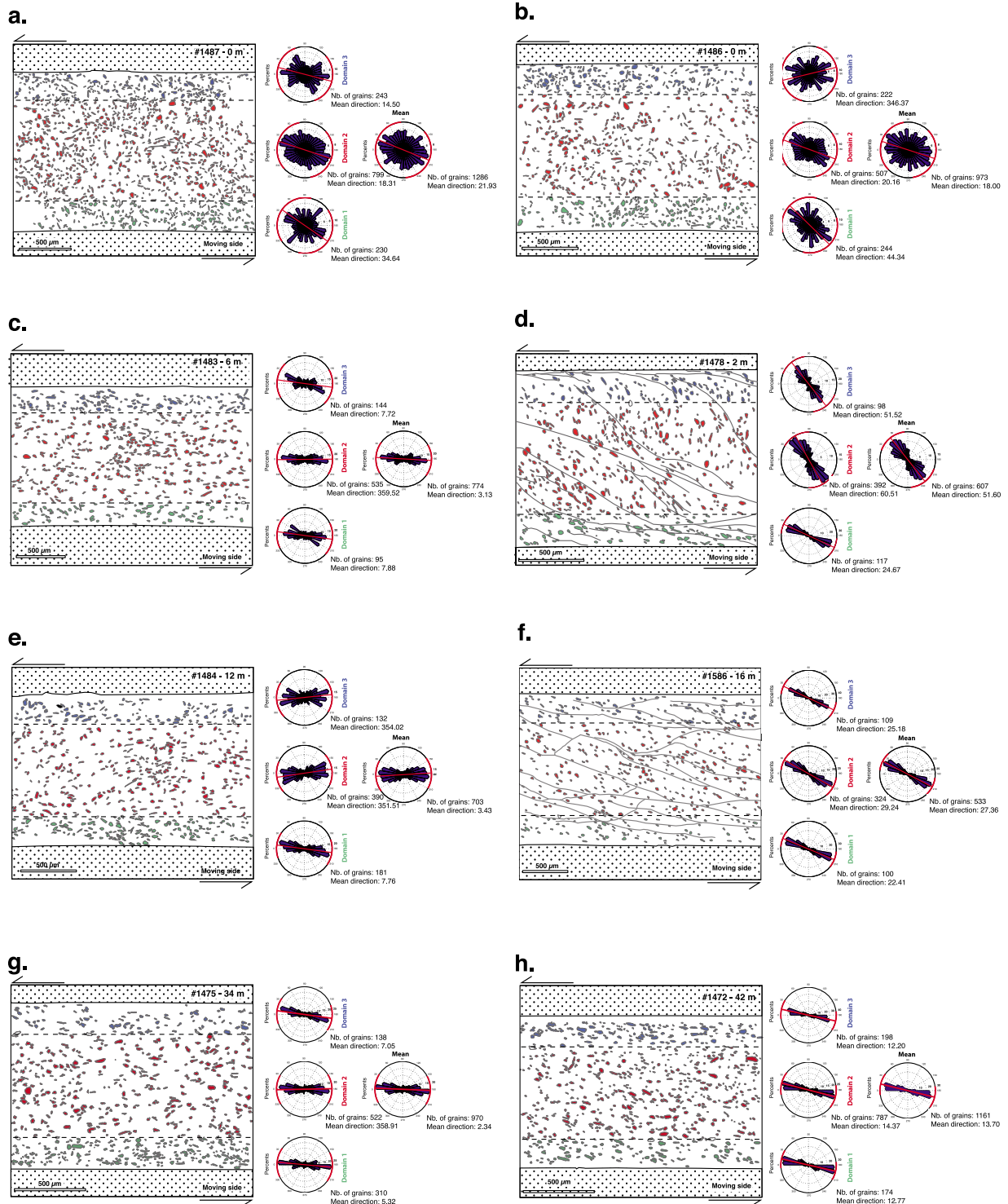


Figure 11. Two-dimensional analysis of talc grain shape preferred orientation based on post-run fault SEM images. Only talc grains with a long axis $\geq 20 \mu\text{m}$ are here considered. A rose diagram is used to represent the different orientation distribution in percent for three different gouge domains. Not all analyzed grains are shown. The color code corresponds to assigned domain. Left column – wet conditions, right column – dry conditions. (a) Initial state in wet conditions, (b) initial state in dry conditions, (c) at 6 m in wet conditions, (d) at 2 m in dry conditions, (e) at 12 m in wet conditions, (f) at 16 m in dry conditions, (g) at 34 m in wet conditions, and (h) at 42 m in dry conditions.

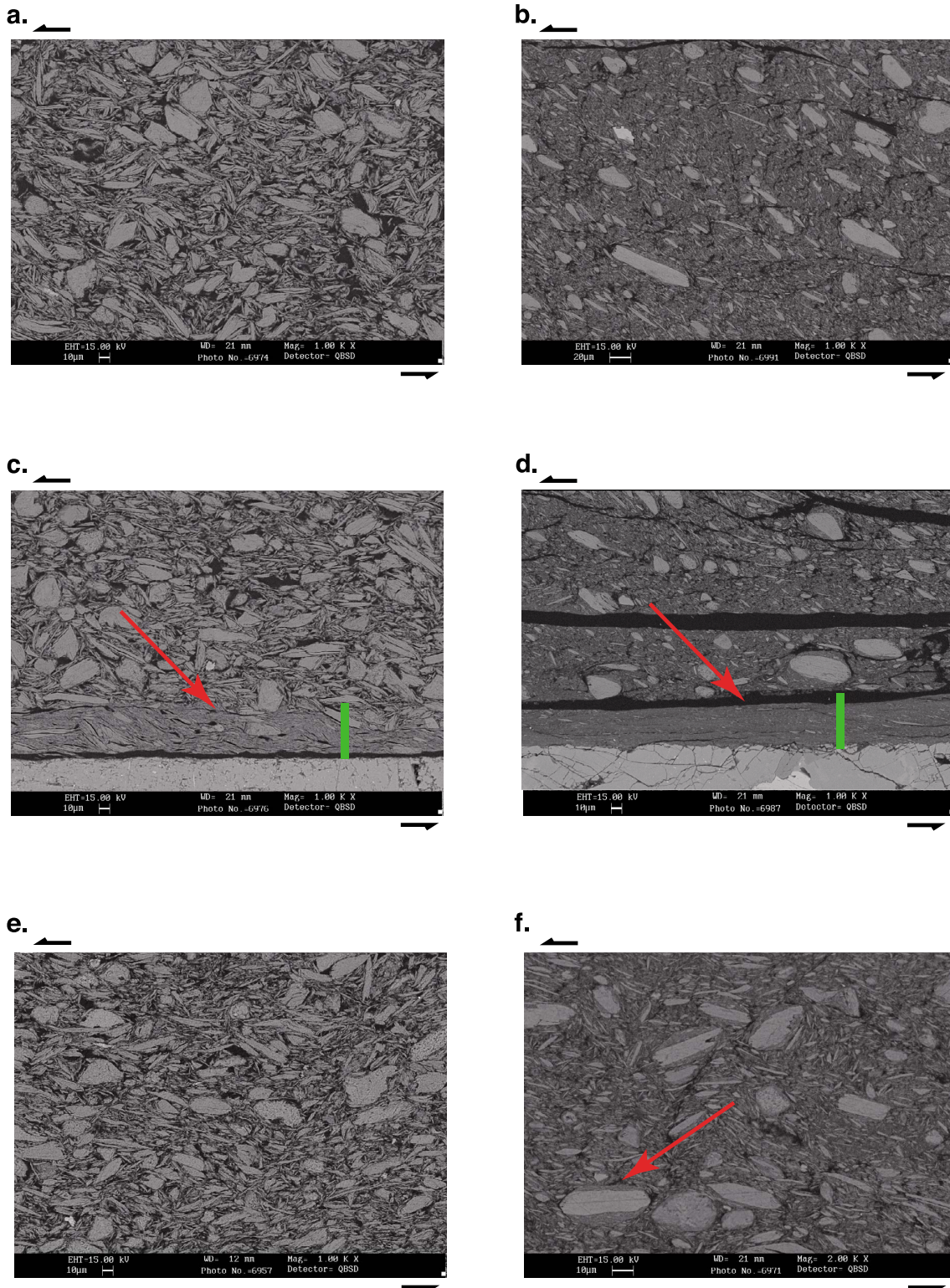


Figure 12. SEM photomicrographs (backscattered electron contrast at 15 kV) of post-run fault gouges for wet (left side) and dry (right side) conditions. Sense of shear is top to the left. (a, b) Central gouge for #1484 (12 m) and #1586 (16 m), respectively. (c, d) Principal Slip Zone indicated by a red arrow for the same samples #1484 and #1586, respectively. The green vertical segments locate position of PIPS sections done for TEM. (e, f) Central gouge for #1475 (34 m) and #1472 (42 m), respectively. A red arrow indicates a grain showing a cortex of irregular and non-concentric fine-grained aggregated material.

drops to ~5% after 34 m of displacement (Figure 12e). This is consistent with the 15% and 1% of *dynamic porosity* for ~2–~15 m and 34 m of displacement, respectively.

[39] Dry experiments show more complicated microstructures. After 2 m of displacement (Figure 11d), we observe the development of open S-oriented shear planes crosscutting the central gouge (i.e., remaining part of the gouge layer that is not the PSZ) with a mean orientation of 29° with respect to shear direction. In the central part of the gouge (domain 2) a stacking arrangement of sigmoidal mm-thick lenses (up to 3.65x0.50 mm) in a C-S structure is observed (Figure 11e). These lenses link the two gouge/cylinder interfaces, frequently branching off from a single C-oriented shear plane laying at around 180 μm from the rotating cylinder. After 16 m of displacement (Figure 11f), we observe S-, C- and rare C'-oriented shear planes crosscutting the fault shear zone. The SPO further strengthens and the mean orientation of clasts (27°) doesn't show significant variations between domains. The abundant very fine-grained matrix is mainly composed of thin platy grains. This matrix surrounds larger platy subangular to subrounded grains (Figure 12b). Some of these grains show a pervasive interlayer delamination. A striking characteristic of many of these clasts is that they are surrounded by a cortex (Figure 12f) made of nm- to μm-thick aggregated grains and show an irregular thickness ranging from 0.5 to 5 μm. This cortex does not show a concentric arrangement. The clast-to-matrix ratio further decreases from ~0.18 down to ~0.11. *Estimated* gouge porosity in the central part remains around 10%, which is lower than the 36% of *dynamic* porosity calculated at 16 m of displacement. Finally, at 42 m of displacement in dry gouge experiments, we observe a strong SPO in the central part of the fault gouge with most of grains that are at low angle to the (C-) shear direction (0° to 30°, 14° as a mean orientation, Figure 11h). Open C-S shear planes have disappeared. The abundant very fine-grained matrix is mainly composed of thin platy grains. This matrix surrounds larger platy subangular to subrounded grains. Some of these grains show significant interlayer delamination. Few platy subrounded grains can also be observed. Again, as for 16 m of displacement, many of these grains are surrounded by an irregular 0.5 to 5 μm-thick cortex of nm- to μm-thick aggregated grains without any concentric arrangement. The clast-to-matrix ratio does not change any further compared to 16 m of displacement. *Estimated* gouge porosity in the central part is around 4%, which is much lower than the 25% of *dynamic* porosity.

[40] Energy Dispersive X-ray Spectrometry (EDX-SEM) conducted on the grains of the central gouge and PSZ displays a high relative atomic density of O, Fe, Si and Mg elements. Additionally, detailed investigations by microscope, SEM and Raman spectroscopy do not clearly show any mineral reaction product such as enstatite or amorphous silica. This work suggests that post-run sheared gouge essentially consists of talc.

3.2.3. SEM and TEM Observations

[41] At 34 and 42 m of displacement, the residual shear stress is achieved for both wet and dry experiments (Figure 2). Detailed examination of post-experiment gouge layers by EDX-SEM element mapping does not display higher relative atomic density of any element. In the central part of the gouge, talc grains are slightly too highly

delaminated along the (001) cleavage planes. They show a preferred orientation with long axis parallel to the shear direction and sheet plane parallel to the shear plane irrespective of humidity conditions (see section 3.2.2). However, detailed investigation by TEM combined to SEM show contrasting fabrics for the wet and dry experiments (Figure 12).

[42] Under dry conditions, talc interlayer delamination produces down to 20 nm-thick and down to 100 nm-long well-crystallized sublamellae in the central gouge (Figure 13a). Aggregates ranging from 50 to 200 nm in diameter, similar to the Clast-Cortex Aggregates [e.g., *Smith et al.*, 2011], can be observed (Figure 13b). These nanometric aggregates are not constituted by a nucleus surrounded by a cortex, but are constituted by a concentric arrangement of talc sublamellae (Figure 13c). EDX-SEM analysis indicates that these aggregates have the same chemical composition as the talc. These nanometric aggregates are commonly found to be together with or flattened between two talc lamellae suggesting shearing, which gives them an apparent soft aspect (Figure 13d).

[43] A striking characteristic of the central gouge and the PSZ is the non-regularly spaced alternance of stacked talc lamellae and porous zones (Figures 13a and 14a). In the PSZ, the relative proportion of porous zones is higher. Associated talc lamellae tend to be thinner (i.e. <100 nm) than in the rest of the gouge. This is in accordance with the grain comminution observed at the thin section scale (see section 3.2.2). Detailed examination of the porous zones indicates that they are composed of aggregates ranging from 50 to 300 nm in diameter (Figure 14a). These nanometric aggregates are constituted by a nucleus surrounded by a concentric arrangement of tens of talc sublamellae. The nucleus consists of one to three 10 nm-diameter sub-aggregates. Lattice fringes (corresponding to the 9 Å-spaced (001) planes) give evidence of the crystallinity of the talc sublamellae forming the nanometric aggregates (Figure 14b). These nanometric aggregates are commonly found in porous zones. They exhibit a nearly perfect sphere-shape suggesting they were packed loosely enough and dispersed during experiment to avoid intense grain contact and consecutive comminution [e.g., *Boutareaud et al.*, 2008]. This gives them an apparent rigid aspect (Figure 14c). Kinking and bending of thinned talc lamellae can be locally observed (Figure 14d).

[44] For dry conditions, 16 m of displacement corresponds to the slip-weakening distance (Figure 2). TEM investigation shows the occurrence of the nanometric aggregates, suggesting their formation before the residual shear stress is reached (Figure 15a).

[45] Under wet conditions, no nanometric aggregate could be observed within the central gouge or the PSZ (Figures 12 and 15b). The PSZ shows a homogeneous fabric, with a large number of talc lamellae and sublamellae with long axis parallel to the shear direction.

4. Interpretations and Discussion

4.1. Microstructural Development

[46] The angular shape of grains, the general decrease of the grain size with increasing displacement, the localization of deformation within the PSZ, the applied high strain rates under low pressure and temperature conditions, and the significant drop in shear stress indicate a brittle mode of deformation at the microscopic scale, whatever initial humidity

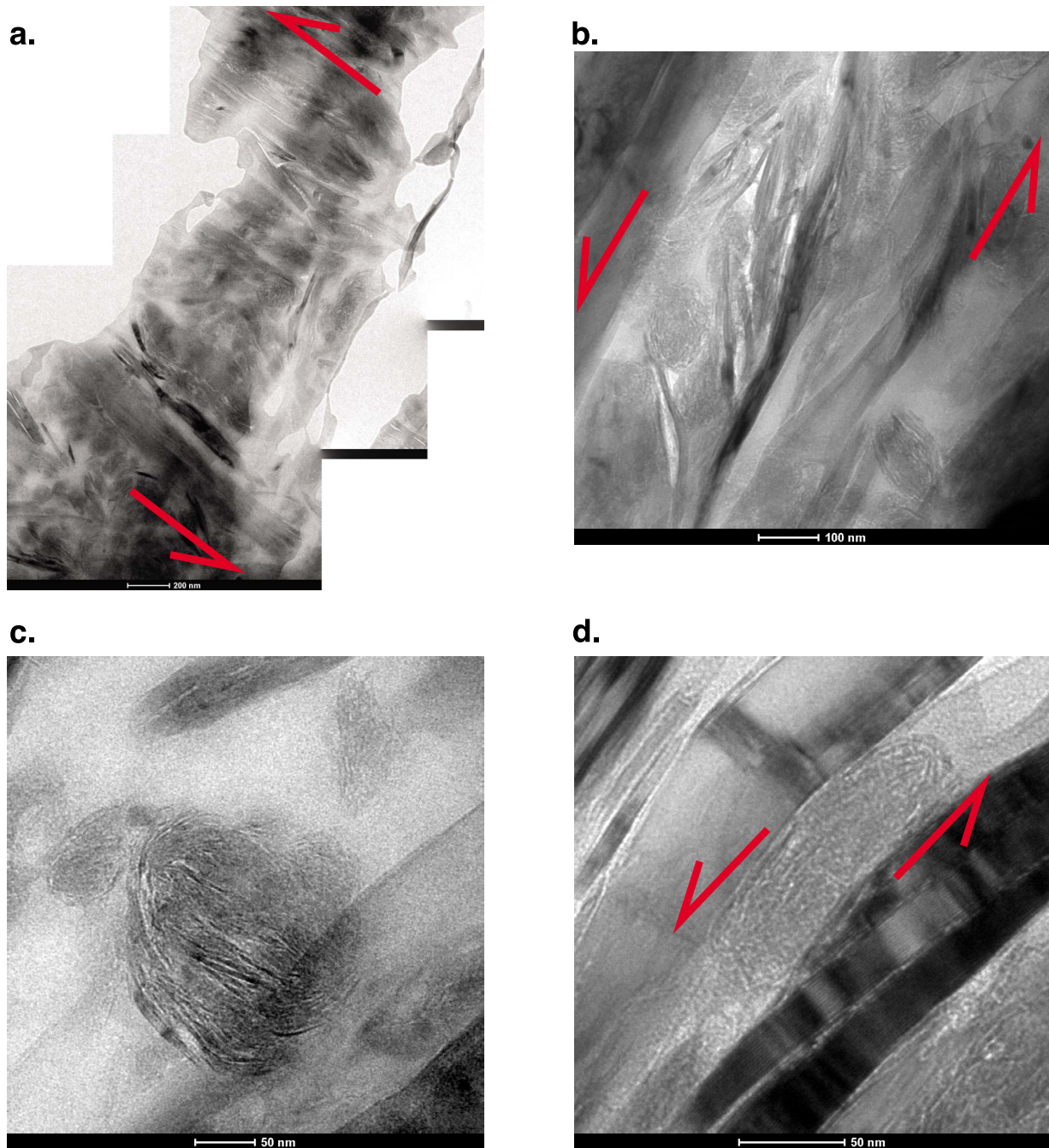


Figure 13. TEM photomicrographs from FIB sections of the central gouge for dry conditions (#1472). Sense of shear is indicated on Figures 13a, 13c, and 13d. (a) Talc lamellae and sublamellae oriented parallel to the sense of shear. (b) Higher magnification image of nanometric aggregates placed between talc lamellae and sublamellae. (c) Example of a nanometric aggregate without any nucleus. (d) Nanometric aggregate flattened between two talc lamellae.

conditions. However, at the thin section scale, the central gouge fabric shows a C-S structure, while the PSZ layer exhibits unrelated shear planes. This suggests distinct distributed deformations throughout these two units during our experiments, which is uncoupling between the central gouge and the PSZ.

[47] We attribute the difference between *estimated* and *dynamic* porosities to three issues. First, we do not take into account the open shear planes in our image analysis. Second, there is an important effect of sorting (smaller particles partially fill the gap between larger particles; e.g., Figures 12b). However, the large differences in the measured values (up to

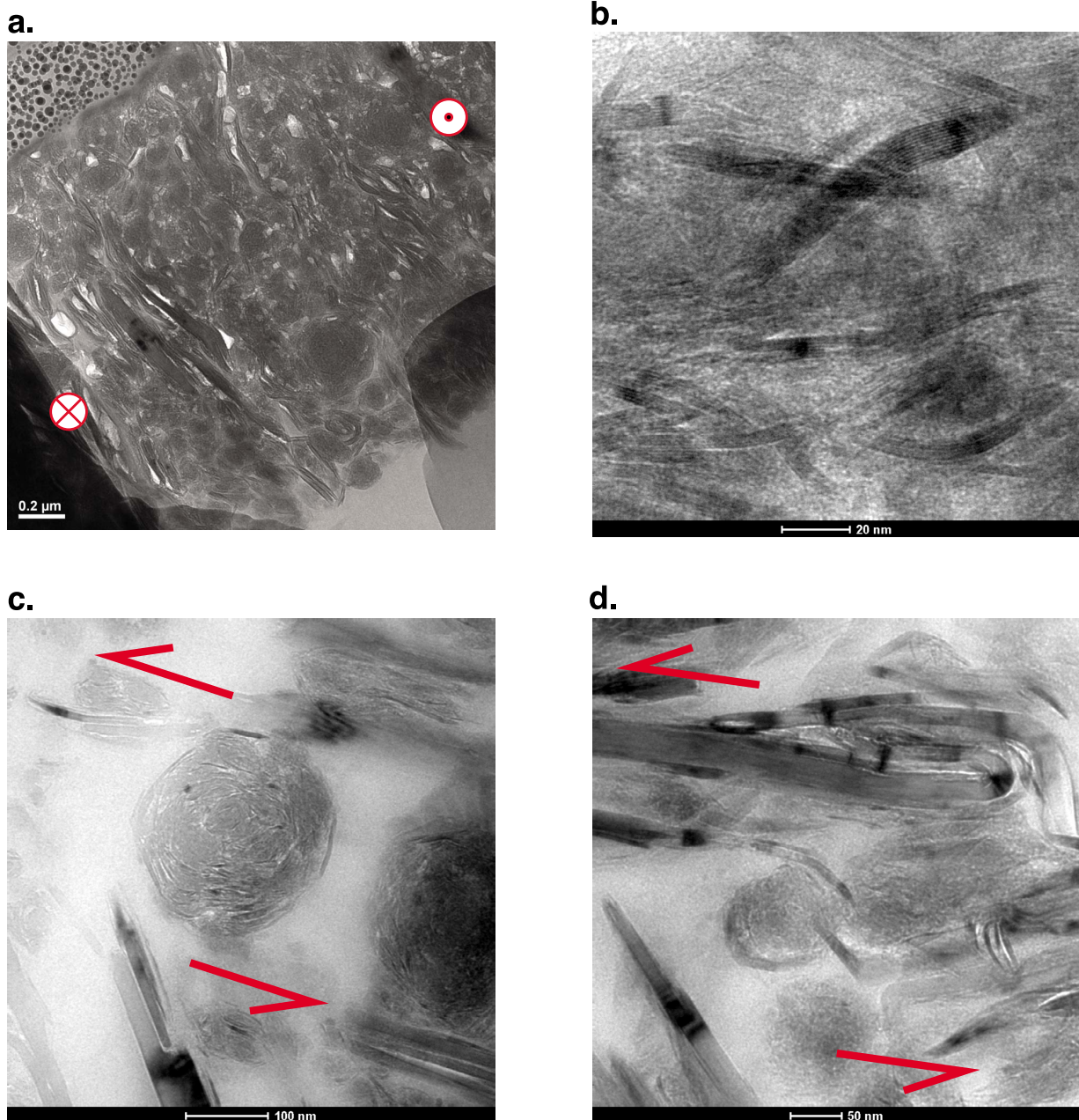


Figure 14. TEM bright field photomicrographs from FIB sections of the PSZ for dry conditions (#1472). Sense of shear is indicated on Figures 14a, 14c, and 14d. (a) Talc lamellae and sublamellae oriented parallel to the sense of shear, and nanometric aggregates. (b) Lattice fringes giving evidence of the crystallinity of the talc sublamellae forming the nanometric aggregates. (c) Example of a nanometric aggregate without nucleus. (d) Talc lamellae survivors are often bent or kinked with respect to the sense of shear.

25%) cannot be fully explained by these two issues. Rather, it seems that the *dynamic* calculated porosity is present during the experiment but collapses once the slip ceases.

[48] The SPO of grains parallel to the shearing direction observed at 6 m of displacement in wet conditions suggests a rapid reorientation of the platy grains in the first meters of displacement (Figure 11). The combination of two mechanisms can be here proposed: pure shear as first [Grunberger *et al.*, 1994; Djéran-Maigre *et al.*, 1998], and general non-

coaxial shear as second. The compaction observed at the beginning of all runs, the decrease by about 10% of the central gouge porosity, and the fault zone gouge fabric is consistent with such assumption.

[49] Since post-run grains are not rounded but platy with angular to subangular edges, rolling is inhibited during shearing in the central gouge whatever initial humidity conditions [Mair *et al.*, 2002]. Thus, accommodation of fault displacement is expected to be achieved by grain sliding

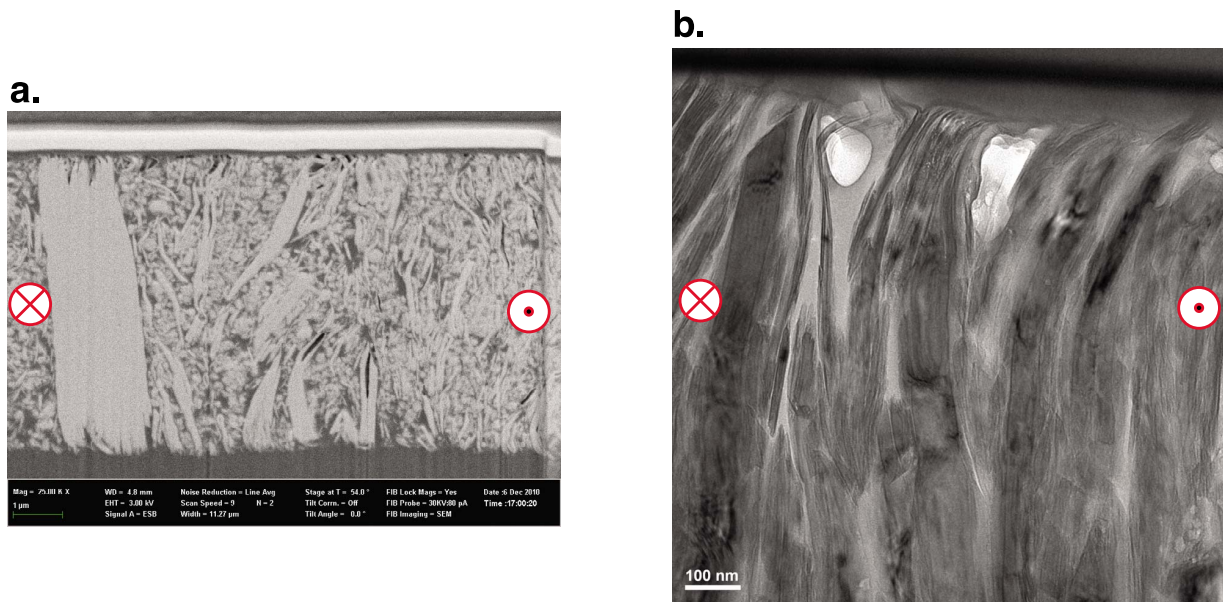


Figure 15. (a) SEM image (backscattered electron contrast at 3 kV) of a FIB-prepared cross section of the PSZ for dry conditions. Corresponding experiment (#1586) was stopped during the slip-weakening. A large number of nanometric aggregates can be observed within the PSZ. (b) TEM photomicrographs from FIB sections of the PSZ for wet conditions (#1472). No nanometric aggregate can be observed.

[Hazzard and Mair, 2003]. Microstructural observation indicates a strong interlayer delamination of talc as strain-induced defect. This suggests frictional sliding along the (001) cleavage planes [Escartin *et al.*, 2008; Viti and Colletini, 2009] as dominant deformation mechanism.

[50] In wet conditions, the absence of any C' -shear planes occurring in the central part of the fault gouge at any displacement, and the stable and high clast-to-matrix ratio (quantifying the amount of comminution) suggests that the amount of displacement accommodated by this part of the gouge is very small [Mair and Marone, 2000]. These observations indicate that the critical resolved shear stress needed to delaminate talc grains is rarely reached by grain sliding in the wet conditions. The absence of C' -shear planes and the lack of dilatancy could be explained by water capillary forces bridging the grain surfaces [Velev *et al.*, 1993; Coelho and Harnby, 1978; Mizoguchi *et al.*, 2006], resulting in the creation of strong adhesion forces to overcome gouge deformation.

[51] In dry conditions, some μm -thick subrounded grains show a cortex of irregular thickness made of very fine-grained aggregated material without any concentric arrangement as for Clast-Cortex Aggregates (see section 3.2.3). This suggests a structural immaturity of the aggregates. This immaturity is possibly related to the absence of rolling prevented from tightly packed grains.

[52] Deformation of the gouge in dry experiments appears to be more complex compared to wet experiments with the occurrence of stacked millimetric sigmoidal lenses bounded by open shear planes. These lenses show a surprisingly high C - S angle ($>45^\circ$) of the internal fabric at 2 m of displacement, and this angle decreases with increasing displacement. This first characteristic indicates an antithetic rotation of the talc grains from an initial state similar to the wet case

observed at 6 m of displacement (Figure 11d). Second, it indicates (more or less) intact lenses with an internal stress-insensitive fabric, suggesting the weakness of internal chain forces [Daniels and Hayman, 2008] and strain localization on the S -oriented shear planes delimiting individual lenses. These stacked lenses that frequently branch off from a single C -oriented shear plane clearly suggest a duplex system. Thus, similarly to natural fault gouges, the deformation spans the gouge system at the early stages of the fault displacement [Hayman *et al.*, 2004; Hayman, 2006]. The observed decrease of C - S angle of the internal fabric and increase in dilatancy, developing porosity along the open shear planes up to the residual shear stress at D_c , could be the result of accommodation of the geometric incompatibility of the stacked lenses, one lens sliding over the other. The decreasing clast-to-matrix ratio with the increasing displacement suggests that slip between individual grains is not as effective as in wet conditions, and that delamination of the talc grains occurs. As a result, the central part of the fault gouge accommodates a larger amount of displacement in dry conditions, compared to wet conditions. Initiation of lens formation might be controlled by some pre-existing gouge heterogeneities. But we do not have yet a complete understanding of this phenomenon.

[53] The μm -thick strongly foliated layers present at and parallel to the gouge-cylinder boundaries, whatever initial humidity conditions, indicate intense localized shearing in comparison to the central part of the gouge. This implies strain partitioning during fault displacement. This type of microstructure has already been reported in natural and experimental cases [Yund *et al.*, 1990; Chester and Chester, 1998; Chambon *et al.*, 2006; Rockwell and Ben-Zion, 2007; Boutareaud *et al.*, 2008; Mizoguchi *et al.*, 2009b; Stünitz *et al.*, 2010; Kitajima *et al.*, 2010] and was defined as the

Principal Slip Zone (PSZ) [Sibson, 2003], that controls earthquake instability [Marone, 1995; Chester and Chester, 1998; Sibson, 2003; Rice, 2006; Boutareaud et al., 2008]. It is recognized to accommodate most of the displacement, and so should provide a path by which fault strength should weaken during shearing. The similarities in fabric of PSZ between wet and dry conditions and associated talc grain delamination suggests frictional sliding along the (001) planes [Escartin et al., 2008; Viti and Collettini, 2009]. On the contrary, the differences in fabric (C-S structure for wet conditions and C- structure for dry conditions), suggest that a smaller amount of displacement is accommodated in wet conditions [e.g., Trouw et al., 2010]. The PSZ thickness is in the range of calculated predictions for earthquake slipping zone width [Rice, 2006], and represents the source of the measured frictional heating [Boutareaud et al., 2010; Kitajima et al., 2010] reported here by T_c and T_p . The absence of any recognized phase transition product (i.e., enstatite) suggests that the temperature of PSZs was lower than 1300°C during experiments, or even lower than 860°C by comparison to previous dynamic data [Escartin et al., 2008].

[54] Both wet and dry experiments show a slip-weakening behavior, but with a higher decreasing rate in wet conditions. Considering statements in the paragraph above, this indicates that water and related microstructure development should strongly affect strain accommodation in talc gouge at seismic slip-velocities.

[55] The relative slippage of the mm-long sigmoidal lenses in duplex structure is sufficient to explain the large dilatancy of the fault zone (up to 0.34 mm for the 1.3 mm-thick faults), and as direct consequence to explain the higher frictional strength for dry conditions during the slip-weakening [e.g., Marone et al., 1990]. The maximum gouge layer dilation is proportional to the applied normal stress (Figure 9).

4.2. Identification of Slip-Weakening Mechanisms

[56] To date, several weakening mechanisms relevant for this type of friction experiment have been reported in the literature. This includes frictional melting [Sibson, 1980; Hirose and Shimamoto, 2005; Di Toro et al., 2006; Nielsen et al., 2008], silica gel production [Goldsby and Tullis, 2002; Di Toro et al., 2004], thermal pressurization of the fluid [Sibson, 1973; Rice, 2006; Boutareaud et al., 2008], fluid pressurization induced by thermal decomposition of the gouge material [Sulem and Famin, 2009; Brantut et al., 2011], flash heating [Rice, 2006; Beeler et al., 2008; Goldsby and Tullis, 2011], or powder lubrication [Han et al., 2010, 2011; Reches and Lockner, 2010; De Paola et al., 2011; Tisato et al., 2012]. No evidence of amorphous material, silica gel, talc decomposition product (enstatite) has been observed in our post-run gouge products from petrographic microscope, SEM, TEM, cathodoluminescence, Raman spectroscopy or XRD observations. Therefore, neither frictional melting, flash heating, silica gel production, nor fluid pressurization induced by thermal decomposition of the gouge material appear to be the cause of the observed slip-weakening behavior, whatever humidity conditions. Thermal pressurization of the fluid, flash heating and powder lubrication remain as possible candidates as discussed below.

[57] The slip-weakening distance (D_c) of talc friction experiments decreases according to a power law for increasing normal stress (Figure 6). The slip-weakening behavior for talc is consistent with recent reported experiments conducted at coseismic slip-velocities from low (<25 MPa) to high (>25 MPa) normal stresses, regardless of fault rock type and related weakening mechanisms [Mizoguchi et al., 2007a; Brantut et al., 2008; Han et al., 2010; De Paola et al., 2011; Niemeijer et al., 2011; Oohashi et al., 2011]. The power law coefficients seem to be closely associated to the fault rock type [Di Toro et al., 2011] and the activation of slip-weakening mechanisms [e.g., Nielsen et al., 2008]. In our talc experiments, the power law dependence is established for the dry conditions at best ($R^2 = 0.87$), whereas no reasonable fit can be obtained for wet conditions suggesting the absence of significant thermally activated mechanisms in wet conditions.

[58] If any slip-weakening mechanism related to any efficient thermal-activation occurs during our experiments, D_c should scale with the fault power density (i.e., the energy exchanged on the PSZs per unit time and unit area equals to $1/(\tau \cdot V)^2$). So D_c should scale with $1/(\tau \cdot V)^2$ or $1/(\sigma^2 \cdot V)$ [e.g., Del Gaudio et al., 2009]. Figure 8 supports such assumption for dry conditions only.

4.3. Proposed Slip-Weakening Mechanisms

[59] The gouge material we sheared in our experiments is not a rock composed of a solid framework with pores fill with water. The gouge material is a non-cohesive mixture of micrometric talc grains and water: it is a mud-like material. This continuum medium can be considered to be isotropic just before we start the experiment: the applied 1 MPa normal stress is supported by all the components of the medium (i.e., fluid and grains). So at first approximation, in the absence of leak, a ‘fluid’ pressure of 1 MPa can be considered when applying 1 MPa normal stress [see Boutareaud et al., 2008]. According to the water phase diagram [Wagner and Pruss, 2002], the water liquid-to-vapor phase transition occurs at 180°C at a fluid pressure of 1 MPa. In Figure 4, our calculation shows that, in wet conditions, T_p reaches this transition temperature only after 3.84 s, i.e., after 5.03 m of displacement, which is posterior to D_c (see Table 1). In dry conditions, this temperature is reached by T_p after 0.31 s, i.e., after 0.40 m of displacement, which is anterior to D_c .

[60] Table 1 shows that D_c values of wet condition experiments are extremely short. For instance, on #1475 D_c is reached after only 3.72 m of displacement, which corresponds to 160°C for T_p and 37°C for T_c (Figure 4). This indicates a too low temperature along the fault plane to raise thermal pressurization by gouge water phase change from liquid to vapor during the slip-weakening [Boutareaud et al., 2008; Sulem and Famin, 2009]. The absence of *i*) high-amplitude peak events in fault thickness (i.e., pulse-like events in fault axial displacement [e.g., Mizoguchi et al., 2007b; Boutareaud et al., 2008]), *ii*) water vapor driven off from the simulated fault for displacements invariably smaller than D_c (Figure 2), concomitant with *iii*) the presence of immature Clast-Cortex Aggregates (see section 3.2.3) is consistent with such assumption.

[61] Estimated porosity of post-run central gouge is high (~10%) as well as the dynamic porosity (~15%), and a permeability value higher than 10^{-20} m^2 can be reasonably

expected considering that the initial gouge did not experience pressures higher than 30 MPa [Behnen and Faulkner, 2011]. This suggests that the hydraulic diffusivity along the fault plane may be sufficient to raise thermal pressurization by thermal expansion of the gouge water during shearing [e.g., Sibson, 1973; Wibberley and Shimamoto, 2005; Mizoguchi et al., 2009b]. Considering that the amount of displacement accommodated by the central part of the gouge and the PSZ is very small (see section 4.1), and the preservation of original large talc grains (see section 3.2.2), we propose thermal pressurization by thermal expansion of a water film in the early centimeters of displacement. This thin film of fluid should be trapped in-between two platy sub-parallel surfaces [e.g., Morrow et al., 2000; Moore and Lockner, 2004; Ferri et al., 2010]. Only the contact surface between the PSZ and the rotating cylinder satisfies the required condition for large displacement accommodation (see Figure 12c). However, regarding the hydrophobic character of talc, we suspect the existence of additional trapped water layers within the central gouge and the PSZ. Ensuing slip shows an increase of T_p at 5.03 m of displacement inducing a phase transition of water (180°C at 1 MPa fluid pressure) as indicated by an increase in measured humidity H (Figure 2e). We infer that the film of fluid is not anymore ubiquitous along the whole fault contact surface at these temperatures [e.g., Moore et al., 1997], and we postulate solid lubrication [e.g., Scholz, 2006] to be the source of heating once the slip achieves the steady state at D_c . So we propose thermal pressurization by thermal expansion of a water film as a possible candidate for slip-weakening in wet conditions.

[62] The exponential decrease of the dynamic shear stress with increasing displacement (Figure 2) appears to be directly related to the progressive reorientation of grains parallel to the sense of shear and disappearance of the mm-long sigmoidal lenses toward the steady state stage at D_c (Figure 11). This indicates a progressive breakdown of the network chain forces through the whole gouge, involving localization of slip along the PSZ. To account for the progressive grain comminution shown by the decrease in clast-to-matrix ratio through central part of the gouge up to D_c (Figure 11, see section 3.2.2), the related temperature increase (Figure 4) and the long-lasting decay in fault strength (Figure 2), we propose a peculiar mechanism named solid lubrication [e.g., Scholz, 2006]. This mechanism consists in frictional sliding between the favorably C-oriented (001) planes of talc lamellae [Escartin et al., 2008; Viti and Collettini, 2009] of the central part of the gouge and the PSZ. This mechanism is enhanced by thermal delamination resulting from exponential frictional heating rate (Figure 4), as suggested by opening of the cleavage of talc grains observed after long-duration cathodoluminescence examinations, probably caused by thermal expansion along the talc crystallographic c axis [Pawley et al., 1995]. The observed nanometric aggregates represent an additional possibility to lubricate the simulated faults during the experiments by rolling and shearing (see section 3.2.2). The mode of formation of the nanometric aggregates is not totally understood. However, development of the nanometric aggregates (and consecutively the importance of the slip-weakening) is likely to be dependent on the talc sublamellae production by temperature rise as slip increases.

[63] The existence of two types of nanometric aggregates, within the central gouge and the PSZ suggests the existence of at most an additional weakening mechanism (see section 3.2.2). The apparent soft aspect of the nanometric aggregates within the central gouge suggests rolling and shearing (Figures 13c and 13d). On the contrary, the apparent rigid aspect of the nanometric aggregates within the PSZ (Figure 14c) suggests rolling [e.g., Worniyoh et al., 2007]. These two types of nanometric aggregates may have the capacity to accommodate relative motion between talc lamellae and sublamellae during shearing at the micro-scale, and so to reduce wear production and consecutive friction at the macro-scale. We use the term powder lubrication to account for the nano-scale lubrication.

4.4. Relevance of the Experiments

[64] Peak shear stress values and the slip-weakening behavior that we obtained on talc powder are consistent with similar data previously reported by several authors at co-seismic slip-rates and low normal stresses for cohesive and non-cohesive rocks [Hirose and Shimamoto, 2005; Di Toro et al., 2006; Mizoguchi et al., 2006; Hirose and Bystricky, 2007; Boutareaud et al., 2008; Han et al., 2007, 2010; Sone and Shimamoto, 2009; Mizoguchi et al., 2009b; Kitajima et al., 2010; Han et al., 2011; De Paola et al., 2011], irrespective of the crustal rock type and related physico-chemical processes. Additionally, differences or similarities in mechanical behavior between clay-rich simulated faults appear to be related to the prevalence of one mechanism over the others. Reported prevailing weakening mechanisms occurring within the slip zone and consistent with our experiments are thermal pressurization and nanopowder lubrication [e.g., Mizoguchi et al., 2007a; Brantut et al., 2008; Faulkner et al., 2011; Reches and Lockner, 2010; Han et al., 2010, 2011; Kohli et al., 2011; Di Toro et al., 2011].

[65] The peak shear stress observed at the onset of shearing during our experiments represents the failure of the gouge strength just before shear localization [e.g., Paterson and Wong, 2004; Mair and Hazzard, 2007; Mair and Abe, 2008]. We attribute the high values of peak shear stress to the absence of a well-developed preferred orientation of talc grains which would allow easy slip along the (001) cleavage plane and the absence of nanometric aggregates at this stage (see section 3.2.2). Teflon friction probably participates to this peak friction value [Sawai et al., 2012]. The lower peak shear stress value in wet conditions is attributed to the presence of a water film trapped along the fault contact surface in-between the PSZ and the rotating cylinder. A representative slide-hold-slide experiment is reported in Figure 10. The aim of this test is not to investigate the occurrence of any healing mechanism since it has been recently shown that phyllosilicates do not re-strengthen during hold periods [e.g., Carpenter et al., 2011]. This test is conducted to test the effect of preexisting gouge microstructures on subsequent slip. This experiment shows a decrease of the peak shear stress when slip is resumed. The peak shear stress value of the third strain-cycle is similar to the peak shear stress value of the second strain-cycle. This experiment suggests first that the gouge fabric development plays a major role on the observed slip-weakening during the first strain-cycle. Second, it indicates that the lower friction

of subsequent slips is related to pre-existing microstructures inherited from the first strain-cycle. These results are consistent with the work of *Collettini et al.* [2009]. These authors reported friction experiments conducted on phyllosilicate-rich gouge samples. They showed that the friction coefficient of a simulated fault with a well-developed foliation is remarkably lower than its powdered equivalent. These results are also coherent with the work of *Mair et al.* [2002]. These authors showed that gouge grain shape characteristics have the capacity to control fault frictional behavior by reducing macroscopic friction in the case of spherical grains in granular material under shear. At least, these results are in agreement with experimental results done on phyllosilicate-bearing simulated faults [e.g., *Bos and Spiers*, 2000; *Numelin et al.*, 2007; *Mizoguchi et al.*, 2009b] reporting a positive correlation between fabric development, shear localization and strain weakening.

[66] Depending on the prevailing fluid flow properties and permeability structure of the fault zone [e.g., *Wibberley et al.*, 2008; *Mitchell and Faulkner*, 2008], mechanical and chemical healing processes occur during the interseismic period [*Sibson*, 1989; *Bos and Spiers*, 2000, 2002; *Nakatani and Scholz*, 2004; *Gratier and Gueydan*, 2007; *Keulen et al.*, 2008]. These processes may have the capacity to wipe out pre-existing fabric of clay-rich fault gouge [*Rutter et al.*, 1986]. So that the gouge starts with a randomized fabric each time a faulting event occurs and localizes along the same gouge zone [e.g., *Boutareaud et al.*, 2010]. Therefore, the degree of preferred orientation of phyllosilicates within the slip zone and the presence of nanometric spherical aggregates represent two important factors that may control the fault mechanical properties during earthquakes.

[67] The strong initial strengthening we observe in our experiments at the first strain-cycle suggests that the absence of nanometric aggregates or pre-existing well-oriented phyllosilicates within the slip zone may determine the occurrence of a frictional barrier for rupture growth into large earthquakes. This strengthening may prevent temperature rise of the gouge during acceleration stage of earthquake faulting, and consecutively the development of thermally activated slip-weakening mechanisms [*Rice*, 2006; *Brantut et al.*, 2010; *Di Toro et al.*, 2011]. This work suggests that the presence of nanometric aggregates or pre-existing well-oriented phyllosilicates within the slip zone should be seriously considered on future theoretical studies of faulting.

5. Summary and Conclusions

[68] We report mechanical data and related microstructures from high-velocity friction experiments conducted on a natural pure talc gouge as simple analogue of the phyllosilicates that compose the gouge of some mature crustal faults. However, talc exhibits a more complex mechanical behavior and microstructural development than expected.

[69] Post-run thin sections show a pervasive 30 μm -thick layer of small talc grains with a shape preferred orientation (SPO) parallel to the fault boundary, irrespective of initial humidity conditions and total displacements. This layer named Principal Slip Zone (PSZ) results from strain localization. It accommodates most of the fault displacement and

produces the heat. In wet conditions, fault gouge fabric exhibits a S-C structure evolving to a C- geometry at higher displacements. Dry experiments appear to be more elaborated with the occurrence of stacked millimetric sigmoidal lenses bounded by μm -thick open shear planes. These lenses progressively disappear with increasing fault displacement, leading to a C- structure in the fault central gouge. Deformation that initially spans the fault system is then progressively fully localized along the PSZ.

[70] All our experiments show a slip-weakening behavior. We propose that the abrupt slip-weakening observed in wet conditions is related to thermal-pressurization by thermal expansion of a water film trapped between talc grains. On the contrary, in dry conditions, the long-lasting weakening is interpreted to be due to the progressive disappearance of geometrically unfavorably oriented large lenses, competing with solid lubrication of favorably C-reoriented talc lamellae combined with nanopowder lubrication within the PSZ and the central gouge. Few studies based on natural and simulated faults report solid lubrication and nanopowder lubrication as possible weakening mechanisms. This feature is probably related to the superimposition of additional mechanisms occurring within the phyllosilicate-rich fault slip zone during the weakening. This suggests that more attention should be paid on gouge microstructures at the nanometric scale for future studies in order to discriminate the weakening mechanisms.

[71] During a co-seismic slip, the first meters of slip-rate increase are critical to overpass the strength barrier to develop the appropriate slip-weakening mechanism(s). Our friction experiments suggest that inherited gouge fabric from past fault sliding has the capacity to play a major role on the slip-weakening for subsequent slip.

[72] **Acknowledgments.** We express our sincere thanks to Emily Brodsky and Amy Kornberg for helping us getting the talc samples from VWR Company. This work would not have been possible without the high-quality thin sections made by Christophe Nevado (Geosciences Montpellier) and by Frowin Pirovino (ETH, Zürich). A.M.B. and S.B. are grateful to Olivier Romeyer (Plateforme d'Analyse Structurale, Université de Savoie) for his technical assistance using SEM. S.B. thanks Karsten Kunze (EMEZ, ETH Zurich) for his support with FIB, providing outstanding sections for TEM observations. M.A. and S.B. want to thank Martiane Cabié and Michael Jublot for their technical assistance during TEM observation at the CP2M in Marseille. We thank also Christian Mensing (ETH Zurich) for TG/DTA measurements. The first author gratefully acknowledges Georg Dresen, Neil Mancktelow, Laurent Louis, Andre Niemeijer, and Chris Spiers for their fruitful discussions on the background of these studies. M.P. wishes to thank Rüdiger Kilian and Renée Heilbronner for stimulating discussion. S.B. thanks Stephen Miller for his helpful comments on earlier drafts of the manuscript. Careful and constructive reviews by Dan Faulkner and Cristiano Collettini helped to improve and strengthen the manuscript. This research was partially funded by an INSU grant (BG/LG/2010-15; Alea, Risques et Catastrophes Telluriques) and by ANR (Programme Catastrophes Telluriques et Tsunamis, ACTS Taiwan, ANR-06-CATT-001-01).

References

- Barrett, S. D. (2002), Software for scanning microscopy, *Proc. R. Microsc. Soc.*, *37*, 167–174.
- Beeler, N. M., T. E. Tullis, and D. L. Goldsby (2008), Constitutive relationships and physical basis of fault strength due to flash heating, *J. Geophys. Res.*, *113*, B01401, doi:10.1029/2007JB004988.
- Behnsen, J., and D. R. Faulkner (2011), Water and argon permeability of phyllosilicate powders under medium to high pressure, *J. Geophys. Res.*, *116*, B12203, doi:10.1029/2011JB008600.
- Bizzarri, A. (2009), What does control earthquake rupture and dynamics faulting? A review of different competing mechanisms, *Pure Appl. Geophys.*, *166*, 741–776, doi:10.1007/s00024-009-0494-1.

- Bos, B., and T. Spiers (2000), Effect of phyllosilicates on fluid-assisted healing of gouge-bearing faults, *Earth Planet. Sci. Lett.*, *184*, 199–210, doi:10.1016/S0012-821X(00)00304-6.
- Bos, B., and C. J. Spiers (2002), Fluid-assisted healing processes in gouge bearing faults: Insights from experiments on a rock analogue system, *Pure Appl. Geophys.*, *159*, 2537–2566, doi:10.1007/s00024-002-8747-2.
- Bouchon, M. (1997), The state of stress on some faults of the San Andreas system as inferred from near-field strong motion data, *J. Geophys. Res.*, *102*, 11,731–11,744, doi:10.1029/97JB00623.
- Boutareaud, S. (2007), Slip-weakening mechanisms at high slip-velocities: Insights from analogue and numerical modellings, Ph.D. thesis, Univ. de Franche-Comté, Besançon, France.
- Boutareaud, S., D. G. Calugaru, R. Han, O. Fabbri, K. Mizoguchi, A. Tsutsumi, and T. Shimamoto (2008), Clay-clast aggregates: A new textural evidence for seismic fault sliding?, *Geophys. Res. Lett.*, *35*, L05302, doi:10.1029/2007GL032554.
- Boutareaud, S., T. Hirose, M. L. Doan, M. Andréani, and D. G. Calugaru (2009), Frictional behavior of talc at seismic slip rates: Preliminary results from high-velocity experiments, *Geophys. Res. Abstr.*, *11*, EGU2009-1948.
- Boutareaud, S., A. M. Boullier, M. Andreani, D. G. Calugaru, P. Beck, S. R. Song, and T. Shimamoto (2010), Clay-clast aggregates, a new textural evidence for seismic faulting, *J. Geophys. Res.*, *115*, B02408, doi:10.1029/2008JB006254.
- Brantut, N., A. Schubnel, J. N. Rouzaud, F. Brunet, and T. Shimamoto (2008), High-velocity frictional properties of a clay-bearing fault gouge and implications for earthquake mechanics, *J. Geophys. Res.*, *113*, B10401, doi:10.1029/2007JB005551.
- Brantut, N., A. Schubnel, J. Corvisier, and J. Sarout (2010), Thermochemical pressurization of faults during coseismic slip, *J. Geophys. Res.*, *115*, B05314, doi:10.1029/2009JB006533.
- Brantut, N., R. Han, T. Shimamoto, N. Findling, and A. Schubnel (2011), Fast slip with inhibited temperature rise due to mineral dehydration: Evidence from experiments on Gypsum, *Geology*, *39*, 59–62, doi:10.1130/G311424.1.
- Calugaru, D. G., J. M. Crolet, A. Chambaudet, C. I. Calugaru, and F. Jacob (2003), Inverse problems for flow and transport in the framework of seismic research, *Cah. Phys.*, *XIV*, 9–24.
- Carpenter, B. M., C. Marone, and D. M. Saffer (2011), Weakness of the San Andreas Fault revealed by samples from the active fault zone, *Nat. Geosci.*, *4*, 251–254, doi:10.1038/ngeo1089.
- Chambon, G., J. Schmittbuhl, and A. Corfdir (2006), Frictional response of a thick gouge sample: 1. Mechanical measurements and microstructures, *J. Geophys. Res.*, *111*, B09308, doi:10.1029/2003JB002731.
- Chester, F. M., and J. S. Chester (1998), Ultracataclastic structure and friction processes of the Punchbowl fault, San Andreas system, California, *Tectonophysics*, *295*, 199–221, doi:10.1016/S0040-1951(98)00121-8.
- Coelho, M. C., and N. Harnby (1978), Moisture bonding in powders, *Powder Technol.*, *20*, 201–205, doi:10.1016/0032-5910(78)80049-7.
- Collettini, C., A. Niemeijer, C. Viti, and C. Marone (2009), Fault zone fabric and fault weakness, *Nature*, *462*, 907–910, doi:10.1038/nature08585.
- Daniels, K. E., and N. W. Hayman (2008), Force chains in seismogenic faults visualized with photoelastic granular shear experiments, *J. Geophys. Res.*, *113*, B11411, doi:10.1029/2008JB005781.
- Del Gaudio, P., G. Di Toro, R. Han, T. Hirose, S. Nielsen, T. Shimamoto, and A. Cavallo (2009), Frictional melting of peridotite and seismic slip, *J. Geophys. Res.*, *114*, B06306, doi:10.1029/2008JB005990.
- De Paola, N., T. Hirose, T. Mitchell, G. Di Toro, C. Viti, and T. Shimamoto (2011), Fault lubrication and earthquake propagation in thermally unstable rocks, *Geology*, *39*, 35–38, doi:10.1130/G31398.1.
- Di Toro, G., D. L. Goldsby, and T. E. Tullis (2004), Friction falls towards zero in quartz rock as slip velocity approaches seismic rates, *Nature*, *427*, 436–439, doi:10.1038/nature02249.
- Di Toro, G., T. Hirose, S. Nielsen, G. Pennacchioni, and T. Shimamoto (2006), Natural and experimental evidence of melt lubrication of faults during earthquakes, *Science*, *311*, 647–649, doi:10.1126/science.1121012.
- Di Toro, G., R. Han, T. Hirose, N. De Paola, S. Nielsen, K. Mizoguchi, F. Ferri, M. Cocco, and T. Shimamoto (2011), Fault lubrication during earthquakes, *Nature*, *471*, 494–498, doi:10.1038/nature09838.
- Di Toro, G., S. Mittempergher, F. Ferri, T. M. Mitchell, and G. Pennacchioni (2012), The contribution of structural geology, experimental rock deformation and numerical modeling to an improved understanding of the seismic cycle. Preface to the Special Volume “Physico-chemical processes in seismic faults”, *J. Struct. Geol.*, *38*, 3–10, doi:10.1016/j.jsg.2012.01.025.
- Djéran-Maigre, I., D. Tessier, D. Grunberger, B. Velde, and G. Vasseur (1998), Evolution of microstructures and of macroscopic properties of some clays during experimental compaction, *Mar. Pet. Geol.*, *15*, 109–128, doi:10.1016/S0264-8172(97)00062-7.
- Escartín, J., M. Andreani, G. Hirth, and B. Evans (2008), Relationship between the microstructural evolution and rheology of talc at elevated pressure and temperature, *Earth Planet. Sci. Lett.*, *268*, 463–475, doi:10.1016/j.epsl.2008.02.004.
- Evans, B. W., and S. Guggenheim (1988), Talc, pyrophyllite and related minerals, *Rev. Mineral.*, *19*, 225–294.
- Faulkner, D. R., T. M. Mitchell, J. Behn, T. Hirose, and T. Shimamoto (2011), Stuck in the mud? Earthquake nucleation and propagation through accretionary forearcs, *Geophys. Res. Lett.*, *38*, L18303, doi:10.1029/2011GL048552.
- Ferri, F., G. Di Toro, T. Hirose, and T. Shimamoto (2010), Evidence of thermal pressurization in high-velocity friction experiments on smectite-rich gouges, *Terra Nova*, *22*, 347–353, doi:10.1111/j.1365-3121.2010.00955.x.
- Goldsby, D. L., and T. E. Tullis (2002), Low frictional strength of quartz rocks at subseismic slip rates, *Geophys. Res. Lett.*, *29*(17), 1844, doi:10.1029/2002GL015240.
- Goldsby, D. L., and T. E. Tullis (2011), Flash heating leads to low frictional strength of crustal rocks at earthquake slip rates, *Science*, *334*, 216–218, doi:10.1126/science.1207902.
- Gratier, J. P., and F. Gueydan (2007), Deformation in the presence of fluids and mineral reactions: Effects of fracturing and fluid-rock interaction on seismic cycles, in *Tectonic Faults, Agent of Change on a Dynamic Earth*, edited by M. R. Handy et al., pp. 319–356, Mass. Inst. of Technol. Press, Cambridge.
- Grunberger, D., I. Djéran-Maigre, B. Velde, and D. Tessier (1994), Measurement through direct observation of kaolinite particle reorientation during compaction, *C.R. Acad. Sci., Ser. II*, *318*, 627–633.
- Han, R., T. Shimamoto, T. Hirose, J. H. Ree, and J. Ando (2007), Ultra low friction of carbonate faults caused by thermal decomposition, *Science*, *316*, 878–881, doi:10.1126/science.1139763.
- Han, R., T. Hirose, and T. Shimamoto (2010), Strong velocity weakening and powder lubrication of simulated carbonate faults at seismic slip rates, *J. Geophys. Res.*, *115*, B03412, doi:10.1029/2008JB006136.
- Han, R., T. Hirose, T. Shimamoto, Y. Lee, and J. I. Ando (2011), Granular nanoparticles lubricate faults during seismic slip, *Geology*, *39*, 599–602, doi:10.1130/G31842.1.
- Hayman, N. W. (2006), Shallow crustal fault rocks from the black Mountain detachments, Death Valley, CA, *J. Struct. Geol.*, *28*, 1767–1784, doi:10.1016/j.jsg.2006.06.017.
- Hayman, N. W., B. A. Housen, T. T. Cladouhos, and K. Livi (2004), Magnetic and clast fabrics as measurements of grain-scale processes within the Death Valley shallow crustal detachment faults, *J. Geophys. Res.*, *109*, B05409, doi:10.1029/2003JB002902.
- Hazzard, J. F., and K. Mair (2003), The importance of the third dimension in granular shear, *Geophys. Res. Lett.*, *30*(13), 1708, doi:10.1029/2003GL017534.
- Heaton, T. H. (1990), Evidence for and implications of self-healing pulses of slip in earthquake rupture, *Phys. Earth Planet. Inter.*, *64*, 1–20, doi:10.1016/0031-9201(90)90002-F.
- Hirose, T., and M. Bystricky (2007), Extreme dynamic weakening of faults during dehydration by coseismic shear heating, *Geophys. Res. Lett.*, *34*, L14311, doi:10.1029/2007GL030049.
- Hirose, T., and T. Shimamoto (2005), Slip-weakening distance of faults during frictional melting as inferred from experimental and natural pseudotachylites, *Bull. Seismol. Soc. Am.*, *95*, 1666–1673, doi:10.1785/0120040131.
- Ji, C., D. V. Helmberger, D. J. Wald, and K. F. Ma (2003), Slip history and dynamic implications of the 1999 Chi-Chi, Taiwan, earthquake, *J. Geophys. Res.*, *108*(B9), 2412, doi:10.1029/2002JB001764.
- Kanamori, H., and E. E. Brodsky (2004), The physics of earthquakes, *Rep. Prog. Phys.*, *67*, 1429–1496, doi:10.1088/0034-4885/67/8/R03.
- Keulen, N., H. Stünitz, and R. Heilbronner (2008), Healing microstructures of experimental and natural fault gouge, *J. Geophys. Res.*, *113*, B06205, doi:10.1029/2007JB005039.
- Kitajima, H., J. S. Chester, F. M. Chester, and T. Shimamoto (2010), High-speed friction of disaggregated ultracataclastic in rotary shear: Characterization of frictional heating, mechanical behavior, and microstructure evolution, *J. Geophys. Res.*, *115*, B08408, doi:10.1029/2009JB007038.
- Kohli, A. H., D. L. Goldsby, G. Hirth, and T. Tullis (2011), Flash weakening of serpentinite at near-seismic slip rates, *J. Geophys. Res.*, *116*, B03202, doi:10.1029/2010JB007833.
- Lapusta, N. (2009), The roller coaster of fault friction, *Nat. Geosci.*, *2*, 676–677, doi:10.1038/ngeo0645.
- Lee, W. H., H. Kanamori, P. C. Jennings, and C. Kisslinger (2002), *The International Handbook of Earthquake and Engineering Seismology*, 81 pp., Academic, Amsterdam.
- Lexa, O. (2003), Numerical approaches in structural and microstructural analyses, PhD thesis, Charles Univ., Prague.

- Lim, S. C., M. F. Ashby, and J. H. Brunton (1989), The effect of sliding conditions on the dry friction of metals, *Acta Metall. Mater.*, **37**, 767–772, doi:10.1016/0001-6160(89)90003-5.
- Mair, K., and S. Abe (2008), 3D numerical simulations of fault gouge evolution during shear: Grain size reduction and strain localization, *Earth Planet. Sci. Lett.*, **274**, 72–81, doi:10.1016/j.epsl.2008.07.010.
- Mair, K., and J. F. Hazzard (2007), Nature of stress accommodation in sheared granular material: Insights from 3D numerical modeling, *Earth Planet. Sci. Lett.*, **259**, 469–485, doi:10.1016/j.epsl.2007.05.006.
- Mair, K., and C. Marone (2000), Shear heating in granular layers, *Pure Appl. Geophys.*, **157**, 1847–1866, doi:10.1007/PL00001064.
- Mair, K., K. M. Frye, and C. Marone (2002), Influence of grain characteristics on the friction of granular shear zones, *J. Geophys. Res.*, **107**(B10), 2219, doi:10.1029/2001JB000516.
- Marone, C. (1995), Fault zone strength and failure criteria, *Geophys. Res. Lett.*, **22**(6), 723–726, doi:10.1029/95GL00268.
- Marone, C., C. B. Raleigh, and C. H. Scholz (1990), Frictional behavior and constitutive modeling of simulated fault gouge, *J. Geophys. Res.*, **95**, 7007–7025, doi:10.1029/JB095iB05p07007.
- Mitchell, T. M., and D. R. Faulkner (2008), Experimental measurements of permeability evolution during triaxial compression of initially intact crystalline rocks and implications for fluid flow in fault zones, *J. Geophys. Res.*, **113**, B11412, doi:10.1029/2008JB005588.
- Mizoguchi, K., T. Hirose, T. Shimamoto, and E. Fukuyama (2006), Moisture-related weakening and strengthening of a fault activated at seismic slip rates, *Geophys. Res. Lett.*, **33**, L16319, doi:10.1029/2006GL026980.
- Mizoguchi, K., T. Hirose, T. Shimamoto, and E. Fukuyama (2007a), Reconstruction of seismic faulting by high-velocity friction experiments: An example of the 1995 Kobe earthquake, *Geophys. Res. Lett.*, **34**, L01308, doi:10.1029/2006GL027931.
- Mizoguchi, K., M. Takahashi, K. Masuda, and E. Fukuyama (2007b), Fault strength drop due to phase transitions in the pore fluid, *Geophys. Res. Lett.*, **34**, L09313, doi:10.1029/2007GL029345.
- Mizoguchi, K., T. Hirose, T. Shimamoto, and E. Fukuyama (2009a), Fault heals rapidly after dynamic weakening, *Bull. Seismol. Soc. Am.*, **99**, 3470–3474, doi:10.1785/0120080325.
- Mizoguchi, K., T. Hirose, T. Shimamoto, and E. Fukuyama (2009b), High-velocity frictional behavior and microstructure evolution of fault gouge obtained from Nojima fault, southwest Japan, *Tectonophysics*, **471**, 285–296, doi:10.1016/j.tecto.2009.02.033.
- Moore, D. E., and D. A. Lockner (2004), Crystallographic controls on the frictional behavior of dry and water-saturated sheet structure minerals, *J. Geophys. Res.*, **109**, B03401, doi:10.1029/2003JB002582.
- Moore, D. E., D. A. Lockner, M. Shengli, R. Summer, and J. D. Byerlee (1997), Strengths of serpentinite gouges at elevated temperatures, *J. Geophys. Res.*, **102**, 14,787–14,801, doi:10.1029/97JB00995.
- Morrow, C. A., D. E. Moore, and D. A. Lockner (2000), The effect of mineral bond strength and adsorbed water on fault gouge frictional strength, *Geophys. Res. Lett.*, **27**(6), 815–818, doi:10.1029/1999GL008401.
- Nakatani, M., and C. H. Scholz (2004), Frictional healing of quartz gouge under hydrothermal conditions: 1. Experimental evidence for solution transfer healing mechanism, *J. Geophys. Res.*, **109**, B07201, doi:10.1029/2001JB001522.
- Nielsen, S., G. Di Toro, T. Hirose, and T. Shimamoto (2008), Frictional melt and seismic slip, *J. Geophys. Res.*, **113**, B01308, doi:10.1029/2007JB005122.
- Niemeijer, A., C. Marone, and D. Elsworth (2010), Fabric induced weakness of tectonic faults, *Geophys. Res. Lett.*, **37**, L03304, doi:10.1029/2009GL041689.
- Niemeijer, A., G. Di Toro, S. Nielsen, and F. Di Felice (2011), Frictional melting of gabbro under extreme experimental conditions of normal stress, acceleration, and sliding velocity, *J. Geophys. Res.*, **116**, B07404, doi:10.1029/2010JB008181.
- Noda, H., and T. Shimamoto (2005), Thermal pressurization and slip weakening distance of a fault: An example of the Hanaore fault, southwest Japan, *Bull. Seismol. Soc. Am.*, **95**, 1224–1233, doi:10.1785/0120040089.
- Numelin, T., C. Marone, and E. Kirby (2007), Frictional properties of natural fault gouge from a low-angle normal fault, Panamint Valley, California, *Tectonics*, **26**, TC2004, doi:10.1029/2005TC001916.
- Oohashi, K., T. Hirose, and T. Shimamoto (2011), Shear-induced graphitization of carbonaceous materials during seismic fault motion: Experiments and possible implications for fault mechanics, *J. Struct. Geol.*, **33**, 1122–1134, doi:10.1016/j.jsg.2011.01.007.
- Panozzo, R. (1983), Two-dimensional analysis of shape-fabric using projections of digitized lines in a plane, *Tectonophysics*, **95**, 279–294, doi:10.1016/0040-1951(83)90073-2.
- Paterson, M. S., and T. F. Wong (2004), *Experimental Rock Deformation: The Brittle Field*, 358 pp., Springer, Berlin.
- Pawley, A. R., S. A. T. Redfern, and B. J. Wood (1995), Thermal expansivities and compressibilities of hydrous phases in the system MgO-SiO₂-H₂O: Talc, phase A and 10 Å phase, *Contrib. Mineral. Petrol.*, **122**, 301–307, doi:10.1007/s004100050129.
- Pec, M., H. Stünitz, and R. Heilbronner (2012), Semi-brittle deformation of granitoid gouges in shear experiments at elevated pressures and temperatures, *J. Struct. Geol.*, **38**, 200–221, doi:10.1016/j.jsg.2011.09.001.
- Piga, L., F. Villieras, and J. Yvon (1992), Thermogravimetric analysis of a talc mixture, *Thermochim. Acta*, **211**, 155–162, doi:10.1016/0040-6031(92)87015-3.
- Reches, Z., and D. Lockner (2010), Fault weakening and earthquake instability by powder lubrication, *Nature*, **467**, 452–455, doi:10.1038/nature09348.
- Rice, J. R. (2006), Heating and weakening of faults during earthquake slip, *J. Geophys. Res.*, **111**, B05311, doi:10.1029/2005JB004006.
- Rice, J. R., N. Lapusta, and K. Ranjith (2001), Rate and state dependent friction and the stability of sliding between elastically deformable solids, *J. Mech. Phys. Solids*, **49**, 1865–1898, doi:10.1016/S0022-5096(01)00042-4.
- Rockwell, T. K., and Y. Ben-Zion (2007), High localization of primary slip zones in large earthquakes from paleoseismic trenches: Observations and implications for earthquake physics, *J. Geophys. Res.*, **112**, B10304, doi:10.1029/2006JB004764.
- Rutter, E. H., R. H. Maddock, S. H. Hall, and S. H. White (1986), Comparative microstructures of natural and experimentally produced clay-bearing gouges, *Pure Appl. Geophys.*, **124**, 3–30, doi:10.1007/BF00875717.
- Saad, Y. (2003), *Iterative Methods for Sparse Linear Systems*, 2nd ed., 528 pp., Soc. for Indust. and Appl. Math., Philadelphia, Pa., doi:10.1137/1.9780898718003.
- Sawai, M., T. Shimamoto, and T. Togo (2012), Reduction in BET surface area of Nojima fault gouge with seismic slip and its implication for the fracture energy of earthquakes, *J. Struct. Geol.*, **38**, 117–138, doi:10.1016/j.jsg.2012.01.002.
- Scholz, C. H. (2006), The strength of the San Andreas fault: A critical analysis, in *Earthquakes: Radiated Energy and the Physics of Faulting*, *Geophys. Monogr. Ser.*, vol. 170, edited by R. Abercrombie et al., pp. 301–311, AGU, Washington, D. C., doi:10.1029/170GM30.
- Shimamoto, T., and A. Tsutsumi (1994), A new rotary-shear high-speed frictional testing machine: Its basic design and scope of research (in Japanese with English abstract), *J. Struct. Geol.*, **39**, 65–78.
- Sibson, R. H. (1973), Interactions between temperature and pore fluid pressure during earthquake faulting: A mechanism for partial or total stress relief, *Nature*, **243**, 66–68, doi:10.1038/physci243066a0.
- Sibson, R. H. (1980), Power dissipation and stress levels on faults in the upper crust, *J. Geophys. Res.*, **85**, 6239–6247, doi:10.1029/JB085iB11p06239.
- Sibson, R. H. (1989), Earthquake faulting as a structural process, *J. Struct. Geol.*, **11**, 1–14, doi:10.1016/0191-8141(89)90032-1.
- Sibson, R. H. (2003), Thickness of the seismic slip zone, *Bull. Seismol. Soc. Am.*, **93**, 1169–1178, doi:10.1785/0120020061.
- Smith, S. A. F., A. Billi, G. Di Toro, and R. Spiess (2011), Principal slip zones in Limestone: Microstructural characterization and implications for the seismic cycle (Tre Monti fault, Central Apennines, Italy), *Pure Appl. Geophys.*, **168**, 2365–2393, doi:10.1007/s00024-011-0267-5.
- Sone, H., and T. Shimamoto (2009), Frictional resistance of faults during accelerating and decelerating earthquake slip, *Nat. Geosci.*, **2**, 705–708, doi:10.1038/ngeo637.
- Stünitz, H., N. Keulen, T. Hirose, and R. Heilbronner (2010), Grain size distribution and microstructures of experimentally sheared granitoid gouge at coseismic slip rates: Criteria to distinguish seismic and aseismic faults?, *J. Struct. Geol.*, **32**, 59–69, doi:10.1016/j.jsg.2009.08.002.
- Sulem, J., and V. Famin (2009), Thermal decomposition of carbonates in fault zones: Slip-weakening and temperature-limiting effects, *J. Geophys. Res.*, **114**, B03309, doi:10.1029/2008JB006004.
- Tisato, N., G. Di Toro, N. De Rossi, M. Quaresimin, and T. Candela (2012), Experimental investigation of flash weakening in limestone, *J. Struct. Geol.*, **38**, 183–199, doi:10.1016/j.jsg.2011.11.017.
- Trouw, R. A. J., C. W. Passchier, and D. J. Wiersma (2010), Atlas of mylonites and related microstructures, 322 pp., Springer, New York.
- Velev, O. D., N. D. Denkov, V. N. Paunov, P. A. Kralchevsky, and K. Nagayama (1993), Direct measurement of lateral capillary forces, *Langmuir*, **9**, 3702–3709, doi:10.1021/la00036a056.
- Viti, C., and C. Colletini (2009), Growth and deformation mechanisms of talc along a natural fault: A micro/nanostructural investigation, *Contrib. Mineral. Petrol.*, **158**, 529–542, doi:10.1007/s00410-009-0395-4.
- Vrolijk, P., and B. A. van der Pluijm (1999), Clay gouge, *J. Struct. Geol.*, **21**, 1039–1048, doi:10.1016/S0191-8141(99)00103-0.
- Wagner, W., and A. Pruss (2002), The IAPWS formulation 1995 for the thermodynamic properties of ordinary water substance for general and

- scientific use, *J. Phys. Chem. Ref. Data*, 31, 387–535, doi:10.1063/1.1461829.
- Ward, R. J. (1975), Kinetics of talc dehydroxylation, *Thermochim. Acta*, 13, 7–14, doi:10.1016/0040-6031(75)80061-X.
- Wesolowski, M. (1984), Thermal decomposition of talc: A review, *Thermochim. Acta*, 78, 395–421, doi:10.1016/0040-6031(84)87165-8.
- Wibberley, C. A. J., and T. Shimamoto (2005), Earthquake slip weakening and asperities explained by thermal pressurization, *Nature*, 436, 689–692, doi:10.1038/nature03901.
- Wibberley, C. A. J., G. Yielding, and G. Di Toro (2008), Recent advances in the understanding of fault zone internal structure: A review, in *The Internal Structure of Fault Zones: Implications for Mechanical and Fluid-Flow Properties*, edited by C. A. J. Wibberley et al., *Geol. Soc. Spec. Publ.*, 299, 5–33.
- Wintsch, R. P., R. Christoffersen, and A. K. Kronenberg (1995), Fluid-rock reaction weakening of fault zones, *J. Geophys. Res.*, 100, 13,021–13,032, doi:10.1029/94JB02622.
- Worniyoh, E. Y. A., V. K. Jasti, and C. F. Higgs (2007), A review of dry particulate lubrication: Powder and granular materials, paper presented at STLE/ASME 2006 International Joint Tribology Conference, Tribol. Div., San Antonio, Tex.
- Yund, R. A., M. L. Blanpied, T. E. Tullis, and J. D. Weeks (1990), Amorphous material in high strain experimental fault gouges, *J. Geophys. Res.*, 95, 15,589–15,602, doi:10.1029/JB095iB10p15589.

1 Talc Lubrication at High Strain Rate

2 Mai-Linh Doan¹, T. Hirose², M. Andréani³, A.-M. Boullier¹, D.-G. Calugaru⁴ and S.
3 Boutareaud⁵

4 ¹*Institut des Sciences de la Terre, CNRS, Université Joseph Fourier, Grenoble, France*

5 ²*Kochi Institute for Core Sample Research, JAMSTEC, Kochi, Japan*

6 ³*Laboratoire de Géologie de Lyon: Terre, Planètes, Environnement,*

7 *UMR 5276, Ecole Normale Supérieure de Lyon et Université Lyon I, Lyon, France.*

8 ⁴*Laboratoire de Mécanique des Fluides et d'Acoustique, UMR 5509, Ecole Centrale De Lyon,*
9 *Ecully, France.*

10 ⁵*Institute for Geologisches Institut, ETH Zürich, Zürich, Switzerland.*

11

12 ABSTRACT

13 Talc is a very soft material that has been found in small quantities in active fault zones. Its
14 presence, even tenuous, is known in numerous active faults. Although talc properties have been
15 investigated at low slip rate, its effects at coseismic rate have not yet been investigated. We
16 perform high velocity friction experiments on serpentine and talc gouges, pioneering the study
17 on friction of mixtures at high velocity. Here we show that a small amount of talc (<5%) is
18 enough to suppress the initial peak of serpentine gouge at seismic slip rate. The neutral slip-
19 weakening favors tremor and slow slip behavior. Talc is efficient from the onset of slip, before
20 the activation of thermally enhanced weakening mechanisms. Easy delamination of talc produces
21 myriads of talc grains that coat serpentine grains and help local shear localization. In wet gouge,
22 water realigns talc platelets and lubricates their interface to overcome jamming. The dynamics of

23 shear localization affects shear resistance at the onset of slip, which is crucial for rupture
24 propagation.

25

26 INTRODUCTION

27 Natural fault gouge is made of multiple minerals of different friction properties. What is
28 the influence of each fraction on the friction properties of a mixture? Several studies have been
29 performed at low slip rate on gouge (Tembe et al, 2010; Moore and Lockner, 2011; Crawford et
30 al, 2008; Niemeijer et al, 2010). However, most of the active faults are earthquake-prone and
31 high velocity friction experiments performed at high velocity uncovered new physical process
32 strongly reducing friction coefficient at high strain rate (DiToro et al, 2011; Niemeijer, 2012).
33 Here, we perform one of the first studies that investigate friction of mixtures at coseismic
34 velocity.

35 We study here an assemblage of talc and serpentine, a natural example of composite
36 gouge, as talc is the product of alteration of serpentinite when in contact with silica-rich water.
37 Primary production of talc occurs within oceanic crust. Secondary talc can be produced along
38 faults bringing silica-rich fluids within serpentine body (Manning, 1995), especially along
39 subduction interface. Therefore, the assemblage of talc and serpentine can be found in a variety
40 of active faults: normal detachment faults (Collettini and Holdsworth, 2004; Ildefonse et al,
41 2007), strike-slip faults intersecting oceanic mélange (e.g. San Andreas fault (Moore and Rymer,
42 2007)) and thrust fault in subduction zones (Manning, 1995). Some of these faults are known to
43 be weak (Moore and Rymer, 2007; Collettini and Holdsworth, 2004) and talc may be a key
44 element to explain this behaviour.

45 Indeed, talc slides easily. It is one of the few minerals that depart from Byerlee law
46 [Byerlee, 1978], with a static friction coefficient less than 0.2 (whereas most minerals have
47 friction coefficient about 0.6-0.8 (Moore and Rymer, 2007)). This may be attributed to the small
48 bonding strength between talc tetrahedral layer (Moore, 2004)], leading to easy delamination
49 (Escartin et al, 2008). Talc has a large stability field (Bose and Ganguly, 1995; Schmidt and Poli,
50 1998; Manning, 1995). It maintains its low friction even at seismogenic depth (Moore and
51 Rymer, 2007; Escartin et al, 2008), contrary to clays that dehydrate above 200°C (Vidal and
52 Dubacq, 2009). When present, talc may be a key element for controlling fault behaviour. When
53 talc was discovered within cuttings of the SAFOD (the San Andreas Fault Observatory at Depth)
54 borehole (Moore and Rymer, 2007), the interest of the earthquake community aroused. However,
55 the cores subsequently recovered from the SAFOD hole showed that the amount of talc is minor
56 (Zoback et al, 2010), at most 3%. Is this quantity negligible or is it enough to alter the fault
57 behaviour?

58 METHODS

59 The following experiments were performed on simulated gouges composed of talc and
60 serpentine. Serpentine comes from natural rock blocs sampled on the Santa Clara Fault,
61 California, mainly composed of lizardite and minor pyroxene content (see supplementary
62 material). The sample was crushed into fine grains smaller than 40 µm. Talc was bought from
63 WVR company. Its purity is >99.9 %. Initial grain size of talc is ~30 µm in average. Each
64 simulated gouge weights about 1g in total with different talc fraction of 0, 2.5, 5, 10, 20 and 30%
65 in weight. The talc and serpentine were weighted separately and then mixed thoroughly during
66 several minutes. Several tens of grams of each proportion were prepared. The simulated gouges
67 are homogeneously mixed with a random orientation of talc grains in serpentine matrix (see
68 Figure S2 in Supplementary Materials).

69 Previous experiments done on pure talc have shown that talc is not weak at high friction
70 velocity and low displacement [Boutareaud et al, 2012; Faulkner et al, 2011] but that talc keeps
71 its low friction coefficient when wet. Hence, to analyze the effect of talc as a weakening
72 component, gouge was saturated with 4 ml of distilled water.

73 All experiments were conducted in a modified rotary-shear, high-velocity friction testing
74 apparatus [Shimamoto and Tsutsumi, 1994; Hirose and Shimamoto, 2005]. The simulated gouge
75 zone was made by that 1g gouge was placed between solid gabbro cylinders with 2.5 cm in
76 diameter. The gouge was saturated, by adding 0.4 ml distilled water into the gouge zone. Teflon
77 sleeve was mounted around the gouge zone to prevent gouge loss during sliding. End surface of
78 the rock cylinder where it contacts with the gouge layer roughen by using #120 SiC powder.
79 High-velocity slip on the simulated fault under normal stress was obtained by pressing together
80 the pair of solid cylindrical gabbro with an air actuator, and then keeping one specimen
81 stationary while the other was rotated at high speed by a servomotor. Experiments were
82 performed at a constant slip velocity of 1.31m/s, normal stress of 1 MPa. Slip on the simulated
83 fault accelerated from 0 to 1.6 m/s in 0.5 s, was maintained at 1.3 m/s, and then decelerated to 0
84 m/s in 0.5 s (Table 1). We measured torque and normal load applied on the gouge layer, rotation
85 speed and axial displacement of the gouge zone [Hirose and Shimamoto, 2005].

86 Teflon ring is known to significantly contribute to the measured torque if no care is taken.
87 We used a loose Teflon ring of standardized dimension to limit its effect on friction. To assess
88 the effect of the Teflon sleeve on the recorded friction experiments, we performed dummy tests,
89 with only the Teflon ring and water inside the ring. The Teflon effect is reproducible and
90 negligible (Supplementary figure 6): the shear stress due to friction on Teflon ring is 0.03 MPa.
91 As the confining pressure is 1 MPa, the error bar on our friction experiment is about 0.04.

92 We stopped the experiments abruptly with the servomotor (in 0.5 s from slip rate of 1.3
93 m/s) to preserve the microstructures during high-speed sliding. Recovered specimens were
94 impregnated with epoxy, cut perpendicular to the gouge layer at ~4 mm inside from a periphery
95 of the specimen and then were thin-sectioned. We observed the thin sections by an optical
96 microscope and an analytical field-emission scanning electron microscope. Electron Diffraction
97 Scattering (EDS) spectral analysis was done to check for detecting any fluorine left by Teflon
98 decomposition but no noticeable fluorine-rich area were found on the EDS map. We conclude
99 that Teflon was not inserted within the gouge and did disturb neither mechanical data, nor
100 microstructure.

101 RESULTS

102 A series of experiments were performed on experimental gouge made of talc and
103 serpentine (cf Supplementary material). Figure 1 shows typical friction history for gouge with
104 the various proportions of talc and serpentine tested. The full set of experiments is presented in
105 supplementary material. To ease comparison between friction curve, the slip dependent-curves
106 were low-pass filtered with cut-off at the frequency of sample rotation (25 Hz equivalent to ~7.8
107 cm), to remove friction fluctuation related to the system misalignment that varies the friction
108 curve by 0.05. Given the small, flat and reproducible torque determined from dummy tests with
109 the Teflon rings (Supplementary figure 5), we did not correct from Teflon contribution the
110 experimental curves.

111 The experiments in wet conditions show a spectacular weakening effect of talc on the
112 mixture (figure 1). Let first investigate the behavior of gouge made of pure serpentine or pure
113 talc. Pure serpentine experiences strong slip weakening, with a peak friction coefficient of 0.5 for

114 dry case that falls exponentially to a steady-state value of ~ 0.2 with a characteristic distance D_c
115 of ~ 7 m. Talc has a very different behavior: it begins to slide without a sharp friction peak and
116 keeps nearly constant friction coefficient of 0.2-0.25. Adding more than 5%wt talc levels off the
117 initial peak in friction (figure 1). With 2.5%wt of talc, there no visible change in friction, but
118 with as only 5%wt of talc, initial friction is reduced to 0.37. Friction levels to this value before
119 rejoining the decay curve of pure serpentine after 3 m of slip. The friction at 10%wt of talc
120 resembles to the friction at 5%wt with slightly lower initial friction value. With more than
121 20%wt of talc, the initial friction value is about 0.3 and decays slowly with displacement.

122 In dry conditions, the effect of talc is null, even at 30% (supplementary material). Both
123 materials start with a large friction peak of 0.8. Talc keeps a larger friction than serpentine, with
124 a characteristic distance D_c of ~ 15 m, larger than the characteristic distance for serpentine and
125 mixture D_c of ~ 4 m. The large dry friction coefficient of talc is attributed to jamming (Boutareaud
126 et al, 2012) preventing the easy sliding along the basal plane of the talc platelets. Jamming did
127 not happen for wet talc, as water facilitated the kinetics of rotation of the talc platelets, until they
128 aligned parallel to the shear direction. Microstructures for dry and wet talc were therefore very
129 different.

130 Microstructures in saturated conditions give insight on the processes at stake during the
131 high velocity weakening. We started with a random packing of talc and serpentine grains,
132 without preferential structure (see supplementary material), but depending on the talc content of
133 the mixture, the microstructure of the slipping zone after 3 meters varies a lot.

134 For pure serpentine and mixture with 2.5%wt talc, a principal shear zone (PSZ) is visible at
135 the boundary between host rock and gouge zone, when the gouge is made of pure serpentine or

136 made with 2.5%wt talc (figure 2d). The PSZ is made of a few clasts inserted in a matrix of grain
137 size about 0.1 μm (figure 2c). The contact between this PSZ and the less deformed gouge zone is
138 a very sharp shear plane (figure 2b, 2d). There is no apparent change in mineralogy; the drop in
139 friction seems to be associated with the development of the fine-grained shear zone, and the
140 increasing amount of nanograins, which have low frictional property [Reches and Lockner, 2010;
141 Han et al, 2011]. The characteristic slip weakening distance is smaller for the dry serpentine than
142 for the wet serpentine, suggesting that thermal pressurization is not the major weakening process
143 for serpentine gouge. Instead, we favor nanograin lubrication.

144 Water has an immediate effect on the peak value of gouge. As talc is hydrophobic, water
145 does not affect the cohesion of the material, as there are no capillary bonds. Free water then
146 lubricates the grains, instantaneously altering the friction coefficient.

147 By adding talc, the gouge structures itself is very different from pure serpentine gouges at
148 same displacement of ~ 3 m. Shear is more distributed within the fault gouge, with some minor
149 shear planes, along which talc platelets align (figure 2f), but no Principal Shear Zone (PSZ) is
150 developed in talc rich samples. Talc grains are smaller and thinner than in the initial state. The
151 thinner talc grains are produced by delamination of larger grains. This delamination is noticeable
152 even after 1 m of slip (figure 3). The delaminated talc produces lineaments of aligned talc sheets,
153 forming incipient shear planes (figure 4). Weak talc provides nucleation points to initiate the
154 shear plane. Talc platelets are also aligned along the well-developed shear planes (figure 4b).

155 DISCUSSION

156 Our experimental results show talc lubricates the serpentine gouge. Adding 5%wt of talc is
157 sufficient to level out the initial friction peak observed for pure serpentine, reducing its value by

158 0.15, which is more than the contribution of both misalignment (0.05) and Teflon friction (0.04).
159 The peak is almost erased at 20%wt of talc and more. Hence, talc is able to reduce the initial
160 friction coefficient by ~50%. There is an immediate action of talc, that prevents the occurrence
161 of the major mechanism of deformation and weakening of serpentine: serpentine grain
162 comminution is reduced in presence of talc.

163 **Weakening mechanisms of talc**

164 We suspect the comminution process by abrasion is a way to overcome the mechanical
165 jamming occurring at the onset on a fast displacement in a granular medium. Jamming prevents
166 the sliding for most part of the gouge, as it is composed of interlocked angular grains. To begin
167 to slide, we need to dislodge some grains, either by sliding along serpentine grains or by crushing
168 asperities. A Principal Shear Zone (PSZ) then localises deformation.

169 We discuss two effects explaining the lubricating effect of talc: the asperity coating of
170 serpentine clasts by talc (figure 3) and the alignment of talc platelets along shear planes
171 localising deformation (figure 4). Both effects are enhanced by talc delamination.

172 *Talc coating*

173 Grain sliding is easier when a talc grain is inserted between two serpentine asperities. To
174 do so we need a large number of talc grains. Delamination provides multiple thin layers from a
175 single talc grain. The thinly delaminated talc grains can then coat the larger serpentine grains,
176 sometimes by kinking or bending to better fit the irregular shape of serpentine grains (Figure 3).
177 We computed the covering power of talc as the ratio of the surface of talc platelets by
178 delamination to the surface of the serpentine clasts, for a given proportion of talc (Supplementary
179 Material). The computation predicts that if talc platelets become as thin as 0.5 μm , 7.5%wt of

180 talc can theoretically cover all serpentine clasts and control friction. Friction data show that the
181 friction coefficient is already significantly lower for 5% and 10%wt of talc. Yet friction data is
182 not exactly similar to talc in an early stage (figure 1). At 30%wt talc and 3 m of slip, talc
183 covering is extensive (figure 2f) but some serpentine grain-to-grain contacts persist, explaining
184 the discrepancy between the mixture and the pure talc grain friction (figure 1). Talc coating
185 increases with strain as talc and serpentine get more mixed and as talc grains get delaminated.

186 *Easier local shear localization*

187 If there is a lot of talc, deformation is accommodated by a lot of thin shear planes (figure
188 2f) widespread, at the expense of the formation of a broad shear zone, that is more often
189 observed for other high velocity friction experiments [Mizoguchi et al., 2009]. Talc helps to
190 initiate these shear planes (figure 4). At a very early stage of slip, the cleavage planes provide
191 nucleation points for the formation of shear plane. Sliding along the talc cleavage helps to extend
192 these incipient shear planes. The delaminated talc platelets align along a plane until talc cannot
193 get delaminated anymore. To create larger shear zone, these incipient shear planes need to
194 connect themselves. Their small width and their long length efficiently concentrate stress and
195 increase the interaction distance between incipient shear planes. The presence of talc along the
196 shear planes enhances its lubricating effect [Collettini et al., 2009]. Talc catalyzes shear
197 initiation, explaining why friction can be affected by small talc content from early slip.

198 Talc therefore structures the gouge geometry. This is a crucial process, as highlighted in
199 the friction experiments done on mixed gouge at low velocity. Indeed, low strain rate
200 experiments involving synthetic homogeneous mixtures of strong and weak materials require a
201 higher threshold in content of the weak phase to significantly change friction properties of the

202 experimental gouge. For instance, Carpenter et al [2009] found no significant weakening for a
203 synthetic mixture of 50% talc and 50% quartz sand compared to pure quartz sand. Tembe et al
204 [2010] found a linear decrease in friction with clay content. Hence, a threshold between 20 and
205 30% of clay is needed to change friction curves in wet conditions by more than 20% [Crawford
206 et al, 2008; Tembe et al, 2010].

207 Friction properties are strongly influenced by the material fabric [Colletini et al, 2009],
208 and the efficiency of talc weakening is increased when its distribution is no more homogeneous
209 within the experimental gouge. Niemeijer et al [2010] found that 4% of talc is sufficient to
210 change a mixture properties provided the gouge is foliated, containing a continuous talc layer to
211 accommodate slip. Similarly, Moore and Lockner [2011] found that 5% of talc could reduce the
212 steady state friction of a mixture of lizardite and talc at 200°C at 0.4, compared to the friction of
213 0.6 of a pure lizardite gouge. Adding 20% of talc reduces the serpentine strength by 50%. They
214 attribute talc efficiency to its capacity to lie continuously within the shear zones pervading the
215 post-mortem gouge. The effect of talc is stronger within serpentine than in quartz because of the
216 platy shape of lizardite. Note, however, the lizardite we used in our experiments does not appear
217 as « platy »: serpentine is aggregated in clasts.

218 In our experiments, we showed that talc influence the early stage of friction of a mixture of
219 talc and serpentine, by self-organising the gouge structure, from the early stage of slip. This rapid
220 effect of talc is important for the dynamics of a rupture along a talc-rich fault, like a subduction
221 plane [Manning, 1995].

222 CONCLUSION: IMPLICATION FOR EARTHQUAKE DYNAMICS

223 We have conducted a series of high velocity friction experiments on gouge made of talc

224 and serpentine. When talc is in proportion above 5%, the initial peak in friction of serpentine is
225 erased. There is no more a barrier to rupture initiation. The smaller peak stress makes it easy to
226 start an earthquake. Frequent earthquakes prevent accumulating large strain energy and hence the
227 start of large earthquake. It can also prevent the propagation of large earthquake generated on
228 other portions of the fault: the small stress drop diminishes the energy release rate that is needed
229 to propagate rupture father along the fault. Rather than large earthquake, deformation may be
230 accommodated by microseismic activity. The special interaction between fault patches induced
231 by a null weakening has been demonstrated as a source episodic tremor and slip behaviour [Ben-
232 Zion, 2012].

233 Hence a deficit in large earthquake, compensated by microseismic activity, is expected in a
234 talc rich serpentine body. An analogue seismic activity is observed on the central segment of the
235 San Andreas Fault or on the downdip limit of plate boundary earthquakes in subduction zone,
236 where the mantle wedge encounters the fluid rich dipping crust [Shelly et al., 2006; Peacock and
237 Hyndman, 1999].

238 ACKNOWLEDGMENTS

239 The work was funded by an INSU 3F Grant. We thank Emily Brodsky and Amy Kornberg, for
240 helping us getting the talc samples. We thank Francis Coeur for preparing the samples. Thin
241 sections were prepared by Christophe Novado (Univ. Montpellier 2) and Frowin Pirovino (ETH,
242 Zürich). FE-SEM was operated by Frédéric Charlot (SMTC, Univ. Grenoble).

243

244 REFERENCES CITED

- 245 Ben-Zion, Y., 2012, Episodic tremor and slip on a frictional interface with critical zero
246 weakening in elastic solid, *Geophysical Journal International*, v. 189, p. 1159–1168, doi:
247 10.1111/j.1365-246X.2012.05422.x.
- 248 Bose, K., and Ganguly, J., 1995, Experimental and theoretical studies of talc, antigorite and
249 phase A at high pressures with applications to subduction processes, *Earth and Planetary
250 Science Letters*, v. 136, p. 109–121.
- 251 Boutareaud, S., Hirose, T., Andréani, M., Pec, M., Calugaru, D.-G., Boullier, A.-M., and Doan,
252 M.-L., 2012, On the role of phyllosilicates on fault lubrication, Insight from micro- and
253 nanostructural investigations on talc friction experiments, *Journal of Geophysical Research*,
254 v. 117, no. B8, B08408, doi: 10.1029/2011JB009006.
- 255 Byerlee, J., 1978, Friction of rocks, *Pure and applied Geophysics*, v. 116, p. 615–626.
- 256 Carpenter, B.M., Marone, C., and Saffer, D.M., 2009, Frictional behavior of materials in the 3D
257 SAFOD volume, *Geophysical Research Letters*, v. 36, no. 5, p. L05302, doi:
258 10.1029/2008GL036660.
- 259 Collettini, C., and Holdsworth, R.E., 2004, Fault zone weakening and character of slip along
260 low-angle normal faults: insights from the Zuccale fault, Elba, Italy, *Journal of the
261 Geological Society*, v. 161, no. 6, p. 1039.
- 262 Collettini, C., Niemeijer, A., Viti, C., and Marone, C., 2009, Fault zone fabric and fault
263 weakness., *Nature*, v. 462, no. 7275, p. 907–10, doi: 10.1038/nature08585.
- 264 Crawford, B.R., Faulkner, D.R., and Rutter, E.H., 2008, Strength, porosity, and permeability
265 development during hydrostatic and shear loading of synthetic quartz-clay fault gouge,
266 *Journal of Geophysical Research*, v. 113, no. B3, p. 1–14, doi: 10.1029/2006JB004634.

267 Escartín, J., Andreani, M., Hirth, G., and Evans, B., 2008, Relationships between the
268 microstructural evolution and the rheology of talc at elevated pressures and temperatures,
269 Earth and Planetary Science Letters, v. 268, no. 3-4, p. 463–475, doi:
270 10.1016/j.epsl.2008.02.004.

271 Eshelby, J.D., 1957, The Determination of the Elastic Field of an Ellipsoidal Inclusion, and
272 Related Problems, Proceedings of the Royal Society of London. Series A, Mathematical and
273 Physical Sciences, v. 241, no. 1226, p. 376–396.

274 Faulkner, D.R., Mitchell, T.M., Behnsen, J., Hirose, T., and Shimamoto, T., 2011, Stuck in the
275 mud? Earthquake nucleation and propagation through accretionary forearcs, Geophysical
276 Research Letters, v. 38, no. L1830, p. 1–5, doi: 10.1029/2011GL048552.

277 Han, R., Hirose, T., Shimamoto, T., Lee, Y., and Ando, J.-I., 2011, Granular nanoparticles
278 lubricate faults during seismic slip, Geology, v. 39, no. 6, p. 599–602, doi:
279 10.1130/G31842.1.

280 Hirose, T., 2005, Growth of molten zone as a mechanism of slip weakening of simulated faults in
281 gabbro during frictional melting, Journal of Geophysical Research, v. 110, no. B5, p.
282 B05202, doi: 10.1029/2004JB003207.

283 Ildefonse, B., Blackman, D.K., John, B.E., Ohara, Y., Miller, D.J., and MacLeod, C.J., 2007,
284 Oceanic core complexes and crustal accretion at slow-spreading ridges, Geology, v. 35, no.
285 7, p. 623, doi: 10.1130/G23531A.1.

286 Johanson, I. a., 2006, Coseismic and Postseismic Slip of the 2004 Parkfield Earthquake from
287 Space-Geodetic Data, Bulletin of the Seismological Society of America, v. 96, no. 4B, p.
288 S269–S282, doi: 10.1785/0120050818.

- 289 Kitajima, H., Chester, J.S., Chester, F.M., and Shimamoto, T., 2010, High-speed friction of
290 disaggregated ultracataclasite in rotary shear: Characterization of frictional heating,
291 mechanical behavior, and microstructure evolution, *Journal of Geophysical Research*, v.
292 115, no. B8, doi: 10.1029/2009JB007038.
- 293 Mair, K., and Abe, S., 2011, Breaking Up: Comminution Mechanisms in Sheared Simulated
294 Fault Gouge, *Pure and Applied Geophysics*, v. 168, no. 12, p. 2277–2288, doi:
295 10.1007/s00024-011-0266-6.
- 296 Manning, C.E., 1995, Phase-equilibrium controls on SiO₂ metasomatism by aqueous fluid in
297 subduction zones: Reaction at constant pressure and temperature, *International Geology*
298 *Review*, v. 37, no. 12, p. 1074–1093.
- 299 Mizoguchi, K., Hirose, T., Shimamoto, T., and Fukuyama, E., 2009, High-velocity frictional
300 behavior and microstructure evolution of fault gouge obtained from Nojima fault , southwest
301 Japan, *Tectonophysics*, v. 471, p. 285–296, doi: 10.1016/j.tecto.2009.02.033.
- 302 Mizoguchi, K., Hirose, T., Shimamoto, T., and Fukuyama, E., 2007, Reconstruction of seismic
303 faulting by high-velocity friction experiments: An example of the 1995 Kobe earthquake,
304 *Geophysical Research Letters*, v. 34, no. 1, p. 2–4, doi: 10.1029/2006GL027931.
- 305 Moore, D.E., 2004, Crystallographic controls on the frictional behavior of dry and water-
306 saturated sheet structure minerals, *Journal of Geophysical Research*, v. 109, no. B3, p. 1–16,
307 doi: 10.1029/2003JB002582.
- 308 Moore, D.E., and Lockner, D. a., 2011, Frictional strengths of talc-serpentine and talc-quartz
309 mixtures, *Journal of Geophysical Research*, v. 116, no. B1, p. 1–17, doi:
310 10.1029/2010JB007881.

311 Moore, D.E., and Lockner, D. a., 2008, Talc friction in the temperature range 25°–400 °C:
312 Relevance for Fault-Zone Weakening, *Tectonophysics*, v. 449, no. 1-4, p. 120–132, doi:
313 10.1016/j.tecto.2007.11.039.

314 Moore, D.E., and Rymer, M.J., 2007, Talc-bearing serpentinite and the creeping section of the
315 San Andreas fault, *Nature*, v. 448, p. 795–797, doi: 10.1038/nature06064.

316 Nadeau, R.M., Foxall, W., and McEvilly, T. V., 1995, Periodic recurrence and spatial clustering
317 in characteristic microearthquakes on the San Andreas fault, *Science*, v. 267, p. 503–507.

318 De Paola, N., Hirose, T., Mitchell, T., Di Toro, G., Viti, C., and Shimamoto, T., 2011, Fault
319 lubrication and earthquake propagation in thermally unstable rocks, *Geology*, v. 39, no. 1, p.
320 35–38, doi: 10.1130/G31398.1.

321 Peacock, S.M., and Hyndman, R.D., 1999, Hydrous minerals in the mantle wedge and the
322 maximum depth of subduction thrust earthquakes, *Geophysical Research Letters*, v. 26, no.
323 16, p. 2517–2520.

324 Reches, Z., and Lockner, D.A., 2010, Fault weakening and earthquake instability by powder
325 lubrication., *Nature*, v. 467, no. 7314, p. 452–5, doi: 10.1038/nature09348.

326 Rice, J.R., 2006, Heating and weakening of faults during earthquake slip, *Journal of Geophysical*
327 *Research*, v. 111, no. B5, p. 1–29, doi: 10.1029/2005JB004006.

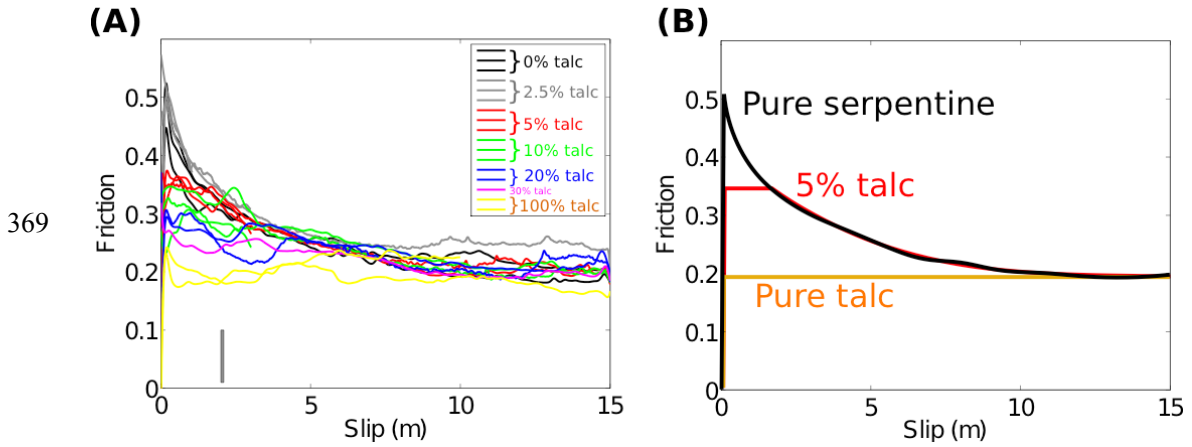
328 Salles, F., Henry, M., and Douillard, J.-M., 2006, Determination of the surface energy of
329 kaolinite and serpentine using PACHA formalism-comparison with immersion experiments.,
330 *Journal of colloid and interface science*, v. 303, no. 2, p. 617–26, doi:
331 10.1016/j.jcis.2006.07.008.

- 332 Sawai, M., Shimamoto, T., and Togo, T., 2012, Reduction in BET surface area of Nojima fault
333 gouge with seismic slip and its implication for the fracture energy of earthquakes, *Journal of*
334 *Structural Geology*, v. 38, p. 117–138, doi: 10.1016/j.jsg.2012.01.002.
- 335 Schmedes, J., Archuleta, R.J., and Lavallée, D., 2010, Correlation of earthquake source
336 parameters inferred from dynamic rupture simulations, *Journal of Geophysical Research*, v.
337 115, no. B3, p. 1–12, doi: 10.1029/2009JB006689.
- 338 Schmidt, M.W., and Poli, S., 1998, Experimentally based water budgets for dehydrating slabs
339 and consequences for arc magma generation, *Earth and Planetary Science Letters*, v. 163,
340 no. 1-4, p. 361–379, doi: 10.1016/S0012-821X(98)00142-3.
- 341 Shelly, D.R., Beroza, G.C., Ide, S., and Nakamura, S., 2006, Low-frequency earthquakes in
342 Shikoku, Japan, and their relationship to episodic tremor and slip., *Nature*, v. 442, no. 7099,
343 p. 188–91, doi: 10.1038/nature04931.
- 344 Shimamoto, T., and Tsutsumi, A., 1994, A new rotary-shear high-speed frictional testing
345 machine: its basic design and scope of research, *Journal of the Tectonic Research Group of*
346 *Japan*, v. 39, p. 65–78.
- 347 Solum, J.G., Hickman, S.H., Lockner, D. a., Moore, D.E., Van der Pluijm, B. a., Schleicher,
348 A.M., and Evans, J.P., 2006, Mineralogical characterization of protolith and fault rocks from
349 the SAFOD Main Hole, *Geophysical Research Letters*, v. 33, no. 21, p. L21314, doi:
350 10.1029/2006GL027285.
- 351 Tembe, S., Lockner, D.A., and Wong, T.-F., 2010, Effect of clay content and mineralogy on
352 frictional sliding behavior of simulated gouges: Binary and ternary mixtures of quartz, illite,
353 and montmorillonite, *Journal of Geophysical Research*, v. 115, no. B3, p. 1–22, doi:
354 10.1029/2009JB006383.

- 355 Di Toro, G., Han, R., Hirose, T., De Paola, N., Nielsen, S., Mizoguchi, K., Ferri, F., Cocco, M.,
356 and Shimamoto, T., 2011, Fault lubrication during earthquakes, *Nature*, v. 471, no. 7339, p.
357 494–8, doi: 10.1038/nature09838.
- 358 Ulmer, P., and Trommsdorff, V., 1995, Serpentine stability to mantle depths and subduction-
359 related magmatism., *Science*, v. 268, no. 5212, p. 858–61, doi:
360 10.1126/science.268.5212.858.
- 361 Vidal, O., and Dubacq, B., 2009, Thermodynamic modelling of clay dehydration, stability and
362 compositional evolution with temperature, pressure and H₂O activity, *Geochimica et*
363 *Cosmochimica Acta*, v. 73, no. 21, p. 6544–6564, doi: 10.1016/j.gca.2009.07.035.
- 364 Zoback, M.D., Hickman, S.H., and Ellsworth, W.L., 2010, Scientific drilling into the San
365 Andreas fault zone, *Eos Trans. AGU*, v. 91, no. 22, p. 197–199.
- 366

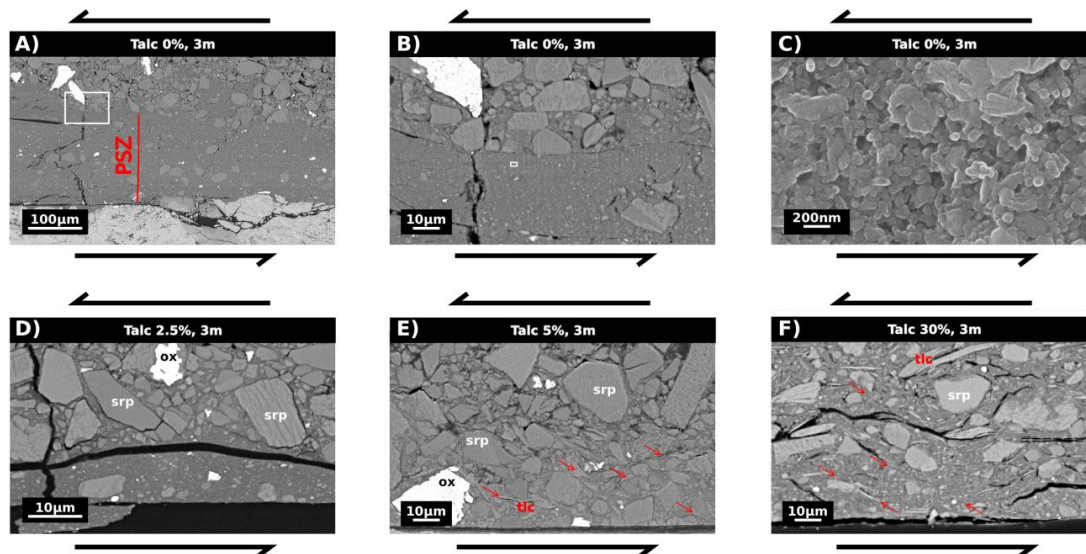
367

368 FIGURE CAPTIONS



370 Figure 1. (A) Friction curves of pure serpentinite, pure talc and various mixtures of talc and
371 serpentinite. Friction decreases sharply if the talc proportion is greater than 10%wt. But 5%wt of
372 talc is sufficient to cut-off the initial peak of friction in serpentinite. Some runs were stopped
373 prematurely after 60 rotations to get the microstructures of figure 2. The grey rectangle gives an
374 estimate the contribution of the Teflon ring to friction. (B) Summary of the experimental curves
375 obtained.

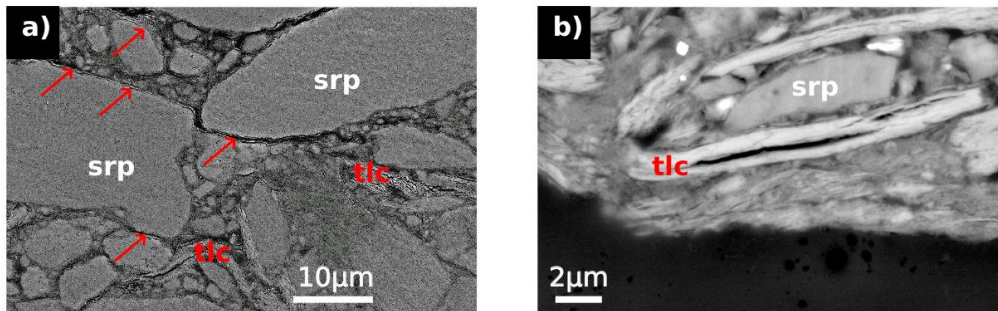
376



377

378 Figure 2. Microstructure of the sliding zone after 3 m of slip observed with a FE_SEM. (A) Pure
 379 serpentinite with a 100 μm-wide Principal Shear Zone (PSZ). White grains are magnetite (iron
 380 oxyde). (B) Focus on the sharp boundary between the PSZ and the main gouge. (C) Zoom on the
 381 submicron grain constituting the PSZ matrix. (D) Mixture with 2.5%wt talc. The PSZ is thinner
 382 but the texture is still similar to the pure serpentinite case. On this photograph, the heterogeneous
 383 color contrast of the serpentinite grains is due to the fact that serpentinite grains are aggregates of
 384 small crystals. (E) Mixture with 5% talc. Comminution of serpentine grains within the PSZ is
 385 reduced. Grains of talc coat the serpentine grains (red arrows). (F) Mixture with 30%wt talc.
 386 There is no developed PSZ, but there are many shear planes characterized by alignment of talc
 387 grains (red arrows).

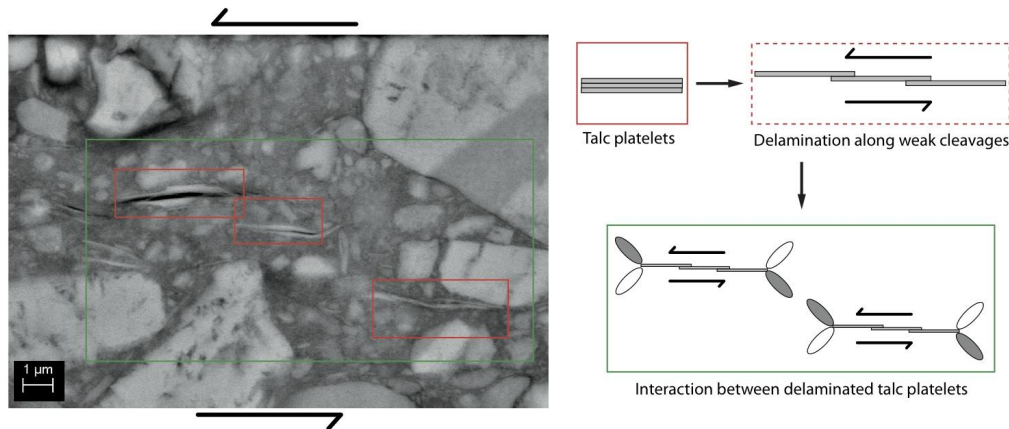
388



389

390 Figure 3. FE-SEM observation of coating of serpentinite grains by talc. The red arrows point to
 391 the thin delaminated talc located at key grain-to-grain contacts. The observations were done on
 392 samples with 3 m in displacement. (a) With 10% talc, a thin layer of delaminated talc (red
 393 arrows) coats the serpentinite clasts (b) With 30% talc, a thick talc can cover and cushion a
 394 whole serpentinite grain.

395

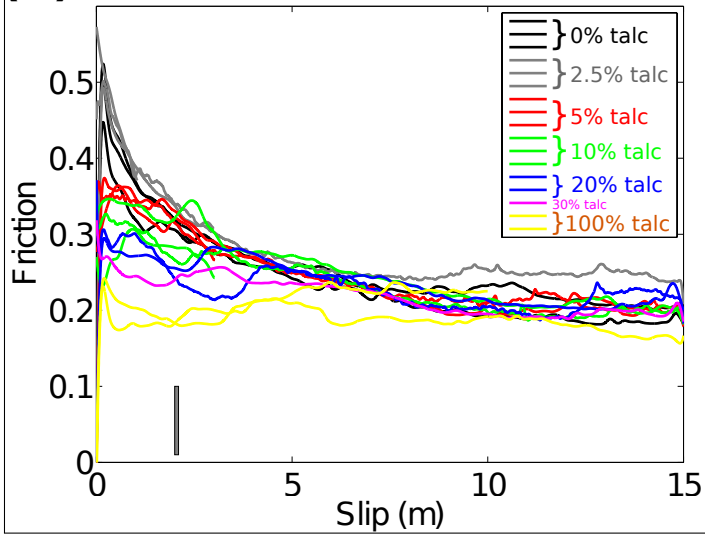


396

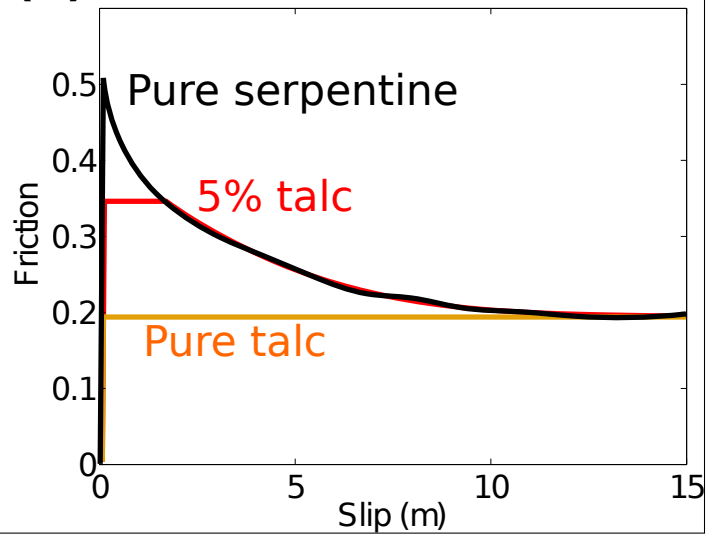
397 Figure 4. Strain localization by talc. (A) SEM image for a 2.5%wt talc with only 1 m in
 398 displacement. (B) Schematic diagram of the shear plane development along talc. All stages of
 399 development are exemplified in the SEM image.

400

(A) [Click here to download Figure: Fig1_new_summary.pdf](#)



(B)



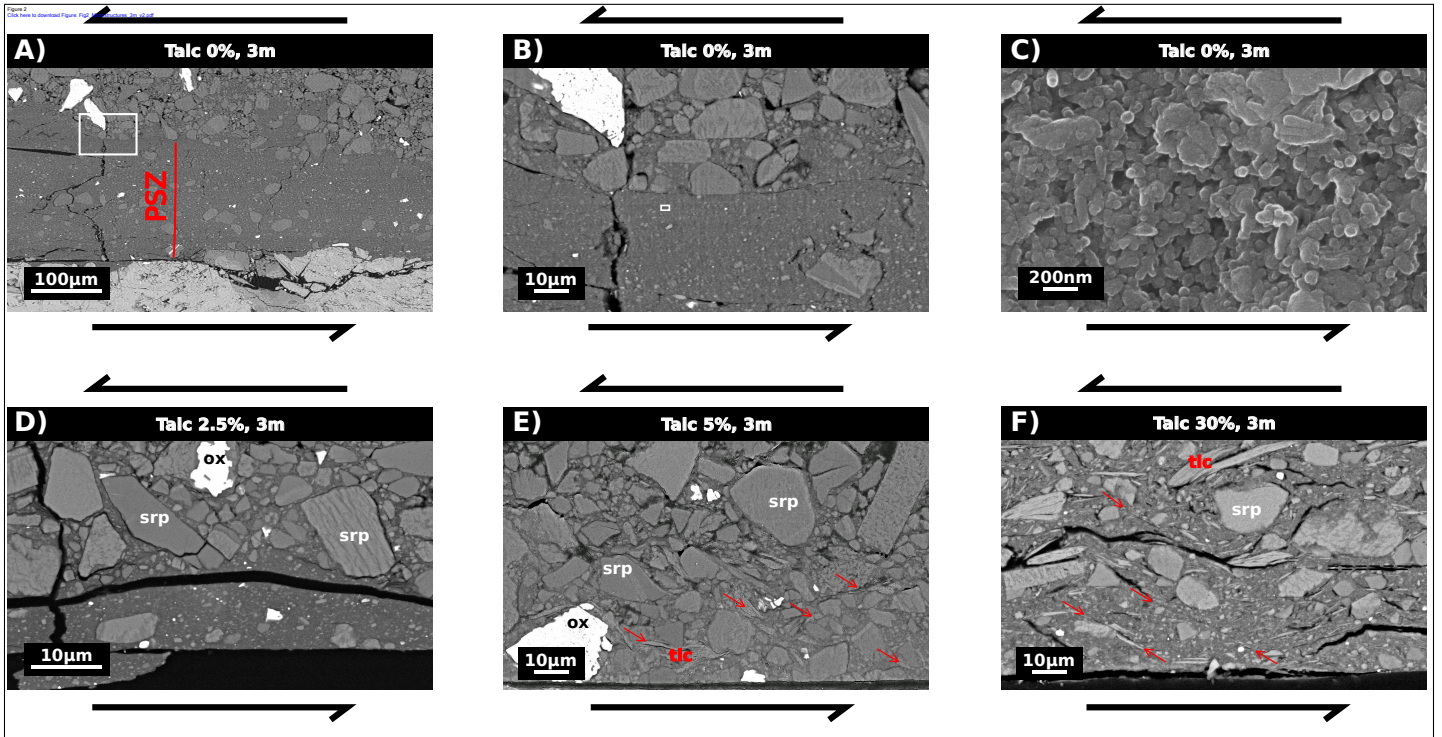


Figure 3
[Click here to download Figure 3 \(1000x1000px\)](#)

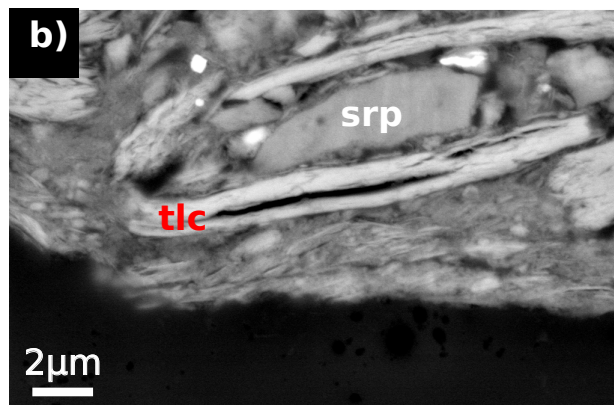
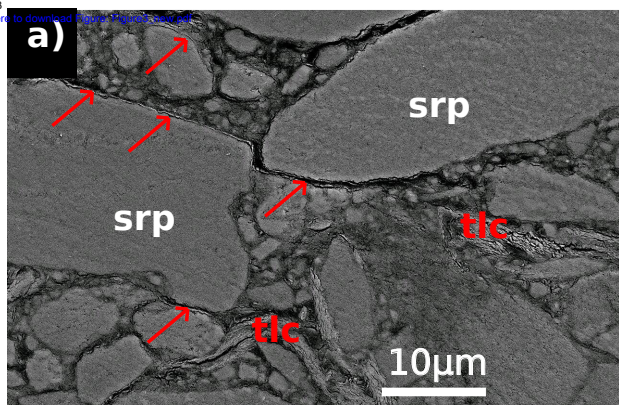
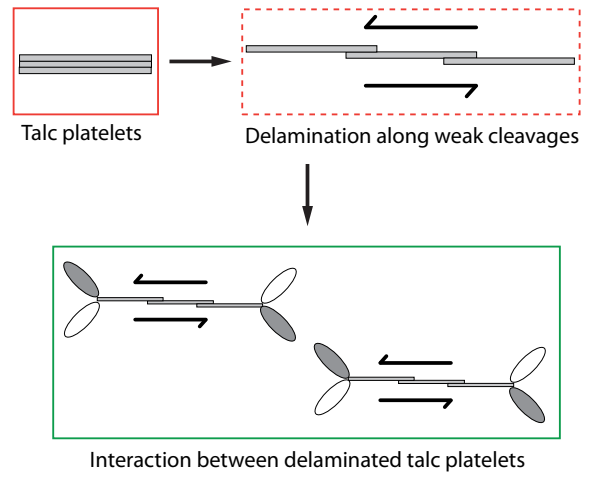
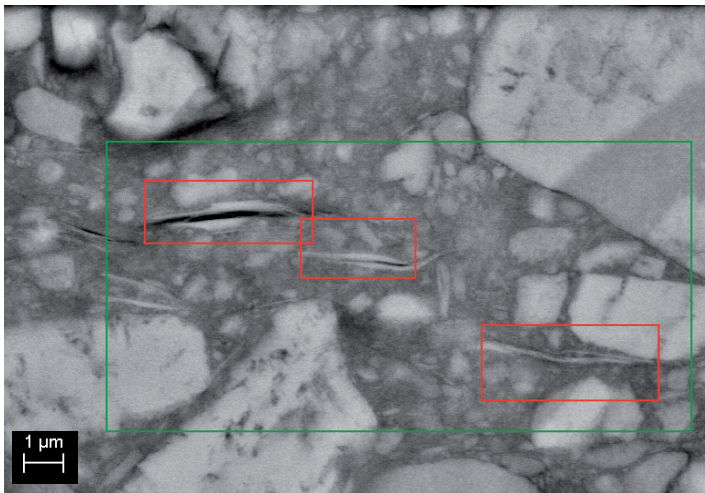


Figure 4

[Click here to download Figure: Fig4_Localization.pdf](#)



C.2 High strain rate damage

Rock pulverization at high strain rate near the San Andreas fault

Mai-Linh Doan^{1*} and Gérard Gary²

In the damage zone around faults, strain is usually localized along fractures, whereas the blocks enclosed by the fractures remain relatively undamaged^{1,2}. Some rocks near the San Andreas fault, however, are pervasively pulverized at distances of up to 400 m from the fault's core³; intense fragmentation at such distances is rarely observed along other fault zones. Moreover, these rocks preserve their original grain shapes, indicating that they experienced low total strain³. Here we use laboratory experiments to show that the intense fragmentation of intact rocks sampled near the San Andreas fault requires high rates of strain ($>150\text{ s}^{-1}$). Our calculations suggest that the combination of the low amount of strain experienced by the pulverized rocks and the high rates of strain indicated by our experiments could be explained by a supershear rupture—a rupture that propagated along the fault at a velocity equal to or greater than that of seismic shear waves.

Northeast of Los Angeles, the Mojave segment of the San Andreas fault shows unusual fault damage. Outcrops have patches of rock finely broken to a scale smaller than the initial grain size of about 1.5 mm; the damage pattern affects mainly crystalline rock that is not extensively weathered, and has only minor clay content^{4,5}. Whereas grain comminution and gouge formation are common within the fault core, where much of the strain occurs, intense pulverization so far from the fault core is unexpected. Here we investigate the role of dynamic loading on the pulverization of rocks near the San Andreas fault by carrying out laboratory experiments on rocks sampled near the fault. We then discuss the implications of these results for the physics of earthquakes.

Dynamic pulverization is a process in which stress localization is inhibited, so that the entire medium can be finely fractured⁶. Strain localization is the consequence of an unstable feedback: the largest pre-existing crack within the material is the most favourable for further fracture propagation, and once extended, it becomes even more amenable to further propagation. As a result, this crack extends at the expense of the others. However, at higher loading rates, this localization process may be inhibited. The favoured crack propagates at a finite rate, limited by the P-wave speed of the medium, and cannot accommodate all of the energy provided to the medium. Other fractures can propagate simultaneously and coalesce to produce numerous small fragments. The sample eventually becomes pulverized⁶.

Dynamic pulverization has already been considered along faults⁷. However, the theory of Reches and Dewers⁷ results in high strain rates for gouge in the fault core, but in much smaller strain rates at several tens of metres away from the core (see Supplementary Discussion). To understand the effect of strain rate on the damage mode, we conducted experiments aimed at understanding the effect of high strain rates on the fragmentation of intact rocks sampled near the pulverized zone of the San Andreas

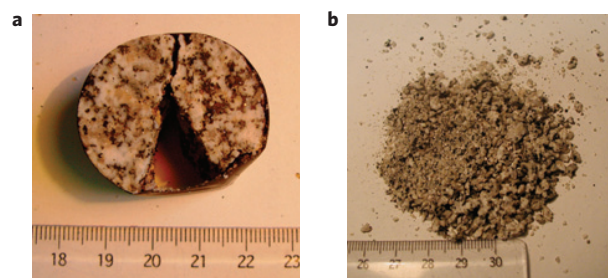


Figure 1 | States of the samples after the experiments. **a**, At a low strain rate (here, 140 s^{-1}), a rock sample splits into a few fragments when deformed in the SHPB apparatus. **b**, At a higher strain rate (here, 400 s^{-1}), the sample was pulverized into numerous fragments with a diameter smaller than the rock initial grain size. The rulers show centimetres.

fault (Supplementary Figs S5 and S6). The experiments were carried out using a split Hopkinson pressure bar (SHPB) apparatus⁸ in the Laboratoire de Mécanique des Solides of the École Polytechnique, Palaiseau, France. This technique⁹ gives average stress, strain and strain rate in the sample for strain rates as large as $2,000\text{ s}^{-1}$. Details are given in the Methods section.

Experimental results yielded three types of final state (Figs 1 and 2): (1) an unbroken state, where insufficient loading did not allow the sample to break; (2) a simple fracturing state, where a sample was split by a few (at most three) longitudinal fractures—a common damage pattern for uniaxial loading at low strain rate; and (3) a multiple fragmentation state, when the sample was broken into multiple fragments, some with a size smaller than 1 mm. The experiments carried out at a strain rate higher than 150 s^{-1} produced finely broken samples, whereas those carried out below 100 s^{-1} gave samples broken into two or three fragments (Fig. 2). The interval of strain rate (100 s^{-1} – 150 s^{-1}) delimits a transition zone between fracturing and pulverization. In this interval, the maximum stress varies from 50 to 100 MPa, with no clear jump.

We now discuss the pertinence of the laboratory results to explain the natural pulverization. As the tested samples were collected in the damage zone of the San Andreas fault, their Young's modulus is small ($10 \pm 3\text{ GPa}$, about one fifth of the tabulated value for granite¹⁰). The static strength of the material ranges between 50 and 90 MPa, about half the tabulated values for intact granite¹¹. These low values suggest that the initial samples were already damaged. This is confirmed by microstructural studies (see the Methods section and Supplementary Figs S7 and S8). All of these cracks competed with the most favourable crack and helped to prevent strain localization along a single fracture. Consequently, we estimate that our threshold strain rate is a minimum value for the transition to fine fragmentation in the field. To verify

¹Laboratoire de Géophysique Interne et Tectonophysique—CNRS—OSUG, Université Joseph Fourier Grenoble I, BP 53, F-38041 Grenoble, France,

²Laboratoire de Mécanique des Solides, Ecole Polytechnique, F-91128 Palaiseau, France. *e-mail: Mai-Linh.Doan@obs.ujf-grenoble.fr.

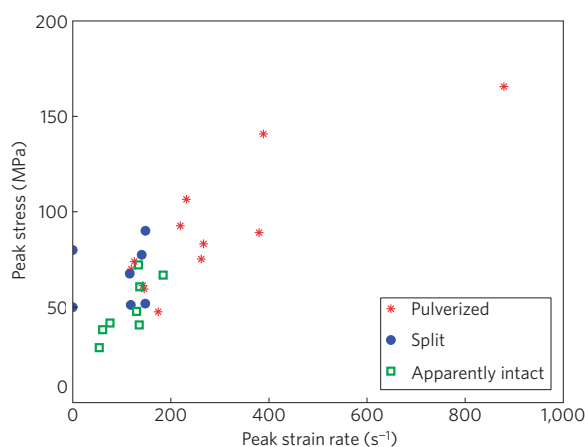


Figure 2 | Experimental results. The final state relative to the peak stress and the peak strain rate. The transition from single crack fracture (blue circles; Fig. 1a) to intense pulverization (red stars; Fig. 1b) depends on strain rate. The threshold occurs between 100 s^{-1} and 150 s^{-1} . Some samples remained unbroken (green squares).

the dependence of our results on the initial damage state, we carried out similar experiments on intact granite samples from Tarn, France (Supplementary Figs S9 and S10). We found a similar transition from sparse fracturing to fragmentation, but at a higher strain rate, about 250 s^{-1} . The fragmentation happens during the first loading (Fig. 3).

Our transition not only delimits different final damage patterns, but also corresponds to an increase in the apparent strength of the sample. These experimental results are in accordance with the statistical theory of Hild¹² for the transition from single to multiple fracturing regimes. In both theory and experiment, rock strength starts to increase with strain rate, once in a pulverization regime. Theoretically, there is an intrinsic increase of the material strength¹³, because the propagation of several small fractures requires more energy than that of a single large fracture. Experimentally, the sample does not instantaneously expand laterally at high strain rates, and hence is dynamically confined. When computing the equivalent constraining stress¹⁰, we retrieve dynamic confining pressures in the range of 2–10 MPa, corresponding to a burial depth of only 80–400 m. This suggests that pulverization may also be found in the shallow subsurface, as confirmed by borehole studies¹⁴.

Grain size analyses were carried out on fractured and pulverized rocks (see the Methods section and Supplementary Tables S2 and S3). Most particles have millimetric dimensions, a little larger than the grain size of pulverized rocks⁵. We do not claim to reproduce the exact state of pulverized rocks, especially its grain size distribution. The natural state is certainly the result of several earthquakes, each one damaging rocks by compressional and shear loading waves. Here, we focus only on the transition between localized fracturing and pervasive fragmentation.

We focused on dynamic pulverization to explain pulverization near faults. Other mechanisms may inhibit the strain localization process. One is the ductile–fragile transition at high confining stress or high temperature¹⁵. However, both parameters are below the transition values (300 MPa, $350 \text{ }^\circ\text{C}$; ref. 15) for crystalline rocks at the ground surface. A second way to inhibit strain localization is to apply fast rotating stress. The sheared zones are then reworked over and over, so that the strain localization is annealed at the expense of the formation of preferential microstructure orientation¹⁶. This mechanism requires large strain, which is not observed in the pulverized rocks from the San Andreas fault because they preserve their original fabric.

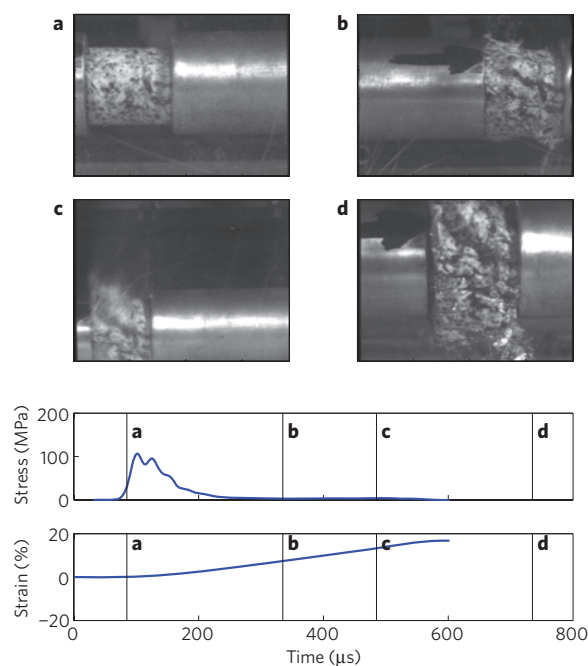


Figure 3 | Time-lapse snapshots of a sample being pulverized. The vertical bars **a–d** in the plots at the bottom denote the times corresponding to the photographs, taken with four independently triggered cameras. The measured stress and strain history is reported in the lower graphs. The sample breaks in an early stage (after **a**), but because of their inertia, the fragments fly away later (**b, c, d**). The sample is fragmented while in compression, and not during stress relaxation.

A high strain rate may be a necessary condition for pulverization, although perhaps not a sufficient condition. Other phenomena can also modulate the onset of pulverization. For instance, rupture along an interface separating material with different elastic moduli can induce tensile loading on only one side¹⁷. As tensile strength is small, damage is facilitated there. This may explain the asymmetry of damage along faults.

There are also some caveats in relating the laboratory experiments to the field observations. Our experiments were carried out under uniaxial loading. The transition strain rate depends on the speed of fracture propagation and on the interaction between cracks, which are controlled by the statistics of the initial crack population and the size of stress shadow zones around each crack. These parameters do not strongly depend on the fracture mode¹⁸. The fracture speed propagation is close to the S-wave speed c_s in all fracture modes. The shape of the stressed areas around a crack tip differs with fracture mode, but its size varies similarly, with stress decaying with distance from the fracture tip r as $1/r^{1/2}$. Hence, the transition from single to multiple fracturing is only weakly dependent on the fracture mode¹⁸. The strain rate condition obtained experimentally is a reasonable approximation to the natural case in that the sample is subject to both shear stress and normal stress.

Figure 2 suggests that the transition from fracturing to pulverization is related to strain rate. An important result of this study is that pulverized rocks appear as markers of high strain rate loading ($> 150 \text{ s}^{-1}$). This result needs to be evaluated in light of the fact that the initial structure of the pulverized rocks found in the field is preserved, which suggests that the pulverized rocks endured low strain.

To determine the conditions that are required to satisfy the twin constraints of high strain rate but low strain, we computed the strain rate and the stress near a crack tip propagating at a constant velocity. Considering distances from the fault ($r = 100 \text{ m}$) that are small relative to the rupture size (more than 10 km), we calculate

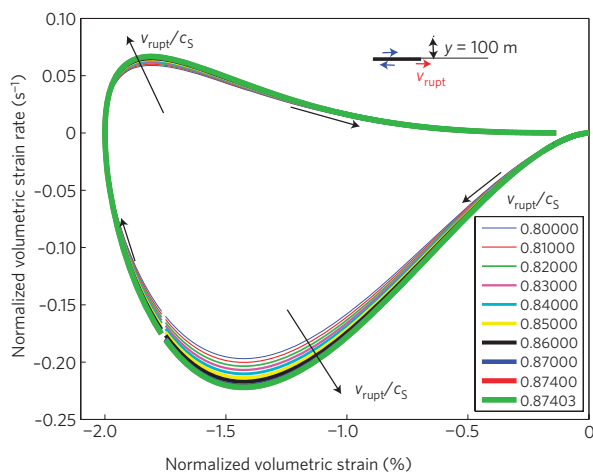


Figure 4 | Dilatational strain rate versus dilatational strain induced by a subshear rupture 100 m from the fault core. We normalized both the strain and strain rate so that the maximum strain amplitude is 2%, corresponding to the order of magnitude of the maximum strain in the pulverized rocks near the San Andreas fault. The curves were computed in plane stress for several rupture speeds, all below the Rayleigh wave speed (here $c_R \sim 0.8740301c_S$). All curves achieve a maximum strain rate less than 0.25 s^{-1} , three orders of magnitude below our experimental 150 s^{-1} pulverization threshold.

an asymptotic development of stress, dependent on the distance to the rupture tip (see Supplementary Discussion for details of the calculations). The first terms of strain and strain rate for a rupture speed below the S-wave speed (subshear rupture) decay as $1/r^{1/2}$ and $1/r^{3/2}$, respectively¹⁹. Figure 4 gives the shear strain rate of rocks located 100 m from the fault supposing that the maximum strain is 2%, a value we believe is representative of the maximum strain sustained by the pulverized rocks. The maximum strain rate remains two orders of magnitude below the experimental threshold strain rate permitting pulverization. Other terms of the Taylor expansion of strain²⁰ give similar or lower strain rates for strains less than 2%. Attaining the experimental threshold is therefore unlikely for subshear rupture in homogeneous material.

In the previous calculation, we made two hypotheses: a homogeneous medium and a subshear rupture. For faults separating two different media, a sharp tensile pulse can be generated in the stiffest part of the fault^{21,22}. If the Weertman pulse induces pulverization, we expect to find pulverized rocks along faults separating different materials, with no evidence for compression. However, pulverized sandstone along the San Andreas fault shows compression features²³. Pulverized rocks are sometimes found on both sides of the San Andreas fault³. Hence, we propose that an alternative mechanism, supershear rupture, generates the high strain rate and pulverizes rocks.

Supershear rupture induces a shock wave. Simple models yield Heaviside functions, modelling sharp fronts and with small decay with distance¹⁹ (see Supplementary Discussion for details). High rates of loading can be reached 100 m from the fault core, as supershear rupture induces a shock wave²⁴ and generates high-frequency displacements²⁵. This is consistent with the discovery of pulverized rocks only near large strike-slip faults: San Andreas and San Jacinto faults in California^{3,5,23}, Northern Anatolia fault in Turkey²⁶, Arima-Takatsuki fault in Japan²⁷, which are the most amenable to supershear rupture. We predict that off-fault pulverization should only be found along large strike-slip faults, and this provides a way to test our hypothesis in the future.

This work offers constraints on the formation of pulverized rocks, which endured deformation rates higher than 150 s^{-1} .

As possible indicators of previous supershear rupture, and independent of seismological observations, pulverized rocks should therefore be considered in the risk assessment of such potentially damaging earthquakes.

Methods

We experimentally damaged rocks sampled near the pulverized zone at high strain rate, using an SHPB apparatus⁸ in the Laboratoire de Mécanique des Solides of the École Polytechnique, Palaiseau, France.

Samples. Samples were collected about 200 m away from the fault core, in the Lake Hughes area (see Supplementary Fig. S5). The rocks were strong enough to be cored. We used this rock material to approximate pulverized rocks as it was before pulverization: the same material, not yet pulverized, but still damaged, as they lay near an active fault.

The samples were taken as boulders in the flanks of a deep gully. As they lay above the bottom of the gully, we assume the boulders were not transported by water, but rather that they fell by gravity from the edges of the gully. The flanks are quite steep, so that the originating outcrops could not be investigated.

Thin sections of the samples (Supplementary Figs S7 and S8) show alteration and dense microfracturing. Hence, we also used samples of Tarn granite, as a supplementary testing. Thin sections in Supplementary Fig. S8 show that the granite is slightly altered but less fractured than the samples from the San Andreas fault.

Experimental device. The experiments were carried out using the device shown in Supplementary Fig. S2. Each sample is inserted between two bars and impacted by a 'striker' arriving with a known speed. The incident stress wave splits into reflected and transmitted waves when it reaches the sample. Incident and reflected waves are measured with a strain gauge on the input bar, and the transmitted wave with a strain gauge on the output bar. Subsequent waves are not recorded as they are superposed at gauge locations and cannot be easily identified.

Processing. Classical processing of the SHPB supposes one-dimensional (1D) propagation of an elastic wave, given the dimensions of the bars (3 m long and 4 cm diameter). Here, we use a very precise measurement of time (with modern data acquisition systems) and a very precise 3D modelling of the wave propagation in bars (based on the Pochhammer and Chree equations) for the computation of forces and displacements at both ends of the specimen. We checked that the forces were identical at the input and output bars, to verify that the sample was homogeneously loaded. Once the quasi-equilibrium of the specimen was verified (equality of input and output forces), we calculated stress, strain and strain rate. A direct measurement of Young's modulus of the specimen is also possible, based on the transient 1D analysis of the test.

Grain size distribution. Some samples were wrapped inside a loose plastic bag attached to the input and output bars of the SHPB apparatus. This allowed us to limit the loss of material during the pulverization of the sample and to conduct grain size analysis (see Supplementary Tables S2 and S3). The grain size distribution of the larger grains was determined by manual sieving by shaking a stack of sieves for 2 min.

Errors in grain size distribution are mainly due to loss of material, which is about 1 g for an initial sample of 25 g. This is also the range of weights measured for each sieve. Hence, the weight of each particle size bin may be underestimated by 100%. Theoretically, all size bins are affected. However, fragmentation experiments produce a large dust cloud that could not be recovered. The contributions of the smallest particles were almost certainly the most underestimated.

Sieving methods measure weight and are biased towards the largest particles, because weight scales as the cube of the particle size. It is therefore difficult to make a quantitative comparison with the natural grain size distribution obtained with a laser granulometer that counts particle number⁵. Still, qualitatively, our grain size is larger than the natural grain size distribution of pulverized rocks, but smaller than the original grain size of our samples.⁷

Modal analysis. We carried out modal analysis of two thin sections drilled within a sample taken near Lake Hughes outcrop (see Supplementary Fig. S5), and one thin section drilled within a sample of Tarn granite. The modal analysis of each thin section was conducted by identifying the mineral located at 315 random points within the thin section. The error estimation can be quantified using the central limit theorem²⁸. If a mineral is found n times for N point counts, the upper limit of the 95% confidence interval is computed as

$$P^u = 100 * \beta(1 - \alpha, n + 1, N - n)$$

where $\alpha = 1 - 0.95$ and β is the inverse of the beta cumulative distribution function. The lower bound of the 95% confidence interval is computed as

$$P_l = 100 * [1 - \beta(1 - \alpha, N - n + 1, n)]$$

Received 18 February 2009; accepted 27 August 2009;
published online 27 September 2009

References

- Caine, J. S., Evans, J. P. & Forster, C. B. Fault zone architecture and permeability structure. *Geology* **24**, 1025–1028 (1996).
- Chester, F. M., Evans, J. P. & Biegel, R. L. Internal structure and weakening mechanisms of the San Andreas fault. *J. Geophys. Res.* **98**, 771–786 (1993).
- Dor, O., Ben-Zion, Y., Rockwell, T. K. & Brune, J. N. Pulverized rocks in the Mojave section of the San Andreas fault zone. *Earth Planet. Sci. Lett.* **245**, 642–654 (2006).
- Wilson, B., Dewers, T., Reches, Z. & Brune, J. Particle size and energetics of gouge from earthquake rupture zones. *Nature* **434**, 749–752 (2005).
- Rockwell, T. K. *et al.* Granulometric and mineralogical properties of pulverized rocks from Tejon Pass on the San Andreas fault and from Tejon Ranch on the Garlock fault, California. *Pure Appl. Geophys.* (in the press).
- Grady, D. E. & Kipp, M. E. in *Fracture Mechanics of Rocks* (ed. Atkinson, B. E.) (Academic, 1989).
- Reches, Z. & Dewers, T. A. Gouge formation by dynamic pulverization during earthquake rupture. *Earth. Planet. Sci. Lett.* **235**, 361–374 (2005).
- Kolsky, H. *Stress Waves in Solids* (Dover Publications, 1963).
- Zhao, H. & Gary, G. On the use of SHPB techniques to determine the dynamic behavior of materials in the range of small strains. *Int. J. Solids Struct.* **33**, 3363–3375 (1996).
- Forrestal, M. J., Wright, T. W. & Chen, W. The effect of radial inertia on brittle samples during the split Hopkinson pressure bar test. *Int. J. Impact Eng.* **34**, 405–411 (2007).
- Lide, D. R. (ed.) in *CRC Handbook of Chemistry and Physics: A Ready-Reference Book of Chemical and Physical Data* 88th edn (Boca Raton, 2008).
- Hild, F., Forquin, P. & Cordeiro da Silva, A. R. Single and multiple fragmentation of brittle geomaterials. *Rev. Franco. Gen. Civ.* **7**, 973–1003 (2003).
- Li, Q. M. & Meng, H. About the dynamic strength enhancement of concrete-like materials in a split Hopkinson pressure bar test. *Int. J. Solids Struct.* **40**, 343–360 (2003).
- Wechsler, N., Allen, E. E., Rockwell, T. K., Chester, J. & Ben-Zion, Y. Characterization of pulverized granite from a traverse and a shallow drill along the San Andreas fault, Little Rock, CA. *Seismological Society of America Annual Meeting, Seismol. Res. Lett.* **80**, 319 (2009).
- Guéguen, Y. & Palciauskas, V. *Introduction to the Physics of Rocks* (Princeton Univ. Press, 1994).
- Bystricky, M., Kunze, K., Burlini, L. & Burg, J. P. High shear strain of olivine aggregate: Rheological and seismic consequences. *Science* **290**, 1564–1567 (2000).
- Ben Zion, Y. & Andrews, D. J. Properties and implication of dynamic rupture along a material interface. *Bull. Seismol. Soc. Am.* **88**, 1084–1094 (1998).
- Huang, C., Subhash, G. & Vitton, S. J. A dynamic damage growth model for uniaxial compressive response of rock aggregates. *Mech. Mater.* **34**, 267–277 (2002).
- Freund, L. B. *Dynamic Fracture Mechanics* (Cambridge Univ. Press, 1990).
- Xu, Y. & Keer, L. M. Higher order asymptotic field at the moving crack tip. *Int. J. Fracture* **58**, 325–343 (1992).
- Ben-Zion, Y. Dynamic ruptures in recent models of earthquake faults. *J. Mech. Phys. Solids* **49**, 2209–2244 (2001).
- Andrews, D. J. & Ben-Zion, Y. Wrinkle-like slip pulse on a fault between different materials. *J. Geophys. Res.* **102**, 553–571 (1997).
- Dor, O., Chester, J. S., Ben-Zion, Y., Brune, J. N. & Rockwell, T. K. Characterization of damage in sandstones along the Mojave section of the San Andreas Fault: Implications for the shallow extent of damage generation. *Pure Appl. Geophys.* **166**, doi:10.1007/s00024-009-0516-z (2009).
- Rosakis, A., Samudrala, O. & Coker, D. Cracks faster than the shear wave speed. *Science* **284**, 1337–1340 (1999).
- Bizarri, A. & Spudich, P. Effects of supershear rupture speed on the high-frequency content of S waves investigated using spontaneous dynamic rupture models and isochrone theory. *J. Geophys. Res.* **113**, B05304 (2008).
- Dor, O. *et al.* Geological and geomorphologic asymmetry across the rupture zones of the 1943 and 1944 earthquakes on the North Anatolian fault: Possible signals for preferred earthquake propagation direction. *Geophys. J. Int.* **173**, 483–504 (2008).
- Mitchell, T. M., Shimamoto, T. & Ben-Zion, Y. Pulverized fault rocks along the Arima-Takatsuki Tectonic line, Japan: Fault structure, damage distribution and textural characteristics. *EGU General Assembly, Geophys. Res. Abstr.* **11**, EGU2009-11751-2 (2009).
- Howarth, R. J. Improved estimators of uncertainty in proportions, point-counting, and pass-fail test results. *Am. J. Sci.* **298**, 594–607 (1998).

Acknowledgements

We thank R. Barre, C. Rousseau, J.-B. Toni, R. Leau and R. Guiguet for their technical help and F. Hild, K. Safa, M. Bouchon and P. Favreau for discussions on this paper; V. D'Hour made preliminary work on Tarn granite. We thank E. Brodsky, F. Renard, J.-P. Gratier, Y. Ben-Zion, S. Boutareaud, P. Molnar and R. Hellmann for reading previous drafts of this manuscript. This work was financially supported by the 3F INSU/CNRS program and by the PPF 'Systèmes Complexes' of the University Joseph Fourier.

Author contributions

M.L.D. proposed and participated in the experiments, processed the data and made the computations. M.L.D. also made the grain size distribution measurements and modal analysis. G.G. developed the SHPB apparatus at the École Polytechnique and was in charge of the experiments.

Additional information

Supplementary information accompanies this paper on www.nature.com/naturegeoscience. Reprints and permissions information is available online at <http://npg.nature.com/reprintsandpermissions>. Correspondence and requests for materials should be addressed to M.L.D.

High strain rate damage of Carrara marble

Mai-Linh Doan¹ and Andrea Billi²

Received 4 August 2011; revised 2 September 2011; accepted 2 September 2011; published 8 October 2011.

[1] Several cases of rock pulverization have been observed along major active faults in granite and other crystalline rocks. They have been interpreted as due to coseismic pervasive microfracturing. In contrast, little is known about pulverization in carbonates. With the aim of understanding carbonate pulverization, we investigate the high strain rate (c. 100 s^{-1}) behavior of unconfined Carrara marble through a set of experiments with a Split Hopkinson Pressure Bar. Three final states were observed: (1) at low strain, the sample is kept intact, without apparent macrofractures; (2) failure is localized along a few fractures once stress is larger than 100 MPa, corresponding to a strain of 0.65%; (3) above 1.3% strain, the sample is pulverized. Contrary to granite, the transition to pulverization is controlled by strain rather than strain rate. Yet, at low strain rate, a sample from the same marble displayed only a few fractures. This suggests that the experiments were done above the strain rate transition to pulverization. Marble seems easier to pulverize than granite. This creates a paradox: finely pulverized rocks should be prevalent along any high strain zone near faults through carbonates, but this is not what is observed. A few alternatives are proposed to solve this paradox. **Citation:** Doan, M.-L., and A. Billi (2011), High strain rate damage of Carrara marble, *Geophys. Res. Lett.*, 38, L19302, doi:10.1029/2011GL049169.

1. Introduction

[2] Pulverized rocks have been recently identified near some major active faults [Dor et al., 2006, 2009; Mitchell et al., 2011] as a rare example of fault damage, where intense microfracturing occurred while the primary rock structure experienced a minimal distortion (i.e., no or minimal shear strain). Intense damage occurred at low shear strain and microfractures permeated the whole rock using original grain boundaries or crosscutting them, thus producing a very fine-grained material with most grains smaller than 1 mm.

[3] The origin of pulverized rocks is still debated. Their occurrence along major faults suggests a connection with fault mechanics and, in fact, experimental data suggest that pulverization is a marker of coseismic damage due to strong earthquakes [Doan and Gary, 2009]. Pulverized rocks may thus provide important clues to advance the understanding of earthquake physics and seismic faults [Reches and Dewers, 2005; Wilson et al., 2005; Dor et al., 2006; Yuan et al., 2011].

[4] The knowledge of natural pulverized rocks is, however, still very limited under many aspects. For instance, known occurrences of pulverized rocks are so far limited to only a

few sites and major faults (all strike-slip, with prominent bimaterial interfaces), namely along the San Andreas Fault system [Wilson et al., 2005; Dor et al., 2006; Rockwell et al., 2009; Wechsler et al., 2011], the Northern Anatolian Fault [Dor et al., 2008], and the Arima-Takatsuki Fault [Mitchell et al., 2011]. Interestingly, occurrence of pulverization is so far limited to a small number of lithologies, mainly crystalline rocks, with the exception of a sandstone outcrop along the San Andreas Fault [Dor et al., 2009].

[5] In carbonate rocks, finely-comminuted fault rocks with grains smaller than 1 mm occur in high shear strain zones (i.e., the fault core [e.g., Storti et al., 2003; Billi and Storti, 2004; Billi, 2005; Agosta and Aydin, 2006; Frost et al., 2009]). In contrast, low-strain, poorly-distorted, fault-related breccias are relatively common, but always in low-strain zones (i.e., the damage zone) and usually with large grains ($>1 \text{ cm}$) [Billi et al., 2003], much larger than for the usual pulverized rocks ($<1 \text{ mm}$). So far, the only exception is the carbonate fault rock observed in central Italy along a seismically-active normal fault cutting through shallow-water Mesozoic limestone, where finely comminuted rock (grains up to c. 1 cm in maximum size), interpreted as pulverized rock for the occurrence of apparently preserved layering, forms a 1-m-thick band running along the fault core on the footwall side [Agosta and Aydin, 2006]. The hangingwall is downthrown and buried so no information is available about a possible bimaterial interface effect. Moreover, the true origin of this rock (i.e., the pulverized limestone) has still to be conclusively ascertained by microscopic observations. Other reported cases of preserved carbonate rocks embedded within pulverized crystalline rocks [see Dor et al., 2006, Figure 5] suggest a scarce propensity of carbonates to pulverization.

[6] To understand why carbonates seem so little prone to pulverization, we ran high strain rate testing of carbonate rocks in the laboratory. As sedimentary carbonates are very heterogeneous, we focused our first study of carbonate dynamic pulverization on the most homogeneous and crystalline variety of carbonate (i.e., the Carrara marble; Figure 1a). Dynamic loading was done with a Split Hopkinson Pressure Bar apparatus [Chen and Song, 2010] to record the uniaxial behavior of samples at strain rates on the order of 100 s^{-1} .

[7] After presenting the experimental method, we relate the evolution of strength and damage pattern to strain and strain rate. We discuss the experimental results in light of the microstructural damage, before concluding on the relevance of our study to seismic faults in carbonates.

2. Method

[8] Experiments were done using a Split Hopkinson Pressure Bar (SHPB) apparatus in the Laboratoire de Mécanique des Solides of the École Polytechnique, Palaiseau, France. Each sample was inserted between two bars impacted by a

¹Institut des Sciences de la Terre, Université Joseph Fourier, Grenoble, France.

²IGAG, Consiglio Nazionale delle Ricerche, Rome, Italy.

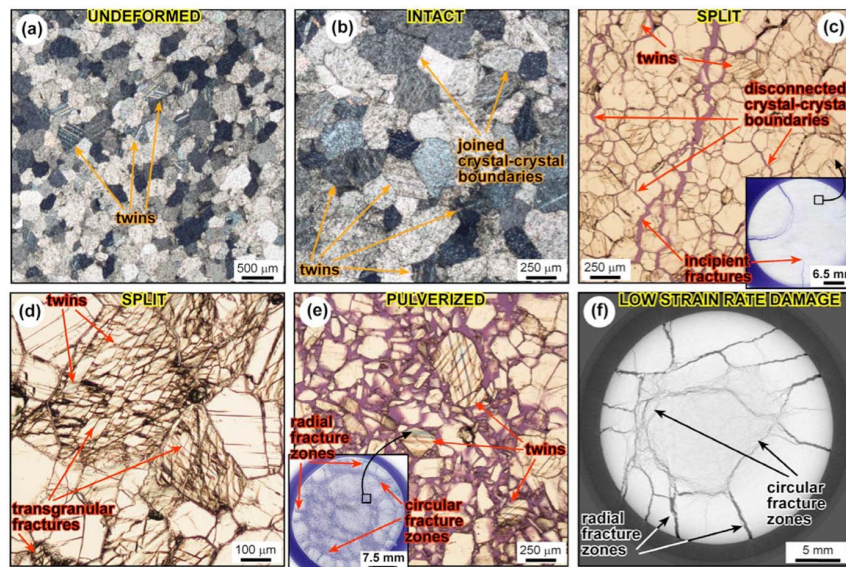


Figure 1. Microphotographs of Carrara marble samples. Figures 1b–1e are perpendicular to loading in the SHPB apparatus and Figure 1f is perpendicular to loading in the low strain rate apparatus. (a) Undeformed Carrara marble (crossed nicols). Note episodic calcite twinning. (b) Apparently intact sample M04 (crossed nicols). Note calcite twinning and joined boundaries between crystals. (c) Split sample M16 (parallel nicols). Note a rather pervasive incipient disarticulation of crystal-crystal boundaries. Inset shows a thin-section parallel and close to the input surface of the cylindrical sample M16. The large microphotograph is taken from the thin-section in the inset. Note the occurrence of incipient radial fractures and incipient disarticulation of crystal-crystal boundaries. At least in places, calcite twinning preceded fracturing as shown by twins cut by fractures. (d) Enlargement from split sample M16 (parallel nicols). Note transgranular fractures cutting through twinned non-distorted grains. (e) Pulverized sample M01 (parallel nicols). Inset shows a thin-section parallel and close to the input surface of the cylindrical sample M01. Note the radial and circular main fracture zones affecting the thin-section. The large microphotograph is taken from the thin-section in the inset and shows a complete disarticulation of the crystal-crystal boundaries plus fractures breaking the original grains, some of which contain calcite twins. (f) Damage pattern of Carrara marble subjected to low strain rate deformation. Note large strain (fractures) occurred under low strain rate.

striker bar arriving at a known velocity. The dimensions of the bars (length: 3 m; diameter: 4 cm) are so that the propagation of elastic waves in the bars is mainly one-dimensional [Gama *et al.*, 2004]. Using the first mode solution of the Pochhammer-Chree equation of wave propagation in bars, forces and displacements applied to the bar ends were retrieved from strain gauges glued on the bars. We checked that the forces were identical at the input and output bars to

ensure that the sample was homogeneously loaded. We could then derive the history of stress, strain, and strain rate experienced by the sample. Due to their short duration, experiments were not servo-controlled. The loading duration is related to the length of the striker bar. Hence, strain tends to increase with strain rate. We compensate for this drawback of the SHPB apparatus by changing the material of the bars and by varying the length of the striker.

Table 1. Summary of Experimental Data

Sample	Length (mm)	Diameter (mm)	Max. True Stress (MPa)	Max True Strain Rate (s^{-1})	Max True Strain (%)	Dissipated Volumetric Energy (MJ/m^3)	Rubber Jacket	Post-experiment State ^a
M01	28.06	25.62	121	202	3.38	2.03	yes	pulverized (red)
M02	27.65	25.64	110	209	3.64	1.88	yes	pulverized (red)
M03	28.65	25.97	103	120	1.82	1.18	yes	pulverized (red)
M04	28.75	25.59	66	42	0.38	0.12	yes	intact (green)
M05	28.31	25.66	101	140	2.19	1.39	yes	pulverized (red)
M07	28.64	25.61	110	205	3.49	1.74	no	pulverized (red)
M08	28.27	25.67	108	131	1.37	1.09	yes	pulverized (red)
M10	28.12	25.68	35	16	0.15	0.02	yes	intact (green)
M12	28.19	25.58	106	84	0.60	0.32	yes	intact (green)
M13	28.49	25.62	99	86	0.73	0.45	yes	split (blue)
M15	28.66	25.66	79	116	1.86	1.05	no	pulverized (red)
M16	28.22	25.63	110	91	0.98	0.74	no	split (blue)
M17	28.46	25.68	127	35	0.69	0.51	no	split (blue)
M18	27.74	25.69	129	68	1.66	1.36	no	pulverized (red)

^aColors in parentheses correspond to the classification of final macroscopic damage of Figure 3.

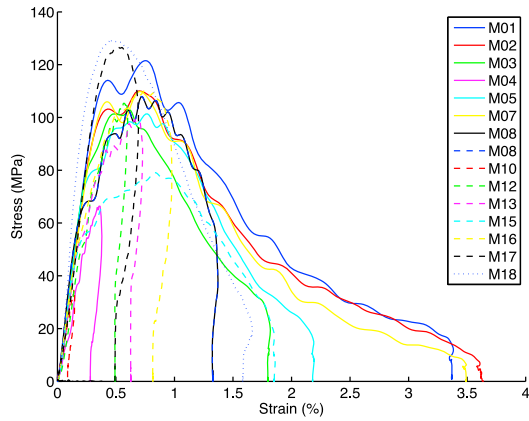


Figure 2. Experimental strain-stress curves of all samples. The peak stress is consistent for all the sample. The Young modulus is also similar, around 10 GPa.

[9] We deformed 14 cylindrical samples (length and diameter: c. 25 mm; Table 1) of Carrara marble. The fine grain size of the Carrara marble (c. 0.2–0.4 mm; Figure 1) is much smaller than the dimension of the sample. Some samples were jacketed with a rubber jacket to preserve and study the post-experiment deformation fabric. We then impregnated these samples with an indurative epoxy resin and cut them to analyze their fabric under an optical microscope (Figure 1).

[10] We also conducted a quasi-static uniaxial compressive test on a jacketed sample using a Schenk press located at the 3SR Laboratory in Grenoble, France, with a strain rate of 10^{-5} s^{-1} only. We used also the X-Ray CT scan tomography of the same laboratory to microstructurally investigate the sample after the quasi-static test (Figure 1f). Details on the

scanning apparatus and processing of data from the X-Ray CT Scan are similar to *Lenoir et al.* [2007].

3. Results

[11] With increasing strain and strain rate, we obtained three main post-experimental deformation fabrics (Table 1): (1) strongly cohesive, apparently intact samples (i.e., apparently intact or with one or two incipient fractures at the most; Figure 1b), (2) poorly cohesive, split samples (i.e., with some main fractures splitting the sample in a few large fragments; Figures 1c and 1d), and (3) uncohesive, pulverized samples (i.e., with diffuse microfractures and most fragments less than 1 mm in size; Figure 1e), where the distance between microfractures is about $500 \mu\text{m}$.

[12] Before failure, the samples experienced similar elastic loading phases (Figure 2), with a Young’s modulus of 20 GPa. The Young’s modulus is not sensitive to strain rate. Strength of the sample is about 100 MPa, similar to the strength recorded in the literature for low strain rate experiments on Carrara marble at room temperature and 5 MPa of confining pressure [*Fredrich et al.*, 1989]. Below the 100 MPa threshold, we do not see any macroscopic diffuse damage (Figures 1 and 3 and Table 1). Note that, in all experiments, there is a permanent strain (Figure 2) suggesting that inelastic processes occurred (e.g., twinning and microfracturing; Figure 1).

[13] Diagrams of strain and strain rate vs. the maximum stress attained in the samples as well as the diagram of strain vs. the energy dissipated in the experiments are shown in Figure 3. These experimental results show that, although an approximate trend toward pulverization with increasing strain rate is visible (see, for instance, results from samples M01, M02, M03, M07, M08, M05, and M15 in Table 1), unlike granite [*Doan and Gary, 2009; Yuan et al., 2011*], in the Carrara marble, the transition between split and pulverized

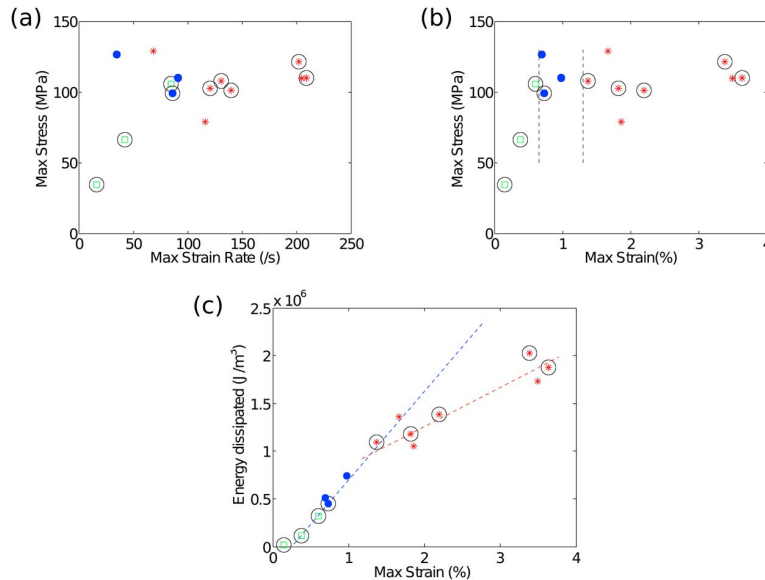


Figure 3. Phase diagrams of the macroscopic damage patterns. (a) Maximum strain rate vs. maximum stress. (b) Maximum strain vs. maximum stress. (c) Dissipated energy vs. maximum stress. Green squares, blue circles, and red asterisks indicate, respectively, apparently intact, split, and pulverized samples. Jacketed samples are indicated with a circle surrounding the damage symbol.

rocks with strain rate is not obvious (Figure 3a). Sample M18, for instance, is pulverized for a strain rate of 68 s^{-1} , whereas sample M13 is simply split by some main macroscopic fractures for a strain rate of 86 s^{-1} (Table 1). In contrast, the post-experiment damage pattern seems well correlated with the total strain accumulated (Figure 3b) rather than strain rate (Figure 3a). Macroscopic fractures appear in split samples when strain exceeds 0.65%, whereas intense microscopic fragmentation (pulverized samples) appears at strains beyond 1.3%. There is, therefore, a narrow interval during which a few macroscopic fractures develop (the interval between vertical dashed lines in Figure 3b). For higher strains, microscopic fractures pervade samples up to their pulverization (strain $> 1.3\%$) by primarily using crystal-crystal boundaries and, more rarely, cutting through crystals (Figure 1). Hence, marble pulverization is primarily controlled by strain rather than strain rate (Figure 3).

[14] In Figure 3, samples that were jacketed are plotted with circled symbols. Their final macroscopic state is the same as the final state of unjacketed samples loaded under the same conditions. Their strain-stress curve is also similar (Figure 2). Hence, jacketing has no effect on the mechanical results (Figure 3). We can safely analyze the sample microstructure and generalize to the whole dataset. The pertinence of our experimental results to explain the natural pulverization of carbonates is discussed in the following sections.

4. Damage Processes

[15] Carbonate rocks display both ductile and brittle behavior even at low confining pressure [Evans and Kohlstedt, 1995]. In our samples, calcite twinning (crystal-plastic deformation) is very moderate even in finely pulverized samples (Figure 1e). Moreover, limited twinning is present also in the undeformed marble (Figure 1a). Hence, plastic energy by twinning is not the main damage process and energy sink in our high strain rate experiments, where, in contrast, fractures play a major role in damage formation (Figure 1) and are most likely the main energy sink.

[16] In the apparently intact samples, the crystal-crystal boundaries appear (under the optical microscope) tightly joined (Figure 1b). In contrast, the same boundaries start to be diffusively disconnected in the split samples (Figure 1c) and become totally disconnected in the pulverized samples, where crystals are split apart from each other, and, in places, transgranular fractures split the original crystals into multiple subgrains (Figure 1e). In some cases, twinning predates fracturing (Figure 1c), whereas in other cases, fractures occur without shearing the pre-existing twins (Figure 1d).

[17] Without confining pressure, the sample splits naturally into several radial fractures. Figure 1c shows that the incipient fractures are radial fractures nucleated from the sample edge, a free surface where the inertial confinement effects [Forrestal *et al.*, 2004] are small. Tensional strength of rock is smaller than the compressional strength [Jaeger *et al.*, 2007] and radial pattern of tensile cracks forms finally. Such pattern has been also observed through X-Ray CT Scan on low strain rate experiments on sand [Desrues *et al.*, 1996] and sandstone [Bésuelle *et al.*, 2003]. This is not what is observed in pulverized samples of Carrara marble, where a new pattern of concentric fractures develops especially at high strain rates (Figure 1d). Several fractures propagate stress-shadowing

each other, a process theoretically predicted by statistical theory of high strain rate damage [Hild *et al.*, 2003].

[18] The pulverized samples finally experience very large lateral expansion. For instance, the final diameter of sample M01 (Figure 1e) is about 3 cm (compared to the initial diameter of 2.5 cm), corresponding to a lateral expansion of 20%, which is enormous compared to the final uniaxial strain experienced by this sample ($\sim 3.4\%$; Table 1). It means that the sample, once pulverized, is not cohesive anymore and, therefore, centrifugal motion of grains is favored rather than creating new fractures across the grains. This inference is also supported by energy dissipation data (Figure 3c) as demonstrated below.

[19] In order to understand the energy related to damage mechanism, we estimate dissipated energy during loading by computing the quantity $\int_0^\infty \sigma \dot{\epsilon} dt$. This quantity corresponds to the area below the stress-strain curves of Figure 2. The way dissipated energy evolves with strain or strain rate depends on the microphysics of damage. Figure 3c shows the dissipated energy vs. strain. Below a strain of 1.3%, both the intact and split samples align along the same line, with a slope of 103 MJ/m^3 . It indicates that the damage mechanism is predominantly proportional to strain, suggesting an incremental damage. For pulverized samples, with strain above 1.3%, the data align with a slope of only 44 MJ/m^3 . This smaller slope means that it is easier to further accommodate strain once rocks get pulverized. In other words, in Figure 3c, with increasing strain, samples switched from a cohesive “rock-like” behavior (steep slope) to a granular “gouge-like” behavior (gentle slope) [Ben-Zion *et al.*, 2011].

5. Application to Faults

[20] The above-discussed experimental results lead us to a few preliminary inferences about high strain rate damage in carbonates along seismic faults. In marble, to obtain the same degree of damage and fine grains as found in natural pulverized crystalline rocks [e.g., Dor *et al.*, 2006], strain larger than 1.3% is needed for a strain rate of about 100 s^{-1} (Figure 3). At low strain rate, uniaxial quasi-static testing of sample M14 up to a total strain of 3% gave a split samples, with a large number of fractures, but not a diffuse microfracturing throughout the entire sample (Figure 1f). This result confirms that pulverization along faults is a high strain rate feature, perhaps a coseismic marker. Then, what are the conditions for pulverization of Carrara marble during an earthquake? Our experimental results show that a minimum strain of 1.3% at about 100 s^{-1} is necessary (Figure 3b). Let us assume subshear propagation along a mode II rupture at constant velocity. We assume a pure elastic case, not taking into account any viscoelastic behavior within the process zone at the fracture tip. We use the same formulas as Reches and Dewers [2005] and Doan and Gary [2009], with a critical stress intensity factor K_{II} equal to $30 \text{ MPa m}^{1/2}$, as in Reches and Dewers [2005], and typical Lamé coefficients $\mu = \lambda = 4 \text{ GPa}$, so that the Young modulus is 10 GPa as for our intact Carrara marble (Figure 2). We then obtain Figure 4, which shows that strain rate of 100 s^{-1} is attainable at distances from the fault core lower than 25 cm. The elastic properties of rock from the damage zone around a fault can be down to 50% lower than the protolith [Faulkner *et al.*, 2006; Lewis and Ben-Zion, 2010], in which case high

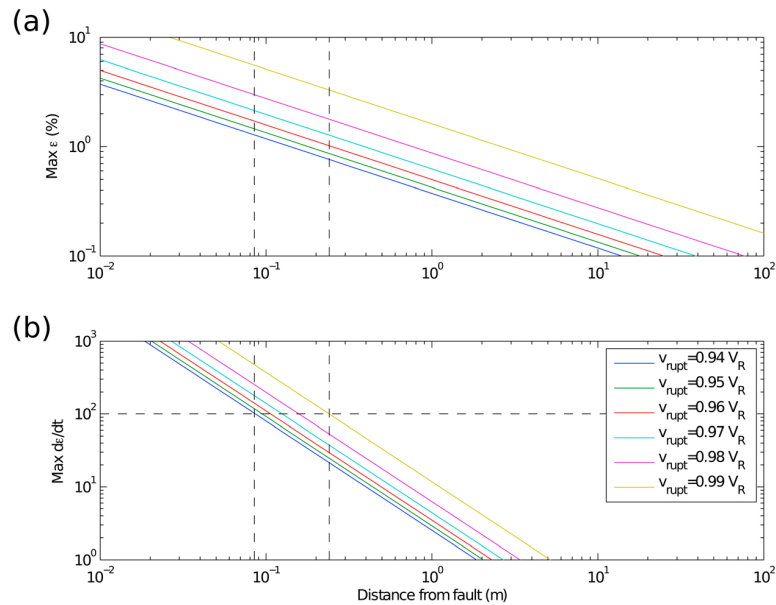


Figure 4. (a) Maximum strain and (b) strain rate experienced during an earthquake by a sample, depending on its distance to fault core. We assumed a subshear rupture of constant velocity v_{rupt} , proportional to the Rayleigh wave speed v_R . We used linear elastic fracture mechanics formalism, with critical stress intensity factor K_{II} equal to $30 \text{ MPa m}^{1/2}$, as by *Reches and Dewers* [2005], and typical Lamé coefficients $\mu = \nu = 4 \text{ GPa}$, corresponding to Young modulus of 10 GPa , as in Figure 2. Dashed lines in the distance vs. maximum strain rate diagram delimit the range of distances from the fault core where a strain rate of 100 s^{-1} is attained. At this distance, strain compatible with the limit strain of Figure 3 is attainable. Hence, pulverization of limestone is possible very close to the fault for a subshear rupture of constant velocity.

strain rate can be reached a little farther from the fault zone (for instance, for $\mu = \lambda = 1 \text{ GPa}$, a strain rate of 100 s^{-1} is attainable up to 40 cm away from the fault core; see auxiliary material).¹ This distance from the principal slip surface (40 cm) is usually well within the high shear strain zone (fault core) both in crystalline and in carbonate rocks [e.g., *Chester et al.*, 1993; *Frost et al.*, 2009]. Hence, it is probable that so close to the fault core, rock pulverization would be soon overprinted by the shear deformation leading to fault gouge development. This could be the case, in part, of the pulverized carbonate rocks signaled by *Agosta and Aydin* [2006] in central Italy. As pulverized rocks have been so far observed several tens of meters away from the fault core [Dor et al., 2006, 2009], exceptional earthquakes, like supershear earthquakes [Doan and Gary, 2009] or a sudden acceleration of the rupture front must be invoked to reach pulverizing high strain rates so far from fault cores.

6. Conclusions

[21] In this paper, we presented how Carrara marble is damaged under uniaxial loading at high strain rate ($c. 100 \text{ s}^{-1}$). At such strain rate, the transition from localized to diffuse damage is controlled by strain rather than strain rate and pulverization happens as soon as a strain above 1.3% is reached (Figure 3). This propensity for getting diffuse damage is paradoxical as pulverization is scarcely observed within carbonate rocks. To overstep this paradox, several explanations may be proposed. One is the fact that the Carrara

marble may not be so representative of sedimentary marine limestone, which is the main carbonate lithotype affected by faults in the crust [Billi et al., 2003; Agosta and Aydin, 2006; Woodcock and Mort, 2008]. An alternative explanation may simply be that carbonate pulverization occurs very close to fault cores (Figure 4), where, subsequently, shear deformation masks all pulverization effects. In the case of bimaterial faults, the dissymmetry in elastic properties on each side of the fault leads to a weaker loading on the weaker side [Ben-Zion and Andrews, 1998]. More generally, damage can also affect the strength of the material. Experiments on granite, for instance, show that pulverizing rocks is easier as rocks accumulate damage through successive earthquakes (M.-L. Doan and V. d'Hour, Effect of initial damage on rock pulverization, submitted to *Journal of Structural Geology*, 2011). The efficiency of healing in carbonates at shallow depths [Renard et al., 2000, Hausegger et al., 2010] may explain the preserved carbonate outcrops observed within pulverized granite, as in the Lake Hughes area along the San Andreas Fault [Dor et al., 2006]. Hence, carbonate rocks may be preserved when juxtaposed with granite. In any case, the discussed paradox calls for further investigation on high strain rate damage of carbonates.

[22] **Acknowledgments.** We warmly thank Gérard Gary for allowing us to work on the Split Hopkinson Pressure Bars of Ecole Polytechnique, and for providing much advice on experimental issues. We thank Mimmo (Petrolab) for thin-sections. The experiments were performed with the equipment of Pascal Charrier and Jacques Desrues (3SR laboratory) for X-Ray tomography of low strain-rate sample, and Jean-Benoit Toni (3SR laboratory) for the low strain rate experiment. We acknowledge funding from INSU 3F and UJF TUNES programs. We thank Yehuda Ben-Zion, Jacques Desrues and Gérard Gary for improving earlier versions of the manuscript. We

¹Auxiliary materials are available in the HTML. doi:10.1029/2011GL049169.

thank Erik Frost for his review that enabled us improve our text about the damage around carbonate faults.

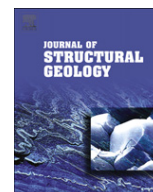
[23] The Editor thanks Erik Frost for his assistance in evaluating this paper.

References

- Agosta, F., and A. Aydin (2006), Architecture and deformation mechanism of a basin-bounding normal fault in Mesozoic platform carbonates, central Italy, *J. Struct. Geol.*, **28**, 1445–1467, doi:10.1016/j.jsg.2006.04.006.
- Ben-Zion, Y., and D. J. Andrews (1998), Properties and implication of dynamic rupture along a material interface, *Geol. Soc. Am. Bull.*, **88**, 1084–1094.
- Ben-Zion, Y., K. A. Dahmen, and J. T. Uhl (2011), A unifying phase diagram for the dynamics of sheared solids and granular materials, *Pure Appl. Geophys.*, doi:10.1007/s00024-011-0273-7.
- Bésuelle, P., P. Baud, and T.-F. Wong (2003), Failure mode and spatial distribution of damage in Rothbach sandstone in the brittle-ductile transition, *Pure Appl. Geophys.*, **160**, 851–868, doi:10.1007/PL00012569.
- Billi, A. (2005), Grain size distribution and thickness of breccia and gouge zones from thin (<1 m) strike-slip fault cores in limestone, *J. Struct. Geol.*, **27**, 1823–1837, doi:10.1016/j.jsg.2005.05.013.
- Billi, A., and F. Storti (2004), Fractal distribution of particle size in carbonate cataclastic rocks from the core of a regional strike-slip fault zone, *Tectonophysics*, **384**, 115–128, doi:10.1016/j.tecto.2004.03.015.
- Billi, A., F. Salvini, and F. Storti (2003), The damage zone-fault core transition in carbonate rocks: Implications for fault growth, structure and permeability, *J. Struct. Geol.*, **25**, 1779–1794, doi:10.1016/S0191-8141(03)00037-3.
- Chen, W., and B. Song (2010), *Split Hopkinson (Kolsky) Bar: Design, Testing and Applications*, Springer, Berlin.
- Chester, F. M., J. Evans, and R. Biegel (1993), Internal structure and weakening mechanisms of the San Andreas Fault, *J. Geophys. Res.*, **98**, 771–786, doi:10.1029/92JB01866.
- Desrues, J., R. Chambon, M. Mokni, and F. Mazerolle (1996), Void ratio evolution inside shear bands in triaxial sand specimens studied by computed tomography, *Geotechnique*, **46**, 529–546, doi:10.1680/geot.1996.46.3.529.
- Doan, M. L., and G. Gary (2009), Rock pulverization at high strain rate near the San Andreas Fault, *Nat. Geosci.*, **2**, 709–712, doi:10.1038/ngeo640.
- Dor, O., Y. Ben-Zion, T. K. Rockwell, and J. Brune (2006), Pulverized rocks in the Mojave section of the San Andreas Fault Zone, *Earth Planet. Sci. Lett.*, **245**, 642–654, doi:10.1016/j.epsl.2006.03.034.
- Dor, O., C. Yildirim, T. K. Rockwell, Y. Ben-Zion, O. Emre, M. Sisk, and T. Y. Duman (2008), Geological and geomorphologic asymmetry across the rupture zones of the 1943 and 1944 earthquakes on the North Anatolian Fault: possible signals for preferred earthquake propagation direction, *Geophys. J. Int.*, **173**, 483–504.
- Dor, O., J. S. Chester, Y. Ben-Zion, J. Brune, and T. K. Rockwell (2009), Characterization of damage in sandstones along the Mojave section of the San Andreas Fault: Implications for the shallow extent of damage generation, *Pure Appl. Geophys.*, **166**, 1747–1773, doi:10.1007/s00024-009-0516-z.
- Evans, B., and D. L. Kohlstedt (1995), Rheology of rocks, in *Rock Physics and Phase Relation: A Handbook of Physical Constants*, AGU Ref. Shelf, vol. 3, edited by T. J. Ahrens, pp. 148–165, AGU, Washington, D. C.
- Faulkner, D. R., T. M. Mitchell, D. Healy, and M. J. Heap (2006), Slip on ‘weak’ faults by the rotation of regional stress in the fracture damage zone, *Nature*, **444**, 922–925, doi:10.1038/nature05353.
- Forrestal, M. J., T. W. Wright, and W. Chen (2004), The effect of radial inertia on brittle samples during the split Hopkinson pressure bar test, *Int. J. Impact Eng.*, **34**, 405–411.
- Fredrich, J. T., B. Evans, and T.-F. Wong (1989), Micromechanics of the brittle to plastic transition in Carrara marble, *J. Geophys. Res.*, **94**, 4129–4145, doi:10.1029/JB094iB04p04129.
- Frost, E., J. Dolan, C. Sammis, B. Hacker, J. Cole, and L. Ratschbacher (2009), Progressive strain localization in a major strike-slip fault exhumed from midseismogenic depths: Structural observations from the Salzach-Ennstal-Mariazell-Puchberg fault system, Austria, *J. Geophys. Res.*, **114**, B04406, doi:10.1029/2008JB005763.
- Gama, B. A., S. L. Lopatnikov, and J. W. Gillespie Jr. (2004), Hopkinson bar experimental technique: A critical review, *Appl. Mech. Rev.*, **57**, 223–250, doi:10.1115/1.1704626.
- Hausegger, S., W. Kurz, R. Rabitsch, E. Kiechl, and F.-J. Brosch (2010), Analysis of the internal structure of a carbonate damage zone: Implications for the mechanisms of fault breccia formation and fluid flow, *J. Struct. Geol.*, **32**, 1349–1362, doi:10.1016/j.jsg.2009.04.014.
- Hild, F., C. Denoual, P. Forquin, and X. Brajer (2003), On the probabilistic-deterministic transition involved in a fragmentation process of brittle material, *Comput. Struct.*, **81**, 1241–1253, doi:10.1016/S0045-7949(03)00039-7.
- Jaeger, J., N. G. W. Cook, and R. Zimmerman (2007), *Fundamentals of Rock Mechanics*, 4th ed., Blackwell, Oxford, U. K.
- Lenoir, N., M. Bornert, J. Desrues, P. Bésuelle, and G. Viggiani (2007), Volumetric digital image correlation applied to X-ray microtomography images from triaxial compression tests on argillaceous rock, *Strain*, **43**, 193–205, doi:10.1111/j.1475-1305.2007.00348.x.
- Lewis, M. A., and Y. Ben-Zion (2010), Diversity of fault zone damage and trapping structures in the Parkfield section of the San Andreas Fault from comprehensive analysis of near fault seismograms, *Geophys. J. Int.*, **183**, 1579–1595, doi:10.1111/j.1365-246X.2010.04816.x.
- Mitchell, T. M., Y. Ben-Zion, and T. Shimamoto (2011), Pulverized fault rocks and damage asymmetry along the Arima-Takatsuki Tectonic Line, Japan, *Earth Planet. Sci. Lett.*, **308**, 284–297, doi:10.1016/j.epsl.2011.04.023.
- Reches, Z., and T. A. Dewers (2005), Gouge formation by dynamic pulverization during earthquake rupture, *Earth Planet. Sci. Lett.*, **235**, 361–374, doi:10.1016/j.epsl.2005.04.009.
- Renard, F., J.-P. Gratier, and B. Jamtveit (2000), Kinetics of crack-sealing, intergranular pressure solution, and compaction around active faults, *J. Struct. Geol.*, **22**, 1395–1407, doi:10.1016/S0191-8141(00)00064-X.
- Rockwell, T., M. Sisk, G. Girty, O. Dor, N. Wechsler, and Y. Ben-Zion (2009), Chemical and physical characteristics of pulverized Tejon Look-out granite adjacent to the San Andreas and Garlock faults: Implications for earthquake physics, *Pure Appl. Geophys.*, **166**, 1725–1746, doi:10.1007/s00024-009-0514-1.
- Storti, F., A. Billi, and F. Salvini (2003), Particle size distributions in natural carbonate fault rocks: insights for non self-similar cataclasis, *Earth Planet. Sci. Lett.*, **206**, 173–186.
- Wechsler, N., E. E. Allen, T. K. Rockwell, G. Girty, J. S. Chester, and Y. Ben-Zion (2011), Characterization of pulverized granitoids in a shallow core along the San Andreas Fault, Litterlock, CA, *Geophys. J. Int.*, **186**, 401–417, doi:10.1111/j.1365-246X.2011.05059.x.
- Wilson, B., T. Dewers, Z. Reches, and J. Brune (2005), Particle size and energetics of gouge from earthquake rupture zones, *Nature*, **434**, 749–752, doi:10.1038/nature03433.
- Woodcock, N. H., and K. Mort (2008), Classification of fault breccias and related fault rocks, *Geol. Mag.*, **145**, 435–440.
- Yuan, F., V. Prakash, and T. Tullis (2011), Origin of pulverized rocks during earthquake fault rupture, *J. Geophys. Res.*, **116**, B06309, doi:10.1029/2010JB007721.

A. Billi, IGAG, Consiglio Nazionale delle Ricerche, c.o. Dipartimento Scienze della Terra, Sapienza Università di Roma, P.le A. Moro 5, 00185, Rome, Italy.

M.-L. Doan, Institut des Sciences de la Terre, Université Joseph Fourier, 1381 rue de la Piscine, F-38041 Grenoble CEDEX, France. (mai-linh.doan@obs.ujf-grenoble.fr)



Effect of initial damage on rock pulverization along faults

Mai-Linh Doan*, Virginie d'Hour

ISTerre, CNRS, Université Joseph Fourier, BP53, 38041 Grenoble Cedex 9, France

ARTICLE INFO

Article history:

Received 3 October 2011

Received in revised form

8 May 2012

Accepted 12 May 2012

Available online 23 May 2012

Keywords:

Dynamic damage

Pulverized rocks

Active fault

High strain rate experiments

Weibull theory

ABSTRACT

Pulverized rocks have been found in the damage zone around the San Andreas Fault, at distances greater than 100 m from the fault core. This damage is atypical in that it is pervasive and strain is not localized along main fractures as expected at these distances from the fault core. With high strain rate experiments, the authors have previously shown that above a strain rate threshold, the localization of strain along a few fractures is inhibited. Pulverized rocks may be generated by seismic waves at high frequency. Here we generalize these conclusions by discussing the effect of the initial fracture network in the sample on the transition from strain localization along a few fractures to diffuse damage throughout the sample. Experimental data are compared with statistical theory for fracture propagation. This analysis shows that the threshold in strain rate is a power law of initial fracture density and that a pre-damaged rock is easier to pulverize. This implies that pulverized rocks observed on the field may result from successive loadings.

© 2012 Elsevier Ltd. All rights reserved.

1. Introduction

Pulverized rocks have been observed near the San Andreas Fault (Wilson et al., 2005; Dor et al., 2006, 2009), and other large strike slip faults: Garlock Fault (Rockwell et al., 2009), Northern Anatolian Fault (Dor et al., 2008), and Arima-Takatsuki Fault (Mitchell et al., 2011). These rocks are found in outcrops of pervasively damaged rocks, which are sometimes as wide as several hundreds of meters. Due to the intense fracturing, individual samples typically crumble into powder when compressed by hand. Rockwell et al. (2009) have shown that the samples are microfractured, resulting in angular fragments about 100 μm in size. These rocks are only moderately chemically altered, so that their weakness cannot be attributed to weathering. High strain is one mechanism to explain the multiplicity of fractures: energy input rate is so high that it could not be accommodated by only a few fractures. A key observation is that the extensive damage of pulverized rocks is associated with small overall strain (Fig. 1). A second explanation for the diffuse damage pattern is high strain rate. With a higher energy supply rate, a single fracture with limited propagation speed cannot accommodate all of the applied energy. At higher strain rate, the finite velocity of stress waves also limits the expansion of the stress shadow zone around a major fracture, and interaction between fractures differs from the low strain rate case (Grady and Kipp, 1989; Hild et al., 2003b).

Pulverized rocks are localized within a few kilometers of the fault, with damage typically increasing closer to the fault core (Mitchell et al., 2011). This suggests that pulverization is related to fault activity. The origin of pulverized rocks is still debated, but most theories assume they are related to coseismic damage. The rarity of pulverization suggests that it is induced by an exceptional event, either by the tensile pulse predicted for rupture along bimaterial interfaces (Andrews and Ben-Zion, 1995), or by the Mach cone of a supershear rupture (Doan and Gary, 2009). Doan and Gary (2009) have shown experimentally that high strain rate loading can generate features similar to pulverization. They used samples from the Lake Hughes area of the Mojave segment of the San Andreas Fault (SAF), about 150 m away from the fault core. As a result of the proximity of the samples to the fault their experimental samples were pre-damaged.

The experiments reported here were conducted in a similar manner; a single, sudden and high energy loading event. Yet, thin sections of natural pulverized rocks reveal sealed microfractures (Fig. 1b), suggesting that the damage may be cumulative, and related to multiple loadings. These observations lead to the question: What is the effect of initial damage on the pulverization properties of rocks? In this paper, we investigate experimentally the effect of initial damage on the fragmentation process. We couple experimental results made on both pre-damaged and intact samples with the theory of Hild and Denoual (Hild et al., 2003a, 2003b; Denoual and Hild, 2000, 2002) to show that the threshold to pulverization decreases with greater initial damage. Hence, as

* Corresponding author. Tel.: +33 4 76 63 52 09; fax: +33 4 76 63 52 52.
E-mail address: Mai-Linh.Doan@obs.ujf-grenoble.fr (M.-L. Doan).

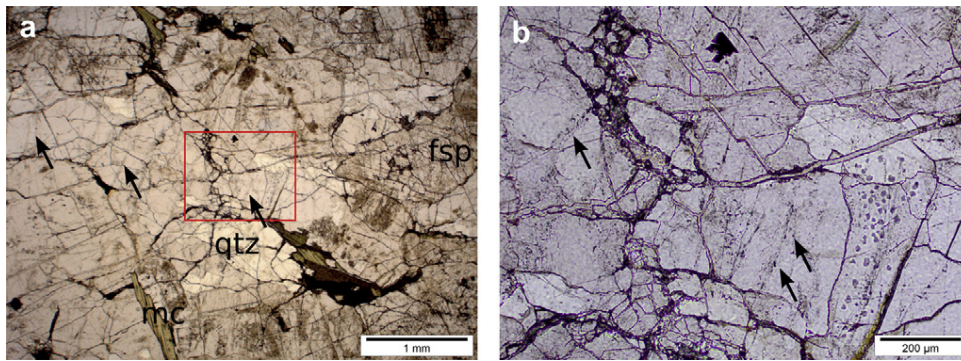


Fig. 1. (a) Thin section of a pulverized rock sampled near Mount Emma Road outcrop, located east of Palmdale, CA, along the Mojave segment of the San Andreas Fault (see also Fig. 3). Thin section was taken in plane polarized light. The outcrop location and description can be found in Fig. 1 of (Dor et al., 2006). Note the dense fracture network crosscutting grains and the preserved interlocked structure of the crystalline rock. The rock is severely damaged but with little shear displacement. Quartz (qtz) and feldspar (fsp) are affected, but the long, weak mica grain (mc) is only cleaved. (b) Zoom within the red rectangle of picture (a). Some sealed microfractures are highlighted by a series of fluid inclusions (black arrows), suggesting that the sample was previously damaged and healed (For interpretation of the references to color in this figure legend, the reader is referred to the web version of this article.).

rocks close to the fault get more and more damaged by successive loadings, pulverization becomes easier.

2. Experimental pulverization of rocks

2.1. Split Hopkinson pressure bars

When performing high strain rate testing, wave propagation time may not be negligible and the deformation measured at an individual strain gage may not be representative of the sample deformation (Nemat-Nasser (2000)). Moreover, classical servo-hydraulic machines have a limited loading velocity range leading to the use of Split Hopkinson Pressure Bars (SHPB) when applying strain rates above 100/s (Nemat-Nasser, 2000). In this study, we induce damage experimentally on protolith samples collected near the pulverized zone of the San Andreas Fault. The samples were loaded uniaxially at strain rate above 50/s, using the SHPB apparatus (Kolsky, 1963) at the Laboratoire de Mécanique des Solides of the École Polytechnique, Palaiseau, France.

Pulverized rocks have thus far only been documented in surface outcrops (Wilson et al., 2005; Dor et al., 2006, 2009, 2008; Mitchell et al., 2011) or in shallow boreholes at depths >50 m (Wechsler et al., 2011). The shallow borehole drilled along the San Andreas Fault provided samples free from surface alteration, that helped evaluate the relative timing of pulverization and surface alteration: Wechsler et al. (2011) argued that pulverization of outcrop rocks along the San Andreas Fault occurred recently, *i.e.* when the samples were at shallow depths. Therefore, we assume that unconfined conditions in our experiments are relevant for understanding rock pulverization, at least along the San Andreas Fault.

Each cylindrical sample is inserted between 2 bars and impacted by a striker bar arriving with a known speed (Fig. 2). The incident stress wave splits into reflected and transmitted waves when it reaches the sample. The incident and reflected waves are then measured with strain gages on the input bar and output bar.

Classical processing of the SHPB assumes 1-D propagation of elastic waves, given the dimensions of the bars (3 m in length by 4 cm in diameter). Here, we have taken into account the dispersion and attenuation processes predicted by the 3D-model of Pochhammer and Chree (Graf, 1991). Due to our sampling rate of 1 MHz, we could reconstruct precisely forces and displacements at both ends of the specimen. We checked that the forces were identical at the input and output bars to verify that the sample was homogeneously loaded. Once the quasi-equilibrium of the specimen is

verified (equality of input and output forces), we calculated the history of stress, strain, and strain rate.

To ensure that the samples were loaded only once, the output bar is shorter than the input bar. Its exit extremity is free to move, allowing the output bar to move away from the sample before any reloading of the sample.

Experiments were conducted with strikers of various lengths (1.20 m, 0.9 m and 0.5 m), and with or without a lead foil inserted at the entry extremity of the input bar, which acts as a pulse shaper. By conducting experiments both with and without the pulse shaper we could decouple strain and strain rate.

2.2. Experiments done on samples from the damage zone of the San Andreas Fault

In this section, we briefly review the experiments (Doan and Gary, 2009) conducted on samples taken from near the San Andreas Fault, at the Lake Hughes outcrop. This outcrop has been described extensively in (Dor et al., 2006) (see their Figs. 1 and 5). Lying west of Palmdale city, CA, this outcrop is located in a narrow valley following the Mojave Segment of the San Andreas Fault. Although the fault itself is not visible, the damage zones of both sides of the fault are visible. The granite of the northern side is severely pulverized, with the intensity of pulverization decreasing rapidly (Fig. 3). The carbonate outcrop on the southern side is much less damaged. Samples were collected about 150 m from the fault core and were derived from the same protolith as the pulverized rocks but not pulverized themselves. The lithology of the samples is described in Table 1. We used this rock material to approximate the initial state before pulverization.

All samples have similar dimensions, 2.5 cm in diameter and 2.5 cm in length. The 1:1 aspect ratio offers a suitable compromise to minimize both stress shadow from sample ends (Paterson and Wong, 2005) and heterogeneity of stress in a long sample when the wave passes (Gama et al., 2004).

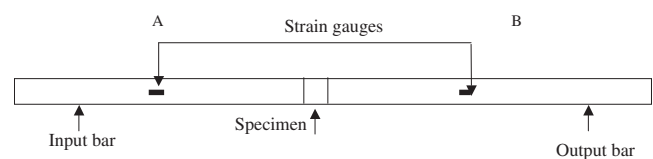


Fig. 2. Schematics of the split Hopkinson pressure bars.

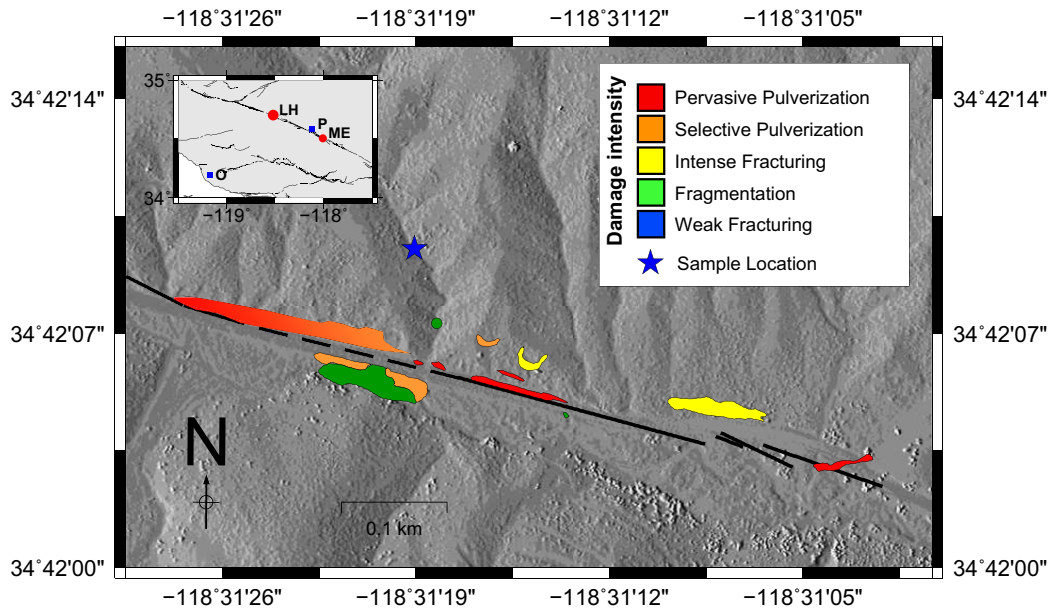


Fig. 3. Location of the samples used in the experiments. We overlay the pulverization map of Dor et al. (2006) and the location of the samples (blue star). We use the same color code as in Dor et al. (2006): red denotes pervasive pulverization, when all crystals in the sample can be crushed by hand; orange for selective pulverization, when some crystals remains intact; yellow for intense fracturing, when crystals retain the original grain size; green for distributed fracturing at the centimeter scale. Our sample can be classified as weakly fractured, with macroscopic large fractures visible in Fig. 5. The digital elevation data were obtained from the GEON project (Prentice et al., 2009). The map was made using Generic Mapping Tools (GMT) software (Wessel and Smith, 1998), using a basic cylindrical projection with a central meridian of longitude equal to $-118^{\circ}30'$ and a standard parallel of latitude equal to $34^{\circ}42'$. The inserted map shows location of some outcrops included in the text: Lake Hughes (LH) outcrop from which the samples for laboratory experiments were taken, Mont Emma Road (ME) outcrop, from which thin sections were made within pulverized rocks (Fig. 1). We also added the location of two major cities of the area, Palmdale (P) and Oxnard (O) (For interpretation of the references to colour in this figure legend, the reader is referred to the web version of this article.).

Three final states could be observed macroscopically:

1. the sample was not damaged
2. the sample was split axially in a few fragments, no more than 5. This is the typical damage observed when a rock sample is uniaxially loaded at low strain rate (Paterson and Wong, 2005).
3. the sample was shattered in multiple small fragments, smaller than the initial grain size of about 1.5 mm. This diffuse damage is reminiscent of pulverized rocks.

No intermediate state was observed between single fracturing and pulverization. Above a strain rate of 150/s, samples are pulverized

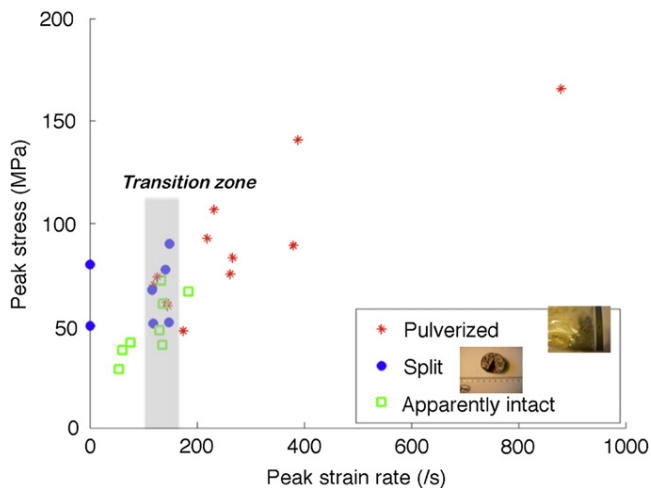


Fig. 4. Final states of damage after dynamic loading of granite from the San Andreas Fault. Results are gathered in a diagram showing strength versus maximum peak strain. There is a transition from single fracturing to multiple fragmentation at strain rates above 150/s (Doan and Gary, 2009).

and there is a sudden transition from failure along a small number of fractures to a pervasively pulverized damage. Doan and Gary (2009) infer that pulverized rocks in the field are the product of coseismic damage, with a strain rate larger than 150/s. They show that such a strain rate is not expected for usual earthquakes propagating at subshear rupture speed. They explain the origin of pulverized rocks as the damage generated by a shock wave, like the Mach wave accompanying a supershear rupture. A Mach wave is a solitary wave that decays slowly with distance. Bhat et al. (2007) show evidence of coseismic damage generated during a supershear rupture up to 5 km from the fault trace. A prediction of our experimental results is that the samples could be pre-damaged before testing, even though they were sampled 150 m from the fault core, a distance at which fracture density levels to the background level for most faults (Mitchell and Faulkner, 2009; Savage and Brodsky, 2011).

Several observations indeed suggest that, though not pulverized, the natural rock used in the first series of experiments was severely damaged. Fig. 5a shows a thin section of the initial state of one of the samples before loading. At the centimetric scale, microfractures are visible from inspection of the whole thin section. At higher magnification, microfractures are also visible at the millimetric and submillimetric scale. The sample is cohesive enough to withstand coring and moderate loading. Yet, experiments described in the next section give an uniaxial strength below 100 MPa, a low value for granitic rock (usually close to 200 MPa, as for Westerly granite (Heap and Faulkner, 2008)).

To investigate the effect of this initial damage on the high strain rate behavior of crystalline rocks, we conducted a further series of experiments of intact granitic rocks.

2.3. Experiments performed on intact rocks

To investigate the effect of damage, we used granite samples from Tarn, France. Fig. 6 shows a thin section of this rock and of the

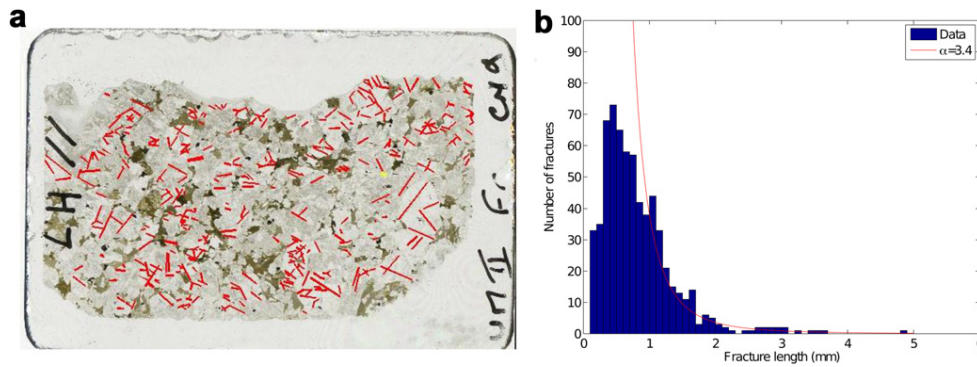


Fig. 5. (a) Thin section cut from a sample from the San Andreas Fault zone, before experiments. The thin section is 4.5 cm long and 2 cm wide. A total of 660 fractures are delineated. (b) Histogram of fracture lengths m delineated in figure (a). Most fractures are smaller than 2 mm. This length corresponds to a. The red line gives a power law fit, $p(l) \propto l^{-\alpha}$, of the fracture length distribution, with a power exponent $\alpha = 3.4$. The fit is poor for small lengths since statistics are not complete for small lengths.

San Andreas Fault rock for comparison. In both cases, the sample is granitic in composition, with a millimetric grain size, significantly smaller than the sample dimension (2.5 cm in diameter, about 2 cm in length). As with the granite near the San Andreas Fault, Tarn granite is slightly weathered, with mechanical alteration of the feldspar grains. Table 1 shows a similar modal composition for both rocks. Hence, we use the Tarn granite as a proxy for the intact, undamaged San Andreas Fault rocks.

Experiments on the Tarn granite are summarized in Fig. 7. It shows three distinct final macroscopic states (Fig. 8): intact, split into a few fragments, or finely fragmented, equivalent to experiments on the SAF granite (Fig. 4). There is no intermediate state between the two latter stages, at least for the strain rates explored here.

Due to the loading duration being controlled by the striker length, there is always an ambiguity between strain rate and total strain accumulated (Doan and Billi, 2011). To compensate for this artifact, we used different strikers. We also used a pulse shaper to smooth the loading front (Chen and Song, 2010).

As shown in Figs. 7 and 9, pulverization can occur at both low and large strains. Very large strains are attained when the sample is pulverized and multiple fragments are ejected: the sample is no longer present to separate the input and output bars and we record artificially large strains.

There are fewer tests completed on the intact Tarn granite than on the pre-damaged San Andreas samples, yet a transition is still visible if we plot strength versus peak strain rate (Fig. 8). When loading at strain rates above 250/s, samples of Tarn granite fragment into fine grains. The transition threshold is larger than for the pre-damaged case. Rock strength also increases from 75 MPa to 150 MPa when the initial sample is less damaged.

One may speculate on the validity of the comparison between the experiments, as the high strain rate experiments were not conducted on the exact protolith of the damaged Lake Hughes granite. However, our results are consistent with two other studies, suggesting that our experiments are valid. The first is a series of experiments made on Westerly Granite by Yuan et al. (2011). This

paper has an outline very similar to Doan and Gary (2009), but is an independent study. They tested with Split Hopkinson Pressure Bars intact samples of Westerly Granite in unconfined and quasi-oedometric confined conditions. They find in unconfined conditions a transition to pulverization for strain rates above 250/s. The strength threshold was also about 150 MPa. The second is a theoretical model of pulverization developed by François Hild and co-authors (Hild et al., 2003b; Denoual and Hild, 2000), that is in agreement with our experimental results. This theory is presented in more detail within the next section, as we will use it to extrapolate our experimental results in the case of multiple loadings.

3. Statistical theory of pulverization

We studied experimentally the two extreme cases of (1) a pre-damaged sample and of (2) an intact sample. To generalize the conclusions drawn from our experimental data to any level of initial damage, we will refer to the theoretical model of transition from single fracturing to multiple fragmentation, that has been proposed by Hild, Denoual and co-workers (Denoual and Hild, 2000, 2002; Hild et al., 2003a, 2003b). This is a statistical theory that determines the strength of a brittle material, depending on whether it is fractured or pulverized. It is a variant of the Weibull statistical theory of strength. After reviewing the Weibull theory for the common low-strain-rate case, we will present the theory of the high strain rate case proposed by Denoual and Hild (2000). Once the two theories are described, a transition between them can be predicted. This section is mathematically-intensive. Symbols used in equations are summarized in Tables 2 and 3.

3.1. Description of the theory

3.1.1. Weibull hypotheses of rock failure

The Weibull model (Weibull, 1951) is a popular model to describe the failure of a sample by a single fracture. In a sample, there exist initial flaws, with different lengths, and hence different

Table 1

Modal composition of the rocks tested. Modal analysis was performed by random selection of 105 points of the available thin sections (two for the San Andreas Fault samples, one for the Tarn Granite). 95% confidence interval of the proportion of each mineral (in percent) is given between square brackets below the average composition.

Sample	Quartz	K-Feldspar	Plagioclase	Biotite	Amphibole, sphene
San Andreas Fault	28.7%	33.3%	20.3%	16.0%	1.6%
Thin section 1	[24.5–33.3]	[28.8–38.1]	[16.5–24.5]	[12.6–19.9]	[0.6–3.5]
San Andreas Fault	28.2%	35.1%	19.9%	14.9%	1.9%
Thin section 2	[24.0–32.8]	[30.7–40.0]	[16.3–24.1]	[11.7–18.7]	[0.8–3.8]
Tarn Granite	32.8%	39.4%	13.8%	14.1%	0%
	[28.4–37.4]	[34.8–44.1]	[10.6–17.4]	[10.9–17.7]	[0–0.9]

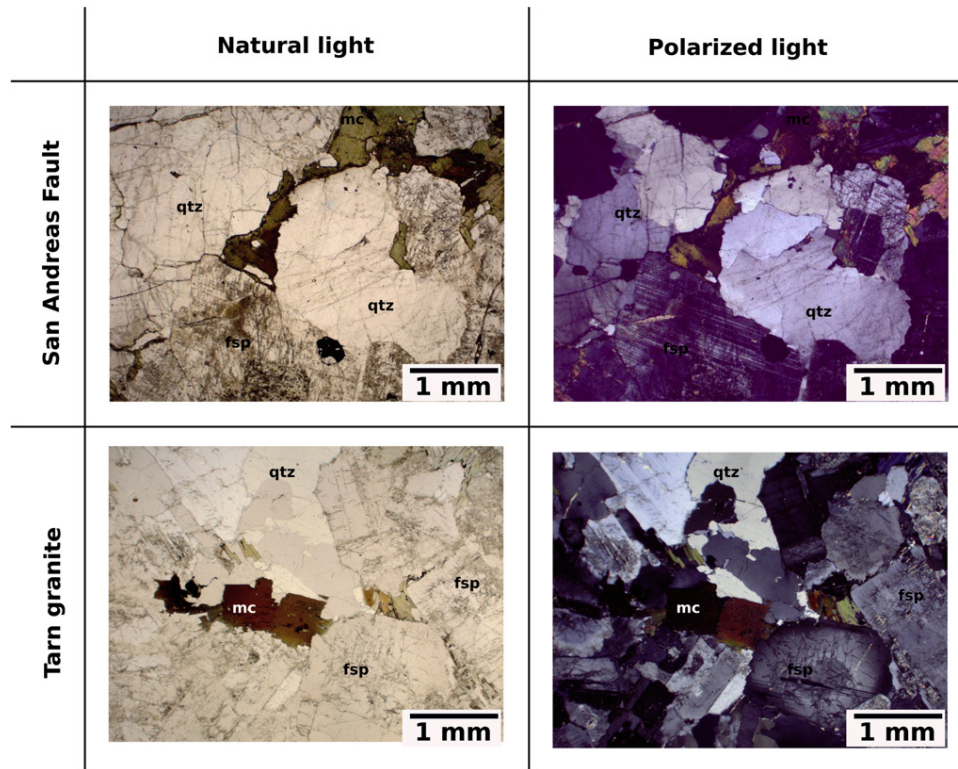


Fig. 6. Thin sections representative of the lithologies tested during the experiments described in this paper. Several minerals are visible: quartz (qtz), feldspar (fsp), mica (mc). Grain size is millimetric in both cases, and therefore much smaller than the sample size. Modal analysis made on the whole thin sections is given in Table 1.

strengths (Fig. 10a). The Weibull model assumes (1) that all flaws are loaded by the same stress, (2) that each flaw will have an independent probability to fail and (3) the breaking of a single fracture will induce the failure of the whole sample; this is the *weakest link hypothesis* (Fig. 10b).

Conditions (1) and (2) assume that the fracture density is low enough for fractures to develop independently, without stress-shadowing effects. If the load is heterogeneous, Hild et al. (2003b) introduced the concept of an effective volume $V_{\text{eff}} = Z_{\text{eff}}V$ to describe the homogeneously loaded portion of a sample in a rock.

Condition (3) can be understood with concepts from linear elastic fracture mechanics. Fractures act as stress concentrators. Linear elastic fracture mechanics states that at the tip of a fracture of length l , the stress σ is amplified as:

$$\sigma_{ij} = \frac{K}{\sqrt{2\pi r}} f_{ij}(\theta) \quad (1)$$

r is the distance to the fracture tip and θ the orientation to the fracture angle. f_{ij} is a known adimensional function. K is the stress intensity factor. Depending on the loading mode, the detail of its expression varies, but it retains the general form:

$$K = Y\sigma\sqrt{l}, \quad (2)$$

where Y is an adimensional geometrical factor and σ is the amplitude of the loading. For instance, for a mode I loading $K = \sigma\sqrt{\pi l}$.

Irwin (1957) have shown that if K exceeds a threshold value K_c then the fracture extends to reach a longer length l . According to Eq. (2), the stress intensity factor then increases. K_c could then be reached with a smaller stress σ : the strength of the fracture is smaller. This positive loopback explains why the failure of a major

flaw can develop catastrophically into the complete failure of the sample (Fig. 10b).

From a uniform stress field σ and a given fracture mode, Eq. (2) predicts that a fracture will fail if it exceeds a threshold length

$$L_c = \left(\frac{K_c}{Y\sigma} \right)^2 \quad (3)$$

We now explore the probability for the occurrence of a fracture longer than L_c .

3.1.2. Weibull statistical model of single fracturation

In most natural samples there is an initial network of fractures. The initial fracture density is labeled λ_0 . If we take a volume V , there is on average a number of N fractures within this volume, with $N = \lambda_0 V$. Fracture density is not the only fracture parameter controlling the sample strength. The length distribution of these fractures is also important. Each fracture has a probability of having a length between l and $l + dl$ given by the probability distribution function $p(l)$. The average density of fractures λ_{L_c} of length greater than a critical length is then $\lambda_{L_c} = \lambda_0 \int_{L_c}^{\infty} p(l) dl$. Hence, the probability of having k fractures of length greater than L_c within the volume V is then given by the Poisson statistics:

$$p_{V,L_c}(k) = \frac{(\lambda_{L_c} V)^k}{k!} e^{-\lambda_{L_c} V} \quad (4)$$

In the weakest link hypothesis, the probability of survival of the sample is given by $p_{V,L_c}(k = 0)$. If the sample does not survive, it fails, and hence the probability of failure is given by

$$p_F = 1 - p_{V,L_c}(0) = 1 - e^{-\lambda_{L_c} V} \quad (5)$$

Sample	Peak strain rate (s)	Peak stress (MPa)	Peak strain (%)	Final state	Photograph
T1	708	313	4.12	Pulverized	No picture
T2	51	97	0.25	Intact	No picture
T7	755	201	8.26	Pulverized	
T9	518	159	4.74	Pulverized	
T10	150	126	0.13	Split	
T12	180	162	0.32	Split	
T13	289	160	0.66	Pulverized	
T14	258	144	0.74	Split	
T15	217	139	0.51	Split	
T17	251	153	0.56	Pulverized	

Fig. 7. Summary of experiments performed on Tarn granite. For each sample, peak stress, peak strain, peak strain rate and a classification of the final damage are reported. When available, a photograph illustrating the post-mortem macrodamage of the sample is also included. The ruler in the photographs is graduated in centimeters.

This relationship scales with the volume under consideration (Weibull, 1951). For instance, if we are interested in a volume $\mathbb{V} = v \times V$, there is no failure in the volume \mathbb{V} if there is no failure within all the v volumes of size V . All these events are independent and we obtain

$$p_{\mathbb{V},L_c}(0) = \left(p_{V,L_c}(0)\right)^v = e^{-\lambda_{L_c}vV} = e^{-\lambda_{L_c}\mathbb{V}} \quad (6)$$

Eq. (5) holds if we replace V by a larger volume \mathbb{V} . The expression of Weibull law is scale independent. Let us assume now that the size distribution $p(l)$ can be described by a power law $p(l) = Cl^{-\alpha}$, where C is a normalizing factor, dependent on the smallest fracture length. Then, we obtain a simple expression for λ_{L_c} :

$$\lambda_{L_c} = \lambda_0 \int_{L_c}^{\infty} Cl^{-\alpha} dl = -\lambda_0 C \frac{L_c^{1-\alpha}}{1-\alpha} \quad (7)$$

Using the above equation and Eq. (2), Eq. (5) then reduces to a Weibull distribution:

$$p_F = 1 - e^{-\left(\frac{\sigma}{\Delta\sigma}\right)^m} \quad (8)$$

where $m = 2(\alpha-1)$ and $\Delta\sigma = (K_C/Y)(m/2CV\lambda_0)^{1/m}$. m is called the shape parameter and $\Delta\sigma$ the scale parameter of the Weibull distribution. The maximum of the associated probability density function is reached at for $\sigma_{\max} = (m-(1/m))^{1/m}\Delta\sigma$ if $m > 1$. From Weibull equations, we obtain the average strength of a sample (Fig. 11):

$$\sigma_{F,\text{static}} = \int_0^{\infty} \frac{dp_F}{d\sigma} \sigma d\sigma = \frac{\Delta\sigma}{m} \Gamma\left[\frac{1}{m}\right] \quad (9)$$

where $\Gamma[x] = \int_0^{\infty} t^{x-1} e^{-t} dt$ is the gamma special function. Therefore the strength of the sample decreases with the initial density of

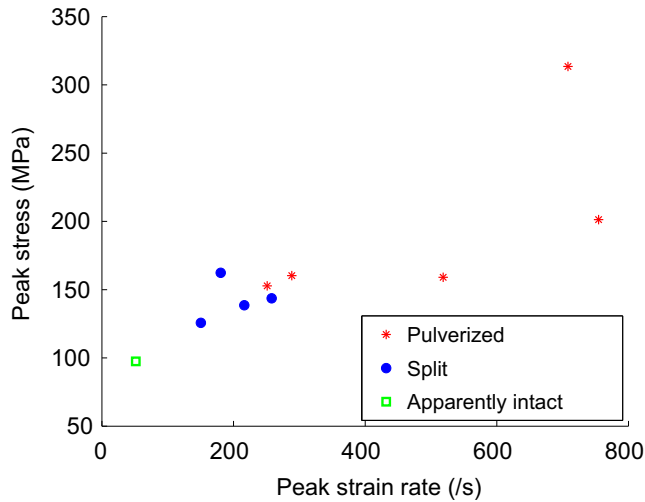


Fig. 8. Final states of damage after dynamic loading of Tarn granite. Results are gathered in a diagram showing strength versus maximum peak strain. As in Fig. 4, there is a transition from single fracturing to multiple fragmentation, but at a higher strain rate, above 250/s.

fractures λ_0 and with its volume, as we have more chance to find a fracture of critical length.

The Weibull model also recognizes that the heterogeneity of samples leads to a variability in sample strength. The standard deviation in sample strength is given as $\Delta\sigma_{F,static} = \Delta\sigma\sqrt{\Gamma(1 + (2/m)) - (\Gamma(1 + (1/m)))^2} \sim (\pi\Delta\sigma/\sqrt{6}m)$. This means that if m is very large, the Weibull distribution is very peaked, and hence has a more uniform strength distribution. By playing between the shape parameter m and the scale parameter $\Delta\sigma$, we can quantify the heterogeneity and the weakness of the sample. The Weibull model statistically predicts the strength of a sample based on microscopic fracture lengths (Jayatilaka and Trustrum, 1977).

To check the validity of the Weibull model for single-fracture samples, we estimated the m Weibull parameter for the pre-damaged San Andreas Fault samples using two approaches (Fig. 12). Fig. 5b gives the length distribution of fractures picked from a thin

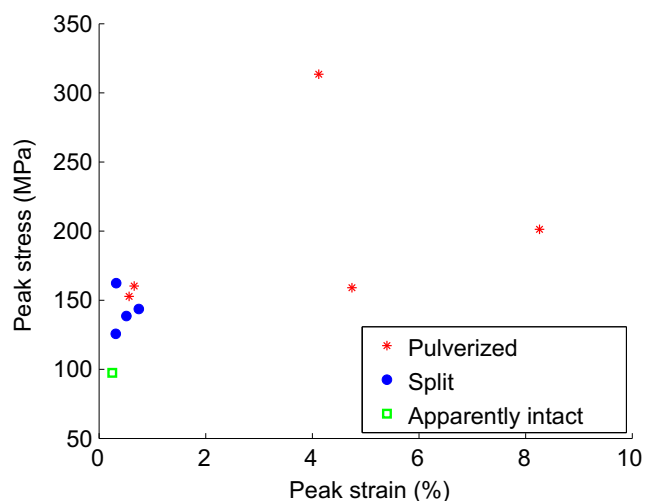


Fig. 9. Strain dependence on the transition from single fracturing to multiple fragmentation, from the summary of experiments in Fig. 5. The extremely damaged, pulverized rocks can withstand loading to artificially large strains; however, two cases (T13 and T17) also show that pulverization can occur at smaller strain.

Table 2

Table of symbols used within the equations of the text – Latin alphabet.

Symbols	Meaning
c	Stress wave velocity
e	Euler number (~ 2.718)
K	Stress intensity factor
l	Length of fracture
L_c	Threshold length of fracture, for which $K > K_c$ or L_c . Fractures longer than L_c will propagate
m	Shape parameter of Weibull distribution. Representative of the sample homogeneity.
n	Number of dimensions of the problem (here 3)
p_F	Probability of failure
P_{ns}	Probability for a fracture longer than L_c to be not overshadowed by another fracture
$p_{V,L_c}(k)$	Probability of having k fractures of length greater than L_c within the volume V
t_c	Characteristic time for a fracture to be interacting with surrounding fracture
t_f	Characteristic time for a fracture to reach failure under a constant stress rate $\dot{\sigma}$
V	Volume of the sample
V_{eff}	Volume uniformly loaded by stress σ
Y	Geometrical factor intervening in stress intensity factor computation
Z_{eff}	Ratio between V_{eff} and V

section, at a centimetric scale. The limited resolution of the image prevents the completeness of the fracture catalog for smaller fractures. Yet, the length distribution of the largest fractures can be roughly matched (Fig. 5) with a fractal coefficient $\alpha = 3.4$, giving an exponential value of $m = 2(\alpha - 1) = 4.8$. This result is slightly larger than the particle grain size distribution found with a laser granulometer by Wechsler et al. (2011), who obtained a grain size distribution matching a power law function with a coefficient α ranging from 2.5 to 3.1 for pulverized rocks collected in a borehole near Mount Emma outcrop along the San Andreas Fault (Fig. 3). We then determined the strength distribution for the samples that were split. The cumulative strength distribution is fitted with a Weibull distribution. We find a scale parameter $\Delta\sigma = 70$ MPa and a shape parameter $m = 5$, that is similar to the experimental value $m = 4.8$ found by fitting the microfracture length distribution. The Weibull theory gives satisfactory results for the samples that were pre-fractured.

Table 3

Table of symbols used within the equations of the text – Greek alphabet.

Symbols	Meaning
α	Coefficient of the power law governing fracture length statistics
$\gamma(\nu, x)$	Lower incomplete Gamma special function
$\Gamma(x)$	Gamma special function
$\Delta\sigma$	Scale parameter of Weibull distribution. Representative of the sample strength.
$\Delta\sigma_{F,static}$	Standard deviation of the strength statistics of a sample quasi-statically loaded
λ_0	Initial fracture density
λ_b	Density of fractures amenable to further propagation and that effectively break
$\lambda_{b,sat}$	Maximum density of fractures that effectively break, at saturation
λ_s	Density of fractures amenable to further propagation but stress-shadowed by other fractures
λ_{L_c}	Density of fractures of length longer than L_c , i.e. of fracture amenable to propagation
σ	Applied stress
$\dot{\sigma}$	Stress rate
$\dot{\sigma}_c$	Transition stress rate from single fracture to multiple fragmentation
$\sigma_{F,dyn}$	Average strength of a sample loaded at high strain rate
$\sigma_{F,static}$	Average strength of a sample quasi-statically loaded
Ω_0	Initial size of the shadow zone around a fracture

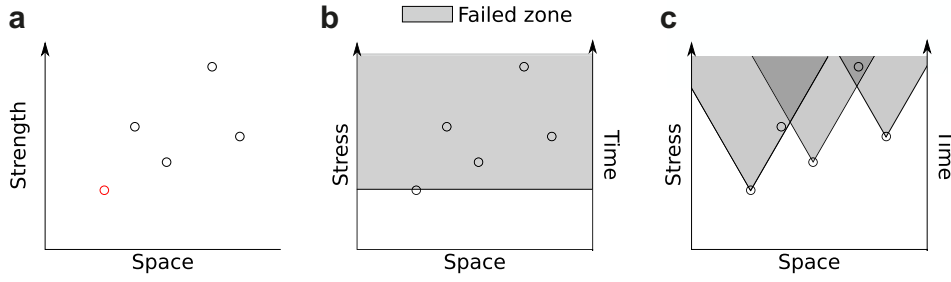


Fig. 10. Schematics of the different theories of failure. (a) Initial flaw model: There is an initial distribution of flaws scattered in space, with different locations, and different strengths. The sample is then loaded at a given stress rate (or strain rate in an elastic solid). There are two extreme cases: (b) Slow strain rate case: The sample is loaded so slowly that the propagation of the weakest flaw is considered instantaneous. Breaking the weakest flaw leads to the failure of the whole sample. (c) High strain rate case: The sample is loaded so rapidly that the finite fracture propagation speed cannot be ignored. This allows the propagation of multiple fractures at the same time. Yet not all fractures propagate, as some can be stress shadowed by other propagating flaws.

3.1.3. The Hild model of multiple fragmentation

When a sample is loaded rapidly, the physics of the interaction between flaws is altered (Fig. 10c). Stress wave propagation has to be taken into account. The weakest flaw takes a finite time to expand, during which time other cracks can also expand. But during that time, some fractures can also enter the shadow zone of others. Hence, the Weibull model has to be modified to take into account these two phenomena. This is what is achieved with the theory of Hild et al. (2003b), which we will summarize and reformulate in this section. Let us assume that a stress σ is applied homogeneously on the material. We saw in Section 3.1.2 that there

is an average density of fractures λ_{L_c} that may break for a stress smaller than σ . Combining Eqs. (3) and (7), λ_{L_c} expresses as

$$\lambda_{L_c} = \lambda_0 \frac{2C}{m} \left(\frac{Y\sigma}{K_C} \right)^m \quad (10)$$

However, only a fraction λ_b of them effectively break, as some are stress-shadowed. The density of shadowed fractures is denoted by λ_s .

$$\lambda_b = \lambda_{L_c} - \lambda_s \quad (11)$$

Let us assume that the area shadowed by an expanding flaw expands as $\Omega(t) = \Omega_0 \times (c(t-t_0))^n$, where n is the dimension of the problem (here $n = 3$), c is the fracture propagation speed, Ω_0 an adimensional coefficient controlling the size of the shadow zone and t_0 the start of fracture propagation. The sample is progressively loaded and stress increases with time: $\sigma = \dot{\sigma}t$. In the case of a purely brittle material, this is equivalent to loading at a constant strain rate. Let us suppose we are now at time t . At $t + dt$, we reach the stress $\sigma + (d\sigma/dt)dt$. At this higher stress, new cracks will begin to break, provided that their strength is between σ and $\sigma + (d\sigma/dt)dt$ and that they are not overshadowed:

$$\frac{d\lambda_b}{dt} = \frac{d\lambda_{L_c}}{dt} P_{ns} \quad (12)$$

We now address the question of how to compute P_{ns} , the probability not to be shadowed? A flaw is not overshadowed if there is no initial fracture on its horizon during previous time steps (Fig. 13). To estimate this, let us consider the probability that a fracture can be overshadowed by another fracture that would have initiated at time t_0 and $t_0 + dt_0$. This is equivalent to slicing the horizon (dashed lines of Fig. 13) several times between t_0 and $t_0 + dt_0$ (horizontal lines of Fig. 13). This is given by the Poisson process that involves the probability of finding a fracture of strength $(d\lambda_{L_c}/d\sigma)(d\sigma/dt)dt = d\lambda_{L_c}/dt|_{t_0} dt_0$ in the affected volume $\Omega(t-t_0)$. The probability that no fracture appears is

$$dP_{ns} = \exp\left(-\frac{d\lambda_{L_c}}{dt}\bigg|_{t_0} \Omega(t-t_0)dt_0\right) \quad (13)$$

We then integrate Eq. (13) for all previous time steps, until $t_0 = 0$, using the scaling relationship of the Weibull distribution (Eq. (6)). The probability for a fracture not being shadowed is then:

$$P_{ns} = \exp\left(-\int_0^t \frac{d\lambda_{L_c}}{dt}\bigg|_{t_0} \Omega(t-t_0)dt_0\right) \quad (14)$$

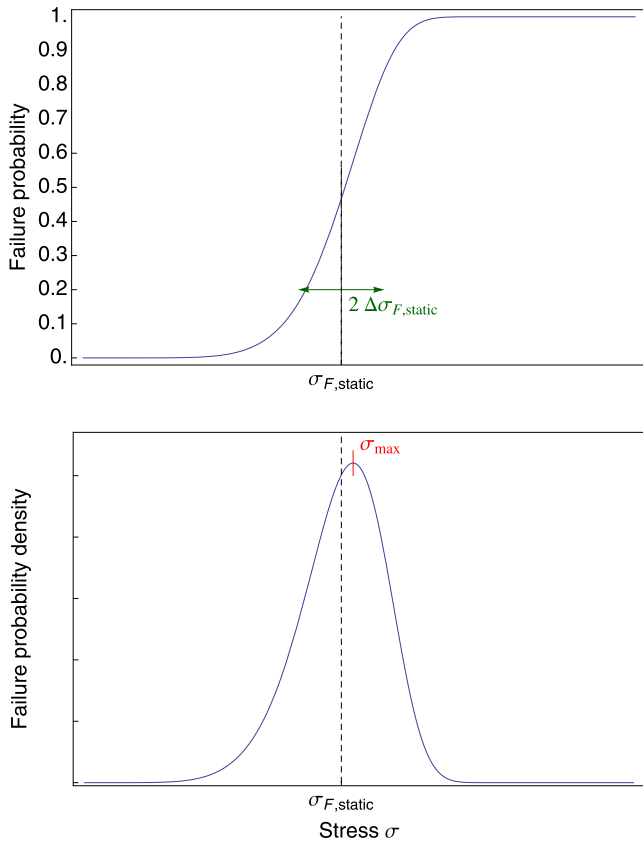


Fig. 11. Failure probability predicted by Weibull equation (Eq. (8)). The shape parameter m and the scale parameter $\Delta\sigma$ control the values of σ_{av} (Eq. (9)) and σ_{max} . In this graph, $m > 1$.

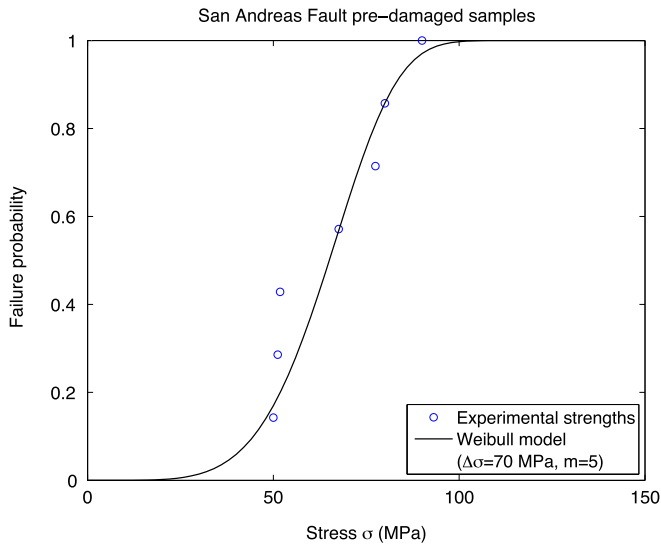


Fig. 12. Experimental determination of the Weibull parameters for the pre-damaged samples from the San Andreas Fault. We consider only the strength of the samples that were single-fractured. The cumulative probability density function is then fitted with a cumulative Weibull distribution, as in Fig. 11. Experimental Weibull parameters are $\Delta\sigma = 70$ MPa and $m = 5$.

We then integrate this equation using the expression of λ_{L_c} from Eq. (10) to obtain

$$P_{ns} = \exp \left[-\lambda_0 \frac{2C}{m} \Omega_0 c^n \frac{m!n!}{(m+n)!} t^{m+n} \left(\frac{\dot{\sigma} Y}{K_C} \right)^m \right] \quad (15)$$

Note that we can simplify the above expression as $P_{ns} = e^{-(m!n!/(m+n)!)\lambda_{L_c}(t)\Omega_0(ct)^n}$, but we prefer to write $P_{ns} = e^{-(t/t_c)^{m+n}}$ to highlight the characteristic time for fracture interaction through stress waves:

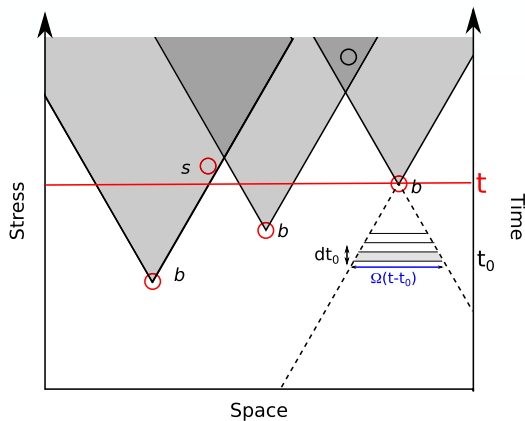


Fig. 13. Graphical representation of the concepts developed in the case of multiple fractures. For a given stress, there are a few preexisting flaws that have a lower stress than σ (red circle, labeled with a subscript c in the main text). Some of them are effectively initiated (subscript b) and their shadow zones (shaded areas) expand as they propagate. Others flaws cannot be activated (subscript s) because they fall within the shadow zone of an initiated crack. To investigate the probability of falling within a shadow zone, we delineate the horizon of the fracture (dashed lines) projected backwards in time, or equivalently backwards in stress as $\sigma = \dot{\sigma}t$. The probability that a crack breaks is computed by combining the probability for an existing flaw to be within the influence area between t_0 and t_0+dt (For interpretation of the references to color in this figure legend, the reader is referred to the web version of this article.).

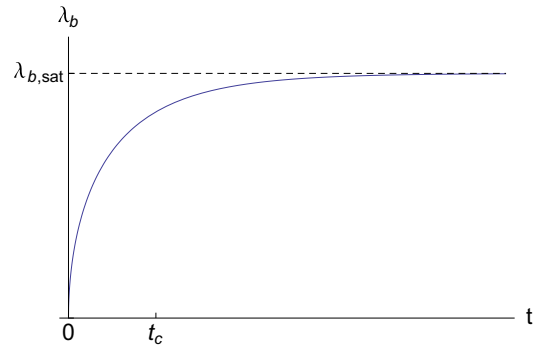


Fig. 14. Time evolution of breaking fracture with time, as predicted by Eq. (18). The fracture population increases with a power law of time, but saturates due to stress-shadowing between propagating fractures.

$$t_c = \left[\frac{2C\lambda_0\Omega_0m!n!c^n \left(\frac{\dot{\sigma} Y}{K_C} \right)^m}{m(m+n)!} \right]^{-\frac{1}{m+n}} \quad (16)$$

The equation is rather large, yet it expresses some intuitive ideas: the characteristic time for fracture interaction decreases with the initial density of fractures λ_0 , with the loading rate $\dot{\sigma}$, the minimal size of the shadow zone around each Ω_0 and with the stress wave velocity c . The characteristic time t_c is to be compared with another characteristic time: the time t_f for the loading to lead to new fracture t_f . We can re-express Eq. (10) as $\lambda_{L_c} = \lambda_0(t/t_f)m$ with

$$t_f = \frac{K_C}{\dot{\sigma} Y} \left(\frac{m}{2C} \right)^{\frac{1}{m}} \quad (17)$$

From Eqs. (10), (12) and (15), we derive λ_b , the density of fractures that will effectively break at stress σ :

$$\lambda_b = \lambda_0 \frac{m}{m+n} \left(\frac{t_c}{t_f} \right)^m \gamma \left[\frac{m}{m+n}, \left(\frac{t}{t_c} \right)^{m+n} \right] \quad (18)$$

where $\gamma[v, x] = \int_0^x t^{v-1} e^{-t} dt$ is the lower incomplete gamma function. The time evolution predicted by the above equation is given by Fig. 14. As $\gamma[v, t] \sim (t^v/v)$ at short times, $\lambda_b \sim \lambda_0(t/t_f)^m$: the more homogeneous the distribution of flaw strengths, the higher is m , and the more sudden is the simultaneous growth of fractures. Note that at small times, $\lambda_b(t) \sim \lambda_{L_c}(t)$: the stress-shadowing phenomenon is not yet efficient. The breaking fractures density saturates rapidly to $\lambda_{b,sat} = \lambda_0(m/m+n)\Gamma[m/m+n](t_c/t_f)^m$, where $\Gamma[x]$ is the Euler gamma function ($\Gamma[v] = \gamma[v, \infty]$). We see that the density of fractures that will effectively break increases if the shadowing process is slow (large t_c) compared to the fracture initiation duration t_f . The above equation can be expressed in terms of applied stress rather than time, by introducing a critical stress $\sigma_c = \dot{\sigma}t_c$. The critical stress scales as $\sigma_c^{n/m+n}$.

Computing analytically the strength of the sample is difficult. We can no longer use the Poisson process underlying the Weibull Eq. (5) as the failures of all subparts of the samples are not independent events anymore, because of the stress-shadowing process. Instead, Denoual and Hild (2000) use a mean-field theory by introducing the concept of macroscopic damage D to exploit the density of broken fractures. They take as a proxy of damage the probability $D = 1 - P_{ns}$. This damage parameter is then inserted in a mean-field theory of stress screening, similar to the strategy developed by Grady and Kipp (1989): the stress that has been considered so far is an effective stress that is different from the applied stress $\sigma_{app} = (1-D)\sigma$. The dynamic strength $\sigma_{F,dyn}$ of the

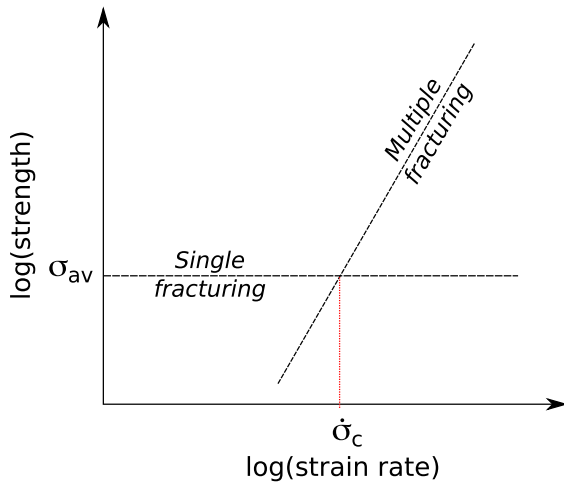


Fig. 15. Strength depends on the pulverization regime. In the case of a single fracture, strength is independent of strain rate. In case of pulverization, strength is a power law of strain rate. The transition between the two regimes happens for a characteristic stress $\dot{\sigma}_c$.

sample is the maximum of the stress applied during the loading. This happens when $(d\sigma/dt) = (d/dt)(\dot{\sigma}t)P_{ns} = 0$, i.e. for $t_{\max} = (1/m+n)^{(1/m+n)}t_c$. The maximum applied stress is therefore $\sigma_{F,\text{dyn}} = e^{-1/m+n}\sigma_c$, whose full expression is

$$\sigma_{F,\text{dyn}} = \left[\frac{2eC\lambda_0\Omega_0 m! n! c^n \left(\frac{Y}{K_c}\right)^m}{m(m+n)!} \right]^{-\frac{1}{m+n}} \dot{\sigma}_c^{\frac{n}{m+n}} \quad (19)$$

Dynamic strength increases with strain rate, with a power law of exponent $(n/m+n)$. Higher strain rate indeed results in smaller fragments, as shown by the experiments of Section 2 but also by Grady and Kipp (1989). This increases the fracture energy created during damage of the rock. This contrasts with the quasi-static loading case, for which strength is independent of strain rate.

3.2. Prediction on the effect of damage on the transition

These theoretical results show that rock strength varies with stress rate (hence for a pure brittle solid, with strain rate). The variation is schematically described in Fig. 15. For a single fragmentation problem, strength is constant. For a multiple fragmentation problem, strength increases as a power law of stress rate. The transition between the two regimes happens when $\sigma_{F,\text{static}} = \sigma_{F,\text{dyn}}$. If we use the damage theory of Denoual and Hild (2000), we get a transition strain rate of

$$\dot{\sigma}_c = \left(\frac{2C\lambda_0}{m}\right)^{-\frac{1}{m}} \frac{K_c c}{Y} \left[\frac{e\Omega_0 n! m!}{(m+n)!} \right]^{\frac{1}{n}} \left(\frac{\Gamma\left[\frac{1}{m}\right]}{m} \right)^{\frac{m+n}{n}} V^{-\frac{m+n}{mn}} \quad (20)$$

This can be also more compactly written as

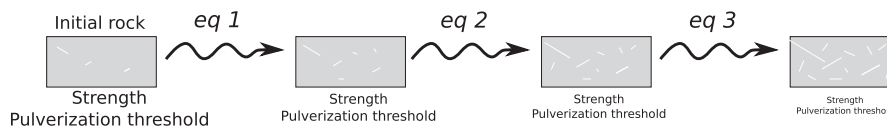


Fig. 16. Schematic evolution of damage as successive earthquakes (eq) further damage the rock. Both rock strength and the strain rate pulverization threshold decrease with successive earthquakes. This leads to a feedback process whereby diffuse damage is increasingly facilitated during subsequent loadings. In other words, the rock becomes progressively pulverized.

$$\dot{\sigma}_c = \left[\frac{e\Omega_0 n! m!}{(m+n)!} \right]^{\frac{1}{n}} \left(\frac{\Gamma\left[\frac{1}{m}\right]}{m} \right)^{\frac{m+n}{n}} \Delta\sigma c V^{-\frac{1}{n}} \quad (21)$$

The threshold in stress rate depends on $\Delta\sigma$, the scale parameter of the Weibull distribution used in the static case, divided by the characteristic time for elastic wave to travel the sample $V^{-1/n}/c$ and by an dimensional factor that depends on the shape parameter m of the Weibull distribution, i.e. the initial fracture size distribution of the sample. This highlights several features. The transition threshold $\dot{\sigma}_c$ from single fracturing to fragmentation decreases with the initial density of fractures λ_0 , with an exponent $1/m$. It also decreases with the volume V of the rock loaded, with an exponent $(m+n/mn)$. The homogeneity of the sample, described by the Weibull shape parameter m , also affects the transition threshold. The three parameters also affect the static strength of the sample (Eq. (9)).

The size dependence might have been problematic to the applicability of our experiments to a fault zone. Yet, pulverized rocks are recognized in the field as (1) a rock sample that is easily crushed within a person's hand and (2) as a rock whose initial structure is preserved, i.e. a rock that has experienced little strain. Condition (1) is tested with samples a few centimeters long, which is the size of our experimental samples. Hence, we consider that the strength and transition from single fracturing to fragmentation determined from our experiments are valid.

The theory predicts a diminution of the strength and the transition threshold to pulverization with initial damage, as they both scale as $\lambda_0^{(-1/m)}$. This confirms the experimental results of Section 2. The intact rock has a static strength of about 150 MPa and a transition strain rate of about 250 s^{-1} . The pre-damaged rock has a strength of 75 MPa, only half the strength of the intact rock. The transition strength for the pre-damaged rock also decreases by almost a factor of two, falling to about 150 s^{-1} . Hence, the theory provides a correct prediction of our experimental results.

4. Application to active faults: development of a zone of pulverized rocks after multiple earthquakes

The diminution of the strength and of the pulverization threshold suggests a scenario for pulverization along active faults in which rocks are pulverized by successive earthquakes (Fig. 16). A first earthquake loads at high frequency the surrounding rocks. If a rupture generates enough high frequencies, the damage is diffuse: multiple fractures propagate, and any decimetric fragment near the fault zone becomes diffusively damaged. The damage induces a reduction in strength of the rock near the fault. It also lowers the threshold in strain rate to switch from localized damage to diffuse damage (i.e. pulverization). It would be easier for the next earthquake to also damage diffusively all the rocks around the fault zone. With successive loadings, the rocks around the fault zone get progressively finely pulverized.

Pulverized rocks have only been identified recently (Wilson et al., 2005). Why don't we see more pulverized rocks? If loading happens at too low a strain rate, damage is localized along a few

fractures. In the portions which experienced little fracturing, their strength and strain rate threshold to pulverization are not modified. Hence, further loading would localize on the weak fractured area but not on the background rock left intact. The diffuse damage pattern found in outcrops of pulverized rocks would not be found if no sufficiently high strain rate loading occurred. Doan and Gary (2009) have demonstrated that such high strain rate loading is rare but may occur, for instance, associated with supershear earthquakes.

The feedback process described above may explain the commonly observed decrease in damage with distance from the fault, including in the case of pulverized rocks. Faulkner et al. (2010) review published profiles of decay of microfracturing with distance from the fault core. If we compare Fig. 4 of Faulkner et al. (2010) with the microfracture decay profile for the pulverized granite of the Arima-Takatsuki fault (Mitchell et al., 2011), we observe that the decay rate for the pulverized fault is among the highest, and as rapid as for the outcrop described by Vermilye and Scholz (1998). Pulverization is very intense close to the Arima-Takatsuki fault, but decays rapidly with distance, although the absolute microfracture density is above what is typically observed along non-pulverized faults. This is also shown on the pulverization map of the Lake Hughes outcrop (Dor et al., 2006), reported in Fig. 3, where pulverized outcrop is localized in patches. This may be explained by our results. Before pulverization, rocks closer to the fault core are more damaged and hence easier to pulverize. During the first pulverizing events, they get even more damaged than rocks located farther from the fault. With successive events, they would experience intense comminution compared to rocks further away. Pulverized rocks would then be found highly localized close to the fault.

The distribution of pre-damaged rocks may also explain the paradox of the Lake Hughes outcrop along the Mojave segment of the San Andreas Fault (Dor et al., 2006), where pulverized granite and undamaged limestone are found on the same side of the fault. The two rocks are likely to have different strengths and are therefore likely to pulverize in different ways. If earthquakes started to homogeneously damage the granite but not the limestone, the feedback loop described above would further differentiate the two rock behaviors relative to loading. Granite would become progressively damaged and easier to pulverize, while the carbonate rock would stay relatively intact and harder to damage.

Several pulverized outcrops have an asymmetric damage pattern (Dor et al., 2006; Mitchell et al., 2011) that has been attributed to the high frequency tensile pulse on the strongest side generated by an earthquake along a bimaterial fault (Shi and Ben-Zion, 2006). As the strongest side gets more damaged and becomes less strong, mature bimaterial faults may not be able to generate such high frequency pulses. Several arguments are in favor of the persistence of the high frequency pulse: (1) The development of an asymmetric pulse is controlled by mechanical properties at the kilometeric scale (2) Pulverized rocks have so far been found only at the surface or at shallow depths (Wechsler et al., 2011). We add a third argument: weaker rocks are more easily pulverized, and if the strongest side experienced pulverization previously, it would become more amenable to further pulverization. This could explain the sharp asymmetry in distribution of pulverized rocks along bimaterial faults.

In this feedback process leading to pulverization, we have ignored the healing process that follows earthquake events. Healing would seal fractures by a wide range of processes that depend on the size of the fractures (Gratier and Gueydan, 2007): thin fractures experience self-healing within days, a process driven by minimization of surface energy, whereas larger fractures require years to heal by pressure solution. Hence large scale-healing of

faults is expected to be driven by pressure solution (Gratier, 2011). Pressure-solution efficiency depends on the solubility of the mineral involved. Dissolution of feldspar and quartz are more efficient at high temperatures, below 5 km depth, whereas dissolution of calcite is more efficient at low temperatures, above 3 km depth for a classical geothermal gradient of 30 K/km (Gratier et al., 2003). For instance, samples taken within the San Andreas Fault at the SAFOD borehole show evidence of intense sealing by calcite, some evidence of feldspar dissolution, but quartz is intact (Gratier et al., 2011). In the case of the pulverized rocks found along the San Andreas Fault, self-healing of former thin fractures is evidenced by the presence of lineaments of inclusion planes. But Fig. 1 shows no sign of dissolution of Feldspar or quartz, consistent with the fact that these rocks were pulverized in the near surface *cit-epWechsler11*. As these rocks are crystalline, no calcite cementation is found. Hence pressure solution did not happen within these rocks: only the thin intragranular fractures with no mismatch would heal. This may explain why the pulverized rocks found along the Mojave segment of the San Andreas Fault (Dor et al., 2006) are still damaged whereas the last large recorded event in the area occurred about 150 years earlier (1857 Fort Tejon earthquake).

5. Conclusions

In this paper we have presented several pieces of evidence suggesting that rocks are easier to pulverize when they are pre-damaged. We first presented experimental results from high strain-rate loading experiments on both pre-damaged and intact granite. Pre-damaged granite is pulverized if the strain rate is higher than 150/s. Instead, two independent studies find a strain rate threshold of 250/s for intact granite. The strain rate threshold is roughly proportional to the sample strength at low strain rate. These experimental results are consistent with the statistical theory of high strain rate proposed by Denoual and Hild (2000) and Hild et al. (2003b).

We propose a scenario in which pulverized rocks may result from successive earthquakes, instead of pulverization occurring by a single event. Yet, to initiate the feedback process leading to pulverization, diffuse damage of rocks around the fault is required to occur by high strain rate loading. This suggests that pulverized rocks are markers of extreme loading. This is consistent with the persistent features associated with the process that may generate high frequency waves around a fault: bimaterial faults (Andrews and Ben-Zion, 1995), or the low roughness of segments prone to supershear rupture (Bouchon et al., 2010).

Acknowledgments

We warmly thank Gérard Gary for accepting us working on the Split Hopkinson Pressure Bars of École Polytechnique, and for providing many advices on experimental issues. We thank Christophe Nevado and Fayçal Soufi for their thin sections. We acknowledge funding from INSU 3F and UJF TUNES programs. We thank Yehuda Ben-Zion, Andy Rathburn and Gérard Gary for their comments on earlier versions of the manuscript. We are grateful to Tom Mitchell and an anonymous reviewer for their constructive reviews and to Mark Simons and Steve Smith for mending the English of the final version of the manuscript

References

- Andrews, D.J., Ben-Zion, Y., 1997. Wrinkle-like slip pulse on a fault between different materials. *J. Geophys. Res.* 102, 553–571.
- Bhat, H.S., Dmowska, R., King, G.C.P., Klinger, Y., Rice, J.R., 2007. Off-fault damage patterns due to supershear ruptures with application to the 2001 M_w 8.1

- Kokoxili (Kunlun) Tibet earthquake. *J. Geophys. Res.* 112, 1–19. doi:10.1029/2006JB004425.
- Bouchon, M., Karabulut, H., Bouin, M.-P., Schmittbuhl, J., Vallée, M., Archuleta, R., Das, S., Renard, F., Marsan, D., 2010. Faulting characteristics of supershear earthquakes. *Tectonophysics* 493 (3–4), 244–253.
- Chen, W.W., Song, B., 2010. Split Hopkinson (Kolsky) Bar Design, Testing and Applications. Mechanical Engineering Series. Springer, New York.
- Denoual, C., Hild, F., 2000. A damage model for the dynamic fragmentation of brittle solids. *Comp. Meth. Appl. Mech. Eng.* 183 (3–4), 247–258.
- Denoual, C., Hild, F., 2002. Dynamic fragmentation of brittle solids: a multi-scale model. *Eur. J. Mech. A.* 21 (1), 105–120.
- Doan, M.-L., Gary, G., 2009. Rock pulverisation at high strain rate near the San Andreas Fault. *Nat. Geosci.* 2, 709–712.
- Doan, M., Billi, A., 2011. High strain rate damage of Carrara marble. *Geophys. Res. Lett.* 38 (38), L19302. doi:10.1029/2011GL049169.
- Dor, O., Ben-Zion, Y., Rockwell, T.K., Brune, J., May 2006. Pulverized rocks in the Mojave section of the San Andreas fault zone. *Earth Planet. Sci. Lett.* 245, 642–654.
- Dor, O., Yildirim, C., Rockwell, T.K., Ben-Zion, Y., Emre, O., Sisk, M., Duman, T.Y., 2008. Geological and geomorphologic asymmetry across the rupture zones of the 1943 and 1944 earthquakes on the North Anatolian Fault: possible signals for preferred earthquake propagation direction. *Geophys. J. Int.* 173 (2), 483–504.
- Dor, O., Chester, J.S., Ben-Zion, Y., Brune, J.N., Rockwell, T.K., 2009. Damage characterization in sandstones along the Mojave section of the San Andreas fault with a new method: implications for the depth and mechanism of rock pulverization. *Pure Appl. Geophys.* 166 (10–11), 1747–1773.
- Faulkner, D.R., Jackson, C.A.L., Lunn, R.J., Schlische, R.W., Shipton, Z.K., Wibberley, C.A.J., Withjack, M.O., 2010. A review of recent developments concerning the structure, mechanics and fluid flow properties of fault zones. *J. Struct. Geol.* 32 (11), 1557–1575. doi:10.1016/j.jsg.2010.06.009.
- Gama, B.A., Lopatnikov, S.L., Gillespie Jr., J.W., 2004. Hopkinson bar experimental technique: a critical review. *Appl. Mech. Rev.* 57 (4), 223–250.
- Grady, D., Kipp, M., 1989. Dynamic rock fragmentation. In: Atkinson, B. (Ed.), *Fracture Mechanics of Rocks*. Academic Press, pp. 429–475.
- Graf, K.F., 1991. *Wave Motion in Elastic Solids*. Dover Publications.
- Gratier, J.-P., Favreau, P., Renard, F., 2003. Modeling fluid transfer along California faults when integrating pressure solution crack sealing and compaction processes. *J. Geophys. Res.* 108 (B2). doi:10.1029/2001JB000380
- Gratier, J.-P., Gueydan, F., 2007. Deformation in the presence of fluids and mineral reactions – Effect of fracturing and fluid–rock interaction on seismic cycles. In: Handy, M., Hirth, G., Hovius, N. (Eds.), *Tectonic Faults*. The MIT Press, Cambridge, Massachusetts, USA, pp. 319–356.
- Gratier, J.-P., Richard, J., Renard, F., Mittemperger, S., Doan, M.-L., Di Toro, G., Hadizadeh, J., Boullier, A.-M., 2011. Aseismic sliding of active faults by pressure solution creep: evidence from the San Andreas fault Observatory at depth. *Geology* 39, 1131–1134.
- Gratier, J.-P., 2011. Fault Permeability and strength evolution related to fracturing and healing episodic processes (Years to Millennia): the Role of pressure solution. *Oil Gas Sci. Technol. Rev. IFP Energies Nouvelles* 66 (3), 491–506.
- Heap, M.J., Faulkner, D.R., 2008. Quantifying the evolution of static elastic properties as crystalline rock approaches failure. *Int. J. Rock Mech. Min. Sci.* 45, 564–573.
- Hild, F., Denoual, C., Forquin, P., Brajer, X., 2003a. On the probabilistic–deterministic transition involved in a fragmentation process of brittle material. *Comp. Struct.* 81, 1241–1253.
- Hild, F., Forquin, P., Cordeiro da Silva, A.R., 2003b. Single and multiple fragmentation of brittle geomaterials. *Rev. Fr. Génie Civil* 7 (7–8), 973–1003.
- Irwin, G., 1957. Analysis of stresses and strain near the end of a crack traversing a plate. *Trans. ASME. Ser. E: J. Appl. Mech.* 24 (3), 361–364.
- Jayatilaka, A.de S., Trustrum, K., 1977. Statistical approach to brittle fracture. *J. Mat. Sci.* 12, 1426–1430.
- Kolsky, H., 1963. *Stress Waves in Solids*. Dover Publications.
- Mitchell, T.M., Ben-Zion, Y., Shimamoto, T., 2011. Pulverized fault rocks and damage asymmetry along the Arima-Takatsuki tectonic line, Japan: fault structure, damage distribution and textural characteristics. *Earth Planet. Sci. Lett.* 308 (3–4), 284–297.
- Mitchell, T.M., Faulkner, D.R., 2009. The nature and origin of off-fault damage surrounding strike-slip fault zones with a wide range of displacements: a field study from the Atacama fault system, northern Chile. *J. Struct. Geol.* 31 (8), 802–816.
- Nemat-Nasser, S., 2000. Mechanical Testing and Evaluation. In: *ASM Handbook*, vol. 8. ASM International, Ch. Introduction to high strain rate testing, pp. 427–428.
- Paterson, M.S., Wong, T.-F., 2005. *Experimental Rock Deformation – The Brittle Field*, second ed. Springer.
- Prentice, C.S., et al., 2009. Illuminating northern California's active faults. *EOS Trans. Amer. Geophys. U* 90 (7), 55.
- Rockwell, T.K., Sisk, M., Girty, G., Dor, O., Wechsler, N., Ben-Zion, Y., 2009. Granulometric and mineralogical properties of pulverized rocks from Tejon pass on the San Andreas fault and from Tejon Ranch on the Garlock fault, California. *Pure Appl. Geophys.* 166 (10–11), 1725–1746.
- Savage, H.M., Brodsky, E.E., 2011. Collateral damage: evolution with displacement of fracture distribution and secondary fault strands in fault damage zones. *J. Geophys. Res.* 116 (B3). doi:10.1029/2010JB007665
- Shi, Z., Ben-Zion, Y., 2006. Dynamic rupture on a bimaterial interface governed by slip-weakening friction. *Geophys. J. Int.* 165, 469–484.
- Vermilye, J.M., Scholz, C.H., 1998. The process zone: a microstructural view of fault growth. *J. Geophys. Res.* 103, 12223–12237.
- Wechsler, N., Allen, E.E., Rockwell, T.K., Girty, G., Chester, J.S., Ben-Zion, Y., 2011. Characterization of pulverized granitoids in a shallow core along the San Andreas fault, little rock, CA. *Geophys. J. Int.* 186, 401–407.
- Weibull, W., 1951. A statistical distribution function of wide applicability. *J. Appl. Mech.* – *Trans. ASME* 18, 293–297.
- Wessel, P., Smith, W.H.F., 1998. Improved version of Generic Mapping Tools released. *EOS Trans. Amer. Geophys. U* 79 (47), 579.
- Wilson, B., Dewers, T., Reches, Z., Brune, J., 2005. Particle size and energetics of gouge from earthquake rupture zones. *Nature* 434, 749–752.
- Yuan, F., Prakash, V., Tullis, T., 2011. Origin of pulverized rocks during earthquake fault rupture. *J. Geophys. Res.* 116, B06309.

Aseismic sliding of active faults by pressure solution creep: Evidence from the San Andreas Fault Observatory at Depth

J.-P. Gratier¹, J. Richard¹, F. Renard^{1,2}, S. Mittemperger³, M.-L. Doan¹, G. Di Toro^{3,4}, J. Hadizadeh⁵, and A.-M. Boullier¹

¹ISTerre (Institut des Sciences de la Terre) Observatoire, Université Joseph Fourier Grenoble, CNRS, BP 53, Grenoble 38041, France

²Physics of Geological Processes, University of Oslo, 0316 Oslo, Norway

³Università di Padova, Via Giotto 1, Padua 35137, Italy

⁴Istituto Nazionale di Geofisica e Vulcanologia, Via di Vigna Murata 605, Rome 00143, Italy

⁵Department of Geography and Geosciences, University of Louisville, Louisville, Kentucky 40292, USA

ABSTRACT

Active faults in the upper crust can either slide steadily by aseismic creep, or abruptly causing earthquakes. Creep relaxes the stress and prevents large earthquakes from occurring. Identifying the mechanisms controlling creep, and their evolution with time and depth, represents a major challenge for predicting the behavior of active faults. Based on microstructural studies of rock samples collected from the San Andreas Fault Observatory at Depth (California), we propose that pressure solution creep, a pervasive deformation mechanism, can account for aseismic creep. Experimental data on minerals such as quartz and calcite are used to demonstrate that such creep mechanism can accommodate the documented 20 mm/yr aseismic displacement rate of the San Andreas fault creeping zone. We show how the interaction between fracturing and sealing controls the pressure solution rate, and discuss how such a stress-driven mass transfer process is localized along some segments of the fault.

INTRODUCTION AND GEOLOGICAL FRAMEWORK

Aseismic deformation is observed in active fault zones, but the mechanisms of deformation are still unclear (Scholz, 2002). Samples collected from the San Andreas Fault Observatory at Depth (SAFOD, California) allow correlation of fault rock microstructures with real-time geophysical data, and therefore provide useful information for identifying such mechanisms. Here we show that a stress-driven mass transfer process, i.e., pressure solution creep (Rutter and Mainprice, 1978), can accommodate the aseismic deformation of the San Andreas fault.

The SAFOD borehole, drilled to 3 km depth, is at the southern part of a 175-km-long creeping section of the San Andreas fault (Fig. 1A). The sliding rate is 28 mm/yr in the central part of the creeping segment, and decreases toward both northern and southern ends (Fig. 1B). The creep rate near the SAFOD site is ~20 mm/yr (Fig. 1B), as measured at the surface within a 20-m-thick fault zone (Titus et al., 2006). Such a narrow creeping zone appears to extend through the entire upper crust, coinciding with a zone of observed microseismicity (Nadeau and Dolenc, 2005). The southernmost part of the creeping section, where the creeping rate gradually falls to zero (Fig. 1B), is a zone of repeating M6 earthquakes, the most recent being the 2004 M6 Parkfield earthquake.

At the SAFOD site, the right-lateral displacement of the San Andreas fault has juxtaposed arkosic sandstones and conglomerates of the Pacific plate against the shale, siltstone, and claystone of the North American plate (Fig. 1C). Microstructural observations of the core samples show evidence of deformation across the damaged zone extending to core-parallel depths of 3150–3410 m (Zoback et al., 2010): shear zones alternate with foliated rocks more or less parallel to the San Andreas fault (Solum et al., 2006). Borehole casing deformation revealed two low-seismic-velocity, actively creeping, zones of foliated rocks (Fig. 1C): a main creeping segment (central deforming zone) at 3300.07–3302.81 m and a secondary creeping segment deforming at lower shear rate (southern deforming zone) at 3191.4–3193 m; both the central and southern deforming zones contain serpentine clasts and

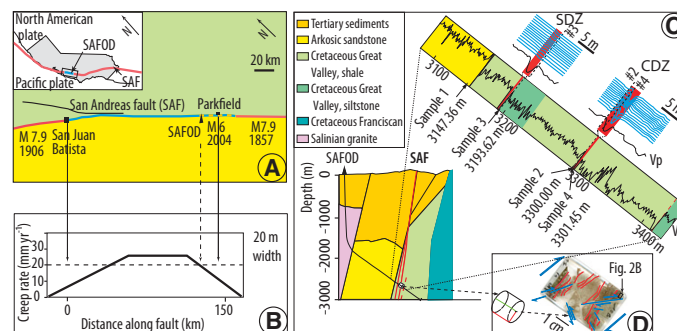


Figure 1. A: Map view of San Andreas fault system showing creeping segment (blue line) with trace of last two M 7.9 earthquakes that currently are locked segments (red lines) and transitional zone of M6 earthquakes (dotted line); coloring corresponds to contact at 3 km depth in C. SAFOD—San Andreas Fault Observatory at Depth. B: Evolution of creep rate along creeping zone (Titus et al., 2006). C: Schematic cross section of SAFOD site, perpendicular to fault; enlargement shows P wave velocity log (Zoback et al., 2010) together with location of four described samples; two creeping faults are highlighted in red; enlargement in vicinity of these creeping zones (top right) shows casing deformation (blue lines) indicating active creep and accurate location of three of the samples. SDZ—southern deforming zone; CDZ—central deforming zone. D: Sketch of thin section (sample 2) perpendicular to foliation (red), with minor faults (blue) (location of Fig. 2B is shown).

highly sheared siltstones (Zoback et al., 2010) without clear displacement discontinuity at their boundaries.

EVIDENCE OF PRESSURE SOLUTION CREEP

Based on the microstructural study of samples from the SAFOD core, we infer that an important mechanism of aseismic deformation is pressure solution creep, which induces pervasive and irreversible deformation of the whole rock. This mechanism is active both in the less deformed samples collected from the damaged zone (sample 1) and in intensely deformed foliated samples of the creeping zone (sample 2) shown in Figure 1D. We show that the most highly deformed zones have the highest amount of strain accommodated by pressure solution. Evidence of pressure solution is revealed using elemental distribution maps in sample 1 (Fig. 2A). Stress-driven dissolution associated with horizontal contraction is demonstrated by the dissolution of Ca-Na feldspars at feldspar-quartz grain impingements along a pressure solution seam, whereas K, Mg, Fe, and Ti (phyllosilicates, Fe and Ti oxides, sulfurs) are passively concentrated in the same seam (Fig. 2A). Fracturing is associated with pressure solution. Contraction perpendicular to the dissolution seam, apparent from the grain shape change (Fig. 2A), was estimated to be ~10%. Since there is no evidence of redeposition in veins nearby, it may be concluded that the soluble species have been transported away from the zone of dissolution.

In sample 2, Ca, Si, and Na are depleted within the solution seams where Mg, Fe, Ti are passively concentrated (Fig. 2B). Such a pressure

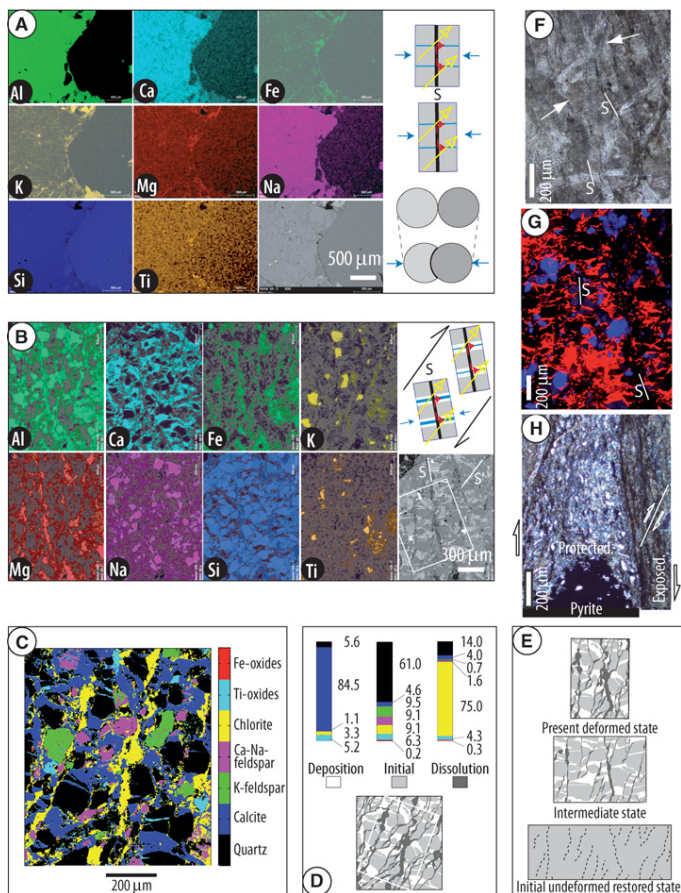


Figure 2. Pressure solution evidence. A and B: Elements distribution from scanning electron microscopy (SEM) analyses for samples 1 and 2, respectively; brighter color indicates higher content; small sketches show diffusive mass transfer path (red arrows) from solution seams (black) (S) to fluid (blue) within vein (white) and fluid flow (yellow). C: Mineralogical distribution in white rectangle area of B (bottom right), sample 2. D: Same area as C. Top—mineral composition of deposition, initial, and dissolution zones. Bottom—areas of three zones are 27%, 58%, and 15%, respectively. E: Present deformed state (top) and restored undeformed state (bottom) of area of white rectangle of D with intermediate deformed state (middle). F: Evidence of stress dissolution of calcite (arrows) within vein with pressure solution seams (S), sample 3. G: Calcite filling of fracture network (orange) perpendicular to solution cleavage (S) (cathodoluminescence, sample 3). H: Stress shadow effect showing evidence of pressure solution grain size reduction from protected to exposed zone with quartz and feldspar depletion, sample 3. (Images A, B, F, G, H can be seen in larger view in the GSA Data Repository¹.)

solution process leads to a foliation oriented at a high angle to the drill-hole axis (Figs. 1C and 1D). In contrast to sample 1, calcite minerals in sample 2 fill a network of veins oriented perpendicular to the solution seams, consistent with an extension parallel to the foliation. Finite deformation can be calculated from mineral distribution (Fig. 2C). Three zones are distinguished (Fig. 2D): (1) a dissolution zone (with passively concentrated chlorites and Fe oxides), (2) a deposition zone (with precipitated calcite and occasional Ti oxides), and (3) an initial zone (predeformation zone composed of quartz, feldspars, and chlorites). Veins open and seal progressively (Mittempergher et al., 2011). Consequently, initial zones are

¹GSA Data Repository item 2011336, Figures DR1 and DR2, is available online at www.geosociety.org/pubs/ft2011.htm, or on request from editing@geosociety.org or Documents Secretary, GSA, P.O. Box 9140, Boulder, CO 80301, USA.

dissolved at the beginning of the pressure solution process, then both initial and deposition zones are progressively dissolved (Figs. 2E and 2F). The relative mass change, $\Delta M/M_0$, is calculated using the passive concentration of insoluble minerals in the dissolution zone compared with the composition of the protected zone between solution seams (Figs. 2D and 2E) as:

$$\Delta M / M_0 = (I_p / I_d) - 1, \quad (1)$$

where I_p and I_d are the content in insoluble minerals in the protected and in the dissolution zone, respectively, and M_0 is the mass of a representative volume element before deformation. Two end members of mass transfer amount are obtained by comparing the composition of dissolution zones with the protected zones: either initial zones or both initial and deposition zones. The two calculations give about the same amounts of relative mass decrease for the dissolution zones (−88% to −90%). A mean value of contraction perpendicular to the foliation of ~60% can be calculated by taking into account the areas of the dissolution zones (Fig. 2D). A mean extension of ~50% perpendicular to the veins is evaluated from the ratio of deposition areas to initial areas (Figs. 2D and 2E). The mass decrease of each soluble mineral that shows no significant differential alteration between protected and dissolution zones can also be calculated (Gratier et al., 2003): quartz, −96%; K-feldspars, −99%; Ca-Na feldspars, −98%; calcite, −94%. Foliation as mineral segregation appears to be linked to the pressure solution creep, with an almost complete disappearance of the soluble minerals in the zones of dissolution. Mass conservation calculations comparing the amounts of dissolved Ca-Na feldspars and deposited minerals in veins show that a large proportion of calcite must come from outside the studied area, brought by episodic fluid flow (Mittempergher et al., 2011). Evidence of dextral shearing is found in thin sections cut normal to the foliation cleavage from both en echelon fractures (Fig. 1D) and crosscutting cleavages (S and S', Fig. 2B). Consequently, the calcite vein network and the solution cleavage surfaces are consistent with a stress-driven mass transfer process that accommodates right-lateral strike-slip movement along the San Andreas fault (Fig. 2B). Similar solution cleavage–vein network texture (Fig. 3A) is recorded in samples collected near the creeping zone of the southern deforming zone (sample 3, Fig. 2G), but accommodating lower finite strain than in the central deforming zone. Pressure solution creep also develops at grain scale by diffusion-accommodated grain sliding (Fig. 3B; Ashby and Verrall, 1973) within highly sheared and foliated shale in which feldspar and quartz are depleted by the pressure solution process. This can be seen both near the southern deforming zone (sample 3, Fig. 2H) and in the middle of the central deforming zone (sample 4, Fig. 3E). Evidence of dissolution is documented at grain contacts in the SAFOD creeping zones (Schleicher et al., 2009).

KINETICS OF PRESSURE SOLUTION CREEP

A key issue is whether pressure solution kinetics are consistent with the measured permanent fault creep rates (Titus et al., 2006). To solve this issue, we propose a model (Fig. 3) where steady-state creeping occurs within a vertical shear zone as much as 10 km deep. We use a pressure solution creep law for quartz and calcite derived from laboratory indentation experiments (Gratier et al., 2009; Zubtsov et al., 2005). The strain rate $\dot{\epsilon}$ derived from the experimental relationship is:

$$\dot{\epsilon} = \Delta d / (d \Delta t) = 8 D w c V_s \left(e^{3 \Delta \sigma_n V_s / RT} - 1 \right) / d^3, \quad (2)$$

where c is the solubility of the diffusing solid, V_s is the molar volume of the stressed solid, R is the gas constant, T is temperature, D is the diffusion constant along the stressed interface, w is the thickness of the trapped fluid phase along which diffusion occurs, t is time, and $\Delta \sigma_n$ is the driving stress as the difference between normal stress on a dissolution surface and the fluid pressure in the vein. In experiments, d is the diam-

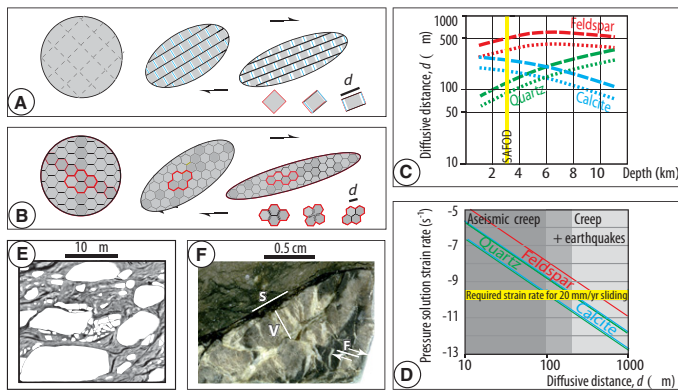


Figure 3. Pressure solution creep mechanisms. A: Mass transfer from solution cleavage (black) to veins (white) with detail of progressive mass transfer process for given element; d is mean diffusion distance between veins along solution cleavage; free fluid in veins is blue. **B:** Diffusion-accommodated grain sliding, with detail of geometry of progressive grain sliding (Ashby and Verrall, 1973); d is mean diffusion distance. **C:** Distance of diffusive mass transfer d versus depth for various minerals required to accommodate 20 mm/yr horizontal displacement rate by pressure solution creep in vertical shear zone of 1 m width (dotted line, strain rate of $3.3 \times 10^{-10} \text{ s}^{-1}$) or 3 m width (dashed lines, strain rate of $1.1 \times 10^{-10} \text{ s}^{-1}$). SAFOD—San Andreas Fault Observatory at Depth. **D:** Pressure solution strain rate versus distance of diffusive mass transfer through entire crust for various minerals; minimum and maximum values for quartz and calcite; yellow line is required strain rate for creeping zone. **E:** Scanning electron microscope image of sample 4, within creeping zone of central deforming zone (CDZ), showing mixing of phyllosilicates (soft smectite, chlorite, in various grays) and soluble-rigid minerals (quartz, feldspars, calcite, serpentine, in white); crack networks (black) are linked to dewatering of smectite during sample preparation. Deformation is accommodated by grain boundary sliding, possibly by diffusion for soluble species. **F:** Remnant of sandstone patch deformed by pressure solution cleavage (S)-veins (V) process embedded in CDZ creeping zone, with microfaults (F) (sample 4). (Images E and F can be seen in larger view in the Data Repository [see footnote 1].)

eter of the indenter. In nature, d can refer either to the spacing between fractures that corresponds to the diffusive mass transfer distance between veins along a dissolution surface (Fig. 3A), to the grain size in the case of diffusion-accommodating grain boundary sliding (Fig. 3B). Such a diffusion-controlled pressure solution creep law is likely to operate in conditions prevailing at 6–10 km, whereas for the lesser depths (2–4 km), a shift from diffusion control to reaction control is predicted (Renard et al., 1999), but only if d exceeds 300 μm , which is not likely here (see following). It is possible to extend the creep law for quartz obtained at 350 $^{\circ}\text{C}$ to lower temperatures within the entire upper crust by assuming an activation energy of 15 kJ/mole (Rutter and Mainprice, 1978). It is also possible to extend the creep law to other minerals such as calcite (Zubtov et al., 2005) and feldspars by changing the solubility and molar volume parameters. Using such creep laws, with a given stress condition, we can estimate the maximum values of d required to accommodate a displacement rate of 20 mm/yr over a 1–3-m-thick shear zone, such as the central deforming zone (Fig. 1C). At 3 km depth, a minimum conservative value for the pressure solution driving stress is the difference between the maximum and the minimum horizontal stress (S_{hmax} and S_{hmin} , respectively). This difference was measured to be ~ 60 MPa, S_{hmin} being very near the overburden stress (Hickman and Zoback, 2004). The same stress value was used for the entire upper crust (Figs. 3C and 3D). With this model, we show that the maximum required distance of mass transfer at 3 km depth varies with mineral composition in the range 90–350 m and 125–500 m for 1 and 3 m width fault zones, respectively (Fig. 3C).

These values are larger than the fracture spacing observed for samples 2 and 3 (solution cleavage-veins process; Figs. 2E–2G). They are also much larger than the observed grain sizes in the foliated zones, as in sample 3 and 4 (diffusion-accommodated grain-sliding process; Figs. 2H and 3E). Since the observed diffusion distances are smaller than a conservatively calculated d value, pressure solution creep can therefore easily accommodate the measured displacement rate of 20 mm/yr. The diffusion-accommodated grain-sliding process can accommodate much larger finite deformations than the solution cleavage-veins process (Ashby and Verrall, 1973). For this reason, with increasing deformation, the part of the rock deformed by the solution cleavage-veins process, which is also relevant to the most rigid part of the deformed zone, is probably progressively dilacerated and dispersed into the creeping zone (e.g., dark gray grains, Fig. 3B). Evidence of large patches of sandstone deformed by the solution cleavage-veins process can be found in the middle of the central deforming zone (sample 4, Fig. 3F). The solution cleavage-veins process appears therefore to be a transitory state of deformation, which testifies to the efficiency of the pressure solution mechanism and is probably superseded by the diffusion-accommodated grain-sliding process within the most deformed regions of creep.

DISCUSSION AND CONCLUSION

Interaction between creep and seismic (microseismic) fracturing is an important issue. Dissolution indenter experiments show that grain-scale fracturing can drastically accelerate the displacement rate accommodated by pressure solution creep (Gratier, 2011); fracturing opens new paths for solute transport along fluid-filled fractures, decreasing the distance of diffusion, d . However, if the fractures are progressively sealed, this effect disappears as sealing increases the distance of mass transfer (d), and consequently reduces the displacement rate. At grain scale in the laboratory, such a microfracture pressure solution sealing process may be observed within no less than a few months. In nature, pressure solution fracture sealing probably takes several years or decades, depending on the spacing and the width of the fractures (Gratier, 2011). This could partially explain the effect of the A.D. 2004 M6 Parkfield earthquake on the creep rate southeast of the SAFOD site: coseismic fracturing activated afterslip creep (Freed, 2007) that progressively decreased with time as the fault healed (Li et al., 2006).

The crucial role of the diffusion distance d is shown in Figure 3D. When d is small enough (10–100 m), steady-state pressure solution creep can accommodate the observed aseismic displacement rate of 20 mm/yr through the entire upper crust. When d is larger (>100 m), pressure solution creep occurs but cannot accommodate the displacement rate and relax the stress. Consequently, small seismic ruptures occur (Fig. 3F), in turn activating pressure solution creep.

Pressure solution creep is compatible with the low heat flow measurements in the creeping section (Zoback et al., 2010), since this process does not generate significant heat. Various explanations have been proposed for the apparent low friction behavior of the creeping zone. Increases in fluid pressure may reduce the frictional resistance to sliding (Scholz, 2002), but elevated fluid pressures were not measured during drilling, although transient increases of fluid pressure may have occurred episodically in the past (Mitttempergher et al., 2011). Talc minerals were found in SAFOD cuttings and should have a weakening effect (Moore and Rymer, 2007), especially if they develop a foliation (Collettini et al., 2009). However, there is as yet no evidence for the presence of continuous layers of talc at SAFOD (Holdsworth et al., 2011). Alternatively, from experiment on cuttings, or laboratory-ground samples, of San Andreas fault creeping zones, Carpenter et al. (2011) and Lockner et al. (2011) found friction values as low as 0.15–0.2, due to the presence of weak phyllosilicate as saponite. It is clear from samples of the San Andreas fault creeping zone (Fig. 3E) that the deformation is accommodated by grain boundary sliding. Friction and

diffusion may compete to accommodate such grain sliding, but it is likely that, at an imposed strain rate, the less energy-consuming process will win. Pressure solution driving forces of 10 and 0.01 MPa are enough to accommodate 10^{-10} s⁻¹ strain rate over 3 m width, with 100 and 10 μm grain size, respectively, for quartz and calcite at 6 km depth. Moreover, saponite becomes unstable above ~150 °C and is unlikely to be found deeper in the fault zone than 3.5–4 km. Consequently, as long as the deformation requires grain boundary sliding involving soluble minerals, pressure solution creep is an efficient mechanism of aseismic creep through the entire upper crust down to more than 10 km.

A final question is why, at a given time, pressure solution creep is localized along some segments of the fault. The answer may be that pressure solution creep needs specific conditions to develop at a significant rate. Soluble minerals such as feldspar, calcite, quartz (Gratier et al., 2003), and serpentine (Andreani et al., 2005) must be present with a reactive fluid phase. The distance of diffusive mass transfer (*d*) must be as small as possible. This requires very fine grained material, possibly related to intense seismic fracturing in the San Andreas fault. Soluble grains must not seal together in order to keep fast diffusive paths along solution seams (Niemeijer and Spiers, 2005). Two processes could avoid such sealing, and occur in the San Andreas fault creeping zones, i.e., passive concentration of phyllosilicates due to soluble species pressure solution depletion (Figs. 2H, 3E, and 3F) and the growth of new phyllosilicates (Holdsworth et al., 2011). In such a way, phyllosilicates get trapped around the soluble species, preventing their sealing and activating diffusive mass transfer. Under these conditions, the process is self-organized through a positive feedback process, which allows pressure solution creep process localization within some fault segments.

ACKNOWLEDGMENTS

We thank S. Hickman and B. Holdsworth for their suggestions on an early version, and F. Agosta, C. Colletini, and J. Imber for their comments on the final version that significantly improved the manuscript. The Grenoble team was partially supported by CNRS-INSU (Centre National de la Recherche Scientifique–Institut National des Sciences de l'Univers) natural hazards program and Agence Nationale de la Recherche ANR-09-JCJC-0011-1. Hadizadeh and Di Toro were partially supported by U.S. National Science Foundation grant EAR-0545472. Di Toro and Mitterpergher were supported by a Progetti di Eccellenza Fondazione Cassa di Risparmio di Padova e Rovigo and by European Research Council Starting Grant Project 205175.

REFERENCES CITED

Andreani, M., Boullier, A.-M., and Gratier, J.-P., 2005, Development of schistosity by dissolution–crystallization in a Californian serpentinite gouge: *Journal of Structural Geology*, v. 27, p. 2256–2267, doi:10.1016/j.jsg.2005.08.004.

Ashby, M., and Verrall, R., 1973, Diffusion-accommodated flow and superplasticity: *Acta Metallurgica*, v. 21, p. 149–163, doi:10.1016/0001-6160(73)90057-6.

Carpenter, B.M., Marone, C., and Saffer, D.M., 2011, Weakness of the San Andrea Fault revealed by samples from the active fault zone: *Nature Geoscience*, v. 4, p. 251–254, doi:10.1038/ngeo1089.

Colletini, C., Niemeijer, A., Viti, C., and Marone, C., 2009, Fault zone fabric and fault weakness: *Nature*, v. 462, p. 907–910, doi:10.1038/nature08585.

Freed, A.M., 2007, Afterslip (and only afterslip) following the 2004 Parkfield, California, earthquake: *Geophysical Research Letters*, v. 34, L06312, doi:10.1029/2006GL029155.

Gratier, J.-P., 2011, Fault permeability and strength evolution related to fracturing and healing episodic processes (years to millennia): The role of pressure solution: *Oil & Gas Science and Technology*, v. 66, no. 3, doi:10.2516/ogst/2010014.

Gratier, J.-P., Favreau, P., and Renard, F., 2003, Modeling fluid transfer along Californian faults when integrating pressure solution crack sealing and compaction process: *Journal of Geophysical Research*, v. 108, no. B2, p. 28–52, doi:10.1029/2001JB000380.

Gratier, J.-P., Guiguet, R., Renard, F., Jenatton, L., and Bernard, D., 2009, A pressure solution creep law for quartz from indentation experiments: *Journal of Geophysical Research*, v. 114, B03403, doi:10.1029/2008JB005652.

Hickman, S., and Zoback, M., 2004, Stress orientations and magnitudes in the SAFOD pilot hole: *Geophysical Research Letters*, v. 31, L15S12, doi:10.1029/2004GL020043.

Holdsworth, R.E., van Diggelen, E.W.E., Spiers, C.J., de Bresser, J.H.P., Walker, R.J., and Bowen, L., 2011, Fault rocks from the SAFOD core samples: Implications for weakening at shallow depths along the San Andreas fault, California: *Journal of Structural Geology*, v. 33, p. 132–144, doi:10.1016/j.jsg.2010.11.010.

Li, Y.G., Chen, P., Cochran, E.S., Vidale, J.E., and Burdette, T., 2006, Seismic evidence for rock damage and healing on the San Andreas fault associated with the 2004 M 6.0 Parkfield earthquake: *Seismological Society of America Bulletin*, v. 96, p. S349–S363, doi:10.1785/0120050803.

Lockner, D.A., Morrow, C., Moore, D.E., and Hickman, S., 2011, Low strength of deep San Andreas fault gouge from SAFOD core: *Nature*, v. 472, p. 82–85, doi:10.1038/Nature09927.

Mitterpergher, S., Di Toro, G., Gratier, J.-P., Hadizadeh, J., Smith, S.A.F., and Spiers, R., 2011, Evidence of transient increases of fluid pressure in SAFOD phase III cores: *Geophysical Research Letters*, v. 38, L03301, doi:10.1029/2010GL046129.

Moore, D.E., and Rymer, M.J., 2007, Talc-bearing serpentinite and the creeping section of the San Andreas fault: *Nature*, v. 448, p. 795–797, doi:10.1038/nature06064.

Nadeau, R.M., and Dolenc, D., 2005, Nonvolcanic tremors deep beneath the San Andreas Fault: *Science*, v. 307, p. 389, doi:10.1126/science.1107142.

Niemeijer, A., and Spiers, C.-J., 2005, Influence of phyllosilicates on fault strength in the brittle–ductile transition: Insight from rock analogue experiments, in Bruhn, D., and Burlini, L., eds., *High-strain zones: Structure and physical properties*: Geological Society of London Special Publication 245, p. 303–327, doi:10.1144/GSL.SP.2005.245.01.15.

Renard, F., Park, A., Ortoleva, P., and Gratier, J.-P., 1999, An integrated model for transitional pressure solution in sandstones: *Tectonophysics*, v. 312, p. 97–115, doi:10.1016/S0040-1951(99)00202-4.

Rutter, E.H., and Mainprice, D.H., 1978, The effect of water on stress relaxation of faulted and unfaulted sandstones: *Pure and Applied Geophysics*, v. 116, p. 634–654, doi:10.1007/BF00876530.

Schleicher, A.M., Tourscher, S.N., van der Pluijm, B.A., and Warr, L.N., 2009, Constraints on mineralization, fluid–rock interaction, and mass transfer during faulting at 2–3 km depth from the SAFOD drill hole: *Journal of Geophysical Research*, v. 114, B04202, doi:10.1029/2008JB006092.

Scholz, C., 2002, *The mechanics of earthquakes and faulting*: Cambridge, Cambridge University Press, 439 p.

Solum, J.G., Hickman, S.H., Lockner, D.A., Moore, D.E., van der Pluijm, B.A., Schleicher, A.M., and Evans, J.P., 2006, Mineralogical characterization of protolith and fault rocks from the SAFOD Main Hole: *Geophysical Research Letters*, v. 33, L21314, doi:10.1029/2006GL027285.

Titus, S.J., DeMets, C., and Tikoff, B., 2006, Thirty-five-year creep rates for the creeping segment of the San Andreas fault and the effects of the 2004 Parkfield earthquake: Constraints from alignment arrays, continuous global positioning system, and creepmeters: *Seismological Society of America Bulletin*, v. 96, p. S250–S268, doi:10.1785/0120050811.

Zoback, M., Hickman, S., and Ellsworth, W., 2010, Scientific drilling into the San Andreas fault zone: *Eos (Transactions, American Geophysical Union)*, v. 91, p. 197–199, doi:10.1029/2010EO220001.

Zubtov, S., Renard, F., Gratier, J.-P., Dysthe, D.K., and Traskine, V., 2005, Single-contact pressure solution creep on calcite monocrystals, in Gapais, D., et al., eds., *Deformation mechanisms, rheology and tectonics: From minerals to the lithosphere*: Geological Society of London Special Publication 243, p. 81–95, doi:10.1144/GSL.SP.2005.243.01.08.

Manuscript received 14 January 2011

Revised manuscript received 31 May 2011

Manuscript accepted 9 July 2011

Printed in USA

1 **Time and space evolution of an active creeping fault zone: insights**
2 **from the brittle and ductile microstructures in the San Andreas**
3 **Fault Observatory at Depth**

4
5 Julie Richard¹, Jean-Pierre Gratier¹, Mai-Linh Doan¹, Anne-Marie Boullier¹, François
6 Renard^{1,2}

7
8 ¹ ISTerre, University Grenoble 1 & CNRS, BP 53, 38041, Grenoble, France

9 ² Physics of Geological Processes, University of Oslo, 0316 Oslo, Norway

10

11

12 **Abstract**

13 Creep processes relax an important part of the tectonic stresses in active faults, either by
14 permanent or episodic processes. Our aim is to better understand such mechanisms of creep
15 and their evolution with time and space. Results are presented from microstructural studies of
16 natural samples collected from the SAFOD drilling site through the San Andreas Fault,
17 California. Fault microstructures recorded the chronology of the deformation. It started from a
18 thick, hundred meters wide deformed zone – corresponding to the present-day damaged zone
19 –mostly accommodated by pressure solution creep and it evolved to a weak creeping zone of
20 meter size, with the dissolution of soluble minerals and the concentration of phyllosilicates
21 leading to a high soft matrix content. In this process, the foliation evolves from a texture with
22 cleavages and veins with parallel orientation to foliation without coherent orientation in the
23 present day creeping zone. Pressure solution creep is favored by the presence of fluids and
24 phyllosilicates and by fracturing and comminuting processes. Conversely, fracture sealing
25 making pressure solution creep less efficient, tends to strengthen the rocks leading to tectonic

26 differentiation. Within the first 3-4 km depth of the crust the creeping mechanism is
27 controlled by the very low friction of the saponite and by diffusive sliding of polymineral
28 clasts embedded into the clay matrix. At greater depths (4-12 km), saponite being transformed
29 into corrensite and then chlorite with much higher friction coefficients, pressure solution
30 diffusive grain boundary sliding is likely to be the controlling creeping mechanism.

31

32 **1 – Introduction**

33 Active continental faults relax stress during short seismic events generating earthquakes. They
34 can also accommodate an important part of the deformation during periods of slow and
35 aseismic sliding by creep. Two types of creep must be distinguished. The first one is a
36 permanent steady-state creep that is associated with specific properties of the fault rocks and
37 their environment. The deformation stays constant through time and the strain rate remains
38 fairly constant (**Burford and Harsh, 1980; Azzaro et al., 2001; Titus et al., 2006**). The
39 second one is recorded on periods ranging from months to decade of years after an
40 earthquake; it can be considered as a post-seismic creep process and occurs either in the lower
41 crust below the seismic fault or in the upper crust around the seismic patches (**Gao et al.,**
42 **2000; Johanson et al., 2006; Murray and Langbein, 2006; Barbot et al., 2009**). In this last
43 case it is also called afterslip process (**Freed, 2007**). Both steady-state creep and post-seismic
44 (afterslip) creep seem to be linked with two important deformation mechanisms:
45 (micro)fracturing on the one hand and healing and sealing processes on the other hand
46 (**Rubin et al., 1999; Gratier et al., 1999; Perfettini and Avouac, 2004; Nadeau et al.,**
47 **2004; Li et al., 2006; Zoback et al., 2010; Gratier et al., 2011**). Those two mechanisms are
48 in competition. Fracturing reduces the strength of the fault rocks and could enhance aseismic
49 deformations whereas sealing processes strengthen the rocks, increasing its cohesion
50 (**Gratier, 2011**). More generally, such processes of coupled dissolution-precipitation

51 reactions create or destroy porosity and are responsible for slow deformations in the mid- to
52 upper-crustal rocks (**Wintsch and Yi, 2002; Putnis, 2002**).

53 Considering the relationships between aseismic deformation and fault processes, identifying
54 creep mechanisms is required to better understand the seismic cycle. Numerous observations
55 have been performed on creep in major active continental faults (**Steinbrugge and Zacher,**
56 **1960; Yu and Liu, 1989; Lee et al., 2005; Titus et al., 2006**) and the questions focus now on
57 the mechanisms responsible of such a behavior.

58 The San Andreas Fault (SAF) is one of the most active continental faults in the world and one
59 of the best surveyed. It is a mature fault divided into segments; some of them experiencing
60 steady-state and/or post-seismic creep. The San Andreas Fault Observatory at Depth
61 (SAFOD) drilling project has given the unique opportunity to study samples coming from the
62 fault core at depth. Numerous studies on creep based on the material provided by this drilling
63 project have been performed (**d'Alessio et al., 2006; Moore and Rymer, 2007; Solum et al.,**
64 **2007; Schleicher et al., 2009a; Schleicher et al., 2010; Janssen et al., 2010; Zoback et al.,**
65 **2010; Gratier et al., 2011; Holdsworth et al., 2011; Janssen et al., 2012; Hadizadeh et al.,**
66 **2012**). A key discovery in the SAF creeping segment is the observation that the creeping
67 process, and more generally sliding on the whole San Andreas Fault, does not lead to local
68 increase of heat, as it would be the case if it was linked to a friction process (**Lachenbruch et**
69 **Sass, 1980**). Consequently, the fault is said to be weak (see below for more details). At least
70 three major mechanisms have been investigated that could weaken the fault and enhance
71 creep deformations. The first one is linked to pore fluid overpressure (**Rice, 1992; Chester et**
72 **al., 1993**), and some studies have brought evidences for episodic fluid overpressure in the
73 fault core (**Mittempergher et al., 2011**), but they also showed that this mechanism alone is
74 not efficient enough to explain the weakness of the fault and the observed creep rate.
75 Moreover, the potential sources of fluid in the fault do not provide a high enough flux (**Fulton**

76 **and Saffer, 2009; Fulton et al., 2009)** and such high fluid pressure events must be episodic
77 and related to earthquake activity (**Mittempergher et al., 2011**), since at present time no
78 evidence of high fluid pressure was found in the borehole (**Zoback et al., 2011**). The second
79 deformation mechanism is frictional sliding. In order to fit the observed low heat flow along
80 the creeping zone, a large amount of very weak minerals is required, such as talc, smectite
81 and clays. Consequently this mechanism depends both on rock composition and on the
82 temperature and pressure conditions (**Moore and Lockner, 2007; Moore and Rymer, 2007;**
83 **Carpenter et al., 2009; Collettini et al., 2009; Carpenter et al., 2011; Lockner et al.,**
84 **2011**). Laboratory experiments also suggest that low friction is correlated to velocity-
85 strengthening behavior that inhibits the nucleation of earthquakes (**Ikari et al., 2011**). Finally,
86 the last creeping process that could accommodate large aseismic deformation without heat
87 production is pressure solution creep (**Rutter and Mainprice, 1979; Schleicher et al.,**
88 **2009b; Gratier et al., 2011**). This deformation mechanism is a stress driven fluid-assisted
89 mass transfer process, widely spread in the rocks of the upper crust (**Gratier et al., 2013a**).
90 Due to local variations in chemical potential related to local stress heterogeneities, soluble
91 species (such as quartz, feldspar, serpentine, etc.) are progressively dissolved, transferred
92 along a fluid phase trapped under stress and either precipitated or were washed away when
93 reaching open pores (**Weyl, 1959; Paterson, 1973**). This leads to a passive concentration of
94 insoluble species (such as phyllosilicates, oxides, etc.) in the zones of dissolution. Such
95 chemical segregation develops a foliation perpendicularly to the direction of the maximum
96 normal stress and consequently leads to a ductile deformation of the rock by spaced or slaty
97 cleavage (**Hobbs et al., 1974; Ramsay, 1967; Siddans, 1972; Wood, 1974**).
98 In the present study, we analyze rock microstructures that have recorded creep, in twelve
99 samples collected from the Phase 3 core of the SAFOD, localized in the damaged zone (about
100 3200 m to 3400 m Measured Depth (**Zoback et al., 2010**), in order to identify the main creep

101 mechanism that occurs nowadays in the SAF. We used optical microscope,
102 cathodoluminescence (CL), Scanning Electron Microscope (SEM), Field Emission Gun
103 Scanning Electron Microscopy (FEG-SEM), Back Scattered Electron imaging (BSE) and
104 Electron Probe Micro–Analysis (EPMA) on thin sections. Additional X-Ray Powder
105 Diffraction (XRPD) analyses on fragments were collected.

106 Eight samples come directly from the most active shearing zone detected in the main hole: the
107 Central Deforming Zone (CDZ), which experiences active creep today. Two types of
108 microstructures can be distinguished in thin sections: (i) foliated zones with an orientation of
109 the foliation in agreement (i.e. parallel) with fault displacement, (ii) foliated zones without
110 coherent orientation, very rich in clays and with very small grain size. Those observations
111 indicate that pressure solution is the main creep mechanism but raise several questions: Are
112 these two types of microstructures characteristic steps of the evolution of pressure solution
113 creep mechanism? Did they develop and evolve in parallel or in series, depending of the
114 initial conditions prevailing in the area? Is there a spatial and temporal evolution of these
115 microstructures? This brings us to the general question: how do the microstructures of
116 creeping zone evolve through time and space? Finally, we propose a model of formation and
117 evolution of those active creeping zones, based on microstructural observations of natural
118 samples.

119

120 **2 – San Andreas Fault and SAFOD borehole**

121

122 **2-1 Geological setting and general features**

123 The San Andreas Fault System, California, is a complex network of faults that spreads over
124 1300 km long and 100 km wide (**Wallace, 1990**), making the junction between the
125 subducting Pacific plate and the North American plate. The San Andreas Fault is the major

126 continental fault of this network, and one of the most active in the world. It is a lithospheric
127 mature dextral strike-slip fault divided into different segments with various mechanical
128 behaviors (**Figure 1a**) (**Steinbrugge and Zacher, 1960; Allen, 1968; Wallace, 1970; Irwin**
129 **and Barnes, 1975**). The creeping segment is experiencing a continuous aseismic slip at a rate
130 ranging between about 28 mm/yr and 33 mm/yr (**Burford and Harsh, 1980; Titus et al.,**
131 **2006**), close to the 34 mm/yr long-term estimated geological slip rate (**Sieh and Jahns, 1984**)
132 and exhibiting a high microseismic activity (**Provost and Houston, 2001**). The creeping zone
133 is bounded by locked segments that experienced some infrequent earthquakes of large
134 magnitude, as the Fort Tejon earthquake in 1857 ($M=7.9$) (**Sieh, 1978**) on the southern locked
135 segment, and the San Francisco earthquake in 1906 ($M=8.2$) on the northern locked segment.
136 The locked segments are also characterized by negligible or nonexistent creep (**Ellsworth,**
137 **1990**). Finally, the Parkfield segment making the junction between the creeping segment and
138 the southern locked one presents a transitional behavior. This segment has shown seven
139 repeating earthquakes of magnitude close to 6 since 1857 (**Bakun and McEvilly, 1984;**
140 **Jackson and Kagan, 2006**), a transitory post seismic creep episode after the last 2004 event
141 (**Titus et al., 2006**) and microseismic activity (**Thurber et al., 2004**).

142 The fault crosses different geological formations and, given the tectonic setting of subduction,
143 the geographical repartition of these formations is not symmetrical on both sides of the fault,
144 especially in the Parkfield area (**Figure 1b**), where the present study is focused. The structure
145 of the fault itself is complex and presents important heterogeneities at depth, with some
146 formations intensively deformed like the Franciscan Complex, and the presence of important
147 body of serpentine close to the Parkfield segment (**McPhee et al., 2004, Li et al., 2004**).

148 Studies also revealed some very specific features in the geophysical and mechanical
149 properties of the SAF. **Brune et al., (1969)** showed that this fault slides with a much lower
150 shear stress than the one predicted by laboratory friction experiments (**Byerlee, 1978**). This

151 property was confirmed by other studies (**Chéry et al., 2004; Boness and Zoback, 2004;**
152 **Townend and Zoback, 2004; Zoback et al., 2010**). Moreover, there is no heat flux anomaly
153 across the creeping segment (**Brune et al., 1969; Lachenbruch et al., 1980**). This last
154 discovery, well-known as the San Andreas stress-heat flow paradox (**Hanks and Raleigh,**
155 **1980; Zoback et al., 1988; Lachenbruch and Sass, 1992**), has raised very early the question
156 about the potential mechanisms that can produce creep, without heat production. Finally,
157 **Mount and Suppe, (1987)** and **Zoback et al., (1987)** brought evidences showing that the
158 orientation of the maximum horizontal compressive stress is at high angle to the fault. This
159 angle increases with depth and ranges from 25° to 69° between 1000 m to 2200 m depth
160 (**Hickman and Zoback, 2004**). All those observations point to a weak fault embedded into a
161 strong crust (**Zoback et al., 1987; Rice, 1992; Zoback, 2000; Fulton et al., 2004; Zoback et**
162 **al., 2010**). Despite some other studies claiming the possibility of a strong fault in a strong
163 crust (**Scholz, 1992; 2000**), the model of a weak fault is now widely adopted for the SAF.
164 When considering the morphology of such a strike-slip fault, a major difficulty is to access
165 the fault core material. Because the exhumed portions lost much information about physical
166 and chemical mechanisms that are acting at depth, drilling at depth directly through the fault
167 was considered the better way to get the opportunity of studying the fault processes in situ
168 (**Zoback et al., 2010**).

169

170 **2-2 SAFOD borehole**

171 The San Andreas Fault Observatory at Depth (SAFOD) drilling project aimed to provide *in*
172 *situ* geophysical borehole data and fault core samples to better constrain the fault rock
173 properties at depth, the conditions for earthquake nucleation, and to find an explanation for
174 the San Andreas stress/heat flow paradox (**Zoback, 2006; Hickman et al., 2007; Zoback et**
175 **al., 2011**). The borehole was drilled close to the town of Parkfield (**Figure 1**), on the eponym

176 fault segment and reached 3 km vertical depth (**Figure 2**). This site was chosen because of its
177 location at the transition between two segments having different mechanical behavior and the
178 presence of patches of repeating microearthquakes located between 2 km and 12 km depth
179 within an aseismic creeping zone (**Nadeau et al., 2004; Zoback et al., 2010**). The drilling of
180 the main borehole was divided into three phases between summer 2004 and summer 2007
181 (**Zoback et al., 2011**).

182 The SAFOD borehole has brought constrains on the fault geometry and geophysical
183 properties of the fault rocks at depth (**Solum et al., 2006; Bradbury et al., 2007; Solum et**
184 **al., 2007; Jeppson et al., 2010; Zoback et al., 2011**), and evidence supporting the model of a
185 weak fault in an otherwise strong crust (**Tembe et al., 2006; Tembe et al., 2009, Zoback et**
186 **al., 2010; Mittempergher et al., 2011**). It was possible to locate at depth the boundaries
187 between different geological formations, (**Figure 2a**) and at least seven relatively large fault
188 zones were crossed by the borehole (**Bradbury et al., 2007**). A 200-meters-wide damaged
189 zone (**Figure 2b** and **Figure 3**) has been detected by the decrease in the velocity of P and S
190 waves and by its low resistivity, comparatively to the other sections of the borehole (**Zoback**
191 **et al., 2011**). Inside this damaged zone, two specific areas were distinguished by their
192 localized active deformation: the South Deforming Zone (SDZ) and the Central Deforming
193 Zone (CDZ). They are characterized by on-going deformation of the steel casing around the
194 borehole, and anomalies in the velocity of P and S waves and in the resistivity were detected
195 as well.

196 Those two shear zones experience active creep deformation and are presented as the active
197 trace of the SAF (**Hickman et al., 2007; Zoback et al., 2011**). Both of them are less than 3
198 meters wide (**Figure 3**). The first one, the SDZ, is located between 3196 m and 3198 m depth
199 (depths are given here relative to Phase 3 Core, see **Table 1** for the matching between the
200 different depth location systems). It is the less active one. The CDZ, located between 3296.5

201 m and 3299 m depth (relative to Phase 3 Core) is the most active deforming zone. Their
202 mineral composition is different from the rocks outside the active deforming areas
203 (**Holdsworth et al., 2011**). It shows important amount of clays, lots of serpentine clasts and
204 very few amount of talc (**Solum et al., 2006; Hickman et al., 2007; Moore and Rymer,**
205 **2007; Holdsworth et al., 2011**).

206

207 **3 – Microstructures in the San Andreas Fault zone**

208

209 **3-1 Location and preparation of the samples**

210 During the three rounds of sample request, several samples were collected to characterize the
211 typical microstructures found in the SAFOD fault zone. Here, we focus on twelve samples
212 close or inside the active creeping zone of the CDZ, to study the deformation microstructures
213 and the mineral composition in this area and to characterize its spatial evolution along the
214 CDZ and at its boundaries. Those observations allow us to propose a model for the
215 microstructural evolution of a creeping zone through space, and to determine the main
216 deformation processes, constraining the time evolution of the fault by using cross-cutting
217 geological relationships.

218 **Figure 3** shows the location of the studied samples. The measured depths are relative to
219 Phase 3 Core (see **Table 1**). Each of these samples, except sample III-2 and part of the sample
220 I-10 were impregnated by resin epoxy and cut in thin sections. At least three thin sections
221 have been done within each sample; along three perpendicular directions relative to the core
222 top (**Figure 2b**).

223 In a first step, we used optical microscope to determine some general features inside and
224 outside the creeping zone. Those observations allowed us to get a first compilation of the
225 most representative thin sections for each sample, on which we performed SEM observations

226 and chemical mappings. A second selection based on this analysis, allowed us to focus on
227 four main thin sections on which we performed microprobe analyses and chemical maps:
228 three samples within the creeping zone, and a fourth one located outside the creeping zone but
229 within the damaged zone.

230

231 **3-2 Sample observations**

232 Previous studies on mineralogy have revealed that the damaged zone is mainly composed of
233 siltstones, mudstones, shales (Solum et al., 2007; Bradbury et al., 2007; Schleicher et al.,
234 2009a), and very fine grey sandstones of the Great Valley sequence (Holdsworth et al.,
235 2011). Concerning the two active creeping zones, they are mainly composed of phyllosilicates
236 minerals (mainly clays) with serpentine clasts as well as lithic clasts coming from siltstone
237 and mudstone rocks, similar to those composing the fault rocks at the boundaries of the
238 creeping zone. These clasts show a wide range of sizes and they are embedded into the clay-
239 rich matrix (Holdsworth et al., 2011; Moore and Rymer, 2012).

240

241 ***3-2-1 Outside of the creeping zone – the damaged zone***

242 The damaged zone appears to be both foliated and fractured. Most of the grains, and more
243 specifically quartz and feldspar grains are highly fractured (Figure 4a,b). The minerals are
244 generally very altered, especially at their boundaries, showing irregular shapes. It is also
245 possible to observe widespread indentations between grains of different or similar nature
246 (Figure 4c,d,f). Networks of numerous calcite veins can be easily identified (Figure 4d,e,f)
247 and are an other typical feature in the damaged zone. We observed them in every thin section
248 outside of the creeping zone. The different red colors of the calcite in cathodoluminescence
249 imaging underline variations in minor elements content (Fe, Mg, ...). As for the other
250 minerals, calcite grains are highly fractured in some areas (Figure 4). Finally, pervasive

251 foliation is the main deformation pattern in this damaged zone. Such foliation may be
252 observed at different scales, from the grain scale to the size of the thin section.

253

254 *3-2-2 Inside the creeping zone*

255 For the samples inside the creeping zone, a major difference is the composition of the rock.

256 X-Ray diffraction analyses performed on all samples from the creeping zone gave an amount
257 of clay ranging from 50% to 70%, well above the phyllosilicates content in the damaged zone.

258 XRD analyses reveal that these clays belong to the smectite group (saponite). Those results
259 are confirmed by SEM and microprobe chemical analysis. Another typical feature inside the

260 creeping zone is the presence of polymineral clasts of various sizes, ranging from 10 μm to 15
261 mm (**Figure 5**). Their composition is very close to the rocks outside of the creeping zone (the

262 damaged zone), except for the clasts of serpentine (**Figure 5a**), which occur rather seldom in
263 the damaged zone. This is the second main difference with the mineral composition outside of

264 the creeping zone. The amount of serpentine in the creeping zone ranges between 10% and
265 15%. XRD and microprobe analyses indicate two kinds of serpentines, chrysotile and

266 lizardite, which were imaged using a FEG-SEM (**Figure 6**). Many polymineral clasts are
267 composed of fractured serpentine with calcite veins. Other clasts are made of quartz and

268 feldspar that are the most common minerals forming the polymineral clasts. It must be noted
269 that most of those polymineral clasts are fractured. Little amounts of chlorite, iron and

270 titanium oxides as well as very rare talc grains can be found in some aggregates. Most of the
271 polymineral clasts have a typical almond shape and their boundaries present evidence of

272 dissolution indenting by pressure solution creep (**Figure 5**). Pressure solution cleavages, with
273 almond shapes, may be seen around aggregates (**Figure 5c**). They are characterized by both

274 concentrations of dark minerals inside the cleavage planes and pressure shadows on the ends
275 of the almond shapes. Calcite growth is most often observed in some pressure shadows of the

276 polymineral clasts (**Figure 5c**). We also noticed the presence of an important amount of very
277 small grains (<10µm) dispersed within the clay matrix (saponite), usually made of serpentine,
278 calcite, quartz, feldspar and iron oxide. It must be underlined that the shapes of their edges are
279 often very irregular (**Figure 6d,e,f and Figure 8**).

280 The last noticeable feature is the very thin shear planes in different directions and different
281 scales, observed in all thin sections (**Figure 5g,h**). It is really difficult to determine a
282 coherence from all those planes and almost impossible to find a main shear sense. However,
283 the thin sections cut perpendicularly to the foliation were fairly less chaotic than those cut
284 parallel. Inside the different shearing planes, oblique and highly folded foliation can be seen,
285 with absolutely no coherent orientation (**Figure 5**). As for the shear planes, the foliation
286 stands at different scales and various orientations. The rotation of the foliation and the shear
287 planes is correlated to the presence of the polymineral clasts at all scales and the small rigid
288 grains.

289

290 **3-3 Interpretations**

291 All those observations gave us evidences to identify the mechanisms that can lead to those
292 microstructures.

293

294 ***3-3-1 Outside of the creeping zone – the damaged zone***

295 The fractured grains can show multiple radial fracturing at their contacts that suggests
296 dynamic fracturing processes (**Sagy et al., 2001**). The alteration of the minerals is attesting of
297 episodic fluid flow through the damaged zone at least during early times, and the multiple
298 grain indentations attest of grain boundary dissolution under stress and sliding. The important
299 calcite vein networks indicate that many fractures have been sealed. Their abundance
300 underlines the importance of healing and sealing processes that were active here. The

301 different red colors of calcite in cathodoluminescence show that several episodes of sealing
302 were probably connected to successive fluid flow episodes (**Mittempergher et al., 2011**).
303 Moreover, as the calcite grains are more fractured than the other minerals, such observation
304 supports the idea of multiple episodes of deformation associating fracturing, sealing and fluid
305 flow through the damaged zone. Several micro- to meso-faults may be identified in the
306 damaged zone (**Mittempergher et al., 2011; Holdsworth et al., 2011; Hadizadeh et al.,**
307 **2012; Solum et al., 2006; Schleicher et al., 2009b**), with displacement ranging from
308 micrometers to centimeters, which could be the markers of the present-day microseismicity.
309 The tectonic layering, associated with the pervasive foliation, attests of pressure solution
310 process, with passive concentration of insoluble minerals, such as phyllosilicates, in pressure
311 solution seams (**Figure 4g,h,i** and **Figure 7**). Deposition veins may occur or not between the
312 spaced cleavages (**Figure 7**). This typical microstructure leads to a localization of the
313 deformation. The amount of total mass decrease at the level of each pressure solution
314 cleavage seam may be estimated at about -88% on those foliated areas, based on the
315 quantification of the decrease of mass proportion of each mineral (**Gratier al., 2011**). Mass
316 transfer modified differently the mechanical properties of the deformed rocks, according to
317 two end member zones with different rheologies: the zone of dissolution and the zone of
318 deposition.

319 In the zone of dissolution, the passive concentration of insoluble species, such as
320 phyllosilicates, activates the kinetics of mass transfers as diffusion along the interface
321 between phyllosilicates and soluble minerals is faster than along healed cracks within soluble
322 mineral grains. This is demonstrated by natural observation (**Gratier, 2011**) and by
323 experiments (**Zubtsov, 2004; Niemeijer and Spiers, 2005**). This leads to a positive feedback
324 process that facilitates the localization of the dissolution. Local weakening is therefore linked
325 both to mechanical and chemical processes: decrease of friction and activation of the

326 dissolution respectively, due to phyllosilicate concentration.
327 Conversely, in the zone of deposition the presence of an important amount of calcite-filled
328 veins tends to strengthen the rocks as it is more difficult to dissolve monomineralic rocks than
329 a mixture of soluble and insoluble grains (**Gratier et al., 2013b**). Dissolution cannot be
330 observed at grain scale in the veins, but only at the boundary of such veins (**Figure 4**), where
331 the thin fluid phase is located. All these features demonstrate strong evidence that pressure
332 solution creep may represent the main mechanism of creep in the damaged zone, outside of
333 the localized creeping zones, that are associated with fracturing and sealing processes.

334

335 *3-2-2 Inside the creeping zone*

336 The observations revealed that polymineral clasts are mainly composed of fractured
337 serpentine with calcite veins. This observation rules out the common statement that serpentine
338 is always a soft mineral. When serpentine minerals are sealed together in clasts, they behave
339 as rigid and soluble bodies that can acquire a brittle behavior. However, like quartz, feldspar
340 and calcite, serpentines are soluble under stress (**Andreani et al., 2004**) and may deform
341 slowly by pressure solution creep in the presence of a trapped fluid phase, especially in
342 mixtures of soluble and insoluble grains.

343 We observed that most of the polymineralic clasts were fractured, however, the size of rupture
344 area (centimeters at most) and the amount of displacement (some micrometers to millimeters)
345 attest of very low magnitude seismic events in the creeping zone. Concerning the other
346 material presents in the creeping zone, i.e. all the small grains of various minerals; we
347 interpret the irregular shapes of their boundaries as evidences for indentation by pressure
348 solution creep.

349 The different features found inside the creeping zone suggest that pressure solution creep
350 process has been active and helped weakening this zone by passive clay concentration.

351 Remnants of the initial state are still trapped in the creeping zone as polymineral clasts of all
352 dimensions (**Figure 5**). To summarize, two mechanisms of deformation compete: the sliding
353 along very low friction coefficient saponite grains, and stress driven mass transfer processes
354 that help accommodating the sliding of the polymineral clasts embedded within the clay-rich
355 matrix.

356

357 **3-4 Microstructures reveal two different deformation mechanisms**

358 To summarize all those observations, both for the creeping zone and the damaged zone could
359 be gathered in two general microstructure groups: (i) foliated domains with clear orientation
360 in the damaged zone, and (ii) foliated domains without preferential orientation in the CDZ.

361 In the first case, the foliation is developed by a pressure solution creep mechanism in a
362 general context of volume decrease but with local redeposition in calcite veins. It is due to
363 massive dissolution of soluble material, and partial redeposition that may also come from
364 advective fluid flow (**Gratier et al 2011**), leading to tectonic layering. The typical
365 characteristics of this microstructure are: (1) an intense fracturing of the material, (2)
366 numerous indentations between the grains and (3) localized redeposition of calcite evidenced
367 by thick and extensive vein networks. This microstructure is widely spread in the damaged
368 zone, outside of the active creeping zones. But we observed it also in some large polymineral
369 clasts (several centimeters) inside the CDZ as remnants of an initial state.

370 The second type of microstructure –foliation without preferential orientation – is associated
371 with both the sliding on clay minerals along numerous micro-shearing planes and the rotation
372 of the polymineral clasts. This microstructure is observed in the active creeping zone only; its
373 main features are: (1) an abundance of soft clay minerals (>50% in the entire composition),
374 (2) a grain size globally smaller than outside of the creeping zone, (3) the presence of
375 polymineral clasts of various sizes and compositions (mainly quartz, feldspars and serpentine

376 minerals with calcite veins) embedded in the clay-rich matrix.

377

378 **4 – Discussion**

379

380 All those natural microstructural observations have implications on the rheological and
381 mechanical behavior of the fault, at different scales. To better understand the mechanisms of
382 aseismic fault creep processes, we detail below the parameters responsible for the onset of
383 creep mechanisms, as well as the interactions between these mechanisms. Still based on these
384 observations, we argue that the microstructures underline a chronology that allows us to
385 propose a 3D model of the creeping zone evolution, through time and that could be
386 extrapolated at depth.

387

388 **4-1 Parameters that control the creeping mechanisms**

389 Based on the sample observations, we found that two different creep mechanisms operate.
390 Inside the damaged zone, there are numerous evidences for pressure solution creep (**Figure**
391 **7**), linked to the development of the foliation (**Schleicher et al 2009b, Holdsworth et al**
392 **2011, Gratier et al 2011, Hadizadeth et al 2013**). Inside the creeping zone, the main
393 mechanism of creep is grain sliding with a crucial role of the low friction in the presence of
394 clay minerals (**Lockner et al 2011, Carpenter et al 2011**), and locally of pressure solution
395 clasts indenting and sliding (**Figure 5 and Figure 8**). Both mechanisms - pressure solution
396 and low friction - require some specific parameters to be activated and efficient, as discussed
397 below.

398

399 ***4-1-1 Pressure solution creep***

400 Pressure solution mechanism requires some specific conditions to occur at the relatively fast

401 strain rate observed in the creeping zone (10^{-10} to 10^{-11} s⁻¹) (**Titus et al., 2006**). Firstly, it is
402 activated by the presence of fluids that must be the solvent of at least one of the minerals
403 contained in the rock (**Weyl, 1959; Rutter, 1976; Paterson, 1973**). Secondly, all conditions
404 being the same, a mixture of insoluble and soluble species deforms more easily by pressure
405 solution than does a monomineralic rock composed of only soluble species. This is because
406 the kinetics of diffusive mass transfer along phyllosilicate/soluble mineral boundaries is much
407 faster than along the boundaries of soluble minerals that can heal (**Zubtsov et al., 2004**).
408 Thirdly, pressure solution is activated by fracturing or by comminution processes, because the
409 strain rate in pressure solution creep rate laws is inversely proportional to the distance of mass
410 transfer d (**Weyl, 1959; Rutter, 1976; Raj, 1982**). The strain rate is proportional to $1/d^3$ for
411 diffusion-controlled pressure solution, and to $1/d^2$ for reaction-controlled pressure solution. In
412 nature, pressure solution is often controlled by diffusion at depth, and it is therefore much
413 more efficient with a mass transfer distance as small as possible. This distance of mass
414 transfer is commonly considered as being the grain size, but it could also be the distance
415 between fractures because fractures can act as shortcuts for diffusion (**Gratier et al., 1999**).
416 However, because fracturing is only transitory, as most often fractures are healed or sealed,
417 this effect annihilates the diffusion shortcutting effect of the fractures. Through time,
418 fracturing accelerates the creep by decreasing d , thus weakening the deformed rocks; whereas
419 healing and sealing processes slow down the creep by increasing d , thus strengthening the
420 rocks. Hence, stress could build-up in the creeping area, leading to new brittle deformation
421 that will accelerate the rate of pressure solution creep and repeat the deformation as a cycle
422 (**Gratier et al., 1999; Gratier and Gueydan, 2007**).

423 Finally at regional scale, one must distinguish two end-members cases. Firstly, pressure
424 solution may occur in a closed system, with diffusive mass transfer through an almost
425 immobile fluid phase: all the dissolved materials recrystallized inside a given volume, at

426 decimeter scale, leading to both cleavage development with tectonic layering and sealing of
427 fractures with development of veins (mainly calcite veins in the SAF context). This case is
428 found in places where there is not enough fluid flow to take out (or bring in) the dissolved
429 materials. Alternatively, in open systems, pressure solution may occur with large fluid flow
430 through the deformed rock, which washes away all the dissolved species or which brings new
431 solute minerals that can precipitate in veins or voids. In this case, either all soluble species are
432 removed from the deformed zone without any deposition, or large deposition is seen in open
433 spaces (**Gratier et al 2013a**).

434

435 *4-1-2 Low friction processes*

436 Laboratory experiments have underlined the importance of gouge mineralogy on the fault
437 zone frictional properties (**Carpenter et al., 2009; Ikari et al., 2009; Ikari et al., 2011a**) and
438 especially for the phyllosilicate-rich fault gouges (**Vrolijk and van der Pluijm, 1999;**
439 **Niemeijer and Spiers, 2006**). An important question raised by those observations is the
440 following: which amount of clays is sufficient to lead to low frictional sliding? **Tembe et al.**
441 **(2010)** performed friction experiments on synthetic gouge mixtures and showed that the
442 friction coefficient depends on the amount of clay as well as the clay mineralogy. Their
443 results are in agreement with the three-regime model of **Lupini et al. (1981)** that describes
444 the degradation of frictional strength with clay content in three sequential phases. **Tembe et**
445 **al. (2010)** imaged the *post-mortem* microstructures and showed that an important decrease of
446 friction coefficient happens when clay forms a connected matrix that separates the remaining
447 grains. This kind of result is also supported by the study of **Colletini et al. (2009)**. In this
448 context, all the deformation is supported and accommodated by the clay structure. According
449 to the experiments of **Tembe et al., (2010)**, the content of clay must be larger than 50% in the
450 case of a montmorillonite/quartz mixture to reach a friction coefficient lower than 0.2 (the

451 average friction coefficient of the CDZ determined by laboratory friction experiments is in the
452 range 0.16 – 0.21 (**Carpenter et al., 2011; Lockner et al., 2011**). Montmorillonite belongs to
453 the smectite group, like saponite, and its mechanical behavior is close to saponite (friction
454 coefficient of montmorillonite < 0.2). Such results that a quite large amount of weak grains in
455 a gouge is necessary to reduce significantly the overall friction have been also simulated,
456 using a discrete elements methods developed to reproduce the frictional properties of fault
457 gouge (**Rathbun et al., 2013**).

458 Consequently, making a low frictional sliding process efficient requires a rock composition
459 with more than 50% of clays if mixed with quartzo-feldspathic materials (**Ikari et al., 2009;**
460 **Tembe et al. 2010; Moore and Lockner, 2011**), as it is the case for the creeping zone of the
461 SAF. Therefore, the most important parameter to activate the low friction creep mechanism is
462 the mineral composition of the fault core: there should be high enough concentration of low
463 friction minerals. Different processes may lead to the concentration of low friction clay inside
464 the creeping zone:

465 (i) The mineral composition of the creeping zone was already different from that of the
466 surrounding rocks. In this case, one must observe some minerals in the creeping zone that are
467 not seen in the damaged zone and that cannot develop from metamorphic reactions. This is
468 the case for the SAF creeping zones: serpentine polymineral clasts are mainly observed in the
469 creeping zones. These clasts embedded in the clay matrix show solution cleavage and
470 associated veins structures that have been rotated during the shear creeping process, attesting
471 of the early development of such structures. The Mg-rich content of such serpentine minerals
472 attests of a generally high Mg content in other minerals, especially phyllosilicates that could
473 have produced the Mg-rich saponite by alteration, similarly to the Mg-rich chlorites produced
474 through corrensite transition.

475 (ii) Low-friction clay minerals were initially present and their proportion has evolved because

476 of the passive concentration of the phyllosilicate minerals associated with pressure solution
477 process in an open system. In such a case, soluble minerals as quartz, feldspars, calcite, and
478 serpentines are removed from the deformed zone, leading to the passive concentration of
479 insoluble species like phyllosilicates. If this process is at work alone, the relative increase of
480 concentration of all insoluble minerals should be the same.

481 (iii) The mineral composition has changed because of growth and/or precipitation of new
482 minerals by metasomatic reactions. For example, saponite is the product of the reaction
483 between quartzo-feldspathic minerals at low temperature. These minerals come from the wall
484 rocks and the serpentine clasts (**Lockner et al., 2011; Moore and Rymer, 2007**). Such
485 assumption relies on fluid flow through the creeping zone, possibly episodic and related to
486 earthquakes.

487 As saw above, in all those cases, the amount of low friction minerals needs to reach
488 ultimately a large concentration (>60%) to be efficient enough to become the main creep
489 mechanism. None of these three assumptions alone can explain our observations. The mineral
490 composition was probably slightly different in the creeping zones than in the surrounding
491 rocks, since it is the only place where serpentinites are so abundant. Serpentinites were
492 deformed in an early stage, because of the important amount of calcite veins associated with a
493 lot of serpentine clasts, but could not accommodate the present large creep rate. Indicators of
494 pressure solution are found in the creeping zone. Passive concentration of phyllosilicates is
495 likely to have occurred at first, but it is only when the initial phyllosilicates were sufficiently
496 rich in Mg that the saponite-rich gouge could be generated. If this were not the case, the
497 missing magnesium may have been brought by fluid advection.

498 As a summary, we found (i) a difference in initial state, for example a higher initial content in
499 Mg with both serpentines and Mg-rich chlorites in the proto-creeping zone; (ii) the
500 observation of early pressure solution creep supports passive concentration of such Mg-rich

501 phyllosilicates; (iii) a part of the clay concentration may be the result of metasomatic
502 reactions, considering the important amount of Mg-rich phyllosilicates required to obtain this
503 clay concentration.

504

505 **4-2 From the damaged zone to the creeping zone: time evolution**

506 Our observations and interpretations document an evolution with time of the mineral
507 composition and an evolution with space of the microstructure from the damaged zone to the
508 creeping zone. This chronology is deduced both from the foliation development and its
509 evolution, and from the observations of the interaction between friction and pressure solution.

510

511 ***4-2-1 How did the foliation develop?***

512 4-2-1-a In the damage zone

513 Pressure solution creep is the main deformation mechanism known to develop a foliation
514 characterized by a tectonic layering (**Figure 7**) with or without associated calcite deposition
515 in veins. Such cleavage or cleavage-and-veins structures develop in an open system with two
516 structural end members: (i) zones where the dissolution of soluble species that were washed
517 away by fluid flow led to the passive concentration of phyllosilicates (**Figure 4j,k,l**), and (ii)
518 zones where calcite precipitation occurred in veins oriented perpendicularly to the cleavage
519 (**Figure 7**). Both end-members may be seen as parallel layers in the damaged zone,
520 amplifying the tectonic layering. Both processes accommodate aseismic deformation leading
521 to an agreement between the orientation of the foliation and that of the fault. The strain
522 reached by such a pressure solution cleavage or cleavage-and-veins structures may be
523 theoretically rather large, up to 60% shortening in some SAFOD samples (**Gratier et al.,**
524 **2011**). However, the actual strain never exceeds such a value for two reasons that are related
525 to the processes at work within the two end-members zones: (i) if most of the soluble species

526 are washed away and if they do not bear a significant differential stress (being dispersed in a
527 soft matrix), pressure solution cannot go on; (ii) if calcite precipitates in veins, the dissolution
528 of such veins is much slower than the dissolution of a mixture of soluble and insoluble
529 species (see § 4-1-1 above). Sixty per cent of shortening in a shear zone is the strain that is
530 associated with a shear strain value (γ) of 1 (**Ramsay, 1967**). In the SAF case, γ is much
531 higher: several kilometers of displacement lead to γ values exceeding 1000, and the actual
532 displacement on the SAF is even higher. Consequently, other mechanisms than such cleavage
533 and cleavage-and-vein deformation must be at work in the creeping zone.

534

535 4-2-1-b In the CDZ

536 Evidence of pressure solution creep is seen within the polymineral clasts (**Figure 5**): most of
537 these closely healed clasts of serpentine, quartz and feldspar are deformed by cleavage-and-
538 veins process, the veins being most often sealed by calcite, as observed in the damaged zone.
539 If there were only quartz and feldspar clast aggregates, one would think that they could have
540 been ripped from the damaged zone. However, there are very few, if any, serpentine clasts in
541 the damaged zone so the only explanation to the presence of such serpentine clasts is that they
542 are the remnants of an initial state of the now creeping zone. They attest of an early stage that
543 is now only seen in the damaged zone. On another hand, the main structure of the present day
544 creeping zone is the foliation without preferential orientation, already described by various
545 authors (**Schleicher et al., 2009a; 2010; Holdsworth et al., 2011**). There are two hypotheses
546 to explain such a specific foliation. First, the sliding of clay minerals may be associated with
547 the development of micro shearing planes and the rotation of the polymineralic clasts whether
548 it be the mineral aggregates or the smaller grains (**Figure 9b**). The rotations of all those rigid
549 objects drag the foliation and contribute to the chaotic microstructure observed (**Figure 9c**).
550 Alternatively, if the clasts cannot rotate between two shear planes, the system is locked, and

551 the only way to continue deforming is to develop constantly new foliations, superimposed on
552 the previous ones (**Figure 9d**). The possible rotation of the polymineral clasts may be linked
553 to their shape ratio and to their interaction with the matrix. Indenting by pressure solution at
554 the boundary of such polymineral clasts suggests that pressure solution accommodated by
555 diffusion contributes to the general grain-clast boundary sliding of all the minerals of the
556 creeping zone. This process can accommodate almost infinite shear values. However, the
557 internal deformation of some clasts (**Figure 5**) is much more complex than what is seen in the
558 damaged zone (**Figure 4**). Such structure, with veins of calcite oriented in almost all
559 directions may indicate that at least part of the clasts fracturing occurs within the creeping
560 zone and is associated with the rotation of the clasts.

561

562 *4-2-2 How do friction, fracturing and mass transfer interact in the creeping processes?*

563 **Figure 10** displays two possible evolutions of a deformed rock undergoing pressure solution
564 creep. They both start in the same manner: pressure solution concentrates phyllosilicates in
565 the solution cleavage seams and deposition and crystallization of calcite occurs inside the
566 fractures that are formed by stress concentration at the grain contacts (**Figure 7**). Starting
567 from this step, two scenarios of microstructure development can be proposed:

568 (i) In the initially stronger rocks, large fractures develop that become sealed with a large
569 amount of calcite (or other soluble minerals) (**Figure 4g,h,i and Figure 5b,g,i**). These
570 monomineralic regions will become stronger, and consequently break, and be sealed again,
571 which will harden them even more (**Figure 10f**). Repeated fractures that are seen both in the
572 damaged zone and in the creeping zone could explain the well-known microseismicity
573 associated with the creeping process along the SAF (**Hadizadeh et al., 2012**). How this
574 process, localized near the creeping zone, remains to be studied in more details, since some of
575 the faults seen in the damaged zone are not necessarily related to creeping process.

576 Conversely, the multi-fractured clasts trapped and embedded into the clay matrix (**Figure 5i**)
577 are deformed during the creeping process.

578 (ii) Conversely, in the initially weaker rocks or at least in the zones where little redeposition
579 occurred, dissolution of soluble minerals washed out by fluid flow led to the passive
580 concentration of phyllosilicates. Such zones are mostly open systems with very little soluble
581 mineral redeposition (**Figure 10d,e**). Only some calcite mineral growth may be seen in
582 pressure shadows of the mineral aggregate patches (**Figure 5c**). Moreover, it has been
583 proposed (**Schleicher et al., 2009b; Schleicher et al., 2010; Holdsworth et al., 2011**) that at
584 least part of the clay minerals may result from precipitation, or alteration of preexisting
585 phyllosilicates or mafic rocks, with more or less episodic fluid flow that could bring Mg-rich
586 fluid from serpentine massifs. This would be an example of dissolution-precipitation reactions
587 that would induce creep (**Wintsch and Yi, 2002**). Alternatively, the creeping zone may have
588 had a slightly different composition from preexisting serpentine – as attested by the presence
589 of serpentine clasts only in the creeping zone – and Mg-rich chlorites. These two cases – i.e.
590 concentration by pressure solution process and transformation of preexisting phyllosilicates –
591 lead to an increase of clay amount, enhancing the same type of behavior: a decrease of the
592 friction value in the creeping zone thanks to the low friction of the saponite and enhancement
593 of stress-driven reactions, both facilitating pressure solution diffusion-controlled grain sliding.
594 Then, preexisting phyllosilicates were progressively transformed into a soft mineral (at least
595 down to 3-4 km depth, which corresponds to the field of stability of saponite), thanks to fluid-
596 rock interactions and possible metasomatic reactions linked to episodic fluid flow through the
597 creeping zone.

598

599 **4-3 From the damaged zone to the creeping zone: the localization process**

600 Interactions between friction, fracturing and pressure solution in the creeping zone also lead

601 to a localization process. There is good evidence that at the beginning of the process, the
602 whole damaged zone was creeping mostly by pressure solution cleavage (**Figure 11**), as it has
603 been observed in other faults (**Faulkner et al., 2003; Gratier et al 2013b**). However,
604 interactions between fracturing and sealing lead to mechanical differentiation. In the initially
605 stronger rock, fracturing and associated sealing strengthen the rocks: the stronger the rock, the
606 more likely it can break and be sealed by new calcite that renders the rock even stronger. Only
607 a default in the sealing process can end this feedback process. Conversely, in the zone with
608 minimum deposition and maximum fluid flow, rocks soften progressively thanks to both
609 effects of the progressive concentration of phyllosilicates activating pressure solution and of
610 the progressive transformation of phyllosilicates into soft clays (at least in the upper part of
611 the crust). This progressive weakening may have been initially induced by the occurrence of
612 successive earthquakes (**Figure 11**) that could have contributed to open the system, favoring
613 episodic fluid flow (**Mittempergher et al., 2011**), and to reduce the grain size, promoting
614 pressure solution. The end-member of such evolution is a zone without any soluble species or
615 with dispersed clasts that do not bear significant differential stress. In such a case, the low
616 friction of clay minerals mostly controls shear strength. It is not clear whether the present
617 creeping zone has already reached this stage in the first 3-4 kilometers, or if diffusive clast
618 sliding still plays a role as a deformation mechanism.

619

620 *4-4 Evolution of the creeping mechanisms with depth*

621 The evolution of creep mechanisms with depth is strongly dependent on rock composition and
622 microstructure. As temperature increases with depth, mineral composition evolves, leading to
623 dissolution-precipitation reactions (**Putnis, 2002; Wintsch and Yi, 2002**). In the San Andreas
624 Fault, saponite clay, which is a stable mineral up to about 110°C, will transform at depth into
625 corrensite that is stable up to 150°C and is likely to evolve into Mg-rich chlorite at greater

626 depth (**Moore and Rymer, 2012**). Those mineral transformations tend to strengthen the
627 creeping zone at depth, because the friction coefficients of these two minerals are much larger
628 (0.6 to 0.7) than the one of saponite (0.2). Therefore, the accommodation of the deformation
629 by low friction minerals is efficient near the surface (up to 3-4 km of depth, **Lockner et al.,**
630 **2011; Carpenter et al., 2011**), but becomes less efficient and more energy consuming with
631 depth. On the other hand, the required conditions for efficient pressure solution creep are
632 fulfilled if a trapped fluid phase is kept within the creeping zone and if some processes of
633 fracturing and comminution have reduced grain size, i.e. the characteristic distance of mass
634 transfer. In such a case, diffusive grain boundary sliding controlled by pressure solution is
635 likely to be the most efficient process at depth. Such a process is comparable to
636 superplasticity (**Ashby and Verall, 1973**). Only the diffusive path is different, either within a
637 trapped fluid phase (**Gratier et al., 2011**), or along dry grain boundaries (**Boullier and**
638 **Gueguen, 1975**). Such process is able to accommodate almost infinite shear deformation
639 (**Figure 12**).

640

641 **5 – Conclusion**

642

643 From microstructural observations of rock samples collected at depth in the active creeping
644 zone of the San Andreas Fault, we propose a model for creep mechanism evolution through
645 time and space for creeping zones. We show that, in a first stage, the creeping zone was
646 relatively large, hundred meters wide, corresponding more or less to the width of the damaged
647 zone. Deformation was mostly controlled by pressure solution creep, attested by the
648 development of cleavage-and-veins structure and foliation parallel to fault displacement.
649 Afterwards, interactions between friction, fracturing and mass transfer led to very localized,
650 meter size, creeping zones without clear parallel foliation. Localization towards such a weak

651 creeping zone was favored by several parameters: (i) the passive concentration of
652 phyllosilicates in zones where other more soluble minerals such as quartz and feldspars were
653 washed away by episodic fluid flow; (ii) the fracturing and comminution processes that
654 increased the rate of mass transfer at grain scale; (iii) the alteration of the phyllosilicates into
655 softer minerals, such as saponite. Conversely, in zones where fractures were sealed, i.e. in the
656 present day damaged zone, pressure solution creep rate is lower because sealing decreases the
657 efficiency of diffusive mass transfer and friction is much higher since phyllosilicate alteration
658 is limited by hampered fluid flow.

659 At the present day, the deformation in the creeping zone within the first 3-4 km is controlled
660 by the very low friction of saponite and by diffusive sliding of polymineral clasts embedded
661 into the clay matrix. At greater depths (4-12 km), saponite is transformed into corrensite, and
662 then into chlorite, both with higher friction coefficients. Hence, pressure solution diffusive
663 grain boundary sliding is likely to be the controlling creeping mechanism. In the damaged
664 zone, pressure solution may still be at work but successive fracturing and sealing processes
665 have strengthen the rocks and the strain rate is very low. Microseismicity accompanying creep
666 may be explained by the multiple/numerous fracturing of the polymineral clasts embedded
667 into the soft matrix of the creeping zone and by ruptures of asperities and heterogeneities at
668 the boundaries and near the creeping zone.

669

669 **References**

670

- 671 Allen, C.R., 1968. The tectonic environments of seismically active and inactive areas along the San
672 Andreas fault system. In W.R. Dickinson and A. Grantz, eds., Proceedings of conference on geologic
673 problems of San Andreas fault system: Stanford, Calif., Stanford Univ. Pubs. Geol. Sci., 11, 70-82.
- 674 Andreani, M., Boullier, A. M., and Gratier, J. P., 2005. Development of schistosity by dissolution
675 crystallization in a californian serpentinite gouge. *Journal of Structural Geology*, 27, 2256-2267.
- 676 Ashby, M. and Verall, R., 1973. Diffusion-accommodated flow and superplasticity. *Acta Metallurgica*,
677 21, 149-163.
- 678 Azzaro, R., Mattia, M., and Puglisi, G., 2001. Fault creep and kinematics of the eastern segment of the
679 Pernicana Fault (Mt. Etna, Italy) derived from geodetic observations and their tectonic significance.
680 *Tectonophysics*, 333, 401-415.
- 681 Bakun, W.H. and McEvilly, T.V., 1984. Recurrence models and Parkfield, California, earthquakes.
682 *Journal of Geophysical Research*, 89, 3051-3058.
- 683 Barbot, S., Fialko, Y., and Bock, Y., 2009. Postseismic deformation due to the M_w 6.0 2004 Parkfield
684 earthquake: stress-driven creep on a fault with spatially variable rate-and-state friction parameters.
685 *Journal of Geophysical Research*, 114, B07405.
- 686 Boness, N.L. and Zoback, M.D., 2004. Stress-induced seismic velocity anisotropy and physical
687 properties in the SAFOD Pilot Hole in Parkfield, CA. *Geophysical Research Letters*, 31, L15S17.
- 688 Boullier, A.M. and Guéguen, Y. 1975. SP-mylonites: origin of some mylonites by superplastic flow,
689 *Contributions to Mineralogy and Petrology*, 50, 93-104.
- 690 Bradbury, K.K., Barton, D.C., Solum, J.G., Draper, S.D., and Evans, J.P., 2007. Mineralogic and
691 textural analyses of drill cuttings from the San Andreas Fault Observatory at Depth (SAFOD)
692 boreholes: Initial interpretations of fault zone composition and constraints on geologic models.
693 *Geosphere*, 3, 299-318.
- 694 Brune, J.N., Hehnyey, T.L., and Roy, R.F., 1969. Heat flow, stress, and rate of slip along the San
695 Andreas Fault, California. *Journal of Geophysical Research*, 74, 3821-3827.
- 696 Burford, R.O. and Harsh, P.W., 1980. Slip on the San Andreas Fault in Central California from
697 alignment array surveys. *Bulletin of the Seismological Society of America*, 70, 1233-1261.
- 698 Byerlee, J., 1978, *Friction of rocks: Pure and Applied Geophysics*, 116, 615–626.
- 699 Carpenter, B.M., Marone, C., and Saffer, D.M., 2009. Frictional behavior of materials in the 3D
700 SAFOD volume. *Geophysical Research letters*, 36, L05302.
- 701 Carpenter, B.M., Marone, C., and Saffer, D.M., 2011. Weakness of the San Andreas Fault revealed by
702 samples from the active fault zone. *Nature Geoscience*, 4, 251-254.
- 703 Chéry, J., Zoback, M.D., and Hickman, S., 2004. A mechanical model of the San Andreas fault and
704 SAFOD Pilot Hole stress measurements. *Geophysical Research Letters*, 31, L15S13.

- 705 Chester, F.M., Evans, J.P., and Biegel, R.L., 1993. Internal structure and weakening mechanisms of
706 the San Andreas Fault. *Journal of Geophysical Research*, 98, 771-786.
- 707 Collettini, C., Viti, C., Smith, S.A.F., and Holdsworth R.E., 2009. Development of interconnected talc
708 networks and weakening of continental low-angle normal faults. *Geology*, 37, 567-570.
- 709 Cox, S. F., and Etheridge, M. A., 1989. Coupled grain-scale dilatancy and mass transfer during
710 deformation at high fluid pressures: examples from Mount Lyell, Tasmania. *Journal of Structural*
711 *Geology* 11, 147-162.
- 712 d'Alessio, M.A., Williams, C.F., and Bürgmann, R., 2006. Frictional strength heterogeneity and
713 surface heat flow: Implications for the strength of the creeping San Andreas fault. *Journal of*
714 *Geophysical Research*, 111, B05410.
- 715 Ellsworth, W.L., 1990. Earthquake history, 1769-1989. In: R.E. Wallace, *The San Andreas Fault*
716 *System, California*. USGS Professional Paper 1515, Washington, 283p.
- 717 Faulkner, D. R., Lewis, A. C., and Rutter, E. H., 2003, On the internal structure and mechanics of
718 large strike-slip fault zones: field observations of the Carboneras fault in southeastern Spain,
719 *Tectonophysics*, 367, 235-251.
- 720 Freed, A.M., 2007. Afterslip (and only afterslip) following the 2004 Parkfield, California, earthquake.
721 *Geophysical Research Letters*, 34, L06312.
- 722 Fulton, P.M., Saffer, D.M., Harris, R.N., and Bekins, B.A., 2004. Re-evaluation of heat flow data near
723 Parkfield, CA: Evidence for a weak San Andreas Fault. *Geophysical Research Letters*, 31, L15S15.
- 724 Fulton, P.M., Saffer, D.M., and Bekins, B.A., 2009. A critical evaluation of crustal dehydration as the
725 cause of an overpressured and weak San Andreas Fault. *Earth and Planetary Science Letters*, 284, 447-
726 454.
- 727 Fulton, P.M., and Saffer, D.M., 2009. Potential role of mantle-derived fluids in weakening the San
728 Andreas Fault. *Journal of Geophysical Research*, 114, B07408, doi:10.1029/2008JB006087.
- 729 Gao, S.S., Silver, P.G., and Linde, A.T., 2000. Analysis of deformation data at Parkfield, California:
730 detection of a long-term strain transient. *Journal of Geophysical Research*, 105, 2955-2967.
- 731 Gratier, J.P., Renard, F., and Labaume, P., 1999. How pressure solution creep and fracturing processes
732 interact in the upper crust to make it behave in both a brittle and viscous manner. *Journal of Structural*
733 *Geology*, 21, 1189-1197.
- 734 Gratier, J-P., and Gueydan, F., 2007. Deformation in the presence of fluids and mineral reactions:
735 effect of fracturing and fluid-rocks interaction on seismic cycle, in: *Tectonic Faults, agent of change*
736 *on a dynamic earth*, edited by M.R. Handy, G. Hirth, N. Hovius, Dahlem Workshop, The MIT Press,
737 Cambridge, Mass., USA. 319-356.
- 738 Gratier, J.P., Richard, J., Renard, F., Mitterpergher, S., Doan, M.L., Di Toro, G., Hadizadeh, J., and
739 Boullier, A.M., 2011. Aseismic sliding of active faults by pressure solution creep: Evidence from the
740 San Andreas Fault Observatory at Depth. *Geology*, 39(12), 1131-1134.

- 741 Gratier, J. P., 2011. Fault permeability and strength evolution related to fracturing and healing
742 episodic processes (years to millennia): the role of pressure solution. *Oil & Gas Science and*
743 *Technology*, 3, 491-506.
- 744 Gratier, J.P., Dysthe, D.K., and Renard, F., 2013a. The role of pressure solution creep in the ductility
745 of the Earth's upper crust. *Advances in Geophysics*, 54, 47-179.
- 746 Gratier, J.P., Thouvenot, F., Jenatton, L., Tourette, A., Doan, M.L., and Renard, F., 2013b. Geological
747 control of the partitioning between seismic and aseismic sliding behaviours in active faults: evidence
748 from the Western Alps, France. *Tectonophysics*, 600, 226-242.
- 749 Hadizadeh, J., Mitterpergher, S., Gratier, J.P., Renard, F., Di Toro, G., Richard, J., and Babaie, H.,
750 2012. A microstructural study of fault rocks from the SAFOD: Implications for the deformation
751 mechanisms and strength of the creeping segment of the San Andreas Fault. *Journal of Structural*
752 *Geology*, 42, 246-260.
- 753 Hanks, T.C., and Raleigh, C.B., 1980. The conference on magnitude of deviatoric stresses in the
754 Earth's crust and uppermost mantle. *Journal of Geophysical Research*, 85, 6083-6085.
- 755 Hickman, S. and Zoback, M., 2004. Stress orientations and magnitudes in the SAFOD pilot hole.
756 *Geophysical Research Letters*, 31, L15S12, doi:10.1029/2004GL020043.
- 757 Hickman, S., Zoback, M., Ellsworth, W., Boness, N., Malin, P., Roecker, S., and Thurber, C., 2007.
758 Structure and properties of the San Andreas Fault in Central California: recent results from the
759 SAFOD experiment. *Scientific Drilling, Special Issue*, 1, 29-32.
- 760 Hobbs, B.E., Means, W.D., and Williams, P.F., 1976. *An outline of structural geology*, Wiley and
761 Sons, New York, 571p.
- 762 Holdsworth, R.E., van Diggelen, E.W.E, Spiers, C.J., de Bresser, J.H.P., Walker, R.J., and Bowen, L.,
763 2011. Fault rocks from the SAFOD core samples: Implications for weakening at shallow depths along
764 the San Andreas Fault, California. *Journal of Structural Geology*, 33, 132-144,
765 doi:10.1016/j.jsg.2010.11.010.
- 766 Ikari, M.J., Marone, C., and Saffer, D.M., 2011. On the relation between fault strength and frictional
767 stability. *Geology*, 39, 83-86.
- 768 Ikari, M.J., Saffer, D.M., and Marone, C., 2009. Frictional and hydrologic properties of clay-rich fault
769 gouge. *Journal of Geophysical Research*, 114, B05409.
- 770 Irwin, P.W., and Barnes, I., 1975. Effect of geologic structure and metamorphic fluids on seismic
771 behavior of the San Andreas fault system in central and northern California. *Geology*, 3, 713-716.
- 772 Jackson, D.D., and Kagan, Y.Y, 2006. The 2004 Parkfield earthquake, the 1985 prediction and
773 characteristic earthquakes: lessons for the future. *Bulletin of Seismological Society of America*, 96,
774 S397-S409, doi:10.1785/0120050821.
- 775 Janssen, C., Wirth, R., Rybacki, E., Naumann, R., Kemnitz, H., Wenk, H.R., and Dresen, G., 2010.
776 Amorphous material in SAFOD core samples (San Andreas Fault): Evidence for crush-origin
777 pseudotachylytes? *Geophysical Research Letters*, 37, L01303, doi:10.1029/2009GL040993.

- 778 Janssen, C., Kanitpanyacharoen, W., Wenk, H.R., Wirth, R., Morales, L., Rybacki, E., Kienast, M.,
779 and Dresen, G., 2012. Clay fabrics in SAFOD core samples. *Journal of Structural Geology*, 43, 118-
780 127.
- 781 Jeppson, T.N., Bradbury, K.K., and Evans, J.P., 2010. Geophysical properties within the San Andreas
782 Fault Zone at the San Andreas Fault Observatory at Depth and their relationships to rock properties
783 and fault zone structure. *Journal of Geophysical Research*, 115, B12423, doi:10.1029/2010JB007563.
- 784 Johanson, I.A., Fielding, E.J., Rolandone, F., and Bürgmann, R., 2006. Coseismic and postseismic slip
785 of the 2004 Parkfield earthquake from space-geodetic data. *Bulletin of Seismological Society of
786 America*, 96, S269-S282, doi:10.1785/0120050818.
- 787 Lachenbruch, A.H. and Sass, J.H., 1980. Heat flow and energetics of the San Andreas Fault Zone.
788 *Journal of Geophysical Research*, 85, 6185-6222.
- 789 Lachenbruch, A.H. and Sass, J.H., 1992. Heat flow from Cajon Pass, fault strength, and tectonic
790 implications. *Journal of Geophysical Research*, 97, 4995-5015.
- 791 Lee, J.C., Angelier, J., Chu, H.T., Hu, J.C., and Jeng, F.S., 2005. Monitoring active fault creep as a
792 tool in seismic hazard mitigation. Insights from creepmeter study at Chihshang, Taiwan. *Comptes
793 Rendus Geosciences*, 337, 1200-1207.
- 794 Li, Y.G., Vidale, J.E., and Cochran, E.S., 2004. Low-velocity damaged structure of the San Andreas
795 Fault at Parkfield from fault zone trapped waves. *Geophysical Research Letters*, 31, L12S06,
796 doi:10.1029/2003GL019044.
- 797 Li, Y.G., Chen, P., Cochran, E.S., Vidale, J.E., and Burdette, T., 2006. Seismic evidence for rock
798 damage and healing on the San Andreas Fault associated with the 2004 M 6.0 Parkfield earthquake.
799 *Bulletin of Seismological Society of America*, 96, S349-S363, doi: 10.1785/0120050803.
- 800 Lockner, D.A., Morrow, C., Moore, D., and Hickman, S., 2011. Low strength of deep San Andreas
801 fault gouge from SAFOD core. *Nature*, 472, 82-85, doi:10.1038/nature09927.
- 802 Lupini, J.F., Skinner, A.E, and Vaughan, P.R., 1981. The drained residual strength of cohesive soils.
803 *Geotechnique*, 31, 181-213.
- 804 McPhee, D.K., Jachens, R.C., and Wentworth, C.M., 2004. Crustal structure across the San Andreas
805 Fault at the SAFOD site from potential field and geologic studies. *Geophysical Research Letters*, 31,
806 L12S03, doi:10.1029/2003GL019363.
- 807 Mittempergher, S., Di Toro, G., Gratier, J.P., Hadizadeh, J., Smith, S.A.F., and Spiess, R., 2011.
808 Evidence of transient increases of fluid pressure in SAFOD phase III cores. *Geophysical Research
809 Letters*, 38, L03301, doi:10.1029/2010GL046129.
- 810 Moore, D.E. and Lockner, D.A., 2007. Talc friction in the temperature range 25°-400°C: Relevance
811 for fault-zone weakening. *Tectonophysics*, 449, 120-132, doi:10.1016/j.tecto.2007.11.039.
- 812 Moore, D.E. and Rymer, M.J., 2007. Talc-bearing serpentinite and the creeping section of the San
813 Andreas fault. *Nature*, 448, 795-797, doi:10.1038/nature06064.

- 814 Moore, D.E. and Lockner, D.A., 2011. Frictional strengths of talc-serpentine and talc-quartz mixtures.
815 Journal of Geophysical Research, 116, B01403, doi: 10.1029/2010JB007881.
- 816 Moore, D.E. and Rymer, M.J., 2012. Correlation of clayey gouge in a surface exposure of serpentinite
817 in the San Andreas Fault with gouge from the San Andreas Fault Observatory at Depth (SAFOD).
818 Journal of Structural Geology, 38, 51-60.
- 819 Mount V.S., and Suppe J., 1987. State of stress near the San Andreas fault: Implications for wrench
820 tectonics. Geology, 15, 1143-1146.
- 821 Murray J. and Langbein J., 2006. Slip on the San Andreas Fault at Parkfield, California, over two
822 earthquake cycles, and the implications for seismic hazard. Bulletin of Seismological Society of
823 America, 96, S283-S303, doi:10.1785/0120050820.
- 824 Nadeau, R.M., Michelini, A., Uhrhammer, R.A., Dolenc, D., and McEvilly, T.V., 2004. Detailed
825 kinematics, structure and recurrence of micro-seismicity in the SAFOD target region. Geophysical
826 Research Letters, 31, L12S08, doi:10.1029/2003GL019409.
- 827 Niemeijer, A.R. and Spiers, C.J., 2006. Velocity dependence of strength and healing behaviour in
828 simulated phyllosilicate-bearing fault gouge. Tectonophysics, 427, 231-253.
- 829 Niemeijer, A.R. and Spiers, C.J., 2005. Influence of phyllosilicates on fault strength in the brittle-
830 ductile transition: insights from rock analogue experiments. High-Strain Zones: Structure and Physical
831 Properties, Geological Society, London, Special Publications, 245, 303-327.
- 832 Paterson, M.S., 1973. Nonhydrostatic thermodynamics and its geologic applications. Reviews of
833 Geophysics and Space Physics, 11, 355-389.
- 834 Perfettini, H., and Avouac, J. P., 2004 Postseismic relaxation driven by brittle creep: A possible
835 mechanism to reconcile geodetic measurements and the decay rate of aftershocks, application to the
836 Chi-Chi earthquake, Taiwan. Journal of Geophysical Research, 109, B02304.
- 837 Provost, A.S., and Houston H., 2001. Orientation of the stress field surrounding the creeping section
838 of the San Andres Fault: Evidence for a narrow mechanically weak fault zone. Journal of Geophysical
839 Research, 106, 11373-11386.
- 840 Putnis, A., 2002. Mineral replacement reactions: from macroscopic observations to microscopic
841 mechanisms, Mineralogical Magazine, 66, 689-708.
- 842 Raj, R., 1982. Creep in polycrystalline aggregates by matter transport through a liquid phase. Journal
843 of Geophysical Research-Solid Earth, 87, 4731-4739.
- 844 Ramsay, J. G., 1967. Folding and fracturing of rocks. MacGraw-Hill Book Company, New York,
845 568p.
- 846 Rathbun, A., Renard, F., and Abe, S., 2013, Numerical investigation of the interplay between wall
847 geometry and friction in granular fault gouge, Journal of Geophysical Research, 118, 878-893.
- 848 Rice, J. R., 1992. Fault stress states, pore pressure distribution, and the weakness of the San Andreas
849 Fault. In Evans B., Wong T.F. (Eds), Fault Mechanics and Transport Properties in Rocks, Academic
850 Press, London.

- 851 Rubin, A.M., Gillard, D., and Got, J.L., 1999. Streaks of microearthquakes along creeping faults.
852 *Nature*, 400, 635-641.
- 853 Rutter, E.H., Maddock, R.H., Hall, S.H., and White, S.H., 1986. Comparative microstructures of
854 natural and experimentally produced clay-bearing fault gouges. *Pure and Applied Geophysics*, 124, 3-
855 30.
- 856 Rutter, E. H., 1976. The kinetics of rock deformation by pressure solution. *Philosophical Transactions*
857 *of the Royal Society of London*, 283, 203-219.
- 858 Rutter, E. H., 1983. Pressure solution in nature, theory and experiment. *Journal of the geological*
859 *Society of London*, 140, 725-740.
- 860 Rutter, E.H. and Mainprice, D.H., 1979. On the possibility of slow fault slip controlled by a diffusive
861 mass transfer, *Gerlands Beitr. Geophysik, Leipzig*, 88, 154-162.
- 862 Sagy, A., Reches, Z., and Roman, I., 2001. Dynamic fracturing : field and experimental observations:
863 *Journal of Structural Geology*, 23, 1223–1239.
- 864 Schleicher, A.M., Warr, L.N., van der Pluijm, B.A., 2009a. On the origin of mixed-layered clay
865 minerals from the San Andreas Fault at 2.5–3 km vertical depth (SAFOD drillhole at Parkfield,
866 California). *Contrib. Mineral. Petrol.*, 157, 173-187, doi:10.1007/s00410-008-0328-7.
- 867 Schleicher, A.M., Tourscher, S.N., van der Pluijm, B.A., and Warr, L.N., 2009b. Constraints on
868 mineralization, fluid-rock interaction, and mass transfer during faulting at 2–3 km depth from the
869 SAFOD drill hole. *Journal of Geophysical research*, 114, B04202, doi:10.1029/2008JB006092.
- 870 Schleicher, A.M., van der Pluijm, B.A., and Warr, L.N., 2010. Nanocoatings of clay and creep of the
871 San Andreas fault at Parkfield, California. *Geology*, 38, 667-670, doi:10.1130/G31091.1.
- 872 Scholz, C.H., 1992. Weakness amidst strength. *Nature*, 359, 677-678.
- 873 Scholz, C.H., 2000. Evidence for a strong San Andreas fault. *Geology*, 28, 163-166.
- 874 Sibson, R. H., 1990. Faulting and fluid flow. In "Fluids in tectonically active regimes of the
875 continental crust." (B. E. Nesbitt, Ed.), pp. 93-132. *Short Course Handbook. Mineralogical*
876 *Association of Canada*.
- 877 Siddans, A. W. B., 1972. Slaty cleavage — a review of research since 1815. *Earth-Science Reviews* 8,
878 205-232.
- 879 Sieh, K.E., 1978. Slip along the San Andreas fault associated with the great 1857 earthquake. *Bulletin*
880 *of the Seismological Society of America*, 68, 1421-1448.
- 881 Sieh, K. E., and Jahns, R.H., 1984. Holocene activity of the San Andreas fault at Wallace Creek,
882 California. *Geological Society of America Bulletin*, 95, 883–896.
- 883 Solum, J.G., Hickman, S.H., Lockner, D.A., Moore, D.E., van der Pluijm, B.A., Schleicher, A.M., and
884 Evans, J.P., 2006. Mineralogical characterization of protolith and fault rocks from the SAFOD Main
885 Hole. *Geophysical Research Letters*, 33, L21314, doi:10.1029/2006GL027285.

- 886 Solum, J.G., Hickman, S., Lockner, D.A. et al., 2007. San Andreas Fault zone mineralogy,
887 geochemistry and physical properties from SAFOD cuttings and core. *Scientific Drilling, Special*
888 *Issue n°1*: 64-67, doi:10.2204/iodp.sd.s01.34.2007.
- 889 Steinbrugge, K.V., and Zacher, E.G., 1960. Creep on the San Andreas fault. *Fault creep and property*
890 *damage. Seismological Society of America Bulletin*, 50, 389-396.
- 891 Tembe, S., Lockner, D.A., Solum, J.G., Morrow, C.A., Wong, T.F., and Moore, D.E., 2006. Frictional
892 strength of cuttings and core from SAFOD drillhole phases 1 and 2. *Geophysical Research Letters*, 33,
893 L23307, doi:10.1029/2006GL027626.
- 894 Tembe, S., Lockner, D., and Wong, T.F., 2009. Constraints on the stress state of the San Andreas
895 Fault with analysis based on core and cuttings from San Andreas Fault Observatory at Depth
896 (SAFOD) drilling phases 1 and 2. *Journal of Geophysical Research*, 114, B11401,
897 doi:10.1029/2008JB005883.
- 898 Tembe, S., Lockner, D.A., and Wong, T.-F., 2010. Effect of clay content and mineralogy on frictional
899 sliding behavior of simulated gouges: Binary and ternary mixtures of quartz, illite, and
900 montmorillonite. *Journal of Geophysical Research*, 115, B03416, doi:10.1029/2009JB006383.
- 901 Thurber, C., Roecker, S., Zhang, H., Baher, S., and Ellsworth, W., 2004. Fine-scale structure of the
902 San Andreas fault zone and location of the SAFOD target earthquakes. *Geophysical Research Letters*,
903 31, L12S02, doi:10.1029/2003GL019398.
- 904 Titus, S.J., DeMets, C., and Tikoff, B., 2006. Thirty-five-year creep rates for the creeping segment of
905 the San Andreas Fault and the effects of the 2004 Parkfield earthquake: constraints from alignment
906 arrays, continuous global positioning system and creepmeters. *Bulletin of the Seismological Society of*
907 *America*, 96, S250-S268, doi:10.1785/0120050811.
- 908 Townend, J., and Zoback, M.D., 2004. Regional tectonic stress near the San Andreas fault in central
909 and southern California. *Geophysical Research Letters*, 31, L15S11, doi:10.1029/2003GL018918.
- 910 Vrolijk, P., and van der Pluijm, B.A., 1999. Clay gouge. *Journal of Structural Geology*, 21, 1039-
911 1048.
- 912 Wallace, R.E., 1970. Earthquake recurrence intervals on the San Andreas fault. *Geological Society of*
913 *America Bulletin*, 81, 2875-2890.
- 914 Wallace, R.E., 1990. General features. In: R.E. Wallace, *The San Andreas Fault System, California*.
915 USGS Professional Paper 1515, Washington, 283p.
- 916 Weyl, P.K., 1959. Pressure solution and the force of crystallization: a phenomenological theory.
917 *Journal of Geophysical Research*, 64, 2001-2025.
- 918 Wintsch, R. P., and Yi, K., 2002, Dissolution and replacement creep: a significant deformation
919 mechanism in mid-crustal rocks, *Journal of Structural Geology*, 24, 1179-1193.
- 920 Wood, D. S., 1974. Current views of the development of slaty cleavage. *Annual Review of Earth and*
921 *Planetary Sciences*, 2, 369-400.

- 922 Yu, S.B. and Liu, C.C., 1989. Fault creep on the central segment of the longitudinal valley fault,
923 eastern Taiwan. *Proceedings of the Geological Society of China*, 32, 209-231.
- 924 Zoback, M.D. et al., 1987. New evidence for the state of stress on the San Andreas fault system.
925 *Science*, 238, 1105-1111.
- 926 Zoback, M.D., Silver, L.T., Henyey, T., and Thatcher, W., 1988. The Cajon Pass scientific drilling
927 experiment: Overview of phase I. *Geophysical Research Letters*, 15, 933-936.
- 928 Zoback, M.D., 2000. Strength of the San Andreas Fault. *Nature*, 405, 31-32.
- 929 Zoback, M.D., 2006. SAFOD penetrates the San Andreas Fault. *Scientific Drilling*, Special Issue, 2,
930 32-33.
- 931 Zoback, M., Hickman S., and Ellsworth W., 2010. Scientific drilling into the San Andreas fault zone.
932 *Eos (Transactions, American Geophysical Union)*, 91, 197–199, doi:10.1029/2010EO220001.
- 933 Zoback, M., Hickman S., Ellsworth W., et al., 2011. Scientific drilling into the San Andreas Faut Zone
934 – An Overview of SAFOD's first five years. *Scientific Drilling*, 11, 14-28.
- 935 Zubitsov, S., Renard, F., Gratier, J. P., Guiguet, R., Dysthe, D. K., and Traskine, V. (2004).
936 Experimental pressure solution compaction of synthetic halite/calcite aggregates. *Tectonophysics*,
937 385, 45-57.
- 938

938 **Figure captions**

939

940 **Figure 1: (a)** Location map of the San Andreas Fault (SAF) and SAFOD borehole in central
 941 California, displaying also the different fault segments. **(b)** Simplified geological map of
 942 central California, matching to the area shown in (a) (modified from the Simplified
 943 Geological Map of California – California Geological Survey).

944

945 **Figure 2: (a)** Simplified NW-SE geologic cross-section of the SAFOD borehole area and its
 946 intersection with the depth division of the SAF into three main strands. Dashed red lines
 947 indicate the two active creeping zones (SDZ and CDZ) (after **Zoback et al., 2010**). A black
 948 square delimitates the area focused in b). **(b)** Simplified cross-section of the SAFOD main
 949 borehole and localization of the sidetrack boreholes used to core samples during Phase 3, in
 950 the damaged zone area (after **Zoback et al., 2011**), and sketch representing the orientation
 951 and the position of the studied samples relative to the oriented core. We cut the thin sections
 952 on those samples according to the three directions represented by the colored sections (blue,
 953 green and yellow). The blue and green sections are parallel to the hole and perpendicular to
 954 the fault and consequently to the foliation, while the yellow section is perpendicular to the
 955 hole and parallel to the foliation.

956

957 **Figure 3:** Localization of the studied samples in a schematic part of the main hole. The
 958 measured depth values are relative to Phase 3 Core. Colors display the different rock
 959 formations, vertical red bars indicate the places where the steel casing is actively deforming
 960 and dotted red lines mark the faults crossed by the borehole.

961

962 **Figure 4:** Main microstructure features observed in thin sections in the samples located
 963 outside the creeping zone. **(a)** Optical microscope picture showing dynamic fracturing with
 964 radial cracks. **(b) (c) (d) (e)** Optical microscope pictures showing the general intense
 965 fracturing of the material as well as the indentations. **(f)** Optical microscope picture with an
 966 example of the numerous indentations between quartz and feldspar grains. **(g) (h) (i)**
 967 Cathodoluminescence images showing the well-developed calcite vein network in bright red,
 968 at different scales. The minerals in blue and green are feldspars and the dark brown ones are
 969 quartz. **(j)** Optical microscope picture presenting an example of foliation developed by
 970 pressure solution mechanism. **(k)** Microprobe BSE image showing the solution cleavages at

971 the grain scale. **(l)** Other example of foliation, developed between shearing planes also by a
 972 pressure solution creep process.

973

974 **Figure 5:** Main microstructure features observed in thin sections of the samples located inside
 975 the creeping zone. **(a-c)** Top: color optical microscope pictures presenting some examples of
 976 the polymineral clasts. Bottom: Microprobe BSE images (in black and white) show the
 977 differences in mineral composition between these aggregates. **(d-f)** FEG-SEM BSE images
 978 showing examples of small grains presenting evidence of pressure solution to their edges.
 979 They also show the abundance of the very small grains (<10µm) inside the clay matrix,
 980 forming the creeping zone material. **(g, h)** SEM BSE images displaying the multiple shearing
 981 planes and their various orientations (yellow lines), as well as the very perturbed foliation
 982 inside the thin shearing planes. Qtz: quartz, Cal: calcite, Serp: serpentine, Fld: feldspar, Chl:
 983 chlorite, Sap: saponite, Fe ox: iron oxide.

984

985 **Figure 6:** Example of two different serpentines. The three pictures are FEG-SEM images,
 986 taken from sample III-0 at the boundary between an aggregate mainly composed of serpentine
 987 and saponite clay. Most of the serpentine forming clasts or present in the aggregates is
 988 lizardite. Chrysotile is located mainly along the boundaries of the serpentine aggregates or
 989 clasts, as here.

990

991 **Figure 7:** Element distribution from Scanning Electron Microscopy (SEM) analyses. Brighter
 992 colors indicate higher concentrations. The passive concentration of several elements (Fe, Mg,
 993 Ti) that belong to insoluble minerals (phyllosilicates and oxydes) underlines pressure solution
 994 cleavage that contributes to a tectonic layering process.

995

996 **Figure 8:** FEG-SEM images showing evidence of pressure solution process at the grain
 997 contacts. **(a)** Striated calcite between two quartz grains. The quartz grain boundaries are also
 998 striated and show evidences of indentations. **(b)** Contact between a calcite grain and a
 999 serpentine grain. The boundaries of the grains are striated and indented, especially in the area
 1000 of contact.

1001

1002 **Figure 9:** Model of clay deformation leading to foliation without preferential orientation. **(a)**
 1003 Initial state, with a normal foliation oriented at about 45° of the shearing plane. **(b)** The
 1004 foliation follows a normal evolution, tending to become parallel with the shearing planes. But

1005 the presence of hard bodies (aggregates and all-size grains) hinders this parallelization and
 1006 stops the development of the foliation. **(c)** The grains start to rotate, continuing
 1007 accommodating the deformation. This rotation is controlled by the sliding of the clay minerals
 1008 one against each other or by pressure solution creep at grain boundaries, when soluble grains
 1009 are in contact or under stress. **(d)** In the case where the grains do not rotate, the system is
 1010 locked. To continue deformation, the only way is to develop a new foliation, superimposed on
 1011 the previous one. This process can be repeated every time the grains lock the system.

1012

1013 **Figure 10:** Model of mineral evolution inside the damaged zone. **(a)** Initial state: the grey
 1014 grains are soluble minerals such as quartz, feldspars, serpentine, etc. **(b)** The deformation
 1015 starts with compression and shearing, which leads to fracturing at indenting contacts and
 1016 activation of pressure solution creep. Soluble minerals start dissolving, calcite (in blue) is
 1017 precipitated into the fractures and phyllosilicates (in brown) begin to be passively
 1018 concentrated. **(c)** A foliation is developed with the passive concentration of phyllosilicates.
 1019 The opening of veins becomes larger. **(d)** Through time, the soluble minerals continue to
 1020 dissolve. Because of fluid circulation, the main part of the dissolved material is transported
 1021 away. Phyllosilicate concentration increases with the growth and crystallization of clay. The
 1022 polymineral clasts start to be formed and act as hard objects. **(e)** Final state: rotation of the
 1023 hard objects. Initially, they were the aggregates protected by the calcite or the monomineralic
 1024 aggregates, harder to dissolve. **(f)** The large calcite veins wedge the system and stop the
 1025 ductile deformation.

1026

1027 **Figure 11:** Schematic model of the evolution of a creeping zone. On the left a creeping zone,
 1028 up to several hundred meters wide, initiates in a zone gathering several conditions favorable
 1029 to pressure solution creep: (i) presence of fluids that can dissolve at least part of the rock, (ii)
 1030 mixture of soluble and insoluble minerals, (iii) small grain size or fractured grains. The
 1031 creeping rate is not necessary efficient to relax the stress so earthquakes occur through this
 1032 zone (middle part). This has two effects: grain size reduction, which activates pressure
 1033 solution creep, and fluid flow enhancement through the pre-creeping zone. These fluids
 1034 evacuate the soluble species and so concentrate phyllosilicates, also favoring pressure solution
 1035 creep. On the right hand side, a meter-wide creeping zone is stable: in the upper part of the
 1036 crust (0 – 3-4 km) creep is favored both by the very low friction of the clay minerals
 1037 (saponite) that derived from both the passive concentration of phyllosilicate and metamorphic
 1038 reactions linked to episodic fluid flows. In the lower part of the crust (3-4 to 10-12 km),

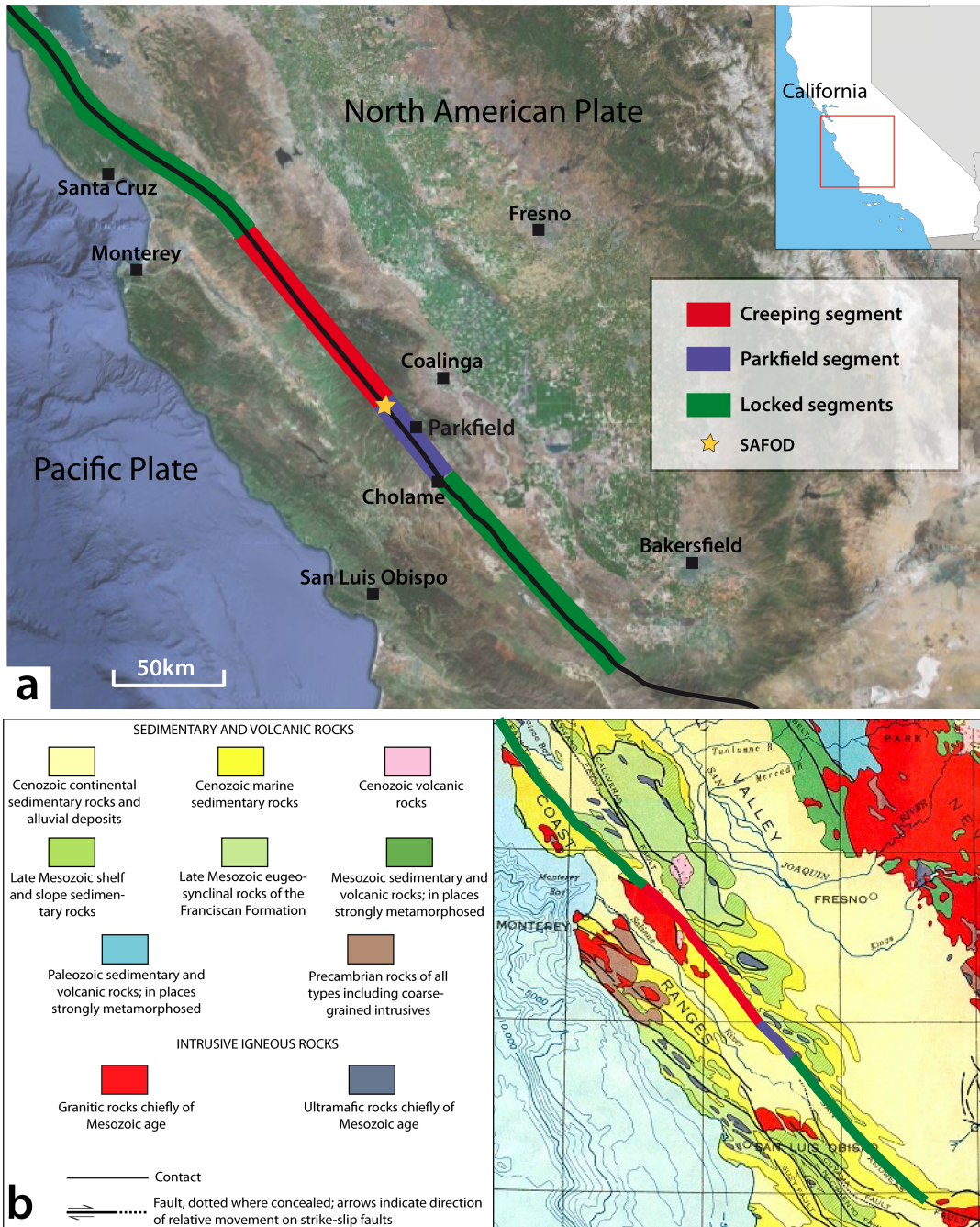
1039 diffusion-accommodated grain-sliding pressure solution creep is efficient enough to
1040 accommodate aseismic sliding.

1041

1042 **Figure 12:** Mineralogical evolution model of a creeping fault zone as a function of time,
1043 depth and creeping zone distance. The blue domain corresponds to the creep mechanism
1044 observed in the damaged zone, in the samples outside of the creeping zone. In this domain,
1045 pressure solution creep is the main creep mechanism. Healing by calcite precipitation permits
1046 to keep up this mechanism through the time as well as at depth. The red domain corresponds
1047 to the creep mechanisms observed within the active creeping zone. Pressure solution creep is
1048 very efficient at the beginning at all depths. However, because there is no or little healing in
1049 this domain because fluids drive away the dissolved materials, the mineralogical composition
1050 evolves through time leading to an increasing concentration of clays in the upper 3-4 km. The
1051 friction coefficient of the creeping domain becomes very low and the sliding of clay layers on
1052 top of themselves could accommodate a large part of the creeping rate. It is completed by
1053 stress driven diffusive mass transfer that accommodates grains and clast aggregates sliding.
1054 Low friction related to saponite is not operative below 3-4 km because of the transformation
1055 of saponite into corrensite then chlorite, which have higher friction coefficients. When
1056 saponite starts to transform into harder minerals with the increase in temperature, the whole
1057 domain becomes stronger and hardly deform by friction. Diffusion-accommodated grain-
1058 sliding pressure solution creep remains efficient and is the main creep mechanism at depth.

1059

1060 **Table 1:** Overview of the location of the studied samples listed with increasing depth along
1061 the borehole (MD) in SAFOD. The Core Section column gives information about sidetrack
1062 boreholes (G43 stands for hole G, Run 4, Section 3). All the samples presented here come
1063 from the Phase 3. In the denomination of samples (Column Samples), the first number
1064 indicates the Round of distribution (II-14 stands for Round II, sample n°14 of the sample set
1065 got from this Round). As the Phase 3 core consists in series of boreholes sidetracking the
1066 Phase 2 hole, the measured depths can vary depending of the considered hole. **Zoback et al.**
1067 **(2010)** give the methodology to correlate the values of the measured depth of Phase 3 with the
1068 Phase 2. Here, for the values of core of Hole G, Runs 4-6, we should add 3.96m to the Phase
1069 3 measured depths to have the corresponding depth with the Phase 2. In the two columns of
1070 MD Phase 2 and MD Phase 3, we give the corresponding values in meters of measured depth
1071 of our samples, taking into account this correction, as the localization of the top and bottom of
1072 the CDZ.



1073

1074

Figure 1

C.3 Borehole geophysics

In situ measurement of the hydraulic diffusivity of the active Chelungpu Fault, Taiwan

M. L. Doan,^{1,2} E. E. Brodsky,¹ Y. Kano,³ and K. F. Ma²

Received 12 May 2006; revised 11 July 2006; accepted 17 July 2006; published 30 August 2006.

[1] Hydraulic diffusivity controls fluid pressure and hence affects effective normal stress during rupture. Models suggest a particularly spectacular example of fluid pressurization during the $M_w = 7.6$ 1999 Chichi earthquake when pressurization may have reduced high-frequency shaking in the regions of large slip if the fault was sufficiently sealed. We investigate in situ hydraulic diffusivity which is the key parameter in such models through a cross-hole experiment. We find a diffusivity of $D = (7 \pm 1) \times 10^{-5}$ m²/s, which is a low value compatible with pressurization of the Chelungpu fault during the earthquake. In most poroelastic media, the hydraulic storativity S lies between 10^{-7} and 10^{-5} , so that the transmissivity T along the fault zone is comprised between 10^{-11} m²/s and 10^{-9} m²/s. The corresponding permeability (10^{-18} – 10^{-16} m²) is at most one hundred times larger than the value obtained on core samples from the host rock. The fault zone is overpressurized by 0.06 to 6 MPa, which is between 0.2% and 20% of the lithostatic pressure. **Citation:** Doan, M. L., E. E. Brodsky, Y. Kano, and K. F. Ma (2006), In situ measurement of the hydraulic diffusivity of the active Chelungpu Fault, Taiwan, *Geophys. Res. Lett.*, 33, L16317, doi:10.1029/2006GL026889.

1. Introduction

[2] The hydraulic diffusivity of the damage zone is a fundamental property of earthquake rupture because it controls the fluid overpressure that can be maintained on a fault. In between earthquakes, this fluid pressure can control failure [Sibson *et al.*, 1975; Nur and Booker, 1972]. For rupture during earthquakes, Rice [2006] and Andrews [2002] both calculated that the length scale over which slip weakening occurs depends critically on the hydraulic diffusivity. Cycles of healing and damage in rocks affect permeability which is dominated by fractures [Ben-Zion and Sammis, 2003].

[3] Permeability, which is the most variable part of hydraulic diffusivity (see description of variables in Text S1 of the auxiliary material¹), is controlled by the fractures in the heavily brecciated fault damage zone surrounding the fault core [Caine *et al.*, 1996]. Laboratory measurements of core samples give a lower bound on the diffusivity [Lockner *et al.*, 2005; Tanikawa *et al.*, 2005; Chen *et al.*, 2005;

Kitamura *et al.*, 2005], but permeability is notoriously scale dependent [Townsend and Zoback, 2000; Manning and Ingebritsen, 1999]. The most important fractures may be on scales much larger than a core sample and therefore it is necessary to measure the properties in situ.

[4] Despite the fundamental importance of hydraulic diffusivity, it has never been successfully measured in situ on an active large-scale fault. Hydraulic tests in deep boreholes intersecting the Nojima fault were attempted by Kitagawa *et al.* [1999, 2002] but they were tapping flow in the hanging wall at least 50 m away from the fault core and therefore at the diffuse end of the damaged zone. In the present study, we study a pair of boreholes intersecting the Chelungpu fault that are perforated closer to the fault core.

[5] Water was pumped out of hole A (Figure 1). The resulting head change propagated along the fault zone to produce a hydraulic anomaly in hole B. We report the results of the experiment and discuss a number of significant complications related to leaks in the well casing. After effectively modeling the leaks, we extract a value of diffusivity for the fault damage zone of $\sim 7 \times 10^{-5}$ m²/s, which is sufficiently low to confine pressurized fluid during an earthquake.

2. Hydraulic Tests on the Chelungpu Fault

2.1. Boreholes of the Taiwan Chelungpu-Fault Drilling Project

[6] The pair of boreholes used for this experiment are separated by 40 m. Both holes are fully cased and cemented in their annuli. Both are perforated only near their intersection with the Chelungpu fault. Hole A is perforated directly above the fault; hole B directly below (Figure 1).

[7] The first borehole (hole A) intersects the fault at a depth of 1111 m within the silty shales of the Chinshui formation, that are sandwiched between the sandstone dominated rocks of the Cholan and Kueichulin formations (Figure 1). The slip is concentrated within a 12 cm thin layer of fine-grained clayish “black material”, which is distinct from the nearby 30 cm thick layer of grayish gouge. The other hole (hole B) intersects regions of black material that are also interpreted as slip zones at 1137.5 m and 1138.0 m [Ma *et al.*, 2005]. In both holes, the fault core is surrounded by breccia and fractured rocks that form a 1-m wide damage zone.

2.2. Pumping Test

[8] We pumped water out of hole A on Nov. 18, 2005 and then continuously recorded the water level in both holes for the following 3 months. The pumping was as fast as

¹Earth Science Department, University of Santa Cruz, Santa Cruz, California, USA.

²National Central University, Chung-li, Taiwan.

³Disaster Prevention Research Institute, Kyoto University, Kyoto, Japan.

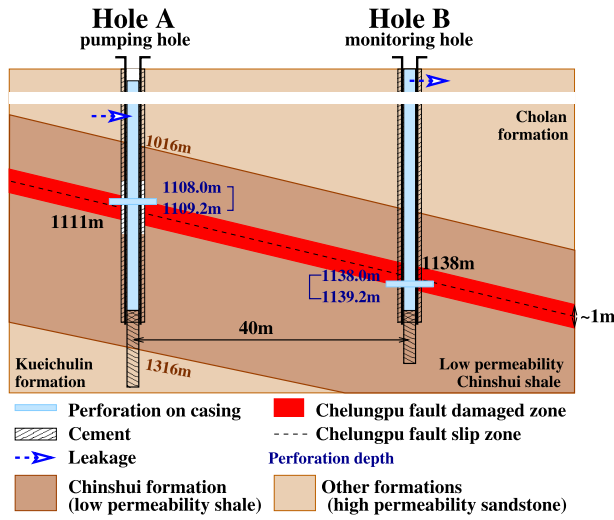


Figure 1. Configuration of the cross-hole hydraulic test on the Chelungpu boreholes. The two holes are separated by 40 m and perforated near the fault with a density of 4 shots per foot. Blue thick numbers indicate the top and bottom depths of the perforations. Perforation location is accurate to within 0.5 m. This schematic is not true scale.

permitted by the hydraulic equipment (about 60 gpm ~ $4 \times 10^{-3} \text{ m}^3/\text{s}$) and its duration was limited to 45 minutes. Figure 2 shows the evolution of water level in hole A during and after the pumping. The water level in the

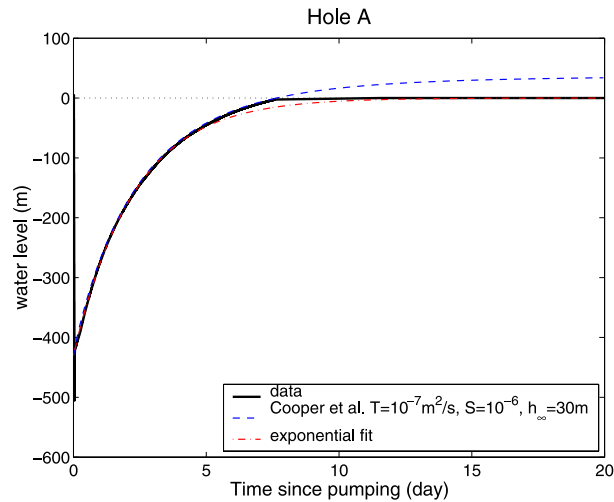


Figure 2. Recovery of the water level in the pumping hole through time. We lowered the water level of hole A by 400 m. (There was a small transient that dropped the level to -500 m while the pump was deployed). The curve fits the evolution predicted by Cooper et al. [1967] with the transmissivity $T = 10^{-7} \text{ m}^2/\text{s}$ and the storativity $S = 10^{-6}$ (blue dashed curve), provided we take into account the overpressure of the leaky aquifer (about 0.3 MPa, equivalent to 30 m of water). This theoretical result does not take into account the fixed level of head at the surface. The red dot-dashed curve depicts the exponential function used in equation (A4) of the auxiliary material to compute analytically the expected response of hole B.

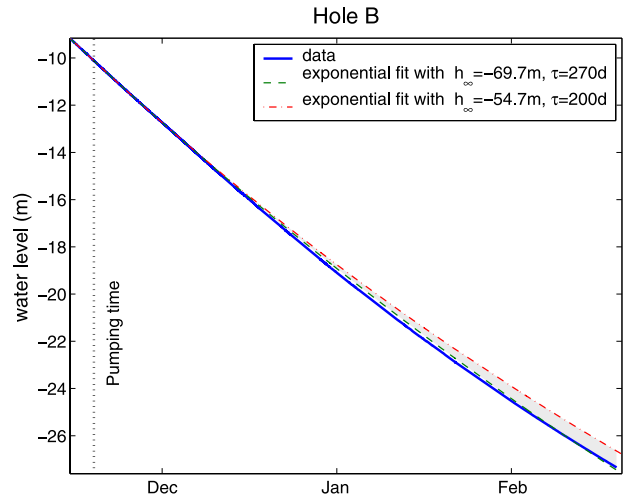


Figure 3. Evolution of the water level in hole B relative to the wellhead. It is compared with the exponential solutions computed with equation (2). We present here the two extreme sets of parameters $\tau = 200$ days, $h_{\infty} = -54.7 \text{ m}$ (top red dot-dashed line) and $\tau = 270$ days, $h_{\infty} = -69.7 \text{ m}$ (bottom green dashed line), that delineate a range of possible fitting exponentials (shaded area). The maximum departure is 70 cm, over a total change of 18 m. The error is thus less than 3.5% over 3 months.

pumping well recovered in one week and then stayed at zero when it reaches the wellhead.

[9] Figure 3 shows the evolution of water level in hole B. Both before and after pumping, the water level continuously decreased due to leaks in the casing resulting in a loss of more than 18 m in 3 months. This large loss from leakage obscures the more subtle drop in water level that was created by the pumping in hole A. Therefore, we need to model and remove the effects of the leaks in hole B so that we can then detect the transient induced by the pumping.

3. Analysis

[10] To recover the hydraulic properties of the fault zone, we analyze how the monitoring well (hole B) responds to the pumping well (hole A). We: (1) model the recovery of water level in hole A, which is the cause of the anomaly in hole B, (2) remove the effects of the leaks in hole B and (3) compare the remaining anomaly with a prediction based on the variations in water level in hole A to recover the hydraulic properties of the fault zone.

3.1. Modeling the Pumping Hole

[11] The sudden change in water level from the pumping in hole A disturbed the aquifers tapped by the well. For a single isotropic poroelastic aquifer with no lateral boundaries, Cooper et al. [1967] computed a solution (see equation (A5) of the auxiliary material). Figure 2 displays the model with the best-fit parameters, which are storativity $S = 10^{-6}$ and transmissivity $T = 10^{-7} \text{ m}^2/\text{s}$. The model of Cooper et al. [1967] does not take into account the overpressure in the aquifer so that the computed curve was shifted by the overpressure in the aquifer, which is 0.3 MPa (equivalent to 30 m of water).

[12] Even before the perforation, hole A was artesian with a flow rate of 10^{-6} m³/s due to a leaky casing. Prior to perforation, a pumping test was done on hole A (C.-S. Chen, personal communication, 2005). The results suggest that the leaks tap an aquifer with an overpressurized hydraulic head of 30 to 50 m and a transmissivity close to 10^{-7} m²/s. These values are similar to those retrieved in Figure 2, indicating that the recovery in hole A is dominated by the leakage rather than by the perforated fault zone.

[13] Although the model of *Cooper et al.* [1967] gives satisfactory results, it does not take into account the constant water level when water reaches the surface. The input signal in hole A was approximated by the exponential fit of Figure 2, which gives slower recovery than the observed data. This exponential approximation will be used in section 3.3 to fit the anomaly in hole B.

3.2. Removal of the First-Order Trend Induced by Leaks in Hole B

[14] Figure 3 shows that the water level in hole B is dominated by a continuous decrease in water level. This decrease existed prior to the perforation in hole B and is due to leakage in the casing. To extract the disturbance due to the pumping in hole A, an accurate approximation of this leakage is needed.

[15] Let us suppose a quasi-permanent radial flow inside the aquifer tapped by the leakage. The flow Q through the leak is given by the Thiem equation:

$$Q = -\frac{2\pi T}{\ln(R_\infty/r_b)}(h_w - h_f) \quad (1)$$

where R_∞ is the radius of influence beyond which the pressure in the formation is undisturbed, r_b is the borehole radius (equal to 7.8 cm for both holes A and B), T is the transmissivity of the formation, h_w is the hydraulic head in the well and h_f is the hydraulic head in the formation. Combined with the conservation of mass of fluid in the borehole, the water level in hole B is described by an exponential function:

$$h_w = h_\infty + (h_w(t_0) - h_\infty)e^{-(t-t_0)/\tau} \quad (2)$$

where $\tau = \pi r_b^2 / c \ln(R_\infty/r_b)$. Notice that the value of h_w does not depend on the choice of t_0 as $h_w(t_0)$ is adjusted appropriately. The leakage is then characterized by two parameters only: the decay time τ and the far-field hydraulic head h_∞ . This is as complex a model as is warranted by the available data.

[16] We calibrate the model of equation (2) using different subsequences of the data of November 2005 in order to find a range of possible values. Using intervals of 6–8 days duration starting at times between Nov. 15 and Nov. 26 yields a range of fit parameters given by the series of curves in the shaded portion of Figure 3. Even though this simple, steady-state model should only be valid for short times, it fits the observed data quite well for 3 months after the pumping.

[17] Figure 4 shows the remaining signal in hole B after the leakage modeled by equation (2) is removed. The first-order exponential trend seen in Figure 3 explains the data

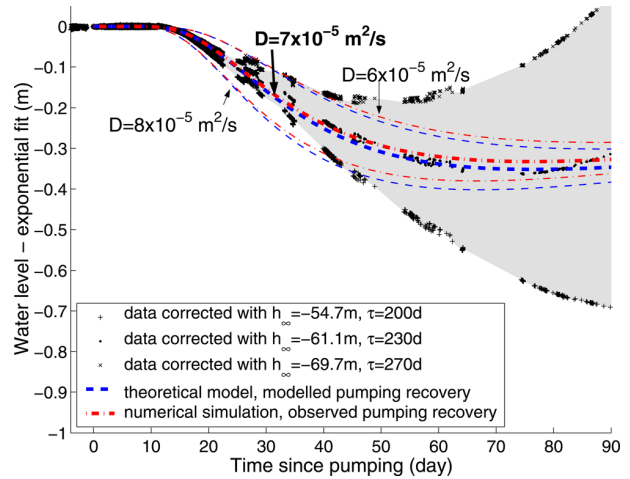


Figure 4. Pumping from hole A observed in hole B. We removed the fit of Figure 3 for the range of parameters described in section 3.2. The extreme parameters are $\tau = 200$ days, $h_\infty = -54.7$ m and $\tau = 270$ days, $h_\infty = -69.7$ m. In all cases, a residual anomaly begins 12 days after pumping. The auxiliary material explains the observed anomaly as the propagation of the disturbance along the fault zone with a hydraulic diffusivity $D = 7 \times 10^{-5}$ m²/s (bold lines), using two different methods: (1) a numerical simulation with the true data from hole A, and (2) an analytical method based on the exponential fit of the recovery data in hole A of Figure 2. Modeled curves for $D = 6 \times 10^{-5}$ m²/s (upper thin lines) and $D = 8 \times 10^{-5}$ m²/s (lower thin lines) provide estimates of the accuracy of our value of hydraulic diffusivity. A set of intermediate parameters gives a candidate experimental curve that would be fitted by the expected curves for $D = 7 \times 10^{-5}$ m²/s.

until 12 days after the pumping in hole A. Twelve days is longer than the duration of any of the calibration intervals. For the entire probable range of parameters, the anomaly in hole B is in the shaded region of Figure 4. In all cases, the anomaly begins suddenly 12 days after the pumping in hole A. The amplitude of the anomaly reaches at most 70 cm, about 90 days after the pumping.

3.3. Hydraulic Diffusivity From the Hydraulic Anomaly Recorded in the Observation Well

[18] We now use our fit of the water level in hole A to predict the anomaly in the corrected water level in hole B.

[19] The anomaly in hole B cannot be explained with models involving a single aquifer that both refills hole A and empties hole B. For instance, the direct application of the standard model of *Cooper et al.* [1967] gives a best fitting curve with a maximum amplitude of 4 m, five times larger than observed. Also, the observations in section 3.1 indicate that hole A is predominantly filled by an aquifer that is separate from the perforated fault zone.

[20] Instead we use a Green function solution that propagates the anomaly from hole A to hole B through a separate aquifer than the one responsible for the recovery of hole A (see auxiliary material). The model can be used to compute analytically the anomaly in hole B as long as an

analytical form is available for the input in hole A. The model has a single parameter: the hydraulic diffusivity of the damaged zone.

[21] Figure 4 shows that the modified model fits the observed anomaly with the hydraulic diffusivity $D = 7 \times 10^{-5} \text{ m}^2/\text{s}$. The input signal used for the computation is the exponential approximation of the recovery in hole A (Figure 2). This approximation has a slower recovery than the observed signal and the calculated anomaly in hole B is expected to be slightly larger than observed.

[22] The prediction is refined with numerical methods in order to use directly the time series of the water level data of hole A of Figure 2 instead of its exponential approximation. Our numerical solution was obtained by the direct implementation of equations (A1) to (A3) of the auxiliary material with the finite elements method software Comsol 3.2. With solutions using both modeled and observed recoveries in hole A, the best fit is obtained with $D = (7 \pm 1) \times 10^{-5} \text{ m}^2/\text{s}$.

4. Discussion

4.1. Identification of the Tested Aquifer

[23] We interpreted the data as the propagation of the pressure front induced by pumping within an aquifer. But which aquifer? Figure 1 suggests three main options: (1) a flow from the leak of hole A to the leak of hole B, (2) a flow between the perforations of one hole and the leak of the other hole, (3) a flow between the perforations of the two holes.

[24] The observed signal might come from the propagation of the pressure disturbance between the leaks of the two holes. However, the leakage of hole A, where water goes into the borehole, differs from the leakage in hole B, where water flows out of the borehole. Moreover, the value of diffusivity found from the cross-hole experiment is much smaller than the one derived for the leakage in hole A. These two observations suggest that the aquifer tapped by the leaks in hole A is not connected to the leak in hole B.

[25] The observed signal might also be due to a connection between the leak of one hole to the perforations of the other hole. In hole A, a cement bonding log shows that the cement in the annular interval between the casing and the borehole wall is missing at the fault zone depth but also reveals that cement plugs of good quality exist over 10 m in the annular interval at 1000 m and 1040 m. The perforations in hole A are therefore decoupled from the permeable Kueichulin formation. No such log exists for hole B. However, if the cement were very poor all along the casing on hole B, the perforations in hole B would have allowed water from the Cholan formation to enter the borehole with a rate similar to the one observed in hole A. This is not what has been observed.

[26] The most plausible hypothesis is a flow between the two perforations of the borehole located at the fault zone. Core studies [Lockner *et al.*, 2005; Tanikawa *et al.*, 2005] suggest that the fault zone has the permeability pattern described by Caine *et al.* [1996]: a fault core less permeable than the host rock, bounded by a damaged zone of enhanced permeability. Since the Chinshui shale is a relatively low permeability rock, it is probable that the easiest path between the perforations is the zone of highest permeability:

the damaged zone of the Chelungpu fault. Because of the weak cement in the annular interval of hole A, the impermeable fault core is short-circuited and does not disturb the propagation of the head anomaly from the perforations of hole A (above the fault core) to the perforations of hole B (below the fault core).

4.2. Estimation of the Permeability of the Fault-Damaged Zone

[27] Most hydromechanical models studying the effect of fault zone deal with permeability. To extract this parameter from the hydraulic diffusivity, the storativity or the specific storage are needed (the storativity S is the specific storage S_s in $1/\text{m}$, integrated over the thickness of the aquifer b : $S = S_s b$). For the black material forming the fault core, Lockner *et al.* [2005] found a specific storage ranging from 1.3 to $7 \times 10^{-7} \text{ m}^{-1}$. However, this highly deformed material differs from the silty shale forming the matrix of the damaged zone. Chen *et al.* [2005] obtained a narrow range of specific storages of $8 \times 10^{-7} \text{ m}^{-1}$ to $3 \times 10^{-6} \text{ m}^{-1}$ on core samples of host rock far from the fault. Large scale media should be more porous and less rigid than core samples as the specific storage of poroelastic media is given by:

$$S_s = \left(\frac{\phi}{K_f} + \frac{1}{K_s} \right) \rho_f g \quad (3)$$

where ϕ is the porosity, ρ_f is the fluid density, g is the gravity acceleration, K_f and K_s are the bulk modulus of water and solid matrix respectively. In the damaged zone, the porosity and the matrix compressibility are expected to be higher than for the host rock. The specific storage might then range from 10^{-7} m^{-1} (laboratory values) to 10^{-5} m^{-1} (large scale value from equation (3)). As cores and logs suggest, the densely damaged zone has a thickness $b \simeq 1 \text{ m}$. The storativity lies in the range $S = S_s b \simeq 10^{-7} - 10^{-5}$.

[28] The transmissivity $T = D \times S$ is then deduced to be between $10^{-11} \text{ m}^2/\text{s}$ and $10^{-9} \text{ m}^2/\text{s}$. Transmissivity T is related to permeability κ through the equation $T = \kappa b \rho_f g / \eta$ where b is the thickness of the aquifer, ρ_f is the density of the fluid and η is the dynamic viscosity of the passing fluid. For water at 50°C and $b \simeq 1 \text{ m}$, the permeability is between 10^{-18} m^2 and 10^{-16} m^2 . This permeability range is larger than the value 10^{-19} m^2 to 10^{-21} m^2 obtained for core samples from the fault slip zone [Lockner *et al.*, 2005] but it is not much larger from siltstone reference samples [Chen *et al.*, 2005]. Chen *et al.* [2005] found a noticeable permeability anisotropy, ranging from 10^{-19} m^2 transversely to bedding and 10^{-18} m^2 parallel to bedding.

4.3. Estimation of the Overpressure of the Fault-Damaged Zone

[29] The overpressure in the fault zone is estimated from the change in flow rate in hole B. In hole B, the rate of water level decrease changed after the perforation of the casing. Prior to perforation, the water level dropped by 24.5 cm/day. After the perforation, the water level decreased only to 22 cm/day. This corresponds to a change in flow rate $\Delta Q = 5 \times 10^{-9} \text{ m}^3/\text{s}$. Assuming an influence radius $R_\infty = 10^5 r_b \simeq 8000 \text{ m}$ in equation (1) (as R_∞ is inside a logarithmic function, the result is little sensitive to the choice of this parameter), the overpressure in the

well is computed to be between 0.06 MPa (0.2% of the lithostatic pressure) and 6 MPa (20% of the lithostatic pressure).

5. Conclusion

[30] We found that the hydraulic diffusivity of the damaged zone around the Chelungpu fault is close to 10^{-4} m²/s. This is to our knowledge the first in situ measurement of hydraulic diffusivity obtained for the damaged zone very near a major crustal fault, as similar experiments performed on other fault drilling projects give rather properties of the aquifers surrounding the fault [Kitagawa *et al.*, 1999, 2002; Cornet *et al.*, 2004].

[31] Our results suggest also that the fault damaged zone is at most moderately overpressurized (at most 20% of the lithostatic pressure), so that the fault recovery which occurred so far did not contribute to the pressure build-up. Much small overpressure is also consistent with our data.

[32] By extrapolating storativity values of core samples, the permeability is constrained to be at most 10^{-16} m², one hundred times the value obtained for unfractured core sample of the host rock. Observations on crystalline rock masses suggest that fracturing enhances the permeability by a factor of 100 to 1000 [Townsend and Zoback, 2000; Manning and Ingebritsen, 1999]. The permeability enhancement of the damaged zone of the fault is then in the lower part of this range. Core samples show extensive calcite crystallization in the breccia zone. A possible explanation of the small enhancement of permeability of the damaged zone is that the recovery of the fault zone is well advanced only 6 years after the Chichi earthquake.

[33] Is the observed hydraulic diffusivity small enough to maintain the pore pressure inside the fault during an earthquake? A naive interpretation suggests that fluid will begin to leak in a time equal to L^2/D , where L is the thickness on the zone of intensive shear during the earthquake, which is at most equal to the thickness of the damaged zone. For our observed values of hydraulic diffusivity and a 1 m wide damaged zone, this leakage time is a couple hours long, much longer than the duration of the earthquake. More careful formulations by Andrews [2002] and Rempel and Rice [2006] still allow pressurization to occur with the observed diffusivity D . Thermal or hydrodynamic pressurization during rupture is still a plausible mechanism.

[34] **Acknowledgments.** We thank Ji-Hao Hung for his information on the wells. We thank Chang-Wei Tsao, "Sonata" Wu, and Hsin-I Lin for their helpful activity on drill site. We are grateful to Andy Fisher for his thoughtful remarks. We thank also Joe Andrews for his constructive suggestions. M. L. Doan and E. E. Brodsky were funded in part by the National Science Foundation. Y. Kano was partially funded by the Kyoto University Active Geosphere Investigations for the 21st Century Center of Excellence (KAGI21).

References

- Andrews, D. (2002), A fluid constitutive relation accounting for thermal pressurization of pore fluid, *J. Geophys. Res.*, *107*(B12), 2363, doi:10.1029/2002JB001942.
- Ben-Zion, Y., and C. G. Sammis (2003), Characterisation of fault zones, *Pure Appl. Geophys.*, *160*, 677–715.
- Caine, J. S., J. P. Evans, and C. B. Forster (1996), Fault zone architecture and permeability structure, *Geology*, *24*(1), 1025–1028.
- Chen, N., W. Zhu, T. F. Wong, and S. Song (2005), Hydromechanical behavior of country rock samples from the Taiwan Chelungpu Drilling Project, *Eos Trans. AGU*, *86*(52), Fall Meet. Suppl., Abstract T51A–1324.
- Cooper, H. H., J. D. Bredehoeft, and I. S. Papadopoulos (1967), Response of a finite-diameter well to an instantaneous charge of water, *Water Resour. Res.*, *3*(1), 263–269.
- Cornet, F. H., M. L. Doan, I. Moretti, and G. Borm (2004), Drilling through the active Aigion Fault: The AIG10 well observatory, *C. R. Geosci.*, *336*(4–5), 395–406.
- Kitagawa, Y., N. Koizumi, K. Notsu, and G. Igarashi (1999), Water injection experiments and discharge changes at the Nojima Fault in Awaji Island, Japan, *Geophys. Res. Lett.*, *26*(20), 3173–3176.
- Kitagawa, Y., K. Fujimori, and N. Koizumi (2002), Temporal change in permeability of the rock estimated from repeated water injection experiments near the Nojima fault in Awaji island, Japan, *Geophys. Res. Lett.*, *29*(10), 1483, doi:10.1029/2001GL014030.
- Kitamura, K., M. Takahashi, K. Masuda, H. Ito, S. Song, and C. Wang (2005), The relationship between pore-pressure and the elastic-wave velocities of TCDP cores, *Eos Trans. AGU*, *86*(52), Fall Meet. Suppl., Abstract T51A–1326.
- Lockner, D. A., C. Morrow, S. Song, S. Tembe, and T. Wong (2005), Permeability of whole core samples at Chelungpu Fault, Taiwan TCDP scientific drillhole, *Eos Trans. AGU*, *86*(52), Fall Meet. Suppl., Abstract T43D–04.
- Ma, K. F., C. Wang, J. H. Hung, S. Song, H. Tanaka, E. Yeh, and Y. Tsai (2005), Dynamics of Chi-Chi earthquake rupture: Discovery from seismological modeling and Taiwan Chelungpu-Fault Drilling Project (TCDP), *Eos Trans. AGU*, *86*(52), Fall Meet. Suppl., Abstract T13A–1353.
- Manning, C. E., and S. E. Ingebritsen (1999), Permeability of the continental crust: Implications of geothermal data and metamorphic systems, *Rev. Geophys.*, *37*(1), 127–150.
- Nur, A., and J. Booker (1972), Aftershocks induced by pore fluid flow?, *Science*, *175*, 885–887.
- Rempel, A. W., and J. R. Rice (2006), Thermal pressurization and onset of melting in fault zones, *J. Geophys. Res.*, doi:10.1029/2006JB004314, in press.
- Rice, J. R. (2006), Heating and weakening of faults during earthquake slip, *J. Geophys. Res.*, *111*, B05311, doi:10.1029/2005JB004006.
- Sibson, R. H., J. M. Moore, and A. H. Rankin (1975), Seismic pumping: A hydrothermal fluid transport mechanism, *J. Geol. Soc. London*, *131*(6), 653–659.
- Tanikawa, W., T. Shimamoto, H. Noda, and H. Sone (2005), Hydraulic properties of Chelungpu, Shuangtung and Shuilikeng fault zones and their implications for fault motion during 1999 Chi-Chi earthquake, *Eos Trans. AGU*, *86*(52), Fall Meet. Suppl., Abstract T43D–08.
- Townsend, J., and M. D. Zoback (2000), How faulting keeps the crust strong, *Geology*, *28*(5), 399–402.
- E. E. Brodsky and M. L. Doan, Earth Science Department, Earth and Marine Sciences Building, University of Santa Cruz, 1156 High Street, Santa Cruz, CA 95064, USA. (ebrodsky@es.ucsc.edu; mdoan@es.ucsc.edu)
- Y. Kano, Disaster Prevention Research Institute, Kyoto University, Gokasho, Uji, Kyoto 611-0011, Japan. (kano@eqh.dpri.kyoto-u.ac.jp)
- K. F. Ma, National Central University, Chung-li 320-54, Taiwan. (fong@rupture.gep.ncu.edu.tw)



Small pressure drop triggered near a fault by small teleseismic waves

M.L. Doan^{a,*}, F.H. Cornet^{b,1}

^a *Earth & Planetary Science Department, Earth & Marine Sciences Building, University of Santa Cruz, 1156, High Street, CA 95064, Santa Cruz, United States*

^b *Department of Seismology, Institut de Physique du Globe de Paris, Casier 89, 4, place Jussieu, 75005, Paris, France*

Received 27 October 2006; received in revised form 22 January 2007; accepted 16 March 2007

Available online 28 March 2007

Editor: C.P. Jaupart

Abstract

We describe a pressure transient triggered near an active fault by seismic waves generated more than 10000 km away during the 2003 $M_w = 7.8$ Rat Island earthquake. In contrast with previous similar observations, the pressure drop occurs simultaneously with the arrival of S waves, and not during the passage of the Rayleigh waves that have larger amplitudes and smaller frequencies. This small 60 Pa drop is compatible with a small slip on the fault, which induced either dilatant damage or a transient disruption in the impermeable barrier the fault constitutes.

© 2007 Elsevier B.V. All rights reserved.

Keywords: dynamic triggering; pore pressure monitoring; active fault long-term monitoring; borehole instrumentation

Water-level changes induced by remote earthquakes have been documented since the Alaskan Earthquake of 1964 [1]. Montgomery and Manga [2] review dozens of such events and compare their distance to the epicenter to the magnitude of the corresponding earthquake. All their data lie above a line that corresponds to a volumetric strain equal to 10^{-8} , and they attribute this limit to instrumentation resolution. Such small a threshold suggests that some of these disturbances are dynamically triggered.

High frequency data shows that these disturbances can be concurrent with the passage of the Rayleigh waves [3]. These pressure changes are often interpreted as changes in permeability, which has also been shown to be altered by seismic waves [4]. Interestingly, triggered seismicity can also start from Rayleigh waves arrival [5]. The relationship between the two triggering phenomena is still not clear.

The Corinth Rift Laboratory is devoted to the joint observation of deformation and fluid pressure in a seismically active area. In addition to pressure data, seismometers and strainmeters monitor the Rift deformation. After a presentation of the borehole intersecting the Aigio fault, we describe the pressure drop induced by the 2003 Rat Island earthquake together with data from a seismometer and a dilatometer located 10 km away from the well. We check the absence of artifact due to the instrumentation or to a change in oceanic loading.

* Corresponding author. Tel.: +1 831 459 1311; fax: +1 831 459 3074.

E-mail addresses: mdoan@pmc.ucsc.edu (M.L. Doan), cornet@ipgp.jussieu.fr (F.H. Cornet).

¹ Tel.: +33 1 44 27 38 97; fax: +33 1 44 27 38 94.

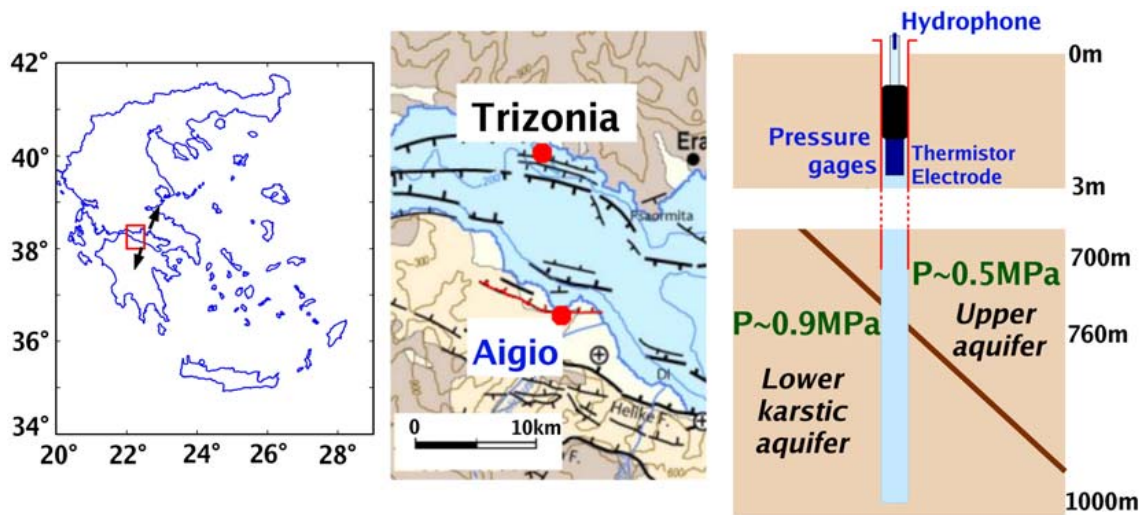


Fig. 1. (Left) The Corinth Rift, Greece, opens at a rate of 1.5 cm/yr. (Middle) In its western part, this activity is accompanied by intense faulting on its southern shore. We will focus on the Aigio fault, in the city of Aigio. (Right) The Aigio fault is intersected at 760 m by the deep Aigio borehole. The fault is surrounded by two aquifers decoupled from the surface by more than 300 m of clay and radiolarite: the upper fractured limestone aquifer with an overpressure of 0.5 MPa and the karstic lower aquifer, with an overpressure of 0.9 MPa. The difference in pressure implies that the fault is a hydraulic barrier. A pressure transducer has been installed at his wellhead. In addition to the pressure records, we consider the data from a hydrophone set up within the wellhead and from a set of seismometer and dilatometer located on Trizonia Island, some 10 km north to the borehole.

Finally, we propose several interpretations for the pressure drop.

1. The Corinth Rift and the Deep Geophysical LABORatory

The Corinth Rift is one of the most active extensional regions in Europe. This 130 km long, 20 km wide gulf separates continental Greece from Peloponnesus (Fig. 1). Its extension rate reaches locally 1.5 cm/yr, accompanied by large earthquakes like the $M_s=6.2$, June 15th, 1995 Aigio earthquake [6]. This earthquake caused up to 3 cm of surface displacement along the Aigio fault on the south-western shore of the Gulf [7], although the main rupture zone was slightly north to the Gulf, on a shallowly dipping fault.

This suggests that the fault may be creeping. GPS data over 11 years ([8], Fig. 4) show that a horizontal movement of 4 mm/yr has been monitored across the Aigio fault. This is similar to the slip rate along the fault obtained by paleoseismologic studies [9]. This motivated the choice of the Aigio fault as the site of the Deep Geophysical LABORatory project (DGLab).

The 1000 m deep AIG10 borehole intersects the active Aigio fault at 760 m (Fig. 1). The well is cased down to 700 m. Cores and logging images provide a precise description of the formations below the casing. The Aigio fault is smeared by a 1 m thick layer of clayish material that acts as a hydraulic barrier separating two different limestone aquifers [10]. The upper one has an

overpressure equal to 0.5 MPa. Its hydraulic conductivity has been estimated to be 8×10^{-8} m/s through production test [11]. The lower aquifer is an artesian karst, with an overpressure of 0.87 MPa. Its high hydraulic conductivity ($1.3 \pm 0.2 \times 10^{-5}$ m/s) is caused by the cavities of metric size intersected by the borehole.

Its instrumentation was installed in September 2003 (Fig. 1). This includes a high-precision absolute pressure transducer, which operates at a sampling rate of 1/8 Hz with a resolution of 10 Pa. Another major sensor is a hydrophone, sampled at 2.5 kHz, that monitors the local high frequency microseismic activity. The installation was operating from fall 2003 to the end of 2004.

Three months after the installation, the wellhead pressure stabilized to about 0.85 MPa, a value very close to the original lower karstic aquifer overpressure (Fig. S2). As expected from the high permeability and storativity of the karst, the recorded pressure variations reflect the changes in the karstic aquifer.

2. Hydraulic transients triggered by teleseisms

2.1. Recordings of the 2003 Rat Island earthquake

On November 17, 2003, a $M_w=7.8$ earthquake occurred below Rat Island in the Aleutian archipelago, some 10000 km away from the AIG10 borehole. The piezometer gave excellent recordings of the seismic waves (Figs. 2 and 4), superimposed with a 60 Pa drop.

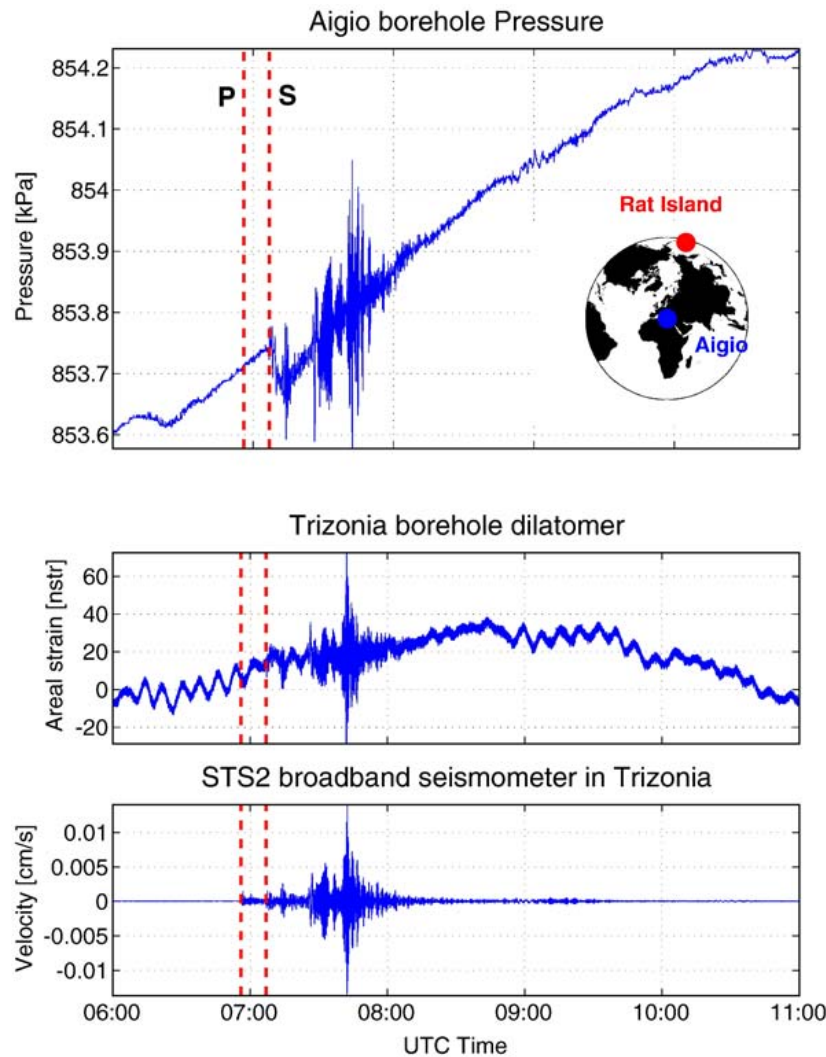


Fig. 2. (Top) The seismic waves generated by the M_w 7.8, November 17th, 2003 Rat Island earthquake are recorded by the pressure transducer of the AIG10 borehole. In addition to the seismic oscillations, a transient pressure drop is visible. The long-term trend is due to tidal variations. Red dashed lines show the arrival time of P and S waves predicted by the program ak135times. (Middle) Recording of the same seismic waves by the borehole dilatometer on Trizonia Island (Fig. 1). Short-term fluctuations induced by the seiches within the Gulf of Corinth are visible. No clear anomaly occurs during the passing of the waves. (Bottom) Recording of the same seismic waves by the broadband seismometer installed on Trizonia Island. (For interpretation of the references to colour in this figure legend, the reader is referred to the web version of this article.)

The drop lasts about 5 min and is followed by a recovery phase about 30 min long. This pressure drop corresponds to a volumetric dilation of 3.5×10^{-9} only.

Complementary information was provided by a STS-2 broadband seismometer and a Sacks–Evertson dilatometer (10^{-10} resolution) located on Trizonia Island, some 10 km to the north of AIG10 borehole (Fig. 1). All sensors record the teleseismic waves but only the AIG10 pressure gauge exhibits a transient.

Fig. 2 shows that the onset of the drop coincides with the arrival of S waves, and not with the passage of the Rayleigh waves as it is usually observed (for instance, all published triggering induced by the Sumatra earthquake occurred with the passing of the Rayleigh

waves [12–14]). This suggests that the environment around the borehole was on the very verge of instability since the small S waves amplitude were able to trigger the hydraulic transient. The amplitude of the areal deformation of the S waves (periods of the order of 30 s) as recorded on the dilatometer is 5×10^{-9} , while the fluid pressure oscillations reach 50 Pa. The particle velocity amplitude is only 0.001 cm/s. The triggered anomaly of Fig. 2 is original by the smallness of its triggering waves, much smaller than the surface waves that usually trigger the seismicity and the hydraulic anomalies so far reported [2].

This pressure transient is coincidental with a sharp signal recorded on the hydrophone located just above

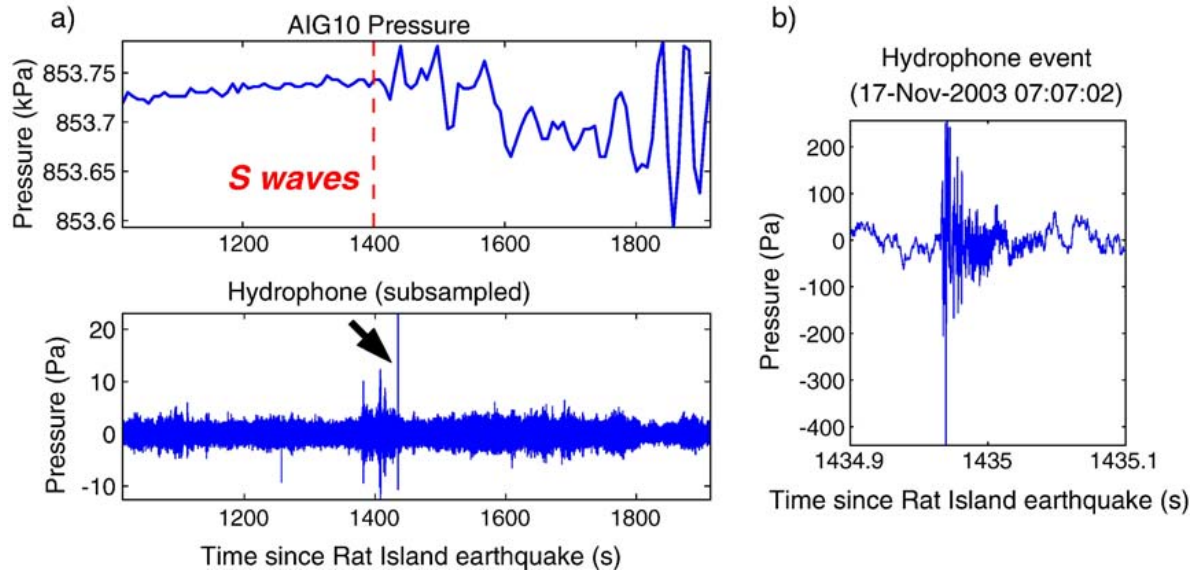


Fig. 3. High frequency event recorded on the hydrophone located at the wellhead of the AIG10 borehole (Fig. 1). The event occurs a few seconds after the first arrival of the S waves and coincides with the onset of the pressure drop. The event duration is only 100 ms long and there are resonant oscillations at 850 Hz.

the well. A zoom of this signal is presented in Fig. 3. It occurs at the beginning of the pressure drop. The signal is quasi-monochromatic with a peak frequency at 850 Hz that possibly corresponds to a resonance of the metallic structure installed at the wellhead. However, similar events have been recorded during the year of operation, most of them being not correlated with a pressure transient. They might be related to the expected creep on the Aigio fault. However, the relationship of the single hydrophone signal with the downhole evolution cannot be assessed. This is regrettable since it is the only complementary anomalous signal observed at that time on the sensors surrounding the piezometer.

2.2. Assessment of signal reliability

We will compare the high frequency pressure oscillations to the dilatometer data to check the good behavior of the sensor. We will also correct the dependence of the hydraulic pressure on external loadings (Earth tides and oceanic load) and check that the drop is not due to a change in these loads.

2.2.1. Recording of seismic oscillations

Seismic waves are obtained by high-pass filtering the data of the pressure gauge p and of the dilatometer data ε_h (Fig. 4). Both data sets are in excellent agreement, as the relationship $p = (-10 \text{ GPa}) \times \varepsilon_h$ holds as long as the Nyquist frequency criterion is satisfied. That means that we consider only periods greater than $2 \times 8 \text{ s} = 16 \text{ s}$. With

seismic velocities of at least 3 km/s, the wavelength of the seismic waves is of at least 48 km. As Trizonia and Aigio are separated by only 10 km, the two sensors record similar seismic waves.

Fig. 4 shows two surprising trends: first, there is a negative sign between the pressure signal and the dilatometer (with a contraction denoted as positive); second, the pressure sensor is also sensitive to shear waves.

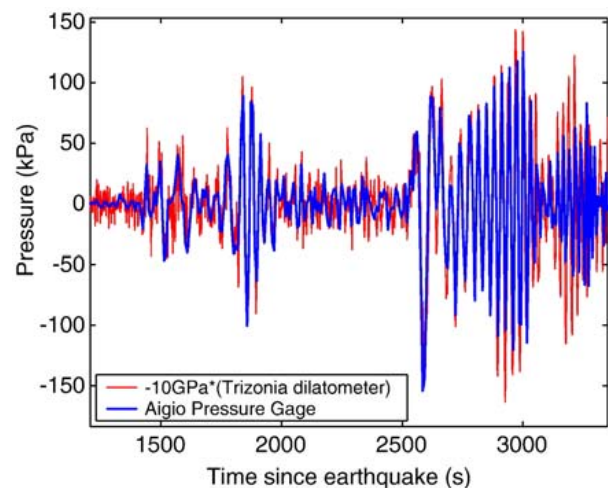


Fig. 4. Comparison of the data from pressure gauge in Aigio and the Sacks–Evertson dilatometer of Trizonia. The dilatometer data has been multiplied by a factor equal to -10 before displaying. Both are high-pass filtered to highlight the seismic waves the sensor felt. The time span shown is when the frequency of the seismic oscillation is below the Nyquist frequency of the pressure transducer, 1/16 Hz.

The opposite sign between the pressure signal at Aigio and the dilatometer in Trizonia is due to the fact that teleseismic waves have a vertical incidence. P waves are compression waves, with compression longitudinal to their propagation direction. Hence the volumetric strain, to which the pressure is sensitive, is dominated by vertical deformation, whereas the borehole dilatometer is only sensitive to the horizontal deformation. The relationship between the two data is:

$$K = \frac{\partial p}{\partial \varepsilon_h} = -3(BK_{ua}) \frac{(1 - 2\nu_{ua})^2}{2\nu_{ut}} \quad (1)$$

where ν_{ut} is the undrained Poisson ratio for Trizonia soil and B , K_{ua} and ν_{ua} are respectively the Skempton coefficient, the undrained bulk modulus and the undrained Poisson ratio of the rock in Aigio. By taking the parameters obtained from the joint analysis of the Earth tides and the oceanic load ($(BK_{ua}) = 17$ GPa, $\nu_{ua} = 0.2$) and assuming $\nu_{ut} = 0.25$, we get a factor $K = -26$ GPa, of the same order of magnitude as the experimental value of -10 GPa. Notice that we did not have to resort to specific ground conditions, as horizontal fractures in [15].

In a pure poroelastic medium, the pressure is sensitive to volumetric strain only and not to shear strain. Is the fact that the pressure sensor records shear waves like S waves due to the presence of fractures that open when they are sheared? Fig. 2 shows that the dilatometer of Trizonia is also sensitive to shear waves. Fig. 4 shows that the Trizonia dilatometer records the same oscillations as the Aigio pressure sensor. Their

sensitivity to the shear waves can therefore be attributed to the P–S conversion at the Earth surface rather than to local effects like fracture compliance to shear stress.

We have checked that the instrument ran correctly during the recording of the pressure drop.

2.2.2. Removal of the external loads

As seen from the tidal analysis, the pressure signal reflects both the ground deformation and the oceanic load. Because of the proximity of the borehole to the seashore (500 m), the last effect accounts for as much as 50% of the tidal oscillations [16].

The sea level of the Gulf of Corinth is affected by stationary waves (seiches) within the Gulf. The Gulf resonates at two major periods: 40 min in the E–W direction and 5 min in the N–S direction. The resonances were excited by wind that day, as the dilatometer data of Fig. 2 shows. Is the observed drop simply a large 5-minute seiche?

We corrected this seiches effect with tide gauge data. First, the tidal variations are removed. The remaining oscillations of the pressure data are supposed to be induced by ocean load. They are then removed by subtracting tide gauge data with a proportionality factor determined by least-square inversion on a test period prior to the Aleutian event (Fig. 5). The seiches are corrected as the amplitude of the 40-minute oscillations is reduced but the observed 5-minute pressure drop remains.

Hence the pressure variation is neither an instrumental artifact, nor an indirect effect of the oceanic loading.

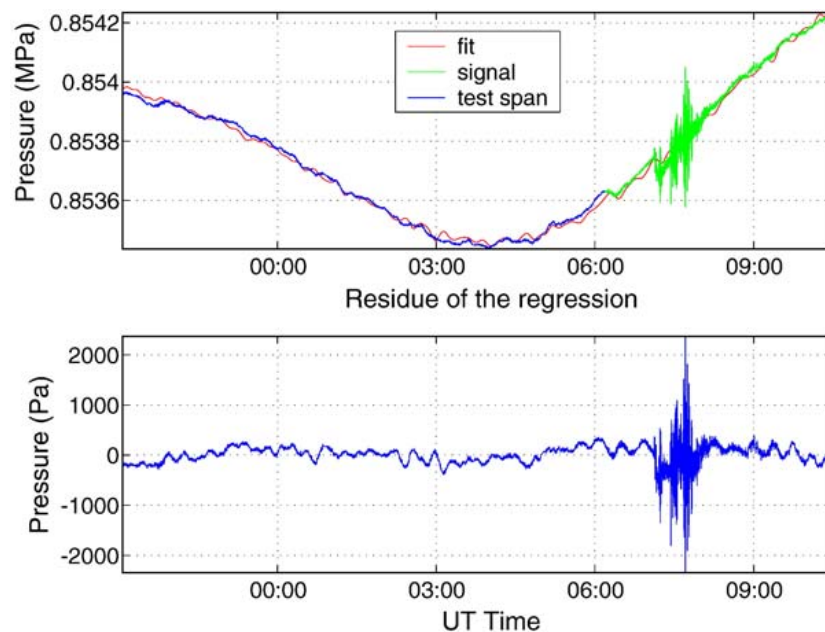


Fig. 5. Removing the effect of earth tides and oceanic loading flattens the long-term signal, and partially reduces the seiches. The anomaly is still clearly visible.

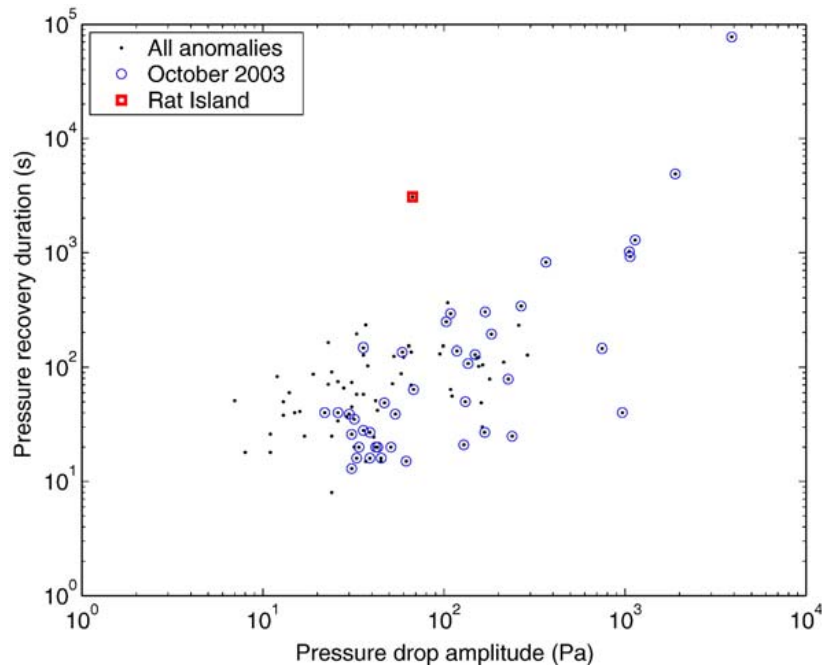


Fig. 6. Comparison of the amplitude of the drop and duration of recovery for hydraulic anomalies recorded in the AIG10 borehole during the year of operation of the instrumentation. The Rat Island drop has much larger duration if one discards the large anomalies that occurred during October 2003.

Something happened near the Aigio borehole. But is it induced by the seismic waves?

2.3. Comparison with other events

Numerous other hydraulic transients have been recorded on site. Is the pressure drop simultaneous with the arrival of the seismic waves by mere chance? To assess this possibility, we compare this transient with the other pressure transients recorded and describe what happened for other teleseismic events.

2.3.1. Other pressure transients

More than 100 short-term hydraulic changes have been recorded during the one year of operation of the pressure sensor. Most of them happened during the first month of recording, with a paroxysmal activity in the beginning of October 2003 (see Fig. S1). If we discard the events recorded at that time, each of the remaining pressure transients recorded has a short duration, with a decay and a recovery of the same duration of 2 min maximum (Fig. 6). By contrast, Fig. 2 shows a decay lasting 5 min and a recovery exceeding 30 min.

Several short pressure transients were recorded in the AIG10 borehole but none like the one of Fig. 2. The pressure drop we recorded is thus not an event which could have occurred at any time, including during the passing of the seismic waves.

2.3.2. Other triggered events

To identify pressure transients induced by seismic waves, we need to be able to separate low frequency pressure transients from high frequency seismic waves. Unfortunately, the sampling frequency is only 8 s, and only large and remote events have seismic waves with frequency low enough for the passing waves not being subsampled.

Among the teleseismic events listed in Table 1, only three events induced seismic waves with amplitude larger

Table 1

List of teleseisms felt by the pressure sensor and the peak-to-peak amplitude of the seismic waves, as recorded by the pressure sensor (only the order of magnitude is given since in most cases, the seismic oscillations are subsampled at the time of the maximum amplitude)

Earthquake	Maximum peak-to-peak amplitude	Triggering?
2003-09-25 Hokkaido $M=8.3$	500 Pa	No hydraulic anomaly
2003-11-17 Rat Island $M=7.8$	500 Pa	Hydraulic anomaly
2003-12-26 Bam $M=6.6$	50 Pa (data missing)	No hydraulic anomaly
2004-05-28 Iran $M=6.3$	150 Pa	No hydraulic anomaly
2004-09-05 Honshu $M=7.2$	200 Pa	No hydraulic anomaly
2004-12-26 Sumatra $M \geq 9$	2000 Pa (data missing)	Hydraulic anomaly

Only two of these events induced a hydraulic anomaly.

than 500 Pa as recorded in the pressure sensor in Aigio. In addition of the Rat Island earthquake, two additional large teleseismic events have been recorded by the permanent borehole instrumentation: the Hokkaido September 25th, 2003 earthquake that did not induce any pressure change, and the December 26th, 2004 Sumatra earthquake that did. Let us observe that the Hokkaido earthquake occurs only 24 h after the installation of the sensor. During the installation, the fault could not be sealed and the karstic aquifer emptied in the upper aquifer. The pressure took three months to stabilize. Only 24 h after the installation, the fluid pressure of each aquifer was still close to its initial values.

Fig. 7 shows the raw pressure record corresponding to the seismic waves of the Sumatra earthquake. The data is spoiled by recording difficulties resulting in an irregular sampling rate and the loss of about half the data. However, a 2-minute data sample around 01:47 UT exhibits oscillations well below the Nyquist frequency. Its mean value is about 50 Pa lower than the mean pressure value observed before the event. This indicates that a pressure drop occurred during the Rayleigh waves. But the precise complete time description of the pressure drop and the recovery period cannot be retrieved. Also, no hydrophone signal was available for this event. We cannot compare further the two triggered events.

That other teleseismic waves are coincidental with a pressure drop supports the hypothesis that the pressure drop is triggered by the seismic waves generated by the Rat Island earthquake.

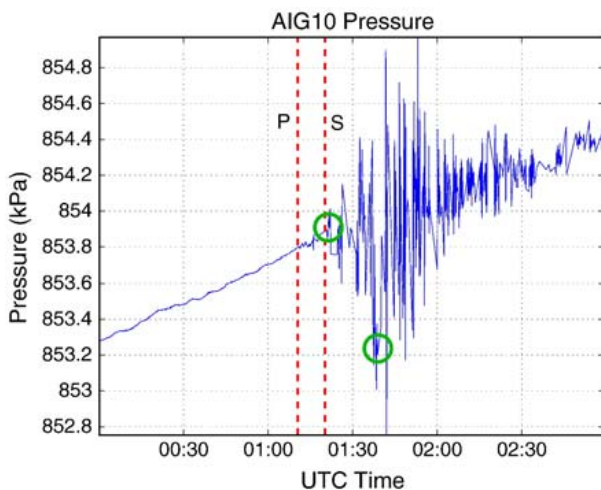


Fig. 7. Record of the pressure response to the seismic waves generated by the December 26th, 2004 Sumatra earthquake. The theoretical P and S waves arrival are denoted by dashed lines. Some samples miss because of acquisition problems but two points seem reliable. They correspond to two 2-minute continuous spans during which the correctly sampled variations are oscillating around a mean value whose coordinates are highlighted by circles. This event thus induced a hydraulic anomaly.

3. Possible mechanisms for the pressure drop

The absence of transients on the Trizonia sensors and the presence of the hydrophone signal hint that the cause of the pressure transient is local to the borehole. Two hypotheses can be formulated: the seismic waves disturbed a possible plug which could have formed inside the borehole during the crisis of October 2003 or the seismic waves disturbed the Aigio fault intersected by the AIG10 borehole.

3.1. A borehole related effect?

In October 2003, the recorded pressure exhibited large drops accompanied by an intense activity on the hydrophone installed at the wellhead (Fig. S1). Did the borehole collapse at that time, and is the transient related to a plug at the fault zone depth where the borehole is the weakest?

Several arguments let us think that the possible plug is not hydraulically significant. If it could clog the well, Fig. 1 shows that a plug at the fault zone would disconnect the surface pressure sensor from the bottom karst (about 0.9 MPa), and the sensor would record the pressure of the upper fractured aquifer (about 0.5 MPa). If the October 2003 crisis had installed an impermeable plug separating the two aquifers, the aquifer tapped by the pressure sensor would be different. But the tidal response of the well is the same before and after the October crisis (Fig. S1). Also after a 3 kPa decrease during the crisis, the pressure became similar to the 0.86 MPa recorded prior to the crisis. This suggests that even if the borehole partly collapsed on October 2003, it is not enough to disturb the hydraulic properties of the well.

Even if we suppose that an impermeable plug exists in the borehole and that we suppose that the seismic waves have disturbed the plug rather than the aquifers or the fault around the borehole, the data do not fit the expected behavior. We would expect the pressure to increase, varying from the low pressure of the fractured aquifer to the higher pressure in the karst. Yet the observed pressure evolution is a drop. We would expect a disturbance of the borehole to be instantaneously felt as the borehole is hydraulically very conducive, whereas the drop lasts 5 min. The slow recovery also suggests that the source is far from the borehole, not right in the borehole.

3.2. A fault related effect?

The Aigio fault is suspected to be creeping and easy to move. Can the pressure transient be due to a slip on

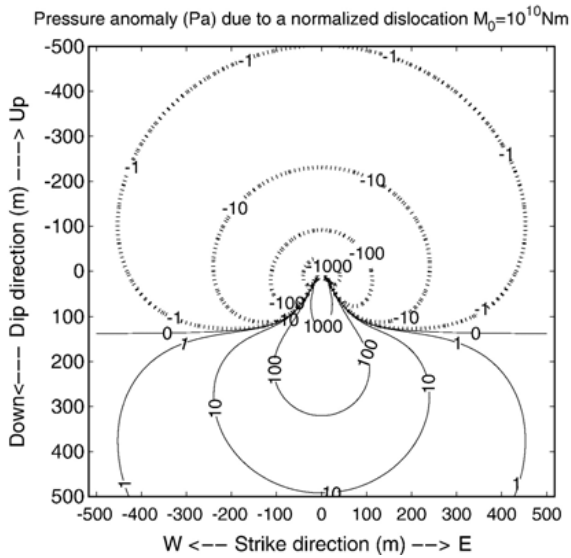


Fig. 8. Pressure induced at the borehole as a function of the slip location on the fault. We used a normalized double couple of moment $M_0=10^{10}$ Nm, occurring on the Aigio fault at (x,y) and parallel to the fault. The hydraulic response is computed as the average of pressure anomalies along the portion of the borehole intersecting the karst (see Appendix). We used a coefficient $-\partial P/\partial \epsilon=BK_u=17$ GPa, determined from tidal analysis, and we assumed that the two Lamé coefficients λ and μ are equal to 10 GPa. The borehole intersects the fault at $(0,0)$. The sign of the induced pressure offset depends on the position of the double-couple along the dip-direction, as explained on the graph.

the fault? A movement on the Aigio fault may induce two measurable effects on pressure record: (1) the undrained response to the coseismic stress changes and (2) the diffusion of the pressure front induced by a sudden disruption of the hydraulic barrier the fault constitutes or by a sudden dilatant damage near the fault.

3.2.1. Coseismic elastic effect

We approximate the slip on the fault by a double couple source of moment M_0 . With radial coordinates (r,θ,ϕ) centered on the dislocation, the pressure disturbance induced around the source is

$$P = BK_u \frac{3M_0 \sin 2\theta \cos \phi}{4\pi r^3 \rho V_p^2} \quad (2)$$

where $BK_u=17$ GPa is the product of the Skempton coefficient and of the undrained bulk modulus and $V_p=5$ km/s is the P wave velocity of the medium.

As the Aigio fault intersects the borehole, the deformation (and hence the pressure change) induced along the borehole is heterogeneous. The pressure measured at the wellhead is shown to be the average over the section of the AIG10 borehole intersecting the

karst of the induced pressure disturbance weighted by permeability along the borehole (see Appendix). As the lower karstic aquifer is extremely permeable, only the disturbances induced below the fault are considered.

Fig. 8 shows that the pressure disturbance generated by a slip with moment $M_0=10^{10}$ Nm (equivalent of a magnitude $M_w=0.6$ or a slip of 1 cm over a surface of $20\text{ m} \times 20\text{ m}$) reaches 60 Pa if the hypocenter is located 100 m away from the center of the borehole. An event of this magnitude is too small to be observed by the sensors located 10 km from the borehole in Trizonia. It is also too large since no sudden coseismic drop was observed on the pressure data.

The fault core has a slipping surface tilted relative to the fault plane by 37° (Fig. 9). As the gouge is 1 m thick, this suggests a slipping plane 1.3 m long. If we suppose that this is the typical dimension of the slipping surface and extrapolate scaling laws of Kanamori and Anderson [17], a typical slip on this surface would have a moment equal to $M_0=10^7$ Nm ($M_w=-1.4$). The coseismic pressure change would then be imperceptible to the pressure sensor.

The smallness of the source is compatible with the large frequencies of the hydrophone signal of Fig. 3. The corner frequency is related to the area of the source S_{source} by $f_c \approx V_s/\sqrt{S_{\text{source}}}$ [18], where V_s is the S wave velocity. Corner frequencies for this event is close to 1 kHz.

However, if the observed pressure transient was only due to the poroelastic response to a slip on the fault, it would be instantaneous, which is not what is observed. This suggests that a slip on the fault should be still smaller, so that the sensor does not feel this poroelastic

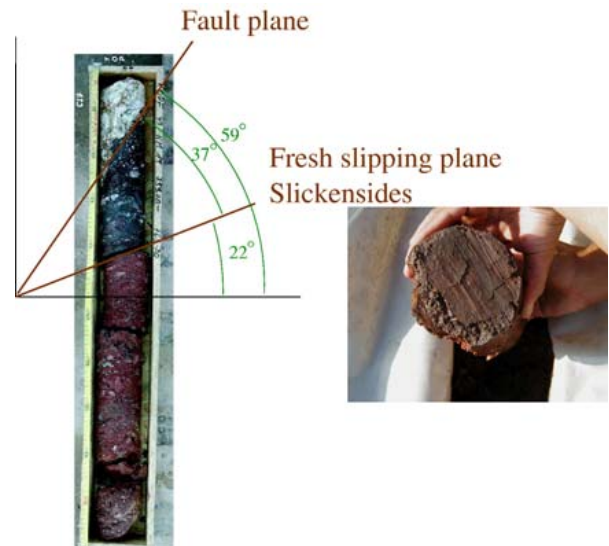


Fig. 9. Photograph of the fault core, exhibiting slickensides tilted to 37° to the plane of the Aigio fault. The box is 1 m long.

response. The signal observed would be an indirect effect.

3.2.2. Sudden removal of fluid from the karst

The long duration of the pressure transient is reminiscent of a diffusive process. For instance, let us consider the Green function in response to a sudden injection of a volume of water V at a distance R [19]. It is given by

$$p(R, t) = \frac{1}{S} \frac{V}{(4\pi Dt)^{3/2}} \exp\left(-\frac{R^2}{4Dt}\right) \quad (3)$$

where D and S are the hydraulic diffusivity and the specific storativity of the medium. This solution predicts a rapid change in pressure followed by a long recovery. This behavior is similar to the pressure drop of Fig. 2.

How can water be removed from the medium? The medium is the karst. A first possibility is that the water has left the karst. The fault acts as a hydraulic barrier separating two aquifers of different pressures. For water to leave the karst, one needs to break this seal. Cores show that slip occurred on a plane tilted relative to the fault plane (Fig. 9). This may help break the hydraulic barrier the fault constitutes. If a movement occurs on such a plane, it could open transiently a path allowing water to leave the karst to the upper aquifer.

Another possibility is that no water quits the karst but that the volume of pores is increased. Dilatancy correlated with damage induced near the fault by the slip on the fault is a possible mechanism for creation of pore volume.

If we suppose that the borehole does not disturb the propagation of the pressure front in the aquifer, the pressure observed in the borehole is the average along the section of the borehole below the fault of the disturbance described by Eq. (3). Supposing that the slip occurred on the fault plane at a distance x_0 from the intersection of the well and the borehole in the down-dip direction and at a distance y_0 in the strike direction, the recorded pressure is modeled as

$$p(t) = \frac{-\left(V \left(\operatorname{Erf}\left(\frac{x_0 \cos(\phi)}{2\sqrt{Dt}}\right) + \operatorname{Erf}\left(\frac{H-x_0 \cos(\phi)}{2\sqrt{Dt}}\right) \right)\right)}{8DH\pi St} \times \exp\left(-\frac{x_0^2(1-\cos(2\phi)) + 2y_0^2}{8Dt}\right). \quad (4)$$

$\phi = 30^\circ$ is the angle between the borehole and the fault plane and $H = 230$ m is the length of the portion of the borehole penetrating the karst. Erf is the error function. The unknown parameters in this equation are the removed volume V and the position of the slip on the fault (x_0, y_0) . Although tidal analysis provides a diffusivity

value $D = 20 \text{ m}^2/\text{s}$, the heterogeneous structure of the karst casts doubt on its applicability at smaller scale, and the diffusivity is also considered as unknown.

Eq. (4) gives a very satisfactory fit of the observed pressure drop (Fig. 10). The number of unknowns (3, if we impose x_0) exceeds the number of observations (2, ie the amplitude of the drop and its duration). It is thus not surprising that two very different sets of parameters fit similarly the results.

From the response of the well to the earth tides, the diffusivity of the karst was assessed to be $D \sim 20 \text{ m}^2/\text{s}$. This constrains the injection of 1.7 m^3 at a distance of 350 m. The sudden passage of such a volume through the fault is improbable.

The karst is a very heterogeneous formation. At a smaller scale, the karst is better approximated as a double porosity medium, with very conductive conduits penetrating a less permeable matrix. The conduits can be seen as an extension of the borehole and are supposed to have the same homogenized pressure. The diffusion is limited by the diffusivity of the matrix. Eq. (4) should be altered to take into account the volume of the conduits but our ignorance of the karst geometry hampers this refinement. To keep Eq. (4), we suppose that the volume of the conduits is negligible. The fit of the pressure drop is then possible with much smaller removed volume. For instance, the data are compatible with the sudden injection of $1.5 \times 10^{-3} \text{ m}^3$ at a distance of 20 m with a diffusivity of $D = 0.05 \text{ m}^2/\text{s}$. Smaller volumes could be attained by further reducing D . With a distance of 20 m, Fig. 8 shows that the minimum magnitude that cannot

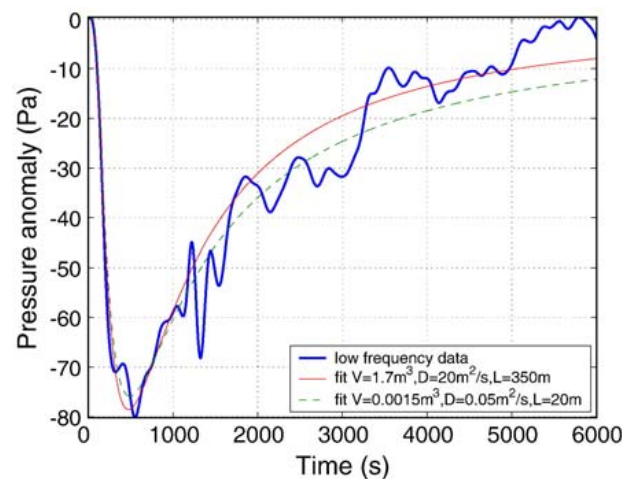


Fig. 10. The pressure data are low-passed and detrended. The pressure drop is fitted with a model in which a volume V of fluid is suddenly removed from the medium at a distance L . The karst is an aquifer with two porosities: the large cavities of the karst with a high hydraulic diffusivity $D = 20 \text{ m}^2/\text{s}$, and the porous matrix with a smaller hydraulic diffusivity $D = 0.05 \text{ m}^2/\text{s}$. Both cases are considered.

generate any coseismic step in pressure (less than the resolution of the sensor of 10 Pa) is only $M_0 = 10^7$ Nm ($M_w = -2$).

We conclude that the pressure drop can be modeled by dilatant damage or by the removal of fluid from the karst induced by the disruption of the hydraulic barrier the fault constitutes.

4. Conclusion

The 2003 Rat Island earthquake induced a transitory pressure drop in a well intersecting an active fault of the Corinth Rift, more than 10 000 km away. This transient of 60 Pa is to our knowledge the smallest recorded pressure anomaly triggered by the seismic waves generated by a teleseism. It is also one of the earliest, as it occurs during the passage of the S waves, which to our knowledge has not been observed before. That S waves trigger the hydraulic transient is surprising since they have also much smaller amplitude than Rayleigh waves. This suggests that the system was on the verge of instability.

Although we lack complementary data to constrain the mechanism of the observed transient, a simultaneous high frequency event on the hydrophone installed at the wellhead suggests that the Aigio fault intersected at the borehole has slipped but with a magnitude less than -2 . The pressure transient can be explained as dilatant damage or as a transient disruption of the hydraulic barrier the fault constitutes. To confirm this speculation, a complete set of sensor including several pressure transducers and hydrophones is to be installed in the well.

If confirmed, the speculated mechanism implies that the hydraulic properties of a fault can dramatically change during its slip. If the slip occurs on a structure nonparallel to the fault plane, fluid can escape very easily and prevent pressure buildup inside the fault during slip weakening mechanisms like fluid pressurization. If the slip induced dilatant damage, it would also reduce pore pressure and prevent pressurization.

Acknowledgments

We are deeply grateful to Emily Brodsky for her support and numerous fruitful discussions. We also thank Steve Hickman for his helpful suggestions. We thank an anonymous reviewer for his comments that helped to substantially improve the manuscript. The CRL development benefited from the support from the Energy Environment and Sustainable Development program of the European Commission (in particular

contract no. EVR1-CT-2000-40005) and from the French CNRS (GDR-Corinth).

Appendix A. From an heterogeneous pressure field along the borehole to the wellhead pressure

Let suppose that the hydraulic anomaly of Fig. 2 is induced by a slip on the Aigio fault. The proximity of the borehole to the source raises a new problem: Eq. (4) predicts a heterogeneous pressure change along the borehole, whereas we record a single data for all the open section of AIG10.

The pressure within the well is uniform, equal to P_b . This pressure varies due to fluid exchange dV at the wall of the borehole. Its sensitivity depends on the compressibility of the fluid K_f and the volume V_b of the well:

$$dP_b = \frac{K_f}{V_b} dV \quad (\text{A.1})$$

The incoming flux is supposed to be purely radial, so that:

$$dV = \int_{\text{open section}} 2\pi r_b \frac{C(z)}{\rho g} \frac{\partial P(r, z)}{\partial r} dz dt \quad (\text{A.2})$$

where $P(r, z)$ is the pressure in the rock expressed in cylindrical coordinates.

The hydraulic conductivity C is linked to the permeability k by the relationship $C = \frac{\rho_f g}{\eta} k$ where ρ_f and η are the density and the dynamic viscosity of water and g is the gravity acceleration.

The pressure gradient is unknown and depends on time. For instance, if there is a sudden step in pressure in the medium surrounding the borehole, homogenization by diffusion will taper pressure discontinuity and the slope will slowly decay with time whereas a pressure front will extend. A problem arises from the absence of a characteristic distance. A typical way to solve the problem is to introduce a “skin” length, for instance the thickness of the mud cake layering the walls of the borehole after drilling. This case is implemented in the hydrological modeling software MODFLOW through the MNW module [20]. However, the intense flow experienced by the borehole during the installation of the sensor flushed this mud cake, and we have to tackle the problem differently.

Let suppose that the exponential profile can be approximated by $\frac{\partial P}{\partial r} = \frac{P(z) - P_b}{\sqrt{\kappa(z) t}}$ where $\kappa(z)$ is the local diffusivity and $P(z)$ the expected pressure along the borehole, as determined from Eq. (3). This supposes that

(1) the pressure front $\sqrt{\kappa(z)t}$, dependent on the local hydraulic diffusivity $\kappa(z)$, is small compared to the variation wavelength of $P(r,z)$, (2) and the lateral diffusion is predominant to the vertical diffusion in the medium. Combining Eqs. (A.1) and (A.2) gives the relationship of pressure in the borehole to the pressure field in the surrounding medium:

$$\begin{aligned} \frac{\partial P_b}{\partial t} &= \frac{2\pi r_b K_f}{\rho g V_b} \int_{\text{open section}} C(z) \frac{P(z) - P_b}{\sqrt{\kappa(z)t}} dz \\ &= \frac{2\pi r_b K_f}{\rho g V_b} \frac{F}{\sqrt{t}} (P_\infty - P_b) \end{aligned} \quad (\text{A.3})$$

with the two constants:

$$F = \int_{\text{open section}} \frac{C(z)}{\sqrt{\kappa(z)}} dz = \int \sqrt{C(z)S(z)} dz \quad (\text{A.4})$$

$$P_\infty = \frac{\int \sqrt{C(z)S(z)} P(z) dz}{\int \sqrt{C(z)S(z)} dz} \quad (\text{A.5})$$

$\kappa(z) = C(z)/S(z)$, where $S(z)$ is the storativity in m^{-1} . P_∞ is a weighted average of the pressure along the borehole. It crosses two different aquifers. F is estimated with the poroelastic parameters determined by tidal analysis [16]. Using the storativity of the upper aquifer of Giurgea et al. [11] $S_u = 10^{-4} \text{ m}^{-1}$, the upper aquifer is found to contribute to 18% to F . This value reduces to 1.5% with a more reasonable value compatible with the expectation of poroelastic theory $S_u = \rho g \phi / K_f \sim 10^{-7} - 10^{-6} \text{ m}^{-1}$. We will retain this choice. The karstic lower aquifer dominates the hydraulic setting of the AIG10 borehole, and F is approximated as $F \approx \sqrt{C_1 S_1 H_1} \sim 8.510^{-4} \text{ m/s}^{1/2}$, where $C_1 = 1.5 \cdot 10^{-5} \text{ m/s}$, $S_1 = 8.4 \cdot 10^{-7} \text{ m}^{-1}$ and $H_1 = 240 \text{ m}$ are respectively the hydraulic conductivity, the storativity and the thickness intersected by the borehole of the lower aquifer.

The solution of the differential Eq. (A.3) is given as:

$$P_b(t) = P_\infty + (P_0 - P_\infty) e^{-2\sqrt{\frac{t}{\tau}}} \quad (\text{A.6})$$

with the characteristic time $\tau = \left(\frac{\rho g V_b}{2\pi r_b K_f F} \right)^2$. The volume of the borehole equals $\pi r_b^2 H_b \approx 22 \text{ m}^3$, since its radius is $r_b \approx 0.17/2 \text{ m}$ and its depth is $H_b = 1000 \text{ m}$. As $K_f \approx 2.2 \text{ GPa}$, $\tau \sim 120 \text{ ms}$. This delay is much smaller than the sampling rate of our high-precision sensor (1/8 Hz), so that the pressure gauge directly measures P_∞ . Note that the

diffusion front will be of 3 mm to 11 cm for the upper aquifer, and of 1.2 m for the lower aquifer. In the last case, we are at the limit of our hypothesis (1) if the dislocation is close to the borehole, inducing a very heterogeneous disturbed pressure field, since $P(\sqrt{D_1 t}, z)$ will differ from $P(0, z)$. However, in that case, the karst structure will render inadequate Eq. (4), which supposes a homogeneous medium. Moreover, the dislocation geometry should be also taken into account.

In conclusion, the pressure recorded by our sensor is equal to the weighted average pressure given by Eq. (A.5). It is dominated by the lower karstic aquifer. Because of our poor knowledge of the network of the karstic conduits, we cannot describe better this aquifer than as a homogeneous porous medium. Our result only gives an order of magnitude for slips on the faults very close to the borehole.

Appendix B. Supplementary data

Supplementary data associated with this article can be found, in the online version, at [doi:10.1016/j.epsl.2007.03.036](https://doi.org/10.1016/j.epsl.2007.03.036).

References

- [1] R. Coble, The effects of Alaskan earthquake of March 27, 1964, on ground water in Iowa, Proc. Iowa Acad. Sci. 72 (1965) 323–332.
- [2] D. Montgomery, M. Manga, Streamflow and water well response to earthquake, Science 300 (June 2003) 2047–2049.
- [3] E. Brodsky, E. Roeloffs, D. Woodcock, I. Gall, A mechanism for sustained groundwater pressure changes induced by distant earthquakes, J. Geophys. Res. 108 (B8) (August 2003), [doi:10.1029/2003GL018485](https://doi.org/10.1029/2003GL018485).
- [4] J.E. Elkhoury, E.E. Brodsky, D.C. Agnew, Seismic waves increase permeability, Nature 441 (2006) 1135–1138.
- [5] E. Brodsky, S. Prejean, New constraints on mechanisms of remotely triggered seismicity at Long Valley Caldera, J. Geophys. Res. 110 (B4) (2005), [doi:10.1029/2004JB00321](https://doi.org/10.1029/2004JB00321).
- [6] P. Bernard, P. Briole, B. Meyer, H. Lyon-Caen, J.-M. Gomez, C. Tiberi, C. Berge, R. Catin, D. Hatzfeld, C. Lachet, B. Lebrun, A. Deschamps, F. Courboulex, C. Laroque, A. Rigo, D. Massonet, P. Papadimitriou, J. Kassaras, D. Diagourtas, K. Makropoulos, G. Veis, E. Papazisi, C. Mitsakaki, V. Karakostas, P. Papadimitriou, D. Papanastassiou, G. Chouliaras, G. Stavrakakis, The $M_s = 6.2$, June 15, 1995 Aigion earthquake (Greece): evidence for low angle normal faulting in the Corinth Rift, J. Seismol. 1 (1997) 131–150.
- [7] I. Koukouvelas, The Egion fault earthquake-related and long-term deformation, Gulf of Corinth, Greece, J. Geodyn. 26 (2–4) (1998) 501–513.
- [8] A. Avallone, P. Briole, A. Agatza-Balodimou, H. Billiri, O. Charade, C. Mitsakaki, A. Nercessian, K. Papazissi, D. Paradissis, G. Veis, Analysis of eleven years of deformation measured by GPS in the Corinth Rift Laboratory area, C. R. Geosci. 336 (4–5) (March 2004) 301–311.

- [9] D. Pantosti, P.M. De Martini, I. Koukouvelas, L. Stamatopoulos, N. Palyvos, S. Pucci, F. Lemeille, S. Pavlides, Paleoseismological investigations of the Aigion fault (Gulf of Corinth, Greece), *C. R. Géosci.* 336 (4–5) (2004) 335–342.
- [10] F.H. Cornet, M.L. Doan, I. Moretti, G. Borm, Drilling through the active Aigion fault: the AIG10 well observatory, *C. R. Géosci.* 336 (4–5) (2004) 395–406.
- [11] V. Giurgea, D. Rettenmaier, L. Pizzino, I. Unkel, H. Hötzl, A. Förster, F. Quattrocchi, Preliminary hydrogeological interpretation of the Aigion area from the AIG10 borehole data, *C. R. Géosci.* 336 (4–5) (2004) 467–475.
- [12] M. West, J. Sánchez, S. McNutt, Periodically triggered seismicity at Mount Wrangell, Alaska, after the Sumatra earthquake, *Science* 308 (2005) 1144–1146.
- [13] S. Sil, J.T. Freymueller, Well water level changes in Fairbanks, Alaska, due to the great Sumatra–Andaman earthquake, *Earth Planets Space* 58 (2) (2006) 181–184.
- [14] M. Miyazawa, J. Mori, Evidence suggesting fluid flow beneath Japan due to periodic seismic triggering from the 2004 Sumatra–Andaman earthquake, *Geophys. Res. Lett.* 33 (2006) L05303, doi:10.1029/2005GL025087.
- [15] S. Hurwitz, M.J. Johnston, Groundwater level changes in a deep well in response to an intrusion event on Kilauea volcano, Hawai'i, *Geophys. Res. Lett.* 30 (22) (2003), doi:10.1029/2003GL018676.
- [16] Doan, M., 2005. Étude in-situ des interactions hydromécaniques entre fluides et failles actives — application au Laboratoire du Rift de Corinthe. PhD Thesis, Institut de Physique du Globe de Paris.
- [17] H. Kanamori, D.L. Anderson, Theoretical basis of some empirical relations in seismology, *Bull. Seismol. Soc. Am.* 65 (5) (1975) 1073–1095.
- [18] R.E. Abercrombie, Earthquake source scaling relationships from -1 to $5 M_L$ using seismograms recorded at 2.5-km depth, *J. Geophys. Res.* 100 (B2) (1995) 24015–24036.
- [19] H.F. Wang, *Theory of Linear Poroelasticity with Applications to Geomechanics and Hydrogeology*, Princeton Series in Geophysics, Princeton University Press, Princeton, NJ, 2000.
- [20] Halford, K., Hanson, R., 2002. User guide for the drawdown-limited, multinode well (MNW) package for the U.S. Geological Survey's modular three-dimensional finite-difference groundwater flow model, versions MODFLOW-96 and MODFLOW-2000. Tech. Rep. 02-293, U.S. Geological Survey.

Present-day principal horizontal stress orientations in the Kumano forearc basin of the southwest Japan subduction zone determined from IODP NanTroSEIZE drilling Site C0009

Weiren Lin,¹ Mai-Linh Doan,² J. Casey Moore,³ Lisa McNeill,⁴ Timothy B. Byrne,⁵ Takatoshi Ito,⁶ Demian Saffer,⁷ Marianne Conin,⁸ Masataka Kinoshita,⁹ Yoshinori Sanada,¹⁰ Kyaw Thu Moe,¹⁰ Eiichiro Araki,⁹ Harold Tobin,¹¹ David Boutt,¹² Yasuyuki Kano,¹³ Nicholas W. Hayman,¹⁴ Peter Flemings,¹⁴ Gary J. Huftile,¹⁵ Deniz Cukur,¹⁶ Christophe Buret,¹⁷ Anja M. Schleicher,¹⁸ Natalia Efimenko,¹⁹ Kuniyo Kawabata,²⁰ David M. Buchs,²¹ Shijun Jiang,²² Koji Kameo,²³ Keika Horiguchi,²⁴ Thomas Wiersberg,²⁵ Achim Kopf,²⁶ Kazuya Kitada,⁹ Nobuhisa Eguchi,¹⁰ Sean Toczko,¹⁰ Kyoma Takahashi,¹⁰ and Yukari Kido¹⁰

Received 6 March 2010; revised 7 May 2010; accepted 12 May 2010; published 2 July 2010.

[1] A 1.6 km riser borehole was drilled at site C0009 of the NanTroSEIZE, in the center of the Kumano forearc basin, as a landward extension of previous drilling in the southwest Japan Nankai subduction zone. We determined principal horizontal stress orientations from analyses of borehole breakouts and drilling-induced tensile fractures by using wireline logging formation microresistivity images and caliper data. The maximum horizontal stress orientation at C0009 is approximately parallel to the convergence vector between the Philippine Sea plate and Japan, showing a slight difference with the stress orientation which is perpendicular to the plate boundary at previous NanTroSEIZE sites C0001, C0004 and C0006 but orthogonal to the stress orientation at site C0002, which is also in the Kumano forearc basin. These data show that horizontal stress orientations are not uniform in the forearc basin within the surveyed depth range and suggest that oblique plate motion is being partitioned into strike-slip and thrusting. In addition, the

stress orientations at site C0009 rotate clockwise from basin sediments into the underlying accretionary prism. **Citation:** Lin, W., et al. (2010), Present-day principal horizontal stress orientations in the Kumano forearc basin of the southwest Japan subduction zone determined from IODP NanTroSEIZE drilling Site C0009, *Geophys. Res. Lett.*, 37, L13303, doi:10.1029/2010GL043158.

1. Introduction

[2] The Nankai Trough Seismogenic Zone Experiment (NanTroSEIZE), a comprehensive scientific drilling project conducted by the Integrated Ocean Drilling Program (IODP), began in 2007 in the Nankai subduction zone, southwest Japan, where M8-class great earthquakes repeat at intervals of 100–200 years as a result of the convergence of the Philippine Sea and Eurasian plates. Establishing the in situ stress state along active subduction zones is critical for understanding the accumulation and release of most of Earth's seismic energy [Lallemand and Funicello, 2009]. Determi-

¹Kochi Institute for Core Sample Research, JAMSTEC, Nankoku, Japan.

²Laboratoire de Géophysique et Tectonophysique, Université Grenoble 1 (Joseph Fourier), Grenoble, France.

³Earth and Planetary Sciences Department, University of California, Santa Cruz, California, USA.

⁴National Oceanography Centre, Southampton, University of Southampton, Southampton, UK.

⁵Center for Integrative Geosciences, University of Connecticut, Storrs, Connecticut, USA.

⁶Institute of Fluid Science, Tohoku University, Sendai, Japan.

⁷Geosciences, Pennsylvania State University, University Park, Pennsylvania, USA.

⁸CEREGE, University Aix Marseille III, Aix-en-Provence, France.

⁹Institute for Research on Earth Evolution, JAMSTEC, Yokosuka, Japan.

¹⁰Center for Deep Earth Exploration, JAMSTEC, Yokohama, Japan.

¹¹Department of Geoscience, University of Wisconsin-Madison, Madison, Wisconsin, USA.

¹²Department of Geosciences, University of Massachusetts Amherst, Amherst, Massachusetts, USA.

¹³Research Center for Earthquake Prediction, Disaster Prevention Research Institute, Kyoto University, Uji, Japan.

¹⁴Institute for Geophysics, Jackson School of Geosciences, University of Texas at Austin, Austin, Texas, USA.

¹⁵Biogeosciences Discipline, Queensland University of Technology, Brisbane, Queensland, Australia.

¹⁶Leibniz Institute of Marine Sciences at Kiel University (IFM-GEOMAR), Kiel, Germany.

¹⁷Département de Géologie, Université de Picardie Jules Verne, Amiens, France.

¹⁸Department of Geological Sciences, University of Michigan, Ann Arbor, Michigan, USA.

¹⁹Institut de Géologie et de Paléontologie, Université de Lausanne, Lausanne-Dorigny, Switzerland.

²⁰Institute of Geophysics, National Central University, Taoyuan, Taiwan.

²¹Research School of Earth Sciences, The Australian National University, Canberra, ACT, Australia.

²²Geological Sciences, Florida State University, Tallahassee, Florida, USA.

²³Department of Earth Sciences, Chiba University, Chiba, Japan.

²⁴Department of Earth and Space Sciences, Osaka University, Toyonaka, Japan.

²⁵Section 4.2, GFZ German Research Center for Geosciences, Potsdam, Germany.

²⁶Marum Research Centre, University of Bremen, Bremen, Germany.

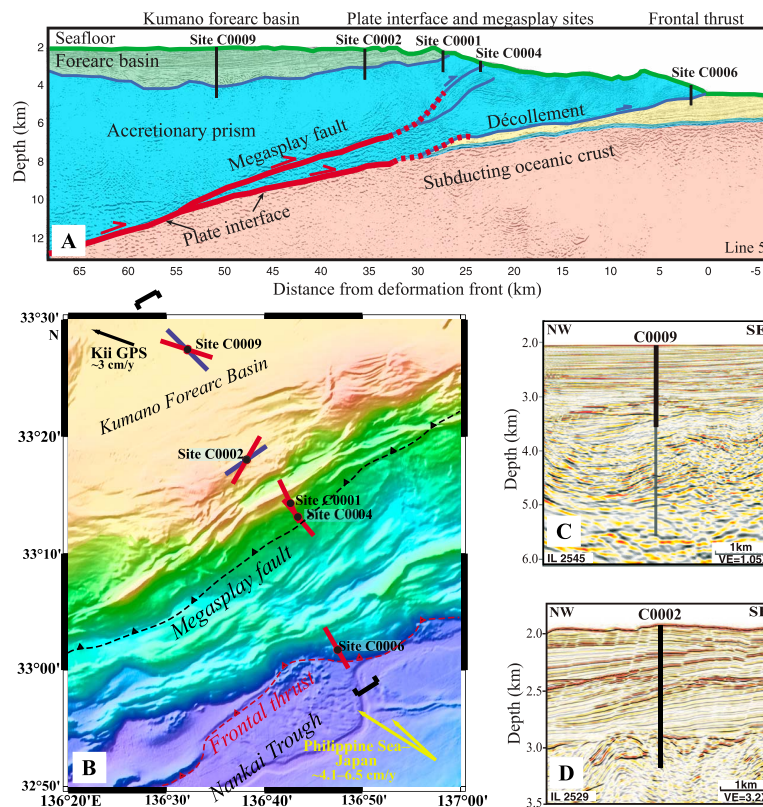


Figure 1. Location and setting of NanTroSEIZE site C0009. (a) Locations of NanTroSEIZE drilling sites and structure of the Nankai subduction zone. Seismic reflection section is after *Park et al.* [2002]. (b) Bathymetric map of the drilling sites and their maximum principal horizontal stress (S_{Hmax}) orientations. Bars at the drilling sites show the S_{Hmax} orientations in boreholes. Blue bars show stress orientations in the accretionary prism below 1285 mbsf at C0009 and below 936 mbsf at C0002 [*Tobin et al.*, 2009]. Dashed lines show megasplay fault and frontal thrust [*Moore et al.*, 2007]. Brackets show location of the cross-section in Figure 1a. Yellow arrows show the far-field convergence vectors between the Philippine Sea plate and Japan [*Heki and Miyazaki*, 2001]; black arrow shows far-field plate motion vector based on geodetic results [*Heki and Miyazaki*, 2001]. (c) Seismic reflection profile through site C0009. The wider line shows interval drilled in 2009, and the narrow line shows planned future drilling. (d) Seismic reflection profile through site C0002. The seismic profiles of Figures 1c and 1d are after *Araki et al.* [2009].

nation of in situ stress is one of the most important scientific objectives of NanTroSEIZE, and also one of the major goals of the IODP as the seismogenic parts of plate margins are often only accessible through drilling.

[3] More than 10 vertical boreholes have been drilled to date along the NanTroSEIZE transect, which is approximately orthogonal to the Nankai Trough axis (plate boundary). In the first stage of NanTroSEIZE (2007–2008), stress orientations were determined from drilling-induced compressive failures (breakouts) and drilling-induced tensile fractures (DITFs) observed in borehole wall images obtained by logging while drilling (LWD) technology [e.g., *Tobin et al.*, 2009; *Chang et al.*, 2009]. This stage involved four drilling sites in which LWD was performed: the initial faulting (frontal thrust) site C0006 at the toe of the accretionary prism, the megasplay sites C0004 and C0001, and site C0002 in the southeastern part of the Kumano forearc basin (Figure 1). In addition, *Byrne et al.* [2009] applied the anelastic strain recovery (ASR) technique to drill-core samples to constrain three-dimensional stress orientations. These consistent results showed that the maximum principal horizontal stress (S_{Hmax}) orientations at sites C0006, C0004,

and C0001 are generally orthogonal to the plate boundary. However, at site C0002, located at the shelf break, these same methods showed that the S_{Hmax} orientation is approximately parallel to the plate boundary. This result is also consistent with seismic reflection profiles and core-scale fault data [*Byrne et al.*, 2009]. Thus, it is of great interest to know the stress orientation farther landward along the NanTroSEIZE transect (northwest of site C0002) in the basin.

[4] During IODP Expedition 319 in the second stage of NanTroSEIZE, D/V *Chikyu* carried out borehole drilling at site C0009, above the asperity of the 1944 Tonankai M8.1 earthquake in the Nankai subduction zone. The borehole penetrated the Kumano basin sediments and the underlying accretionary prism. In a depth range from approximately 700 mbsf (meters below seafloor) to the target depth of 1600 mbsf, wireline logging was carried out including caliper, the Fullbore Formation MicroImager (FMI) borehole resistivity images and porosity, P and S wave velocities, resistivity [*Saffer et al.*, 2009]. We used the borehole images and caliper data to identify DITFs and breakouts that could be interpreted in terms of principal horizontal stress

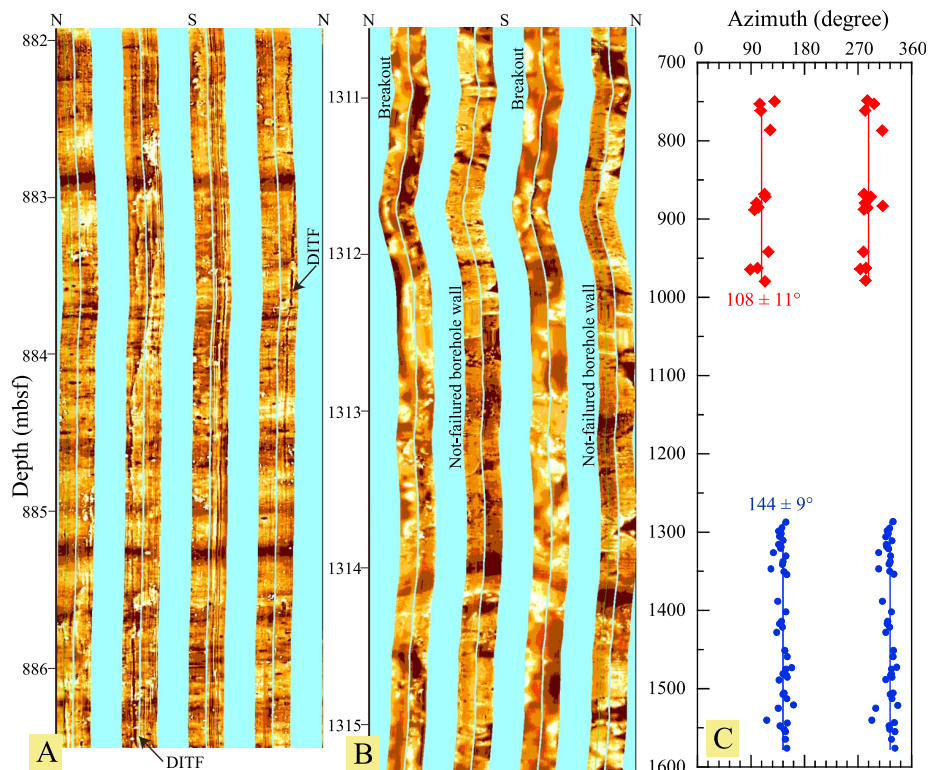


Figure 2. Borehole wall images and S_{Hmax} orientations at site C0009. (a) Electrical images of borehole walls around 884 mbsf showing drilling-induced tensile fractures (DITFs). Blank regions between columns are unimaged portions of the borehole wall between the FMI arms. (b) Electrical image around 1313 mbsf showing breakouts. (c) S_{Hmax} azimuthal distribution determined from DITFs (diamonds) and breakouts (circles). Vertical lines show the average azimuths, and numbers show the average azimuth values and their standard deviations.

orientations [Zoback *et al.*, 2003; McNeill *et al.*, 2004; Lin *et al.*, 2007].

2. Wireline Logging

[5] A deep borehole was drilled at site C0009 from the seafloor, at 2054 m water depth, to approximately 700 mbsf by traditional riserless drilling and from 700 mbsf to the target depth of 1600 mbsf by riser drilling, which was the first successful application of this technique in scientific ocean drilling. From 0 mbsf to 1285 mbsf the borehole crossed the basin and possible slope deposits of the early prism (lithologic units I–III), and from 1285 mbsf to total depth at 1600 mbsf (Unit IV) within underlying early accretionary prism sediments or slope deposits [Saffer *et al.*, 2009].

[6] Immediately after drilling reached the target depth, two runs of wireline logging were conducted from approximately 700 mbsf to 1600 mbsf. The first run included a two-arm caliper and a six-arm caliper, however, without azimuth data for the caliper arms. The second wireline logging run had azimuth information and included FMI. The FMI tool has four arms at 90° angles; an arm with a pad and a flap takes one column of FMI image (Figures 2a and 2b). Because the 12.25-inch (approximately 31 cm) drilling bit was large in comparison to the available pad-flap size, the FMI images covered only about 50% of the borehole walls (Figures 2a and 2b). The two pairs of FMI arms at the same azimuthal position with the pads also measured the borehole

diameter in two orthogonal directions, serving as a four-arm caliper tool.

[7] Because both breakouts and DITFs are dependent on in situ stress conditions, we can use information on their azimuth to determine orientations of in situ principal stresses in the plane perpendicular to the borehole axis. As breakouts and DITFs are both formed during or shortly after drilling, they are records of the present-day stress state. The borehole FMI images enable both the breakouts and DITFs to be identified and the horizontal stress orientations to be determined. In principle, the width (span) of breakouts can constrain the S_{Hmax} magnitude on the basis of the minimum principal horizontal stress (S_{Hmin}) magnitude and rock compressive strength. This was difficult in practice at site C0009 because breakout width data were poorly resolved owing to the relatively poor coverage of FMI images. Usually, one pair of caliper arms stops at breakouts (elongations) because their spring forces them open wider into the breakout, therefore it is possible to determine the azimuths of breakouts from caliper data, but this is not possible for DITF data because the tensile fractures are narrower than the caliper arms. At site C0009, FMI images are a crucial supplement to caliper data, providing direct and visual evidence to characterize breakouts.

3. FMI Image Analyses for DITFs and Breakouts

[8] Over approximately 900 m of the C0009 borehole, several DITFs and many breakouts were recognized in the

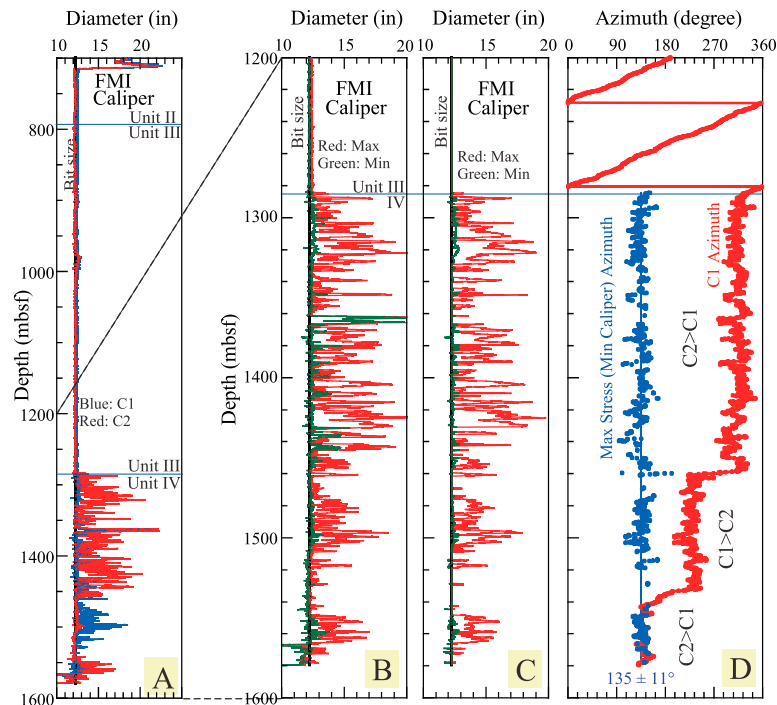


Figure 3. Caliper records from site C0009. (a) Borehole diameters determined by FMI calipers for the whole surveyed depth range. FMI calipers measure two diameters in orthogonal directions, labeled C1 and C2, every 6 inches (approximately 15 cm). Profiles in Figures 3b through 3d correspond to this profile from 1200 to 1600 mbsf. (b) Raw FMI caliper data in terms of maximum and minimum diameters. (c) Selected FMI caliper data meeting the three quality criteria given in the text. (d) C1 azimuth (red dots and line) of FMI caliper and S_{Hmax} azimuth (blue dots) determined from the selected data shown in Figure 3c. The average value and standard deviation of the S_{Hmax} azimuth is $N135^{\circ}E \pm 11^{\circ}$.

FMI images (Figures 2a and 2b). The DITFs occurred in a depth range of 749–980 mbsf (forearc basin sediments and slope deposits of Pleistocene and Pliocene age, Unit II–III [Saffer *et al.*, 2009]), and the breakouts occurred in the depth range of 1288–1578 mbsf (possible accretionary prism or slope deposits, late Miocene, Unit IV). The boundary between Unit III and IV was defined by an unconformity (UC3), at 1285 mbsf, where an age gap of approximately 1.8 Ma was recognized [Saffer *et al.*, 2009]. Between 980 and 1285 mbsf (early forearc basin sediments or slope deposits, Pliocene, Unit III), neither DITF nor breakouts were found (Figure 2c). Breakouts or DITFs, if present, should be found in pairs on opposite sides of the borehole wall (180° apart), if the rock strength around the borehole are almost uniform (homogeneous lithology). DITFs should also be perpendicular to the borehole wall, hence very straight. These characteristics were valuable in distinguishing breakouts and DITFs from other borehole wall failures such as washouts and pre-existing structural fractures. Furthermore, we distinguished breakouts as being wider than fractures and without the sharp, straight boundaries of tensile fractures. Using these criteria, we recorded the azimuth data of breakouts and DITFs from the FMI images and plotted the S_{Hmax} azimuth (Figure 2c). Our analysis of DITFs and breakouts in the FMI images yielded average S_{Hmax} azimuths and its standard deviation of approximately $N108^{\circ}E \pm 11^{\circ}$ in the shallower depth range (749–980 mbsf, determined from 14 DITFs) and $N144^{\circ}E \pm 9^{\circ}$ in the deeper range (1288–

1578 mbsf, 42 breakouts) (Figure 2c). The variation in the measured azimuth data probably reflects localized stress orientation changes around minor faults, fractures, and lithologic boundaries [Lin *et al.*, 2010].

[9] Because P-wave velocity increased and resistivity decreased with lithologic unit changes from III to IV [Saffer *et al.*, 2009], it is reasonable to infer the compressive strength and Young's modulus in Unit IV are higher than those in Unit III, respectively. Thus, the presence of breakouts in the stronger formation (Unit IV), and not in the weaker formation (Unit III), is interesting, because in general breakouts occur easily in weaker rock if the stress magnitudes are the same. Certainly, this observation means that stress state in Unit IV distinctly differs with that in Unit III. In principle, breakout occurs once the circumferential stress σ_c at the borehole wall in the minimum stress azimuth exceeds the rock compressive strength. This stress σ_c is expressed as $\sigma_c = 3S_{Hmax} - S_{Hmin} - P_p - P_m$, where P_p and P_m are pore pressure and mud pressure, respectively [Zoback *et al.*, 2003]. Thus, σ_c is mainly controlled by S_{Hmax} . Therefore, a further possible interpretation is that the S_{Hmax} magnitude in Unit IV is higher than that in Unit III. If this interpretation is true, this suggests that the harder/stronger formation bears a higher loading than the softer/weaker formation. That is, the S_{Hmax} magnitude in accretionary prism (Unit IV) may be obviously higher than that in the forearc basin sediments (Unit III). At the same time, these observations indicate that the S_{Hmax} magnitude profile may be not a simple direct proportion relation with depth. If the

coupling strength of the unconformities is weak, it may be the other possible reason for this phenomenon except the different formation hardness.

4. Caliper Data Analyses for Breakouts

[10] The FMI caliper data showed that at depths above 1285 mbsf (in units II and III) the two orthogonal diameter profiles (C1 and C2) were almost identical, showing no clear borehole elongations, which suggests that almost no breakout occurred (Figure 3a). Clear borehole elongations were recognized, showing the presence of breakouts, below 1285 mbsf in Unit IV. All three types of caliper (two-, four- and six-arm calipers) yielded nearly the same borehole maximum diameter profiles. This reproducibility suggests that one pair of the FMI caliper arms always finds the maximum elongated position. Moreover, the azimuth of the FMI arms rotated freely in the circular part of the borehole above 1285 mbsf but indicates a dominant azimuth in the elongated part of the borehole below 1285 mbsf, even though the two caliper pairs exchanged positions at depths around 1460 and 1535 mbsf (Figure 3d). This behavior also shows that caliper arms reliably report the elongated borehole position.

[11] In identifying breakouts from the four-arm caliper data, we used three criteria for controlling data quality similar to *Plumb et al.* [1985]. First, the larger caliper diameter should be sufficiently greater than the smaller diameter such that the difference between the two diameters C1 and C2 is at least 0.05 times the drilling diameter D , in this case approximately 15 mm or 0.6 inches. Second, the smaller caliper diameter should not exceed 1.05 D . Third, both diameters should not be significantly less than the bit diameter, that is, C1 and C2 $>$ 0.95 D . This generated a subset of the data of 1061 measurements (Figure 3c) which displays gaps due to borehole caving around 1360 mbsf and due to constriction (probably from drilling generated cuttings and/or cavings) around 1570 mbsf (compare Figures 3b and 3c). Another gap at 1520–1540 mbsf reflects a nearly circular borehole and the absence of continuous breakouts (Figure 3c).

[12] We determined the profile of S_{Hmax} azimuths below 1285 mbsf by adding 90° to the S_{Hmin} azimuth shown by the orientation of maximum borehole elongation in the selected FMI caliper data (Figure 3d). The average azimuth and its standard deviation were N135°E and 11° , respectively, and showed no clear trend with depth. The average azimuth obtained from the FMI images differed by 9° from that from the caliper data, probably because poor image coverage (about 50%) resulted in inaccuracies in picking breakouts. Therefore, we believe that the stress azimuth data from caliper should be more accurate than those from FMI image.

[13] With respect to comparison of the stress orientations in shallower (obtained from DITFs (Figure 2c)) and in deeper (from caliper breakouts (Figure 3d)) ranges, there was a notable difference in azimuths from the shallower to the deeper levels; a clockwise rotation of approximately 30° . This rotation is significant because the standard deviations of the azimuth are around 10° . Similarly, at drilling site C0002 about 20 km away from C0009 in the seaward part of the Kumano forearc basin, stress orientations rotated clockwise (Figure 1b) at depths below 936 mbsf, at the

transition from basin-slope deposits to prism [*Tobin et al.*, 2009].

5. Stress Orientations at NanTroSEIZE Sites

[14] In order to interpret the regional significance of the stress orientations, we need first consider the significance of the change in stress orientations with depth. The orientations at both C0009 and C0002 rotate clockwise from basin sediments to the underlying accretionary prism or prism slope deposits (Figure 1b). The stress rotation with depth might be caused by i) the effect of a strike slip fault with depth-dependent strength [e.g. *Chéry et al.*, 2004], ii) a decoupling between the basin and the accretionary wedge, and iii) reorientation of stress field across an angular unconformity that separates rocks with different elastic properties. The recent identification of strike-slip faulting along the shelf edge [*Martin et al.*, 2010] and within a few hundred meters of C0002 suggests the first cause may apply at this site. At site C0009, which is several kilometers from the fault zone at the shelf edge either cause ii or iii might apply.

[15] In the relatively shallow drilled depth range of the NanTroSEIZE sites (less than approximately 1600 mbsf at all the sites), the S_{Hmax} orientations at site C0009 was slightly different with the S_{Hmax} orientations at sites C0001, C0004, and C0006, and significantly different with the orientation at site C0002 which is closer to C0009 than the other sites (Figure 1b). In addition, the S_{Hmax} orientations at site C0009 are correlated to the plate motion. In details, the orientation at deeper depths (Unit IV) is nearly parallel to the convergence vector between the Philippine Sea plate and Japan (yellow arrows in Figure 1b); whereas the orientation at shallower depths appears to be more nearly parallel to the geodetically-determined motion of the Kii Peninsula (black arrow in Figure 1b). This parallelism between the shortening direction of Kii Peninsula and the stress orientations above the unconformity suggest that these data are more appropriate for explaining the surficial plate motion in hanging wall than the data below the unconformity. However, the S_{Hmax} orientations at sites C0001, C0004 and C0006 are more orthogonal to the margin strike. These results may imply a possible interpretation of deformation partitioning structure, that is, the oblique plate convergence is being partitioned into trench-parallel and right-lateral slip and thrusting. Evidence for right-lateral slip on east-northeast trending faults, consistent with strain partitioning, has been found along the outer-arc high in the Tokai [*Huchon et al.*, 1998] and in the To-Nankai areas [*Martin et al.*, 2010] (Figure 1b).

[16] The S_{Hmax} orientations at C0009 and C0002 are nearly at right angles to each other. A seismic reflection profile at C0002 in the basin running NW–SE (Figure 1d) displays a clear sequence of normal faults [e.g., *Tobin et al.*, 2009]. Moreover, ASR data on cores from site C0002 showed a normal fault stress regime, indicating an extensional deformation pattern [*Byrne et al.*, 2009]. These results are consistent with the stress orientation at C0002 being perpendicular to the plate boundary. In contrast to C0002, normal faulting is more sparse in the landward part of the basin, in the vicinity of site C0009 (Figure 1c).

6. Conclusions

[17] In the borehole at NanTroSEIZE site C0009, we determined horizontal stress orientations at the center of the Kumano forearc basin in the Nankai subduction zone, Japan. We identified and characterized borehole breakouts and drilling-induced tensile fractures by using wireline logging FMI images and caliper data.

[18] Among the four NanTroSEIZE sites drilled before C0009, three (C0001, C0004, and C0006) show S_{Hmax} almost orthogonal to the plate boundary, whereas the fourth site, C0002, drilled at the seaward edge of the basin, shows S_{Hmax} parallel to the shelf edge or plate boundary. In contrast to these results, new stress orientation results obtained in this study at site C0009 at the center of the Kumano forearc basin show S_{Hmax} generally parallel to the convergence direction. Overall, the regional stress patterns suggest strain partitioning during oblique plate convergence. The boreholes penetrated through basin sediments into the underlying accretionary prism and/or slope deposits at both sites C0009 and C0002, and at both sites the stress orientations rotated clockwise, indicating changes of stress state with depth. In addition, the presence of breakouts in Unit IV, and not in Unit III at C0009, possibly suggests that S_{Hmax} magnitude in accretionary prism (Unit IV) may be higher than that in the forearc basin sediments or slope deposits (Unit III).

[19] **Acknowledgments.** This research used data provided by the IODP. The authors gratefully acknowledge the support provided by the D/V *Chikyu* drilling crew, logging staff, and laboratory technicians. Discussions with Asuka Yamaguchi and Pierre Henry were helpful for preparing the manuscript. Part of this work was supported by Grants-in-Aid for Scientific Research 19540453, 22403008 (JSPS), and 21107006 (MEXT), Japan.

References

- Araki, E., T. Byrne, L. McNeill, D. Saffer, N. Eguchi, K. Takahashi, and S. Toczko (2009), NanTroSEIZE Stage 2: NanTroSEIZE riser/riserless observatory, *Integr. Ocean Drill. Program Sci. Prosp.*, 319, doi:10.2204/iodp.sp.319.2009.
- Byrne, T. B., et al. (2009), Anelastic strain recovery reveals extension across SW Japan subduction zone, *Geophys. Res. Lett.*, 36, L23310, doi:10.1029/2009GL040749.
- Chang, C., et al. (2009), Constraining in situ stress tensor in the Kumano forearc basin, Nankai, based on borehole wall failure analysis, *Eos Trans. AGU*, 90(52), Fall Meet. Suppl., Abstract T21C-1832.
- Chéry, J., M. D. Zoback, and S. Hickman (2004), A mechanical model of the San Andreas fault and SAFOD Pilot Hole stress measurements, *Geophys. Res. Lett.*, 31, L15S13, doi:10.1029/2004GL019521.
- Heki, K., and S. Miyazaki (2001), Plate convergence and long-term crustal deformation in central Japan, *Geophys. Res. Lett.*, 28, 2313–2316, doi:10.1029/2000GL012537.
- Huchon, P., et al. (1998), Pervasive dextral strike-slip faulting within the backstop of the Eastern Nankai wedge confirmed by the deep-towed seismic data (Kaiko-Tokai 1996 cruise), *C. R. Acad. Sci.*, 326, 869–875.
- Lallemand, S., and F. Funiciello (2009), *Subduction Zone Geodynamics*, doi:10.1007/978-3-540-87974-9, Springer, Berlin.
- Lin, W., et al. (2007), Current stress state and principal stress rotations in the vicinity of the Chelungpu fault induced by the 1999 Chi-Chi, Taiwan, earthquake, *Geophys. Res. Lett.*, 34, L16307, doi:10.1029/2007GL030515.
- Lin, W., et al. (2010), Localized rotation of principal stress around faults and fractures determined from borehole breakouts in hole B of the Taiwan Chelungpu-fault Drilling Project (TCDP), *Tectonophysics*, 482, 82–91, doi:10.1016/j.tecto.2009.06.020.
- Martin, K. M., et al. (2010), Possible strain partitioning structure between the Kumano forearc basin and the slope of the Nankai Trough accretionary prism, *Geochim. Geophys. Geosyst.*, 11, Q0AD02, doi:10.1029/2009GC002668.
- McNeill, L. C., M. Ienaga, H. Tobin, S. Saito, D. Goldberg, J. C. Moore, and H. Mikada, (2004), Deformation and in situ stress in the Nankai Accretionary Prism from resistivity-at-bit images, ODP Leg 196, *Geophys. Res. Lett.*, 31, L02602, doi:10.1029/2003GL018799.
- Moore, G., et al. (2007), Three-dimensional splay fault geometry and implications for tsunami generation, *Science*, 318, 1128–1131, doi:10.1126/science.1147195.
- Park, J.-O., et al. (2002), Splay fault branching along the Nankai subduction zone, *Science*, 297, 1157–1160, doi:10.1126/science.1074111.
- Plumb, R. A., et al. (1985), Stress induced borehole elongation: comparison 769 between the four-arm dip meter and the borehole televiwer in the Auburn 770 geothermal well, *J. Geophys. Res.*, 90, 5513–5521, doi:10.1029/JB090iB07p05513.
- Saffer, D., et al. (2009), NanTroSEIZE Stage 2: NanTroSEIZE riser/riserless observatory, *Integr. Ocean Drill. Program Prelim. Rep.*, 319, doi:10.2204/iodp.pr.319.2009.
- Tobin, H., et al. (2009), Expedition 314 summary, in *NanTroSEIZE Stage 1: Investigations of Seismogenesis, Nankai Trough, Japan, Proc. Integr. Ocean Drill. Program*, 314/315/316, doi:10.2204/iodp.proc.314315316.111.2009.
- Zoback, M. D., et al. (2003), Determination of stress orientation and magnitude in deep wells, *Int. J. Rock Mech. Min. Sci.*, 40, 1049–1076.
- E. Araki, M. Kinoshita, and K. Kitada, Institute for Research on Earth Evolution, JAMSTEC, Natsushima-cho 2-15, Yokosuka 237-0061, Japan.
- D. Boutt, Department of Geosciences, University of Massachusetts Amherst, 611 North Pleasant St., Amherst, MA 01003, USA.
- D. M. Buchs, Research School of Earth Sciences, The Australian National University, 61 Mills Rd., Bldg. J1, Canberra, ACT 0200, Australia.
- C. Buret, Département de Géologie, Université de Picardie Jules Verne, 33, rue Saint Leu, F-80039 Amiens CEDEX, France.
- T. B. Byrne, Center for Integrative Geosciences, University of Connecticut, 354 Mansfield Rd., Storrs, CT 06269, USA.
- M. Conin, CEREGE, University Aix Marseille III, F-13545 Aix-en-Provence CEDEX, France.
- D. Cukur, Leibniz Institute of Marine Sciences at Kiel University (IFM-GEOMAR), Düsternbrooker Weg 20, D-24105 Kiel, Germany.
- M.-L. Doan, Laboratoire de Géophysique et Tectonophysique, Université Grenoble 1 (Joseph Fourier), BP 53, F-38041 Grenoble CEDEX 9, France.
- N. Efimenko, Institut de Géologie et de Paléontologie, Université de Lausanne, CH-1015 Lausanne-Dorigny, Switzerland.
- N. Eguchi, Y. Kido, K. T. Moe, Y. Sanada, K. Takahashi, and S. Toczko, Center for Deep Earth Exploration, JAMSTEC, Showa-machi 3173-25, Kanazawa-ku, Yokohama 236-0001, Japan.
- P. Flemings and N. W. Hayman, Institute for Geophysics, Jackson School of Geosciences, University of Texas at Austin, J. J. Pickle Research Campus, Bldg. 196, 10100 Burnet Rd., Austin, TX 78758, USA.
- K. Horiguchi, Department of Earth and Space Sciences, Osaka University, 1-1 Machikaneyama, Toyonaka, Osaka 560-0043, Japan.
- G. J. Huftile, Biogeosciences Discipline, Queensland University of Technology, GPO Box 2434, Brisbane, Qld 4001, Australia.
- T. Ito, Institute of Fluid Science, Tohoku University, 2-1-1 Katahira, Aoba-ku, Sendai 980-8577, Japan.
- S. Jiang, Geological Sciences, Florida State University, 108 Carraway Bldg., Tallahassee, FL 32306, USA.
- K. Kameo, Department of Earth Sciences, Chiba University, 1-33 Yayoi, Inage, Chiba 263-8522, Japan.
- Y. Kano, Research Center for Earthquake Prediction, Disaster Prevention Research Institute, Kyoto University, Gokasho, Uji, Kyoto 611-0011, Japan.
- K. Kawabata, Institute of Geophysics, National Central University, 300 Chung-Da Road, Chung Li City, Taoyuan 32001, Taiwan.
- A. Kopf, Marum Research Centre, University of Bremen, Leobener Strasse, MARUM Building, D-28359 Bremen, Germany.
- W. Lin, Kochi Institute for Core Sample Research., JAMSTEC, Monobe-otsu 200, Nankoku, Kochi 783-8502, Japan. (lin@jamstec.go.jp)
- L. McNeill, National Oceanography Centre, Southampton, University of Southampton, European Way, Southampton SO14 3ZH, UK.
- J. C. Moore, Earth and Planetary Sciences Department, University of California, Santa Cruz, CA 95064, USA.
- D. Saffer, Geosciences, Pennsylvania State University, 310 Deike Bldg., University Park, PA 16802, USA.
- A. M. Schleicher, Department of Geological Sciences, University of Michigan, 2534 CC Little Bldg., 1100 North University Ave., Ann Arbor, MI 48109, USA.
- H. Tobin, Department of Geoscience, University of Wisconsin-Madison, 1215 W. Dayton St., Madison, WI 53706, USA.
- T. Wiersberg, Section 4.2, GFZ German Research Center for Geosciences, Telegrafenberg, D-14479 Potsdam, Germany.



Quantification of free gas in the Kumano fore-arc basin detected from borehole physical properties: IODP NanTroSEIZE drilling Site C0009

Mai-Linh Doan

Institut des Sciences de la Terre, CNRS, Université Joseph Fourier, BP 53, F-38041 Grenoble CEDEX 9, France (Mai-Linh.Doan@obs.ujf-grenoble.fr)

Marianne Conin and Pierre Henry

Université Aix-Marseille III, CNRS, CEREGE, Europole de l'Arbois, BP 80, F-13545 Aix en Provence, France

Thomas Wiersberg

Helmholtz Zentrum Potsdam, Deutsches GeoForschungsZentrum, Section 4.2, Telegrafenberg, D-14473 Potsdam, Germany

David Boutt

Department of Geosciences, University of Massachusetts Amherst, 611 North Pleasant Street, 233 Morrill Science, Amherst, MA 01003, USA

David Buchs

Research School of Earth Sciences, The Australian National University, 61 Mills Road, Building J1, Canberra, ACT 0200, Australia

Demian Saffer

Geosciences, Pennsylvania State University, 310 Deike Building, University Park, PA 16802, USA

Lisa C. McNeill

National Oceanography Centre, Southampton, University of Southampton, European Way, Southampton SO14 3ZH, UK

Deniz Cukur

Department of Energy Resources Engineering, Pukyong National University, 599-1, Daeyeon 3-Dong, Nam-Gu, 608-737 Busan, South Korea

Weiren Lin

Kochi Institute for Core Sample Research, JAMSTEC, Monobe-otsu 200, Nankoku 783-8502, Japan

[1] The Kumano fore-arc basin overlies the Nankai accretionary prism, formed by the subduction of the Philippine Sea Plate beneath the Eurasian plate offshore the Kii Peninsula, SW Honshu, Japan. Seismic surveys and boreholes within the framework of the Nankai Trough Seismogenic Zone Experiment (NanTroSEIZE) project show evidence of gas hydrates and free gas within the basin. Here we use high-quality borehole sonic data from Integrated Oceanic Drilling Program (IODP) Site C0009 to quantify the free gas distribution in the landward part of the basin. The Brie theory is used to quantify gas content from sonic logs, which are calibrated from laboratory measurements on drill cores. First, we show that the sonic data are



mainly sensitive to the fluid phase filling the intergranular pores (effective porosity), rather than to the total porosity that includes water bound to clay minerals. We then compare the effective porosity to lithodensity-derived porosity that acts as a proxy for total porosity. The combination of these two data sets also allows assessment of clay mineralogy of the sediments. Second, we compute free gas saturation and find a gas-rich interval that is restricted to a lithological unit characterized by a high abundance of wood fragments and lignite. This unit, at the base of the fore-arc basin, is a hydrocarbon source that should be taken into account in models explaining gas distribution and the formation of the bottom-simulating reflector within the Kumano fore-arc basin.

Components: 6600 words, 6 figures, 2 tables.

Keywords: gas saturation; sonic data; porosity; clay mineralogy; Kumano fore-arc basin; NanTroSEIZE.

Index Terms: 7299 Seismology: General or miscellaneous; 8169 Tectonophysics: Sedimentary basin processes; 3004 Marine Geology and Geophysics: Gas and hydrate systems.

Received 13 July 2010; **Revised** 22 November 2010; **Accepted** 30 November 2010; **Published** 28 January 2011.

Doan, M.-L., M. Conin, P. Henry, T. Wiersberg, D. Boutt, D. Buchs, D. Saffer, L. C. McNeill, D. Cukur, and W. Lin (2011), Quantification of free gas in the Kumano fore-arc basin detected from borehole physical properties: IODP NanTroSEIZE drilling Site C0009, *Geochem. Geophys. Geosyst.*, 12, Q0AD06, doi:10.1029/2010GC003284.

Theme: Mechanics, Deformation, and Hydrologic Processes at Subduction Complexes, With Emphasis on the Nankai Trough Seismogenic Zone Experiment (NanTroSEIZE) Drilling Transect

Guest Editors: D. Saffer, P. Henry, and H. Tobin

1. Introduction

[2] Porosity is a key factor for understanding the compaction and diagenesis of basin sediments [Aagaard and Jahren, 2010]. In situ porosity is commonly derived from sonic velocities [Mavko *et al.*, 1998]. However, interpretation of the sonic properties of clays is complex, because clays have two kinds of water storage: water bound to the clay mineral and water contained in intergranular voids. How each kind of porosity contributes to sonic velocity is unclear [Avseth *et al.*, 2005]. To better understand the relationship between clay porosities and clay sonic properties, we combine core and high-quality logging data acquired during the Integrated Oceanic Drilling Program (IODP) Expedition 319 at Site C0009, within the Kumano fore-arc basin, offshore the Kii Peninsula, Japan.

[3] Expedition 319 was conducted as part of the Nankai Trough Seismogenic Zone Experiment (NanTroSEIZE), a coordinated, multiexpedition drilling project implemented by IODP. The NanTroSEIZE project aims to understand the formation of the Nankai fore arc and its seismogenic zone [e.g., Kinoshita *et al.*, 2006]. Extensive seismic studies conducted in advance of drilling provide evidence of gas within sediments filling the Kumano

fore-arc basin (Figure 1, see also Moore *et al.* [2009]). For example, a laterally extensive horizontal bottom-simulating reflector (BSR) extends throughout the basin, marking the base of the gas hydrate stability zone. Other strong reflectors may also suggest the presence of gas accumulations in the lowermost basin sediments above the older accretionary prism (Figure 1). Site C0009 was drilled in riser mode, enabling recovery of cuttings and monitoring of mud gas for the first time in IODP history and allowing the newest logging technology to be deployed in the riser hole [Saffer *et al.*, 2009, 2010]. In particular, the Schlumberger SonicScanner™ wireline logging tool recorded shear wave velocity within the unconsolidated sediments (Figure 2), providing key data needed to quantify gas accumulations.

[4] Here we evaluate porosity and gas content in the fine-grained basin filling sediments using P wave velocity (V_p) and S wave velocity (V_s) logging data. Such porosity evaluation is an important contribution, because there were no direct porosity measurements from Site C0009, with the exception of a ~90 m thick cored interval at the bottom of the hole. We calibrate the relationship between sonic properties and clay porosities from measurements on core samples, taking into account the physical and chemical properties of the clay minerals. We

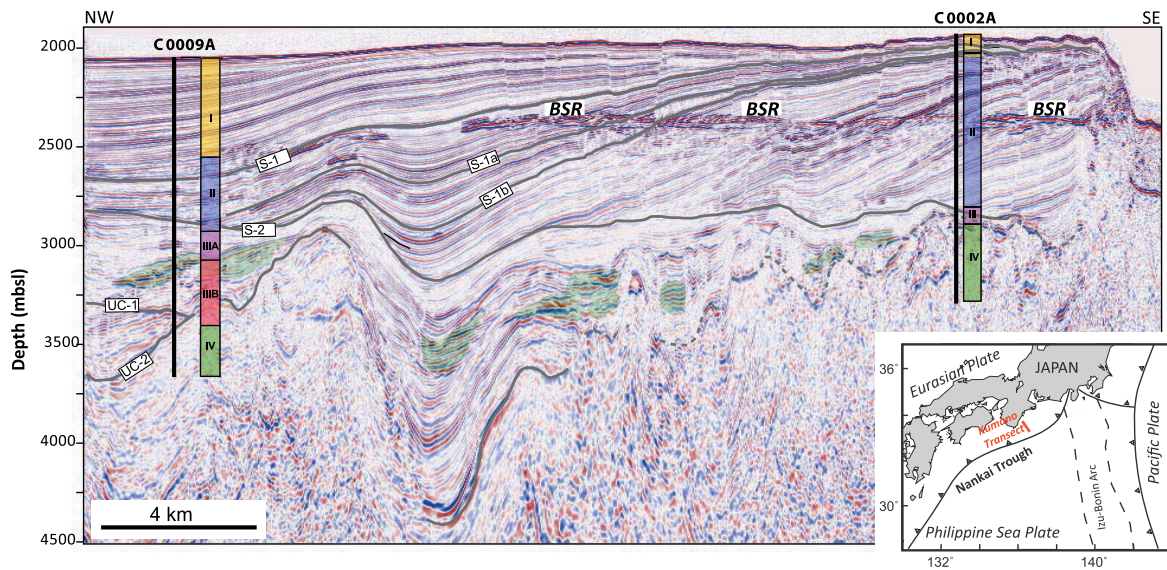


Figure 1. Seismic section across the Kumano fore-arc basin modified from Moore *et al.* [2009] and Saffer *et al.* [2010], showing the location and simplified stratigraphic columns for Sites C0009 and C0002. Possible gas pockets at the base of the basin, identified from seismic reflection images, are highlighted in green. The bottom-simulating reflector (BSR) that extends along the basin is also noted.

then perform an inversion from sonic velocity to determine porosity and water saturation. The results we obtain are consistent with other logging data, such as resistivity logs. Finally, we examine the

relationship between the presence of organic matter and gas content and compare the data from Site C0009 with previously collected core and logging data from Site C0002, another IODP site drilled

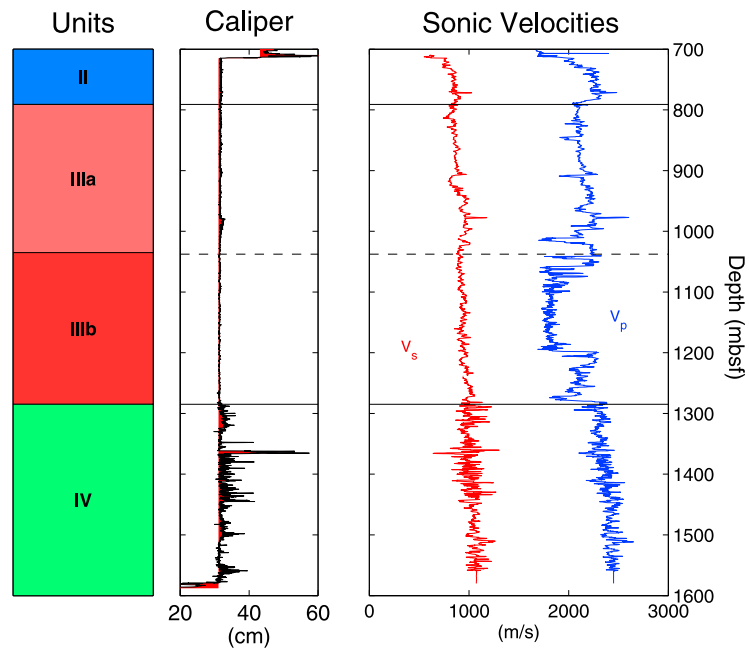


Figure 2. Sonic data from Hole C0009. In Unit IV, the data are noisier where the hole quality is degraded, as indicated by the caliper data.



15 km away, at the seaward edge of the Kumano Basin (Figure 1) [Kinoshita *et al.*, 2009].

2. Fore-Arc Basin Stratigraphy

[5] The two holes drilled within the Kumano Basin (at Sites C0002 and C0009) penetrated the thick sediments of the fore-arc basin, to total depths of 1401 m below seafloor (mbsf) and 1604 mbsf, respectively (Figure 1). Four main lithological units within the basin section were defined at Site C0009, by combining cuttings analysis with logging data [Saffer *et al.*, 2009]. These units correlate broadly with the units identified at nearby Site C0002 [Kinoshita *et al.*, 2009; Saffer *et al.*, 2010]. The four units recognized at Site C0009, from the seafloor to the bottom of the hole, are described in sections 2.1 through 2.4.

2.1. Unit I (0–467 mbsf)

[6] Although Site C0009 was drilled and cased down to 703.9 mbsf without coring or cuttings collection, a nearby 80 m deep geotechnical borehole, wireline gamma ray log measurements recorded from the seafloor during drilling and seismic profiles collectively provide good control on the nature of the shallowest drilled sediments. These data suggest that Unit I is composed of silty mudstone with cyclical sand-rich layers that range from ~10 to 50 m in thickness.

2.2. Unit II (467–791 mbsf, Upper Fore-Arc Basin)

[7] This unit is defined based on analysis of cuttings from 703.9 mbsf to 791 mbsf and logging data over its entire thickness. It is composed predominantly of unconsolidated silty mud, with silt and sand interbeds and minor interbeds of volcanic ash.

2.3. Unit III (791–1285 mbsf, Lower Fore-Arc Basin)

[8] This unit is defined on the basis of cuttings and wireline logs and is dominated by silty mudstone. The unit is subdivided into Subunits IIIa and IIIb; the boundary between the two subunits is marked by an abrupt increase in wood lignite fragments (concentrated in Subunit IIIb). Cuttings samples from within Unit III overall display a high total organic carbon (TOC) content (Figure 3), however the cuttings composition may not be representative of the average sediment [Saffer *et al.*, 2010]. Mud

gas monitoring detected higher hydrocarbon concentrations from this unit relative to those above and below. In contrast, the correlated stratigraphic unit at Site C0002 is devoid of wood/lignite fragments and the TOC of the sediments is low (less than ~0.5%wt). At Site C0002, this unit is interpreted as a starved section within the early fore-arc basin or as a trench slope deposit predating formation of the fore-arc basin [Kinoshita *et al.*, 2009].

2.4. Unit IV (1285–1604 mbsf)

[9] This unit is primarily composed of consolidated silty mudstone with minor silt interbeds. The sedimentary facies resembles Unit IV at Site C0002, which was interpreted as accreted sediments (Figure 1) [Kinoshita *et al.*, 2009]. Unit IV at Site C0009 lacks the level of deformation observed in its equivalent at Site C0002 and is therefore interpreted either as a weakly deformed package of accreted trench sediments, as trench slope sediments deposited over accreted sediments of the early prism or as earliest fore-arc basin deposits [Saffer *et al.*, 2010].

3. Sonic Data

[10] The SonicScanner™ generates high-quality sonic data. It uses 3 monopole sources (2 near field, located 30.5 cm from the nearest receiver and 1 far field, located 3.353 m from the nearest receiver) and records *P* waves on an array of 13 receivers. Frequencies for the monopole emitter span 5–20 kHz. The SonicScanner™ also measures shear wave velocity in two orthogonal directions. The dipole emitters are located 4.572 m and 5.182 m from the base of the receiver arrays and the frequency range is 300 Hz–8 kHz. Figure 2 shows the azimuthally averaged sonic velocities recorded at Site C0009. Both *P* and *S* waves were recorded and identified, even in soft unconsolidated clay-dominated sediments. Unfortunately, the azimuthally averaged shear wave velocity values are the only shear wave data available for Site C0009. However, shipboard *P* wave measurements on core samples from the base of the borehole show that the seismic anisotropy is less than 5%, at a confining pressures above ~15–20 MPa (Figure 4). Therefore, we assume the medium to be nearly isotropic.

[11] Different patterns of sonic velocity are observed between Units II, III and IV (Figure 2). In Unit II, V_p and V_s increase with depth, from 1900 m/s to 2300 m/s and from 765 m/s to 900 m/s, respectively. At the top of Unit III, a decrease in sonic

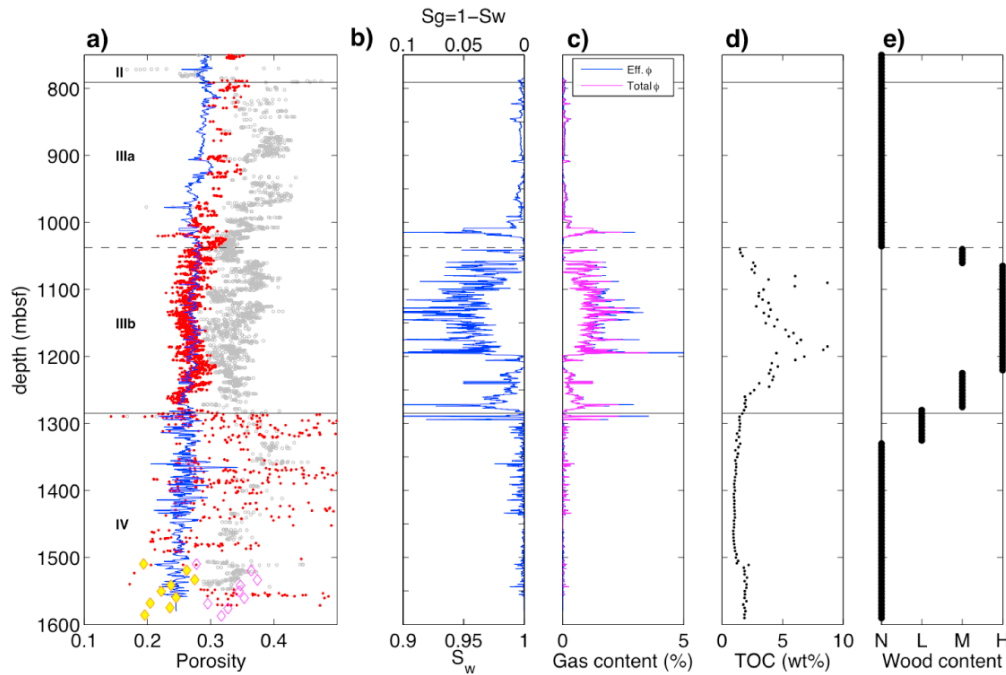


Figure 3. Results from the inversion of Brie equations (a) using the matrix parameters derived from effective porosity data (Table 1, yellow diamonds, black line in Figure 5). The corresponding porosity profile (solid blue line) is consistent with the effective porosity estimated from resistivity logs (red dots), using data with a standoff less than 0.01 in. (0.25 mm). The estimated porosity is lower than the total porosity, as computed from the lithodensity log (gray circles) or the core moisture and density (purple open diamonds). (b) Water saturation derived from effective porosity data. (c) Profile of gas content $\varphi(1-S_w)$ determined by using the effective porosity (black lines in Figure 5) and total porosity (purple lines in Figure 5). Both inversions yield the same free gas content. (d) Total organic carbon (TOC) content determined from analysis of the cuttings. (e) Wood content abundance determined from visual inspection of cuttings during Expedition 319 [Saffer *et al.*, 2010]. (N, no presence; L, low content; M, medium content; H, high content).

velocity, most obviously seen in the S wave data, accompanies the transition to muddier sediments. Within Unit III, both P and S wave velocities increase with depth, except in some regions where V_p drops sharply, which we interpret as a function of the presence of free gas (discussed below). Within Unit IV, the borehole experienced stability problems, with frequent occurrence of drilling-induced compressive failure (i.e., borehole breakouts [Lin *et al.*, 2010]), resulting in noisier sonic data. However, an increase in sonic velocity with depth is still distinguishable, especially in the P wave data (Figure 2).

4. Brie Equations for Clay

[12] Sonic velocities provide information on the mechanical compliance of the sediment framework. At a given effective pressure, two main factors

control the P and S wave velocities of a porous medium: (1) porosity and (2) free gas within the pore fluid. To quantify both parameters, we combine elastic theory of porous media and empirical sonic data. The classical Willy model of sonic velocity does not appropriately describe the sonic properties of clay-rich sediments [Mavko *et al.*, 1998], therefore, we use an alternative model developed by Brie *et al.* [1995]. This is a semi-empirical model that takes into account the dependence of sonic velocity on porosity and water saturation. The advantage of this model is its use of a small number of coefficients. These coefficients have been validated by empirical fits to several logging data sets [Brie *et al.*, 1995].

[13] The basis of the Brie model is the Biot-Gassmann equation for porous media, which relates the bulk modulus of the fluid-filled material (K) to the modulus of the dry porous medium (K_{dry}), the

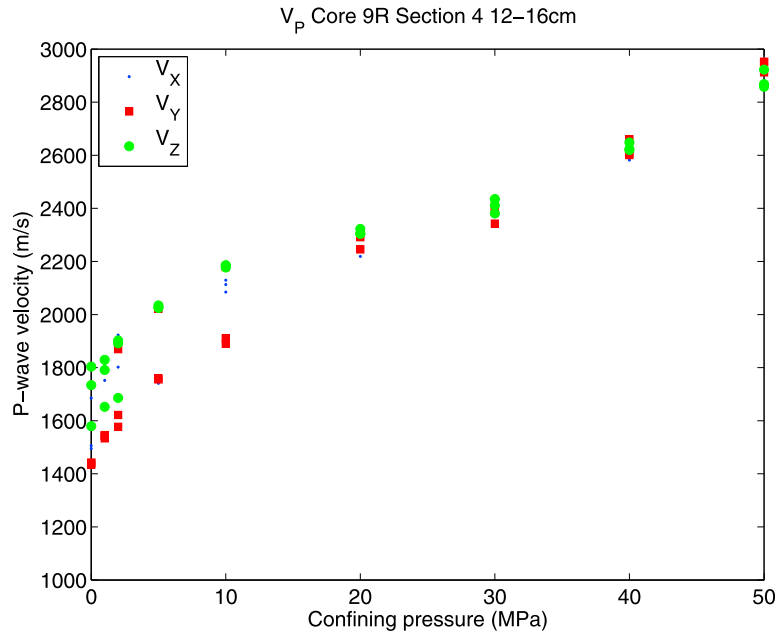


Figure 4. Shipboard P wave velocity data measured in section 4 of core 9 (approximate depth of 1588.5 mbsf) at several confining pressures. Core samples were first soaked in brine, covered by an impermeable layer of silicone, and then placed in a confining vessel. The P wave velocity was measured along the X, Y, and Z directions, where Z is oriented to the bottom of the hole and X and Y correspond to two horizontal directions. At confining pressures greater than 15–20 MPa, the samples become nearly isotropic.

bulk modulus of the solid (K_s), the modulus of the fluid (K_f) and the porosity ϕ :

$$K = K_{dry} + \frac{\left(1 - \frac{K_{dry}}{K_s}\right)^2}{\frac{\phi}{K_f} + \frac{1 - \phi}{K_s} - \frac{K_{dry}}{K_s^2}} \quad (1)$$

Brie et al. [1995] proposed obtaining the elastic moduli from P wave velocity (V_p) and S wave velocity (V_s),

$$\left(\frac{V_p}{V_s}\right)^2 = \frac{K}{\mu} + \frac{4}{3}, \quad (2)$$

where μ is the shear modulus of the material. Provided the material is isotropic and linear elastic, this solution holds for both dry and wet conditions and for both the porous material or solid grains by simply changing the indices of K and μ .

[14] The theory of *Brie et al.* [1995] states that the ratio K/μ is the same for solid grains and for a porous material with pore spaces filled by a very compressible fluid,

$$\frac{K_s}{\mu_s} = \frac{K_{dry}}{\mu_{dry}} \quad (3)$$

Brie et al. [1995] combine equation (3) with an empirical relationship,

$$\mu_{dry} = \mu_s(1 - \phi)^c, \quad (4)$$

and found experimentally that the coefficient $c = 8$ for clays.

[15] For a water-saturated medium (without gas, $S_w = 100\%$), higher porosity results in reduced V_p but a higher V_p/V_s ratio. In the classical $1/V_p$ versus V_p/V_s crossplot, curves similar to the solids lines (black and purple) of Figure 5 should be followed, moving toward the upper right-hand corner as porosity increases. These curves are in good agreement with the logging data collected at Site C0009.

[16] Equations (3) and (4) are the core of the theory of *Brie et al.* [1995] and are commonly used in log data analysis [*Ellis and Singe, 2007*]. Other laws can be used, such as the Hertz-Mindlin theory that derives shear and bulk moduli for a packing of similar spheres from elastic interactions at grain contacts [*Mindlin, 1949*]. However, these first-principle theories do not fit experimental data for clays, because their underlying assumptions are not satisfied. More details of alternative theories

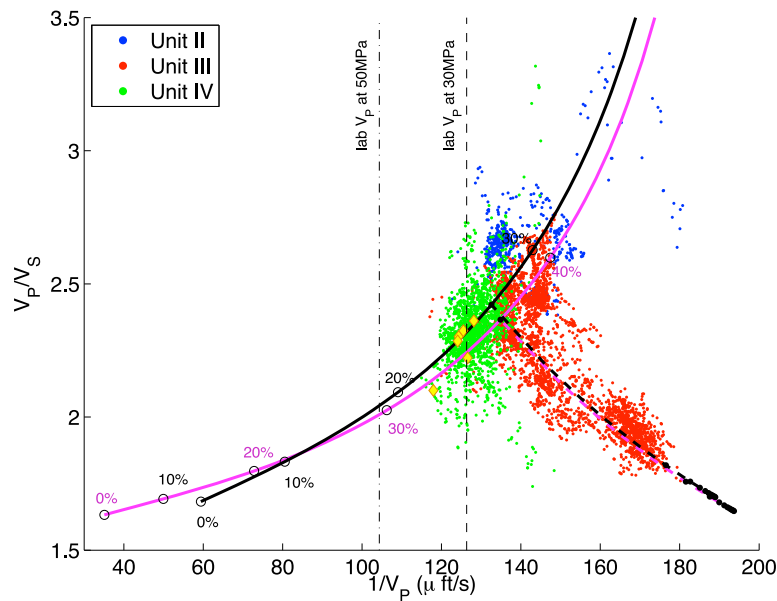


Figure 5. Crossplot of V_p/V_s ratio versus P wave slowness from sonic log data. The log data are given as point clouds. Data from Unit II are in blue, data from Unit III are in red, and data from Unit IV are in green. Among the data from Unit IV, we highlight with yellow diamonds the value of V_p and V_p/V_s obtained at depths where effective porosity was determined on core samples. The theoretical Brie curves for a fully saturated medium have been obtained using the effective porosity data (black solid line) and for the total porosity (purple solid line). Open circles indicate velocities from the Brie model for porosities of 0%, 10%, 20%, 30%, and 40%. Dashed lines show the effect of gas, assuming a porosity of 27% if using effective porosity (thick black dashed line), or 37% if using total porosity (thick purple dashed line). For reference, we also show the laboratory V_p values (see Figure 4) for a confining pressure of 30 MPa and 50 MPa.

tested during this study are provided as auxiliary material.¹

[17] In the case of partial water saturation ($S_w < 100\%$), the fluid modulus K_f is computed as a Reuss average,

$$\frac{1}{K_f} = \frac{S_w}{K_w} + \frac{1 - S_w}{K_g}, \quad (5)$$

where K_g is the gas modulus and K_w the water modulus. In equation (5), we ignore the coupling between the fluid and the solid skeleton. At low water saturation, a meniscus forming between grain particles alters the skeleton stiffness. This effect is not incorporated into our calculations, but the high water saturation estimated from our inversion (Figure 3) confirms that this effect can safely be neglected. With more free gas, or a lower water saturation, the fluid becomes much more compliant and V_p decreases. However, shear waves do not propagate in fluids, so V_s is independent of the fluid phase filling the pores. Therefore, V_p is strongly

affected by gas, whereas V_s is not (see Figure 2). The black and purple dashed lines in Figure 5 show the relationship between $1/V_p$ and V_p/V_s when water saturation varies for a given porosity. With reduced water saturation, or greater free gas content, a given data point ($1/V_p$, V_p/V_s) moves toward the lower right-hand corner.

5. Calibration of Brie Equations for Clays From IODP Site C009

[18] Figure 5 shows SonicScanner™ log data ($1/V_p$ versus V_p/V_s) in Units II, III and IV. Units II and IV exhibit a trend typical of fully water-saturated media, but data from Unit III are shifted toward a lower V_p/V_s . This excursion is a strong indication of the presence of free gas. We use the theory of *Brie et al.* [1995] to quantify the porosity and the water saturation. We take the bulk modulus of water as equal to 2.2 GPa [*Lide*, 1991], and the gas is presumed ideal, so that its bulk modulus is presumed equal to the hydrostatic pressure and remains negligible relative to the water bulk modulus. As in the work by *Brie et al.* [1995], we assume that the

¹Auxiliary materials are available in the HTML. doi:10.1029/2010GC003284.



coefficient c is equal to 8, as the sediments encountered at the bottom of the hole are mainly composed of clay. We also evaluated different values of the coefficient c ($c = 7$ and $c = 9$), and the results are similar for each case (Figure S2).

[19] Two key parameters still remain unknown within the Brie theory: the solid grain bulk modulus K_s and the grain shear modulus μ_s , or their equivalents, the grain P wave and S wave velocities. These two parameters are poorly known, because (1) cores were only retrieved at the bottom of the hole in a ~ 90 m interval within Unit IV, and (2) shipboard P wave velocity measurements made at high confining pressure do not document the properties of the solid grains, as discussed further below.

[20] The onboard P wave velocity measurements provide only a lower bound on the grain P wave velocity. After the samples were recovered from a depth of >1500 mbsf, they were soaked in brine and coated with an impermeable silicone layer. Hence, P wave velocities measured on these samples were performed under undrained conditions, in which the true effective confining pressure is now well constrained. In such conditions, the pore pressure within the sample is equal to $B\sigma_c$ where σ_c is the confining pressure, and B is the Skempton coefficient of the material, which may be as high as ~ 0.9 for clay [Wang, 2000]. The porosity of the samples at high confining pressure is therefore nonnegligible and hence the measured sonic velocity is not representative of the grain properties.

[21] Therefore, we proceeded in two stages. First, we calibrated the matrix parameters to the logging data within the cored interval. Second, we applied these parameters to the rest of the borehole. A key assumption here is that the grain properties are not affected by effective pressure. This assumption is more likely to be valid if the sediments are cemented. From the core data, we consider two kinds of porosity. In clay minerals, water can be either bound to hydrous minerals (e.g., smectite), or located in pore spaces between the grains [Mitchell and Soga, 2005]. Effective porosity refers to the volume of water contained only in the intergranular pore spaces [Ellis and Singe, 2007], whereas total porosity is the intergranular volume plus the volume of water bound to clay minerals and is computed from moisture and density (MAD) measurements [Blum, 1997; Henry, 1997]. The water bound to the hydrated minerals is a function of the number of cations present between the layers of hydrated minerals [Ransom and Hegelson, 1994]. The number of cations can be obtained from cation exchange capacity (CEC)

measurements [Henry, 1997; Bourlange et al., 2003; Conin et al., 2008]. The effective porosity (ϕ_e) is expressed as

$$\phi_e = \phi_t - n \cdot \frac{m_w}{\rho_w} \cdot \text{CEC} \cdot \rho_g \cdot (1 - \phi_t), \quad (6)$$

where ϕ_t is the total porosity, CEC is the cation exchange capacity (in moles per kilogram of dried sample), m_w is the water molar mass (0.018 kg. mol⁻¹), ρ_w is the water density (1024 kg.m⁻³), ρ_g is the grain density (2650 kg.m⁻³), and n is the average number of water molecules per cation charge.

[22] The CEC was measured by exchanging the cations with cobaltihexamine chloride [Orsini and Remy, 1976]. Total porosity, bound water content, and effective porosity were determined on core samples from the bottom of the borehole (Figure 3), but unfortunately cuttings samples from the rest of the borehole were not reliable for this purpose.

[23] For sediments containing swelling clay, there is some ambiguity whether the matrix in the Brie model should include the bound water and thus whether the Brie equation should be a function of the effective porosity (Table 1) or the total porosity (Table 2). For either case, the best fitting P and S wave velocities for the matrix are determined from core sample data and then used to invert the downhole sonic velocity logging data set. If we assume that the Brie equations correspond to the total porosity, the P wave velocity of the solid grains required to fit the sonic properties with the MAD porosity is ~ 8000 m/s, which is unrealistic. Instead, the use of effective porosity in the Brie equations results in a solid grain P wave velocity of ~ 5000 m/s, which is consistent with the values used by Brie et al. [1995]. This suggests that V_p and V_p/V_s are mostly sensitive to the intergranular pores of the sediments and to their fluid content (i.e., effective porosity), rather than to the total porosity that also includes the bound water. The values of solid grain velocities obtained from the Brie equations are then used to invert for porosity ϕ and water saturation S_w profiles down the borehole (Figure 3). We find that the gas saturation does not exceed 5% and that the effective porosity varies little with depth.

6. Reliability of the Inversion

[24] To check the validity of our extrapolation of data from Unit IV core samples to Unit III, we



Table 1. Core Data Used for Determining the Matrix Sonic Properties, Assuming the Brie Equations Involve the Effective Porosity, i.e., the Total Porosity Minus the Bounded Water^a

Sample Depth (mbsf)	V_p From Log	V_p/V_s From Log	Effective Porosity From Core	Matrix P Wave (Local Inversion)	Matrix V_p/V_s (Local Inversion)	Matrix P Wave (Global Inversion)	Matrix V_p/V_s (Global Inversion)
1509.7	2584 m/s (118 s/ μ ft)	2.10	19.4%	4486 m/s (59 s/ μ ft)	1.64	5130 m/s (59 s/ μ ft)	1.68
1519.2	2378 m/s (128 s/ μ ft)	2.36	26.2%	5255 m/s (67 s/ μ ft)	1.69		
1533.3	2408 m/s (127 s/ μ ft)	2.22	27.5%	5733 m/s (62 s/ μ ft)	1.60		
1541.4	2451 m/s (124 s/ μ ft)	2.30	23.7%	4927 m/s (53 s/ μ ft)	1.70		
1550.4	2428 m/s (126 s/ μ ft)	2.33	22.2%	4542 m/s (58 s/ μ ft)	1.72		
1559.7	2456 m/s (124 s/ μ ft)	2.29	24.5%	5130 m/s (68 s/ μ ft)	1.68		

^aThe bound water content was measured from cation exchange capacity measurements. As there are two unknowns (V_p for matrix, V_p/V_s for matrix) for two data (V_p from log, V_p/V_s from log), if we assume we know the porosity, then the inversion can be performed at each depth.

compare the computed porosities to values derived from resistivity measured along the borehole by the Schlumberger MCFLTM (Micro-Cylindrically Focused Log) tool (Figure 3a). Site C0009 was drilled with a very low resistivity mud ($\sim 0.05 \Omega\text{m}$) containing NaCl, KCl and NaOH. As ions are transported within the mud filtrate as it invades the formation, the invading fluid has a resistivity (R_f) about 20 times lower than the typical clay resistivity of $1 \Omega\text{m}$. Therefore within this invaded zone near the borehole wall, the clay surface conductivity can be neglected and effective porosity can be derived from rock resistivity (R) using Archie's law [Archie, 1942],

$$R = a \frac{R_f}{\phi^m}, \quad (7)$$

where a and m are chosen to equal 1 and 2, respectively, based on those computed for similar sediments drilled in the fore-arc basin at IODP Site C0002 [Conin et al., 2008]. The resistivity of the invaded zone is measured with the wireline MCFLTM tool, but unfortunately poor borehole conditions prevent its use in Unit IV. As shown in Figure 3a, porosities estimated from the resistivity data agree well with the effective porosities computed from the sonic data within Unit IIIb. Within Unit IIIa, the two independent data sets exhibit similar fluctua-

tions but are offset from each other by a few percent. Although lithologies in Units IIIa and IIIb are broadly similar, cuttings retrieved from Unit IIIa were insufficiently cohesive to allow moisture and density data measurements [Saffer et al., 2010]. This may explain why the matrix sonic velocities obtained from Unit IV do not apply to Unit IIIa. Within Unit II and Unit IIIa, the correlation between porosities derived from the sonic data and those derived from resistivity logs is poor. This is likely a result of incorrect parameters within the Brie equation or an inappropriate resistivity model for the sandier lithologies present in these units. In particular, for the less consolidated sediments of Unit IIIa, the assumption that the matrix properties have little dependence on effective pressure and hence on depth is probably not valid. Matrix properties would therefore evolve with depth, and the calibration made on the cores at the bottom of the well would not be valid for Unit IIIa.

[25] Another test of the suitability of our inversion is to compute the total gas content as $\varphi(1-S_w)$ (Figure 3c). As gas is not bound to clay minerals, this value should be the same for our inversion using either the total porosity or the effective porosity. The use of total porosity instead of the effective porosity in the Brie equations does not significantly

Table 2. Core Data Used for Determining the Matrix Sonic Properties, Supposing the Brie Equations Involve the Total Porosity

Sample Depth (mbsf)	V_p From Log	V_p/V_s From Log	Total Porosity From Core	Matrix P Wave (Local Inversion)	Matrix V_p/V_s (Local Inversion)	Matrix P Wave (Global Inversion)	Matrix V_p/V_s (Global Inversion)
1509.8	2580 m/s (118 s/ μ ft)	2.08	27.8%	6541 m/s (47 s/ μ ft)	1.58	8686 m/s (35 s/ μ ft)	1.63
1519.6	2375 m/s (128 s/ μ ft)	2.37	36.4%	5917 m/s (52 s/ μ ft)	1.10		
1533.4	2405 m/s (127 s/ μ ft)	2.22	37.4%	6865 m/s (44 s/ μ ft)	1.11		
1541.8	2418 m/s (126 s/ μ ft)	2.27	34.7%	8580 m/s (36 s/ μ ft)	1.65		
1550.8	2448 m/s (125 s/ μ ft)	2.21	34.5%	5816 m/s (52 s/ μ ft)	1.09		

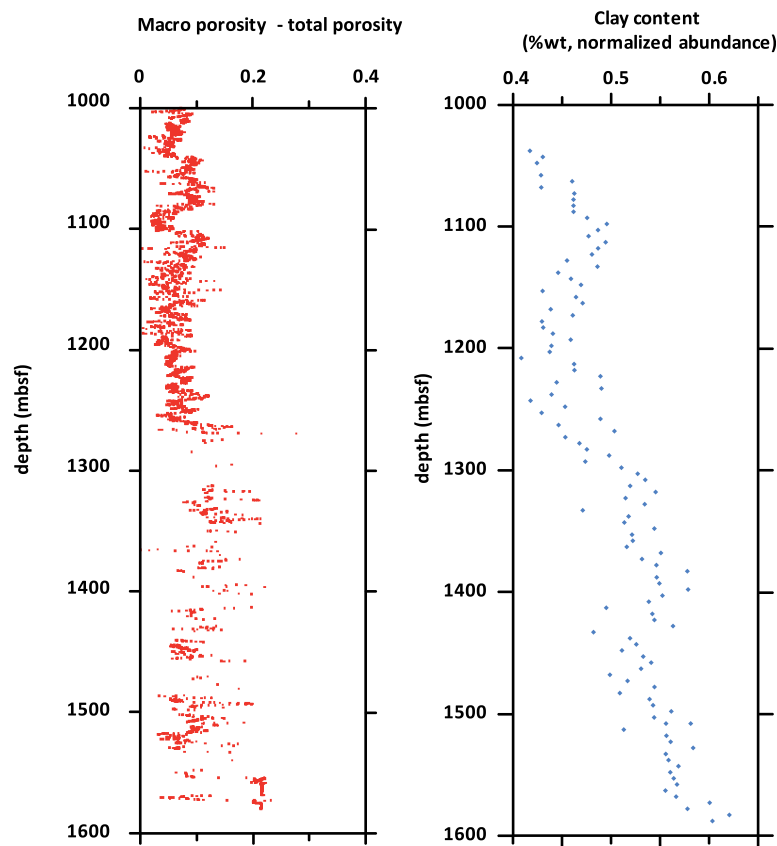


Figure 6. Comparison of water content bound to clay minerals and the total clay content from XRD analyses [Saffer *et al.*, 2010]. Bound water content is computed by differentiating the effective porosity (or macroporosity) derived from the sonic log from the total porosity derived from lithodensity log.

change the computed gas content profile (Figure 3c), exhibiting a peak of 2% of the rock volume. Thus, gas content is generally independent of matrix sonic parameters and is robustly determined by our analysis.

[26] This low gas saturation favors the use of the simple equation (5) for describing the triphasic state. In equation (5), the formation of menisci on the skeleton compliance is ignored as gas saturation was expected to be low. Our results are therefore self-consistent. From these analyses, we believe that our inverted porosities and gas contents are reliable for Units IIIb and IV.

7. Discussion

[27] The effective porosity we compute is ~10% smaller than the porosity obtained from the lithodensity log (Figure 3a). This porosity is calculated from the bulk density log (ρ_b) using the assumption

of a constant grain density (ρ_g) of 2.65 g/cm³, which is consistent with direct measurements on cuttings, and of a constant water density (ρ_w) of 1.024 g/cm³ [Blum, 1997]:

$$\phi = \frac{\rho_b - \rho_g}{\rho_w - \rho_g}. \quad (8)$$

The mass balance described by equation (8) involves the total porosity [Brown and Ransom, 1996], as does the calculation of core and cuttings sample porosity values from moisture and density data, which generally agree with the lithodensity log values. In Units IIIb and IV, the difference between the effective porosity (e.g., derived from the sonic log or electric resistivity log) and total porosity (e.g., derived from the lithodensity log) reflects differences in hydrous clay mineral abundance. The difference between the two porosity calculations correlates well with the total clay content measured on core samples (Figure 6), suggesting that this



difference may also be related to the bound water or interlayer water of clay minerals.

[28] The gas saturation we compute ranges from ~0 to 5% (f 3b). The downhole distribution of gas appears very heterogeneous, with several zones of increased gas content. The thickest of these zones extends from 1050 mbsf to ~1200 mbsf and also includes the highest level of gas saturation. The upper extent of this zone coincides with the Unit IIIa-IIIb boundary (1037.7 mbsf) where three shallow faults dipping 3°–10° to the NW have been recognized in log images and interpreted as thrust faults [Saffer *et al.*, 2010]. The base of this zone is located at the depth of a broad maximum in total organic content (TOC), as defined from cuttings samples [Saffer *et al.*, 2010]. This correlation is consistent with the in situ production of gas from local degradation of organic matter, possibly combined with upward gas migration within Unit IIIb. Observations at Site C0009 indicate that sediments deposited in the lower Kumano fore-arc basin, beneath a regional seismic surface (interface S2, in Figure 1), are a likely source of the gas. Considering the heat flow of 40 mW/m² measured at nearby Site C0002 and estimated downhole temperatures of ~50°C at ~1600 mbsf at Site C0009 and < 40°C at 1200 mbsf at Site C0002 [Kinoshita *et al.*, 2009; Saffer *et al.*, 2010], gas produced at these depths is most likely biogenic.

[29] The seismically traceable layer that includes Unit III at Site C0009 and its equivalent at Site C0002 is thickest in two minibasins, one located around Site C0009 and one forming a syncline ~6 km SE of Site C0009 (Figure 1). The overlying Unit II is a sequence of muddy and sandy turbidites tilted to the north by about 5° and onlapping seismic surface S2 [Saffer *et al.*, 2010]. At Site C0002, Unit II hosts gas hydrate at the level of the BSR at about 400 mbsf. The organic matter generating the gas hydrate is likely not local to Site C0002, as neither lignite nor wood were found in the sediments of any Unit at C0002. Gas may therefore have migrated to this site to form the gas hydrate. We suggest that the gas originates from organic rich layers in the basins buried below seismic surface S2, migrates upward, and accumulates in the dipping layers of coarser sediments deposited above the seismic surface. Subsequently, the gas would migrate updip toward the southern (seaward) edge of the Kumano Basin in the vicinity of Site C0002. This may explain why the BSR displays a stronger reflectivity in the seaward part of the basin (near Site C0002) and not immediately above

the deep basins further landward, near Site C0009 (Figure 1).

8. Conclusions

[30] We used high-quality sonic data obtained at Site C0009 to infer the porosity and gas saturation within the sediments of the Kumano fore-arc basin, offshore Japan. Two primary results are generated from these analyses. First, our results show that the effective porosity affects the sonic properties of the clay sediments at the bottom of the borehole (~1500 mbsf). We generate consistent results if we compare the effective porosity derived from CEC analysis on core samples, porosity estimated from the resistivity logs, and the results of our inversion of sonic log data. We also obtain good agreement between the total porosity derived from litho-density data and the total porosity from moisture and density data on core samples. As a result of these reliable and consistent data sets, we can estimate the water content stored in the intergranular porosity, a parameter otherwise difficult to obtain in a borehole with limited coring.

[31] Second, we provide further constraint on the porosity and gas saturation within the Kumano Basin sediments. We infer that a substantial amount of water, corresponding to about 10% porosity, is bound to clay minerals. The gas saturation does not exceed 5%, but this is enough to alter the *P* wave velocity profile substantially. Our inversion results show that the gas distribution is heterogeneous, but that most of the gas occurs within a lithologic unit having a high organic carbon content. This suggests that in situ bacterial gas production is the primary factor controlling free gas distribution at Site C0009 and probably within the fore-arc basin as a whole. However, the distribution of free gas and gas hydrate at the scale of the Kumano fore-arc basin suggests that gas is ultimately able to escape from the organic carbon rich layers deposited in the lower part of the basin and migrate obliquely along permeable fractures and/or dipping sand layers to shallower and more seaward parts of the basin.

Acknowledgments

[32] The authors gratefully acknowledge the support provided by the D/V *Chikyu* drilling crew, logging staff, and laboratory technicians. This work benefited from interaction with the Expedition 319 Scientific Party. We thank also the editor and an anonymous reviewer for their help with improving this



paper. This research used samples and data provided by the Integrated Ocean Drilling Program (IODP). European authors would like to thank ECORD for their support, and the French authors are furthermore grateful to INSU. The CEC measurements were made in the INRA soil laboratory of Arras.

References

- Aagaard, P., and J. Jahren (2010), Special issue introduction: Compaction processes—Porosity, permeability and rock properties evolution in sedimentary basins, *Mar. Pet. Geol.*, 27(8), 1681–1683, doi:10.1016/j.marpetgeo.2010.07.001.
- Archie, G. E. (1942), The electrical resistivity log as an aid in determining some reservoir characteristics, *JPT J. Pet. Technol.*, 5, 1–8.
- Avseth, P., T. Mukerji, and G. Mavko (2005), *Quantitative Seismic Interpretation*, Cambridge Univ. Press, Cambridge, U. K., doi:10.1017/CBO9780511600074.
- Blum, P. (1997), Physical properties handbook: A guide to the shipboard measurement of physical properties of deep-sea cores, *Tech. Note 26*, Ocean Drill. Program, College Station, Tex. (Available at <http://www-odp.tamu.edu/publications/tnotes/tn26/INDEX.HTM>)
- Bourlange, S., P. Henry, J. C. Moore, H. Mikada, and A. Klaus (2003), Fracture porosity in the decollement zone of Nankai accretionary wedge using Logging While Drilling resistivity data, *Earth Planet. Sci. Lett.*, 209, 103–112, doi:10.1016/S0012-821X(03)00082-7.
- Brie, A., F. Pampuri, A. F. Marsala, and O. Meazza (1995), Shear sonic interpretation in gas-bearing sands, paper presented at 70th Annual Technical Conference and Exhibition, Soc. of Pet. Eng., San Antonio, Tex.
- Brown, K. M., and B. Ransom (1996), Porosity corrections for smectite-rich sediments: Impact on studies of compaction, fluid generation, and tectonic history, *Geology*, 24(9), 843–846, doi:10.1130/0091-7613(1996)024<0843:PCFSRS>2.3.CO;2.
- Conin, M., S. Bourlange, P. Henry, and the Expeditions 314/315/316 Scientists (2008), Interpretation of LWD resistivity from Nankai accretionary wedge in the light of clay physico-chemical properties, *Eos Trans. AGU*, 89(53), Fall Meet. Suppl., Abstract T31B-1999.
- Ellis, D. V., and J. M. Singe (Eds.) (2007), *Well Logging for Earth Scientists*, 2nd ed., Springer, Dordrecht, Netherlands, doi:10.1007/978-1-4020-4602-5.
- Henry, P. (1997), Relationship between porosity, electrical conductivity and cation exchange capacity in Barbados wedge sediments, *Proc. Ocean Drill. Program Sci. Results*, 156, edited by T. H. Shipley, P. Blum, and J. M. Bahr, pp. 137–149, Ocean Drill. Program, College Station, Tex.
- Kinoshita, M., G. Moore, R. von Huene, H. Tobin, and C. Ranero (2006), The seismogenic zone experiment, *Oceanography*, 19(4), 28–38.
- Kinoshita, M., H. Tobin, J. Ashi, G. Kimura, S. Lallemand, E. J. Scream, D. Curewitz, H. Masago, K. T. Moe, and the Expedition 314/315/316 Scientists (2009), *Proceedings of the Integrated Drilling Program Expeditions*, vol. 314/315/316, doi:10.2204/iodp.proc.314315316.2009, Ocean Drill. Program, College Station, Tex.
- Lide, D. R. (Ed.) (1991), *CRC Handbook of Chemistry and Physics*, 72nd ed., CRC Press, Boca Raton, Fla.
- Lin, W., et al. (2010), Present-day principal horizontal stress orientations in the Kumano forearc basin of the southwest Japan subduction zone determined from IODP NanTroSEIZE drilling Site C0009, *Geophys. Res. Lett.*, 37, L13303, doi:10.1029/2010GL043158.
- Mavko, G., T. Mukerji, and J. Dvorkin (1998), *The Rock Physics Handbook*, Cambridge Univ. Press, Cambridge, U. K.
- Mindlin, R. D. (1949), Compliance of elastic bodies in contact, *J. Appl. Mech.*, 16, 259–268.
- Mitchell, J. K., and K. Soga (2005), *Fundamentals of Soil Behavior*, 3rd ed., John Wiley, Hoboken, N. J.
- Moore, G. F., et al. (2009), Structural and seismic stratigraphic framework of the NanTroSEIZE Stage 1 transect: Kumano 3D seismic survey [online], *Proc. Integrated Ocean Drill. Program Exped.*, 314/315/316, 46 pp., doi:10.2204/iodp.proc.314315316.102.2009.
- Orsini, L., and J. C. Remy (1976), Utilisation du chlorure de cobaltihexamine pour la détermination simultanée de la capacité d'échange et des bases échangeables des sols, *Sci. Sol.*, 4, 269–275.
- Ransom, B., and H. C. Helgeson (1994b), A chemical and thermodynamic model of dioctahedral 2:1 layer clay minerals in diagenetic processes: Regular solution representation of interlayer dehydration in smectite, *Am. J. Sci.*, 294, 449–484, doi:10.2475/ajs.294.4.449.
- Saffer, D., L. McNeill, E. Araki, T. Byrne, N. Eguchi, S. Toczko, K. Takahashi, and the Expedition 319 Scientists (2009), NanTroSEIZE Stage 2: NanTroSEIZE riser/riserless observatory, *Integr. Ocean Drill. Program Prelim. Rep.*, 319, doi:10.2204/iodp.pr.319.2009.
- Saffer, D., L. McNeill, T. Byrne, E. Araki, S. Toczko, N. Eguchi, K. Takahashi, and the Expedition 319 Scientists (2010), *Pacific Equatorial Age Transect*, *Proc. Integr. Ocean Drill. Program*, 319, doi:10.2204/iodp.proc.319.2010.
- Wang, H. F. (2000), *Theory of Linear Poroelasticity with Applications to Geomechanics and Hydrogeology*, Princeton Univ. Press, Princeton, N. J.

1 **A full permeability profile of Kumano Forearc Basin and Accretionary** 2 **Wedge sediments, Nankai Trough from modeling of electrical data**

3 Mai-Linh Doan¹, Demian Saffer², David Boutt³, Lisa McNeill⁴

4 1 ISTerre, CNRS, Université Joseph Fourier, Grenoble, France

5 2 Pennsylvania State University, State College, USA

6 3 University of Massachusetts,

7 4 National Oceanography Centre Southampton, University of Southampton, Southampton, UK

8 Corresponding author: Mai-Linh.Doan@ujf-grenoble.fr; ISTerre, BP53, 38041 GRENOBLE Cedex 9, FRANCE

9 **Abstract**

10 During the Integrated Oceanic Drilling Program (IODP) Expedition 319, Site C0009
11 borehole was drilled within the Kumano Basin, a forearc basin related to the Tō-Nankai
12 subduction trench offshore the Kii peninsula, and underlying accretionary wedge sediments.
13 This was the first scientific ocean drilling borehole drilled with riser technology, which
14 enables the use of drilling mud. Because of its higher density, mud was overpressurized
15 relative to the in-situ fluid pressure. By quantifying this process, we could estimate the
16 hydraulic parameters along the borehole.

17 The HRLA tool (High Resolution Laterolog Array) simultaneously records apparent
18 resistivity for different depths of penetration. By inverting the HRLA data, we could compute
19 the varying invasion diameter down the borehole, which can then be converted into
20 permeability. This data is complementary to the direct permeability measurements done with
21 the wireline Modular Testing Tool (MDT): it enable the extrapolation of the point-wise
22 hydraulic tests to the full borehole.

23 Results indicate that permeability at the metric scale varies little with depth (over the
24 1600 m borehole extent), changing significantly only when entering a new lithology unit.
25 Within each lithological unit, permeability remains almost constant, in contrast with porosity
26 profiles that decrease more sharply with depth. The permeability values are several orders of
27 magnitude larger than the permeability measured from cores. The permeability we derived is
28 at the metric and seems therefore to be controlled by the fracture density.

29 **1) Introduction**

30 The Nankai Trough Seismogenic Zone Experiment (NanTroSEIZE) aims to understand
31 the mechanics of the Tō-Nankai subduction zone and its accretionary prism, the location of
32 several historic earthquakes of magnitude greater than 8. The most recent earthquakes
33 occurred in 1944 and 1946 [Kinoshita *et al.*, 2006]. The NanTroSEIZE program is a
34 coordinated, multi-expedition drilling project within IODP, with several holes drilled along a
35 transect perpendicular to the Nankai trough (figure 1). Hole C0009A was drilled within the
36 sediments of the Kumano forearc basin and underlying accretionary wedge sediments. The
37 expedition included several breakthroughs in academic oceanic drilling [Araki *et al.*, 2009]:
38 e.g. first riser deployment, first cuttings and first mud gas recovery and analysis. The
39 HRLATM (High Resolution Laterolog Array) could be used to recover first-class electric data.
40 In this paper, we show how these data highlight the invasion of the overpressured mud filtrate
41 into the formation and provide indirect but continuous information on permeability.

42

43 We aim to quantify invasion within Hole C0009A, that extends down to 3600 mbsl
44 (1600 mbsf), with casing to 700 mbsf. Only the last 90 meters of the borehole were cored,
45 however cuttings collected throughout the majority of the borehole were used to decipher
46 sedimentology. Integration of cuttings analysis with logging data allowed the recognition of
47 four main lithological units [Saffer *et al.*, 2010]:

- 48 • Unit I (shallow forearc basin sediments) extends above the logged section and is
49 not discussed in this paper.
- 50 • Unit II extends from 700 mbsf to 790mbsf consisting of shallow forearc basin
51 sediments. It is composed predominantly of unconsolidated silty clay, with some
52 silt and sand interbeds and minor interbeds of volcanic ash.

- 53 • Unit III extends from 790mbsf to 1280mbsf (lower forearc basin sediments). It is
54 dominated by silty mud and mudstone. Subunits IIIa and IIIb are separated by a
55 sub-horizontal fault contact identified in logging images. Sediments at the base of
56 Unit III (the 1168–1280 mbsf interval) appear to be similar to the lower Unit III
57 at Site C0002. Gas monitoring showed intense degassing in this unit.
- 58 • Unit IV extends below the unconformity at 1280mbsf representing a 3.3 Myr
59 hiatus. It is primarily composed of consolidated silty mudstone and minor silt
60 interbeds. In terms of sedimentary facies, this unit resembles the Unit IV accreted
61 sediments below the forearc basin at nearby Site C0002 but clear evidence of
62 accretion in a trench setting is lacking at Site C0009. It is therefore interpreted
63 either as a weakly deformed package of accreted trench sediments, or as trench-
64 slope deposits overlying the early prism.

65 ***2) Deriving permeability from invasion of the formation by borehole fluids***

66 To ensure borehole stability during drilling and to prevent blowouts, borehole mud is
67 overpressured relative to the formation pore pressure. This tends to induce the invasion of
68 drilling mud into the formation sediments/rocks, hence invasion can be used as a passive in-
69 situ hydraulic test. Quantifying this phenomenon can provide an estimate of formation
70 permeability at the scale of invasion (a few tens of centimeters). As data are acquired along
71 the whole borehole, we can generate a full permeability profile, that complements the point-
72 wise hydraulic tests conducted during Expedition 319 with the MDT (Modular Dynamic
73 formation Tester) wireline tool and the permeability measurements on cores.

74 **2 a) Laterolog data**

75 The HRLATM laterolog wireline tool records simultaneously the apparent resistivity data
76 for six electrode configurations. Mode 0 has the shallowest depth of penetration and is mainly
77 sensitive to the borehole fluid. Mode 5 exploits the full tool length (24.ft) to reach a depth of
78 penetration of 50 inches. Vertical resolution reaches 12" (~30 cm). The different depths of
79 penetration give insight into the lateral heterogeneities of the formation, and especially to the
80 extent of invasion of the rock formation by the borehole fluid.

81 The apparent resistivity curves recorded in Hole C0009A are given in Figure 1. The
82 resistivity curve for the smallest depth of penetration is separated from the resistivity curve
83 for the largest depth of penetration, indicating lateral contrasts in resistivity. Drilling mud has
84 a high content of NaCl, KCl and NaOH, and is very conductive. Hence mud filtrate
85 significantly lowers the electrical resistivity of the invaded zone, and strongly affects the
86 shallowest penetration HRLA measurements.

87 A first inspection of the raw permeability shows a good correlation between the ratio of
88 the two deepest HRLA resistivities and the different lithological units. From a visual
89 inspection, we can estimate that unit II is much more invaded than units III and IV, and
90 presumably more permeable. Invasion within each lithological unit seems broadly
91 homogeneous, with major changes only at unit boundaries.

92 **2 b) Quantifying invasion from electrical data**

93 To better quantify the extent of invasion, we need to invert the spatial variation of
94 resistivity from the electrical data.

95 We assume the invasion front is sharp. There are therefore three axisymmetric zones: (1)
96 the borehole, of radius r_b , filled with mud, whose resistivity R_m is very small due to the large
97 quantity of salt and soda inserted within the liquefied mud; (2) the invaded zone of diameter

98 d_{inv} , its resistivity R_{x0} ; and (3) the rock formation of resistivity, traditionally named “true
 99 resistivity” R_t . The five parameters of the model (r_b , d_{inv} , R_m , R_{x0} and R_t) can be
 100 determined from the five recorded resistivity measurements.

101 We used the Schlumberger Geoframe software to invert the invasion data for all logged
 102 depths. Results were tested by computing the HRLA results computed with two direct models
 103 made with COMSOL (<http://www.comsol.com/products/multiphysics/>) and Getfem++
 104 (<http://download.gna.org/getfem/html/homepage/index.html>).

105 Data are summarized in Figure 2a, together with the duration time between drilling and
 106 logging.

107 **2 c) Hydrologic model of invasion**

108 Invasion of the medium by borehole fluid is controlled by the hydraulic properties of the
 109 medium. If the borehole were perfectly cylindrical and if the medium were isotropic, the fluid
 110 diffusion of the medium is expressed as

$$111 \quad \frac{\partial p}{\partial t} = \frac{D_{th}}{r} \frac{\partial}{\partial r} \left(r \frac{\partial p}{\partial r} \right) \quad (1)$$

112 where D_{th} is the hydraulic diffusivity in m^2/s . The hydraulic diffusivity is the
 113 combination of the permeability k in m^2 , of the specific storage of medium S_s in Pa^{-1} , and of
 114 the fluid viscosity η (in Pa.s)

$$115 \quad D_{th} = \frac{k}{\eta S_s} \quad (2)$$

116 We assume that the fluid invasion process does not affect the borehole overpressure
 117 $\Delta p = p_{mud} - p_{formation}$. Using Laplace transform, Carslaw and Jaeger (1959) compute the
 118 solution of this problem as a series, whose first order solution is

119
$$p = \Delta p \sqrt{\frac{r_b}{r}} \operatorname{erfc}\left(\frac{r - r_b}{\sqrt{D_{th} t}}\right) \quad (3).$$

120 We infer the flow rate coming out of the borehole on a section of length L as

121
$$Q = -2\pi r_b L \frac{k}{\eta} \frac{\partial p}{\partial r} \Big|_{r=r_b} = -2\pi \frac{k}{\eta} L r_b \Delta p \left(-\frac{1}{2r_b} - \frac{2}{\sqrt{\pi D_{th} t}} \right) \quad (4).$$

122 From mass conservation, the fluid invading the formation to an invasion radius $r_{inv} = \frac{d_{inv}}{2}$ has
 123 percolated through the borehole wall during the invasion time t_{inv} , taken as the duration time
 124 between drilling and logging.

125
$$\int_0^{t_{inv}} Q dt = \pi (r_{inv}^2 - r_b^2) L \phi \quad (5)$$

126 Using equation (4), we express the total volume of borehole fluid invading the formation as

127
$$\int_0^{t_{inv}} Q dt = \frac{k}{\eta} L \Delta p \left(t_{inv} + 8r_b \sqrt{\frac{\pi t_{inv}}{D_{th}}} \right) \quad (6)$$

128 Inverting this equation, we retrieve the permeability from the invasion diameter, the invasion
 129 duration and porosity:

130
$$k = \frac{\eta}{t} \frac{\phi}{\Delta p} (r_{inv}^2 - r_b^2) + 32 \frac{\eta}{t} \frac{S_s}{\pi} r_b^2 + \frac{8r_b}{\pi} \frac{\eta}{t} \sqrt{\frac{S_s}{\Delta p}} \sqrt{\pi \phi (r_{inv}^2 - r_b^2) + 16r_b^2 S_s \Delta p} \quad (7)$$

131 Typically $S_s \approx 10^{-10} \text{Pa}^{-1}$ and $\Delta p \approx (\rho_{mud} - \rho_w)gh \approx 7 \times 10^6 \text{Pa}$. Hence $S_s \ll 1/\Delta p$, and the

132 above equation simplifies to

133
$$k = \frac{(r_{inv}^2 - r_b^2) \eta \phi}{t_{inv} \Delta p} \quad (8)$$

134 **2 d) Permeability results**

135 Several parameters need to be determined to use equation 8. In the controlled environment
 136 of riser drilling at Hole C0009A, most parameters could be retrieved (Table 1).

137 For each logging depth, we retrieved the duration time between drilling operations and
138 logging. We compile this information in Figure 2b.

139 A full profile of effective porosity (porosity contributing to the storage and transportation
140 of external fluids) has been obtained from extrapolation of core data (in part of the borehole)
141 with the help of sonic data (for the entire borehole section discussed here) (Doan et al, 2011).
142 The major unknown is η , the viscosity of the fluids circulating through the formation. It
143 ranges between $72 \times 10^{-3} \text{Pa} \cdot \text{s}$, the viscosity of the mud inserted within the borehole, and
144 $210^{-3} \text{Pa} \cdot \text{s}$, the viscosity of pure water. We used a viscosity of $20 \times 10^{-3} \text{Pa} \cdot \text{s}$, to fit the
145 permeability results determined from the MDT dual packer tool at 1540 mbsf, a measurement
146 similarly conducted at the metric scale.

147 Figure 2c gives the permeability results computed from this operation. There is no
148 significant variation in permeability with depth within each lithological unit, but variability
149 between units. In unit II, average permeability is $k = 3 \times 10^{-16} \text{m}^2$, in unit III:
150 $k = 1.5 \times 10^{-16} \text{m}^2$, in unit IV: $k = 8 \times 10^{-17} \text{m}^2$. Poor borehole conditions in unit IV prevent a
151 good quantification of permeability except in the short section in gauge, near 1540 mbsf,
152 where the MDT tests were conducted.

153 Permeability differences are clearly a function of lithology, varying between units. The
154 more sandy unit II (upper Kumano forearc basin) has the highest permeability, greater than
155 the finer grained unit III of the lower Kumano forearc basin. In unit IV, the discrepancy
156 between effective and total porosity (figure 4) suggest large clay content. This may explain
157 why permeability diminishes although fracture permeability is higher within this unit, which
158 is interpreted as the upper part of the early accretionary prism. We note that our results are
159 reliable only in the cleanest part of the borehole, where it is kept in gauge, which suggests that
160 fracture density is only moderate in these borehole sections.

161

162 **3) Discussion**

163 **3 a) Mud cake**

164 Clay particles within the mud should build a mud cake isolating the borehole from the
165 formation. In case of Hole C0009A, several clues indicate that mud cake is very poor. First,
166 the inversion of the HRLA results suggests a large invasion diameter. This result is confirmed
167 by the dual-packer hydraulic test with the Modular Dynamic Formation Tester (MDT). Boutt
168 *et al.* (2012) could numerically fit the data of the MDT hydraulic test, only if an invaded zone
169 30 cm thick preexists. Second, the gamma-ray data is flat (non-variable), whereas drill
170 cuttings suggest lithological variation downhole. Spectral gamma-ray data should decipher
171 the contribution of the K-Cl rich borehole mud and of the K-rich clay within the formation.
172 Yet, the K content within the formation is non-variable. This suggests that the K-Cl rich
173 borehole fluid saturated the formation.

174 Good quality mud cake would limit the invasion radius and hence should be considered
175 when estimating permeability from invasion. However, because of ample evidence of a
176 poorly developed mud cake, we can assume that the permeability data derived here from the
177 inversion of invasion is a valid estimate.

178 **3 b) Comparison with other hydrological data from the borehole**

179 The permeability derived from the laterolog data is a good complement to the Modular
180 Dynamic formation Tester (MDT) tool results. This tool gave two different types of data. The
181 first one is the dual-packer test, in which a pumping test is conducted within a chamber of 1 m
182 borehole length separated by two packers. Boutt *et al.* (2012) interpret the dual-packer test at a
183 depth of ~1540 mbsf and derive a formation permeability equal to $k = (8 \pm 3) \times 10^{-17} \text{ m}^2$,

184 which is the same order of estimate as the permeability computed from electrical invasion in
185 this study.

186 The other type of MDT hydraulic test is the single probe test. A metallic hose is punched
187 through the mud cake to perform a mini slug-test. A small volume of water (a few cc) is
188 pumped out and the recovery documents the hydraulic properties of the local formation.
189 Several single-probe tests were performed down the C0009A borehole (figure 2b). Many of
190 these test results agree well with the permeability profile determined from invasion here. The
191 other test results give larger permeability than the invasion-derived values. Poor mud cake
192 development may explain this trend: as the borehole fluid can contribute to the pressure
193 recovery of the single probe test, recovery from pumping tests is faster, yielding larger
194 apparent permeability. Also, the electrical method measures formation properties at the metric
195 scale (relative to centimetric scale for the single probe test), and therefore may average out the
196 permeability variations sampled by the single-probe. The permeability profile we derive from
197 log-derived invasion values is therefore smoothed.

198 All hydraulic tests performed *in situ* yield permeability results much larger than the core
199 permeability (around 10^{-19}m^2 [Boutt et al, 2012; Saffer et al, 2013]) in unit IV. This has been
200 attributed to the presence of fractures at the metric scale, most common in this unit (likely
201 accretionary wedge material).

202 The HRLA data are recorded over lengths reaching 24ft (~7.3m), with a nominal vertical
203 resolution of 12" (~30cm). The permeability data derived from HRLA data therefore have the
204 same scale as the MDT data, which explains the consistent results.

205 **3 c) Physical control of permeability within the Kumano Basin**

206 In clay minerals, water can be either bound to hydrous minerals (e.g. smectite), or located
207 in pores between the grains [Mitchell and Soga, 2005]. Effective porosity refers to the volume

208 of water contained only in the intergranular pores [Ellis and Singe, 2007]. Total porosity
209 corresponds to the sum of this volume and the volume of water bound to clay minerals and is
210 computed from Moisture And Density measurements [Blum, 1997; Henry, 1997]. Bound-
211 water content is computed from Cation Exchange Capacity (CEC) measurements [Henry,
212 1997; Bourlange et al., 2003; Conin et al. 2011]. Total porosity, bound water content, and
213 effective porosity, were determined on core samples (Figure 3b), but cuttings from the rest of
214 the borehole were not reliable for this purpose. Using high-quality sonic data, Doan et al
215 [2011] were able to extrapolate both total and effective porosity from core along the whole
216 C009A borehole (figure 3b). Sonic data have a large depth of penetration. They are therefore
217 less sensitive to poor borehole condition than electric data. Hence, the porosity profile of
218 figure 3b covers a larger portion of the borehole than the permeability data of figure 3a.

219 There is a general trend of reduction of porosity with depth, with no sharp changes in
220 porosity when entering lithological units, contrary to permeability. Effective porosity is much
221 lower than total porosity, especially in unit IV, where it reaches 15%. This suggests large
222 amount of bound water, and therefore large clay content (Doan et al, 2011).

223 Although the effect of scale on permeability is attributed to fractures (Boutt et al, 2012),
224 permeability correlates with the microphysical properties assumed to control core
225 permeability. Figure 4a shows that permeability is positively correlated with macroporosity,
226 derived from sonic data. Permeability is also negatively correlated to clay content retrieved
227 from cutting and core data (figure 4b). That dependence of macroscopic data on small-scale
228 properties in a fracture-dominated medium may be an indirect effect on the control of the
229 fracture pattern by lithology.

230 **4) Conclusion**

231 In this paper we show that a full and reliable formation permeability profile can be
232 derived from resistivity log data, in this example from the Kumano forearc basin and upper
233 accretionary prism of the Nankai Trough forearc. We use a simple model of invasion of the
234 formation by the borehole fluid from these continuous log data to extend the precise but
235 point-wise MDT results.

236 Combining these techniques and results, we find that the formation permeability range at
237 the metric scale is much larger than the permeability determined from cores (see also Boutt et
238 al (2012) for extended discussion about scale effects). Permeability is constant within each
239 lithological unit but varies between units, suggesting that compaction and loading history is
240 not a significant controlling parameter of permeability within the Kumano basin. Surprisingly,
241 the lowest permeability was recorded in the accretionary wedge unit (below the Kumano
242 forearc basin), which is more fractured, but also richer in water-bounding clay. Precisely
243 defining how these competing parameters determine hydrologic properties at a range of scales
244 is therefore crucial for proper assessment of the hydraulic properties of accretionary wedge
245 and basin materials, one of the objectives of the subsequent phases of rising drilling of the
246 NantroSEIZE project.

247

247 **Bibliography**

- 248 Blum, P. (1997), Physical properties handbook: a guide to the shipboard measurement of
249 physical properties of deep-sea cores, *ODP Tech. Note*, 26. doi:10.2973/odp.tn.26.1997
- 250 Bourlange, S., Henry, P., Moore, J.C., Mikada, H. and A. Klaus (2003), Fracture porosity in
251 the decollement zone of Nankai accretionary wedge using Logging While Drilling
252 resistivity data. *Earth Planet. Sci. Lett.*, 209, 103-112.
- 253 Boutt, D.F., Saffer, D.M., Doan, M-L., Lin, W., Ito, T., Kano, Y., Flemings, P., McNeill,
254 L.C., Byrne, T., Hayman, N.W., and Moe, K-T (2012), Scale dependence of in-situ
255 permeability measurements in the Nankai accretionary prism: The role of fractures,
256 *Geophys. Res. Lett.*, 39, L07302, doi:10.1029/2012GL051216.
- 257 Conin M., Henry P., Bourlange S., Raimbourg, H. And T. Reuschlé (2011), Interpretation of
258 porosity and LWD resistivity from the Nankai accretionary wedge in the light of clay
259 physicochemical properties: Evidence for erosion and local overpressuring, *Geochem.*
260 *Geophys. Geosyst.*, 12, Q0AD07, doi:10.1029/2010GC003381.
- 261 Carslaw, H. C., and J. C. Jaeger (1959), *Conduction of Heat in Solids*, Oxford Univ. Press,
262 New York.
- 263 Doan, M.-L., M. Conin, P. Henry, T. Wiersberg, D. Boutt, D. Buchs, D. Saffer, L. C.
264 McNeill, D. Cukur, and W. Lin (2011), Quantification of free gas in the Kumano fore-arc
265 basin detected from borehole physical properties: IODP NanTroSEIZE drilling Site
266 C0009, *Geochem. Geophys. Geosyst.*, 12, Q0AD06, doi:10.1029/2010GC003284.
- 267 Ellis, D. V. and J.M. Singe (2007), *Well logging for Earth scientists*, 2nd edition, Springer,
268 601-602

269 Henry, P. (1997), Relationship between porosity, electrical conductivity and cation exchange
270 capacity in Barbados wedge sediments, in : T.H. Shipley, P. Blum and J.M. Bahr (Eds.),
271 Proc. ODP Sci. Results 156, Ocean Drilling Program, College Station, TX, 137-149.

272 Kinoshita, M., Tobin, H., Ashi, J., Kimura, G., Lallemand, S., Screaton, E.J., Curewitz, D.,
273 Masago, H., Moe, K.T., and the Expedition 314/315/316 Scientists (2009). Proc. IODP,
274 314/315/316: Washington, DC (Integrated Ocean Drilling Program Management
275 International, Inc.). doi:10.2204/iodp.proc.314315316.2009

276 Mitchell and Soga, K. *Fundamentals of soil behavior* (2005). 3rd edition. J. Wiley & Sons.

277 Moe, K.T., Ito, T., Lin, W-L., Doan, M-L, Boutt, D., Kawamura, Y., Khong, C-K., McNeill,
278 L.C., Byrne, T., Saffer, D., Araki, E., Eguchi, N., Sawada, I., Flemings, P., Kano, Y., Moore,
279 C., Kinoshita, M., & Tobin, H. (2012), Operational Review of the First Wireline In Situ Stress
280 Test in Scientific Ocean Drilling, Scientific Drilling, doi: 10.2204/iodp.sd.13.06.2011

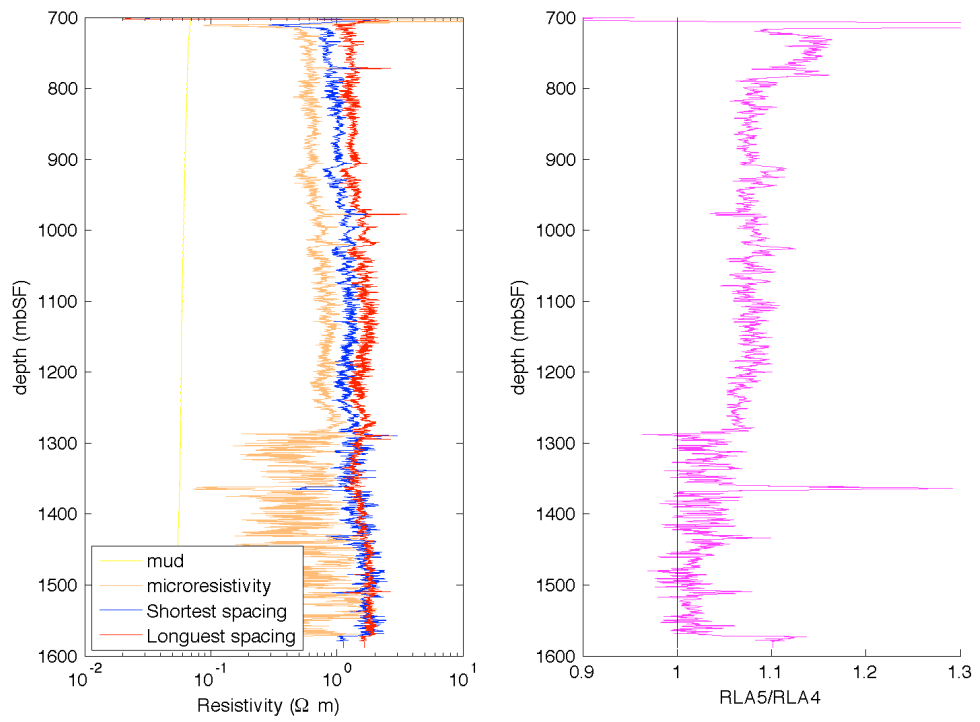
281 Saffer, D., L. McNeill, E. Araki, T. Byrne, N. Eguchi, S. Toczko, K. Takahashi, and the
282 Expedition 319 Scientists (2009), NanTroSEIZE Stage 2: NanTroSEIZE riser/riserless
283 observatory. IODP Prel. Rept., 319. doi:10.2204/iodp.pr.319.2009.

284 Saffer, D., L. McNeill, E. Araki, T. Byrne, N. Eguchi, S. Toczko, K. Takahashi, and the
285 Expedition 319 Scientists (2010), NanTroSEIZE Stage 2: NanTroSEIZE riser/riserless
286 observatory. IODP Rept., 319. doi:10.2204/iodp.pr.319.2010

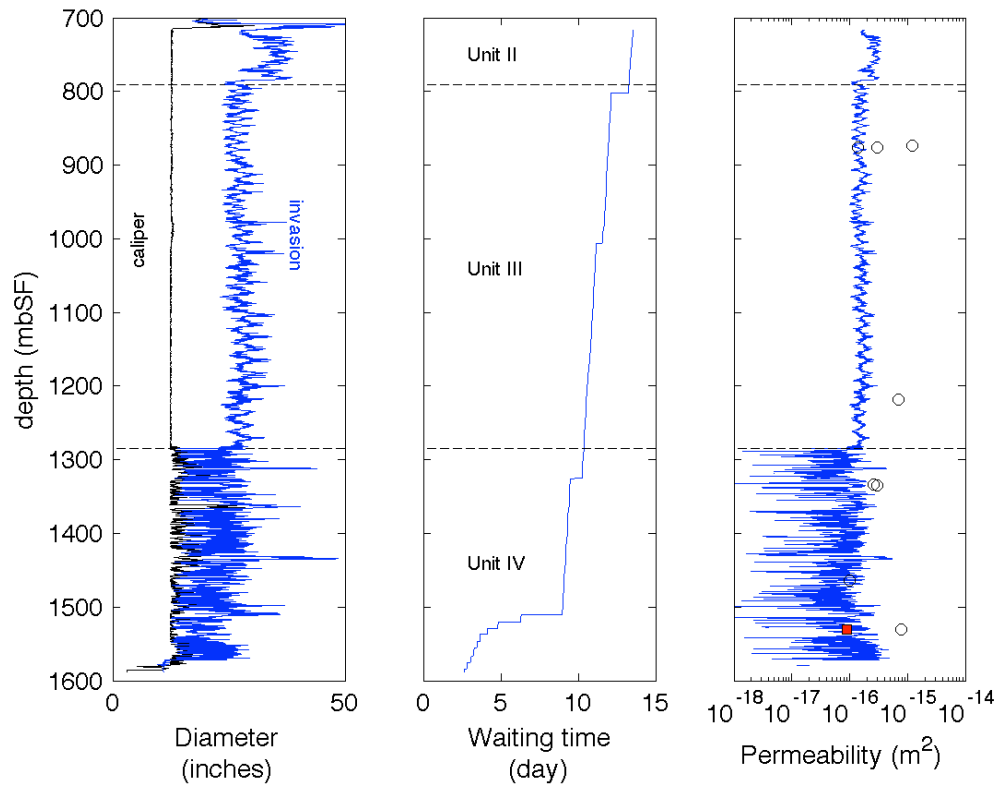
287 Saffer, D.M., P.B. Flemings, D. Boutt, M-L. Doan, T. Ito, L. McNeill, T. Byrne, M. Conin,
288 W. Lin, Y. Kano, E. Araki, N. Eguchi, and S. Toczko. In situ stress and pore pressure in
289 the Kumano Forearc Basin, offshore SW Honshu from down-hole measurements during
290 riser drilling. Geophys.

291

292

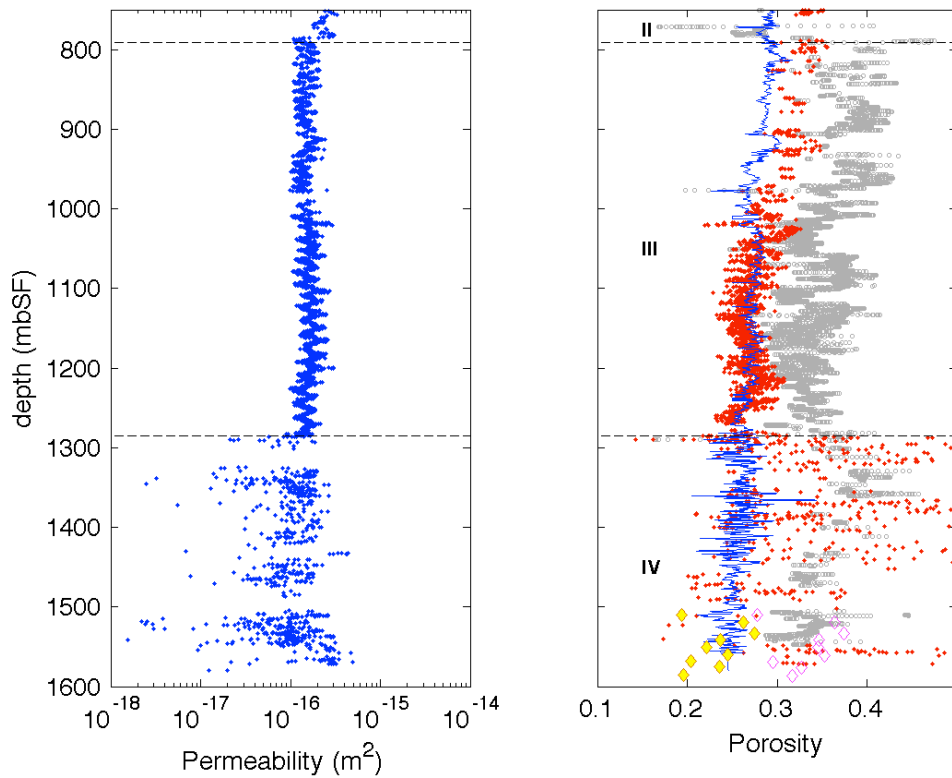


292
 293 **Figure 1 Electrical data collected within Hole C0009A.** The HRLA tool records apparent
 294 resistivities for various depths of penetration. Mud conductivity and resistivity of the invaded
 295 zone were recorded independently.



296

297 **Figure 2: Inversion of HRLA data at Hole C0009A.** a) Estimation of invasion extent from
 298 inversion of HRLA data. b) Duration time of invasion process, between opening of the hole
 299 by drilling and logging time, from driller logs. c) Computation of permeability profile,
 300 compared with MDT results, either single probe (black circles) or dual-packer (red square).



301

302 **Figure 3. Comparison of the full permeability profile derived from inversion of invasion**

303 **and the full porosity profile derived from sonic data at Hole C0009A. a) Permeability data**

304 **derived from inversion. We kept data with good borehole conditions ($rb < 12.5''$) . b)**

305 **Effective porosity data derived from sonic data [Doan et al, 2012] (solid blue line) is**

306 **consistent with the effective porosity data derived from Archie law applied the resistivity of**

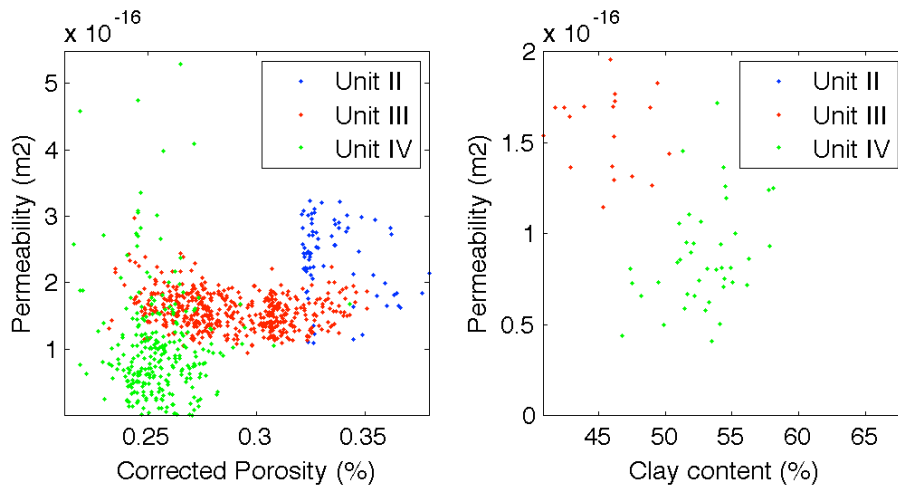
307 **the invaded zone (red dots, with extensive porosity overestimation where borehole conditions**

308 **are poor) and the effective porosity derived from cores (yellow diamonds). Effective porosity**

309 **is less than the total porosity, as computed from the lithodensity log (gray circles) or the core**

310 **moisture and density (mauve open diamonds).**

311



311
 312 **Figure 4. Relationship between permeability and other hydrological parameters, Hole**
 313 **C0009A.** (a) Cross-plot between the full metric-scale permeability profile derived from
 314 inversion of invasion and macroporosity derived from sonic data. Macroporosity is the
 315 intergranular porosity, with interconnected pores expected to control the matrix permeability.
 316 (b) Cross-plot between permeability and clay content derived directly from cuttings and core
 317 data.

318

r_b	Borehole radius	HDMX/2 (maximum caliper diameter)
d_{inv}	Diameter of invasion	Inversion of HRLA laterolog data
Δp	Difference between pressure in the well and in the borehole	MDT pore pressure - hydrostatic pressure
η	Fluid viscosity	20 Pa·s
ϕ	Macroporosity	From SonicScanner data (Doan et al, 2011)
t_{inv}	Duration of invasion	Time between drilling (from driller's log) and logging

319

320 Table 1: List of parameters used in the inversion, and their origin.